# JET PROPULSION LABORATORY
## CALIFORNIA INSTITUTE OF TECHNOLOGY
### PASADENA, CALIFORNIA

Thermo Electron Engineering Corporation, 85 First Avenue, Waltham, Massachusetts 02154

FINAL REPORT FOR THE

THERMIONIC RESEARCH PROGRAM

TASK IV  CONTRACT NO. 950671

VOLUME I

2 August 1965

by

S. Kitrilakis
F. Rufeh
D. Lieb
L. van Someren
J. Weinstein

Prepared for

Jet Propulsion Laboratory
Pasadena, California

Thermo Electron Engineering Corporation, 85 First Avenue, Waltham, Massachusetts 02154

FINAL REPORT FOR THE

THERMIONIC RESEARCH PROGRAM

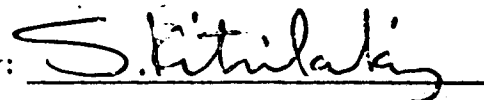TASK IV  CONTRACT NO. 950671

VOLUME I

2 August 1965

by

S. Kitrilakis
F. Rufeh
D. Lieb
L. van Someren
J. Weinstein

Prepared for

Jet Propulsion Laboratory
Pasadena, California

Approved by: S. Kitrilakis

S. Kitrilakis
Research Manager

2

# TABLE OF CONTENTS

## VOLUME I

## TABLE OF CONTENTS (continued)

TABLE OF CONTENTS (continued)

TABLE OF CONTENTS (continued)

TABLE OF CONTENTS (continued)

# LIST OF ILLUSTRATIONS

LIST OF ILLUSTRATIONS (continued)

## LIST OF ILLUSTRATIONS (continued)

## LIST OF ILLUSTRATIONS (continued)

## LIST OF ILLUSTRATIONS (continued)

LIST OF ILLUSTRATIONS (continued)

13

## LIST OF ILLUSTRATIONS (continued)

## LIST OF ILLUSTRATIONS (continued)

LIST OF ILLUSTRATIONS (continued)

LIST OF ILLUSTRATIONS (continued)

# LIST OF TABLES

18

# CHAPTER I

## INTRODUCTION

The purpose of this experimental program was to generate detailed and highly accurate data on the important parameters involved in the operation of a thermionic converter. These data have been taken over a very broad range of parametric variation, so that they will have general validity for future hardware designs, and so that they may be used for insight and substantiation in analytical work leading to a thorough understanding of the physics involved in the conversion process itself. Such understanding will in turn allow further design optimization of hardware converters and provide the guide lines for future experimentation in thermionics and related fields.

Thermo Electron has performed substantial parametric experimentation in the past,[1,2,3,4] and each study has helped point the way to increased converter performance and to further experimentation. At the same time each program has indicated the need for improved test vehicles and measuring equipment to provide greater accuracy and flexibility in experimentation.

The accomplishment of the above objectives required that considerable effort be spent on the design and fabrication of a suitable test converter and instrumentation. Nevertheless, this emphasis on the experimental tools proved to be justified in terms of the quality of the results. Measurements of surface work function, of electron heating, and of the effect of interelectrode spacing changes were performed with much greater accuracy and resolution than ever before, so that the end product was not simply a better description of known effects but the discovery of new relationships among converter parameters.

19

The most obvious demonstration of the results due to the improved equipment and methods of data acquisition is the rapid progress in the analysis and correlation of the conversion process variables. Although further refinements are required in the formulation of a physical model and its mathematical description, a significant step forward has been taken as a result of this work.

A very impressive advance in performance was made by using CsF additive. Increases in power density of 100 to 400 percent have been demonstrated. This improvement is the result of the action of CsF on the emitter surface. This advance is regarded as preliminary, and its confirmation is the subject of future work.

The work with cesium fluoride fell short of the original objective in terms of the quantity of data generated. This was due to unexpected difficulties in handling this additive and the much greater time periods required for the establishment of equilibrium under certain conditions.

In conclusion, it can be said of the first year of this program that it contributed a wealth of parametric data which will provide an important source for diode designers and theoreticians for some time to come; it took a major step forward in the understanding of the converter process, and it provided a firm basis for future improvements in performance and converter physics.

20

# CHAPTER II
## SUMMARY

The first task of this program was the development of a versatile and reliable test converter. All the requirements set for the test vehicle and instrumentation were met even though some were extremely stringent. The converter is equipped with an "active" collector guard ring which can be kept at all times at the same electric potential and temperature as the collector. Extreme variations in heat flux and power output can be handled by the converter. The instrumentation allows accurate measurement and control of all important parameters over very wide ranges. The design, fabrication and calibration of the test converter are given in Chapter III. The instrumentation and its functions are discussed in detail in Chapter IV.

The preparation of the rhenium and tungsten emitter surfaces was carefully controlled, and the results were documented in detail. Both are described in Chapter V so that the emitter surface preparation can be duplicated by any worker in the field desiring to do so, and the surfaces with which all the data were generated are clearly defined. The surfaces that resulted from the treatment outlined in Chapter V were stable at converter operating conditions as far as could be determined.

Once well defined and stable emitter surfaces were produced, their most important property with respect to thermionic conversion, the average work function, was determined. The emitter work function without cesium coverage and as a function of cesium pressure, the collector work function as a function of cesium pressure, and related experiments are reported in Chapter VI. The scatter in the present measurements has been greatly reduced in comparison with previously available data. The reproducibility of the emitter surface preparation

21

techniques is clearly demonstrated by the extremely close agreement of the results of the two rhenium emitters Re-15 and Re-16. The limitations and region of validity of the various methods of work function measurement are clearly defined.

The parametric data of Chapter VII constitute the most accurate and complete such set generated to date. These data have been extended in the present work to cover the parametric variation of emitter temperature, spacing, and collector temperature as well as cesium reservoir temperature, which was the only one used in the past. In addition to their value as a cross-check of the variable cesium reservoir temperature parametric data, these new types of experiments serve the very valuable function of demonstrating directly the dependence of performance on each parameter. This information is of value to the designer, since he can clearly determine the trade-offs among his design variables. It is of even greater value to the physicist concerned with the analysis of the behavior of the converter since, in effect, the answer to his problem lies in the synthesis of the individual dependences into a unified model.

The static data presented in Chapter VII have confirmed the equivalence of static and dynamic testing, as expected. They have also yielded a very useful measurement of electron heating of the collector.

The work with CsF additive is presented in Chapter VIII. It includes work function measurements of the bare tungsten surface and in the presence of CsF only. CsF causes a large increase in the tungsten work function, which is a function of the surface temperature and the pressure of the additive. Activation energy measurements were hampered by the long time periods required for equilibrium to be established.

The performance data generated with Cs and CsF in the device is indeed significant. The effect of the CsF on the emitter is very pronounced, since the Cs reservoir temperature required to achieve a given emission level in the presence of CsF is 30 to 100 °K lower than for the cesium-only case. The 100° reduction is equivalent to a reduction of 0.6 eV in work function. The significance of this is that the same performance can be attained at ten times the spacing as shown by output data in this chapter. At the same spacing an increase of power output of 100 to 400% has been recorded.

The beneficial effects of CsF could not be maintained for more than 30 hours of operation in this experiment. The reasons for this behavior are discussed in Chapter VIII, and future experiments are expected to demonstrate stable operation.

The analytical work of Chapter IX constitutes a significant advance in the understanding of the conversion process. The mathematical description of the converter behavior formulated here corresponds to experimental results quite well, although further refinements will have to be made, especially with regard to the role of collector temperature.

In conclusion, this work has contributed to research converter and instrumentation technology, to the understanding of converter physics, and to the documentation and improvement of converter performance.

CHAPTER III

THE TEST CONVERTER

A.   GENERAL

A new test converter was designed for the experiments to be carried out in this program.   The new design is based on previously used test converters, and has incorporated many features aimed at generating better quality data and providing better control of the test variables. As in the past, planar electrodes are used, but an active guard ring is provided on the collector side.   This feature is aimed at eliminating edge effects and rendering the conversion process as close to one-dimensional as possible.   The interelectrode spacing, as well as the electrode and cesium reservoir temperatures, can be varied over very wide ranges.

The gap between the collector and the guard ring is of the order of half a mil, and the level of the collector face is maintained 0. 0005 inch above the guard ring face.   This geometrical arrangement assures that the collector face will protrude slightly above the guard ring, so that, when the diode is shorted, the emitter will, in fact, short to the collector, unless the collector and emitter faces are not parallel.

Figure III-1 shows the test vehicle in the vacuum enclosure, and Figure III-2 shows the converter cross section.   They will be used to describe the features of the device.   A table of nomenclature follows Figure III-1.   The emitter structure (19) is joined to the guard ring structure (38) by means of the bellows assembly (28, 29).   This bellows assembly consists of flexible flanges (28) and (29) and ceramic parts (24) and (25).   It allows for the adjustment of the spacing between the emitter and collector using the micrometers.   The entire assembly is
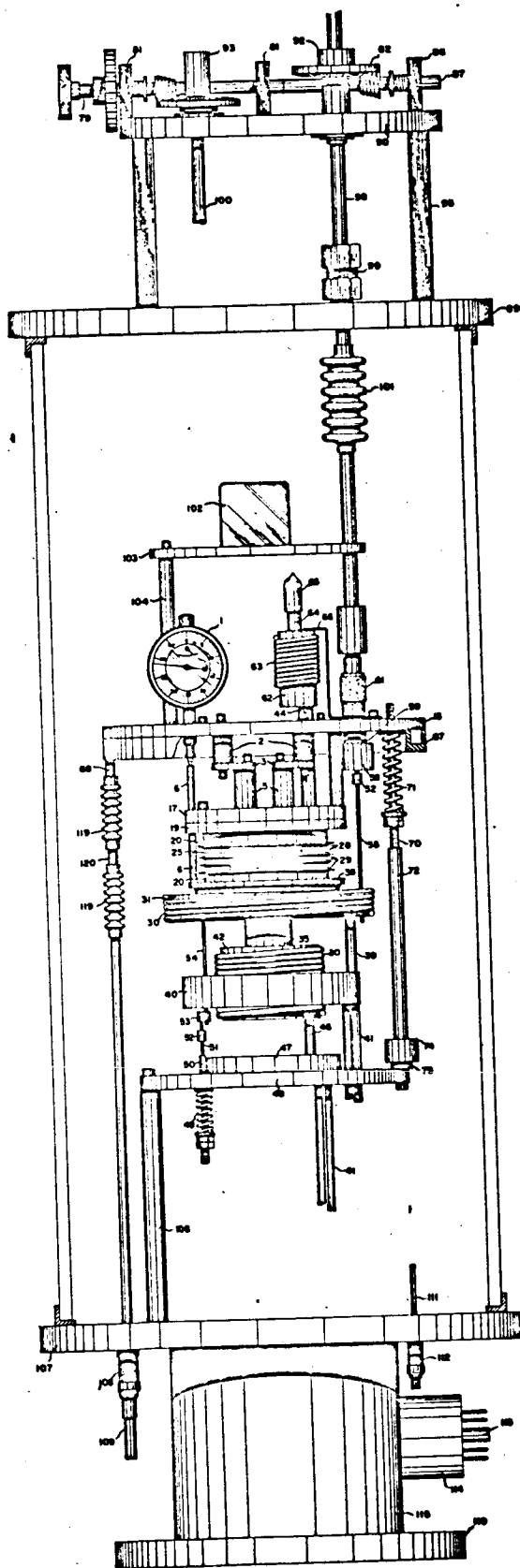
Figure III-1.  Overall Assembly of Converter.

## TABLE OF NOMENCLATURE

### for Figure III-1

| | | | |
|---|---|---|---|
| 1. | Dial Indicator | 26. | Emitter Sleeve |
| 2. | Insulator | 27. | Emitter Shield |
| 3. | Gun Holder | 28.⎫ | Bellows Flanges |
| 4. | Pin | 29.⎭ | |
| 5. | Filament Support | 30. | Guard Ring Heater |
| 6. | Sapphire Rod | 31. | Guard Ring Heater Block |
| 7. | Filament Lead | 32. | Flexible Flange Retainer |
| 8. | Filament | 33. | Flexible Flange Adapter |
| 9. | Emitter | 34. | Flexible Flange |
| 10. | Cavity Piece | 35. | Collector |
| 11. | Filament Shield | 36. | Collector - Guard Ring Spacer |
| 12. | Shield Support | 37. | Sapphire Balls |
| 13. | Insulator | 38. | Guard Ring |
| 14. | Gun Base | 39. | Guard Ring Heater Support Rod |
| 15. | Top Plate | 40. | Guard Ring Cooler |
| 16. | Top Plate Support Rod | 41. | Water Tube |
| 17. | Top Plate Support Ring | 42. | Collector Heater |
| 18. | Cesium Reservoir Tubulation | 44. | Cesium Tubulation |
| 19. | Emitter Support Plate | 46. | Collector Heater Support Rod |
| 20. | Bellows Adapter | 47. | Collector Cooling Plate |
| 21. | Emitter Shield Retainer | 48. | Support Plate |
| 22. | Emitter Shield Base | 49. | Spring |
| 23. | Emitter Shield Insulator | 50. | Tension Rod |
| 24.⎫ Seal | | 51. | Tension Wire |
| 25.⎭ | | 52. | Wire Retainer |

26

TABLE OF NOMENCLATURE for Figure III-1 (continued)

| | | | |
|---|---|---|---|
| 53. | Insulator | 78. | Gear |
| 54. | Tension Wire | 79. | Shaft |
| 55. | Tension Wire | 80. | Gear |
| 56. | Tension Wire Insulator | 81. | Plate |
| 57. | Rod | 82. | Bevel Gear |
| 58. | Micrometer Adapter | 83. | Shaft |
| 59. | Ball Bearing | 84. | Bearing |
| 60. | Ball Bearing Retaining Washer | 85. | Spring Retaining Washer |
| 61. | Micrometer | 86. | Bearing Housing |
| 62. | Cesium Reservoir | 87. | Shaft |
| 63. | Cesium Reservoir Heater | 88. | Bearing |
| 64. | Evacuation Tubulation Adapter | 89. | Top Plate |
| 65. | Evacuation Tubulation | 90. | Mechanism Support Plate |
| 66. | Cooling Strap | 91. | Shaft Adapter |
| 67. | Water Cooling Ring | 92. | Gear Adapter |
| 68. | Cooling Water Outlet | 93. | Gear Adapter |
| 69. | Cooling Water Inlet | 94. | Shaft |
| 70. | Guide Rod | 95. | Support Rod |
| 71. | Compression Spring | 96. | Bearing |
| 72. | Guide Rod Base | 97. | Bearing Retainer Washer |
| 73. | Stud | 98. | Shaft |
| 74. | Insulator Shade | 99. | Gland |
| 75. | Insulator | 100. | Shaft |
| 76. | Sapphire Rod Retaining Pin | 101. | Bellows |
| 77. | Anti-Backlash Spring | 102. | Prism |

TABLE OF NOMENCLATURE for Figure III-1 (continued)

| | | | |
|---|---|---|---|
| 103. | Prism Support Plate | 112. | Lead Wire Feedthrough |
| 104. | Prism Support Plate Rod | 113. | Octal Plug |
| 105. | Stud | 114. | Octal Plug Adapter |
| 106. | Support Plate Rod | 115. | Base Plate Neck |
| 107. | Base Plate | 116. | Sapphire Spacer |
| 108. | Water Feedthrough | 117. | Leadthrough Adapter |
| 109. | Water Tube | 118. | Water Tube |
| 110. | Base Plate Lower Ring | 119. | Bellows |
| 111. | Lead Wire | 120. | Bellows Adapter |

28
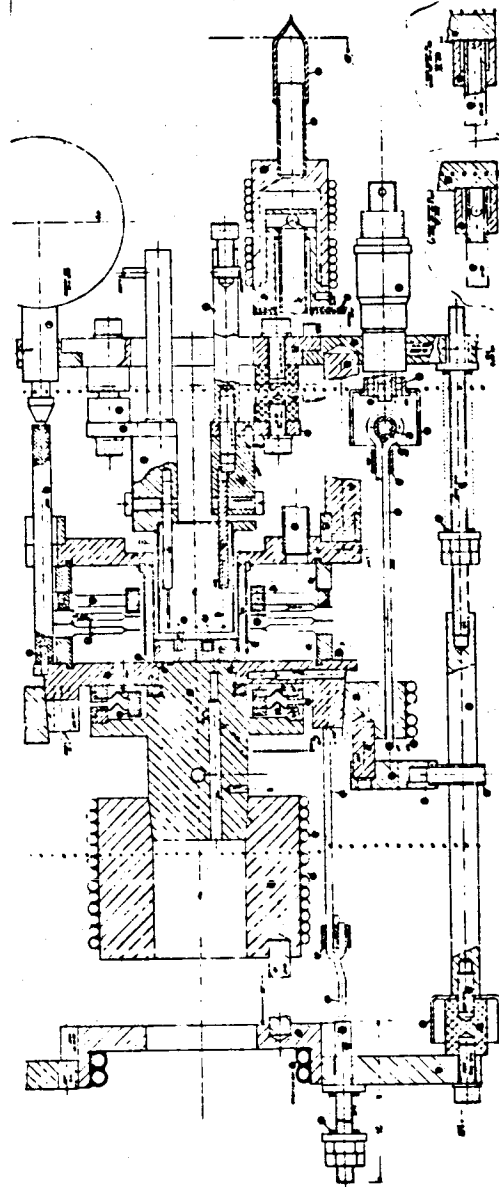
Figure III-2. Advanced Cesium Test Vehicle.

prefabricated and was thoroughly tested before installation into the emitter-collector structure. A sample assembly was subjected to 500 cycles and subsequently shown to be leak-tight before fabrication of the first converter.

The emitter structure is connected rigidly to the top plate (15), and the guard ring structure is connected rigidly to the bottom plate (48). The collector structure is also rigidly attached to the bottom plate. A spring (71) pushes part No. 15 upwards, thus tending to open the interelectrode spacing. This force is balanced by a rod (55) attached to the end of the micrometer (61), which is rigidly fastened to the top plate (15). The adjustment of the spacing is achieved by rotating the spindle of micrometer (61). There are three such micrometers, and all can be operated from outside the bell jar by means of shafts protruding through the top plate of the bell jar, via the seals (99). These shafts are connected to a spiral gear mechanism located on top of the bell jar. Once the emitter base and collector base are made parallel to each other by individual adjustment of the micrometers, the micrometer drive shafts are ganged together and thereafter move synchronously when the spacing is adjusted by turning the knob (79).

Since the spacing adjustment mechanism just described is apt to bend under stress while the device is operating, the measurement of the spacing is done independently of this mechanism. Three quartz rods (6) are fastened rigidly to the guard ring support plate (38); three dial indicators are fastened rigidly on plate (15) opposite the quartz rods. As the emitter assembly is moved the rods transmit this motion to the indicator anvils. The dial indicators measure any relative

motion occurring in the emitter assembly. Moreover, since the forces involved here are very small, one expects that the quartz rods will not deform in any manner as the spacing is adjusted, and will continue to give a true reading of spacing.

The top plate (15), to which the dial indicators and micrometers are attached, is water-cooled to insure proper operation. The water is admitted through the tube (109), introduced to the cooling ring (67) by flexible bellows joints (119), and exhausted in a similar manner. This feature assures that all the sensitive spacing-adjustment mechanisms will be maintained close to room temperature. The top plate (15) also serves as a low-temperature shield for any stray radiation that might strike these instruments.

Similar water-cooling provisions are made for the guard ring and collector, the temperature of which is adjusted by a balance between the heat input to the collector and guard ring heaters (30) and the cooling of the water coil. The main collector is equipped with a heat flux measuring section which will allow the execution of experiments aimed at obtaining electron cooling and radiation correlations with performance parameters.

The guard ring consists of an annular piece (38) separated from the collector (35) by a series of sapphire balls (37) and a sapphire ring (36). The guard ring is electrically insulated from the collector with a flexible-diaphragm leadthrough (34), and external springs are used to ensure that the guard and collector maintain the same position with relation to one another. The collector has been equipped with a thermocouple in close proximity to the collector surface, as well as two other

thermocouples, in order to measure accurately the heat transfer from the collector. The heat transfer section (35) and the heaters (42) have been designed to minimize the temperature drop from the collector surface to the heat sink (47). The cesium reservoir (62) is located near the emitter assembly, and in that manner the path between the liquid cesium reservoir and the interelectrode spacing has been considerably shortened. The objective here is to minimize transpiration effects, especially in the case of cesium fluoride, which past experience has shown has difficulty establishing equilibrium between the interelectrode space and the reservoir volume. A prism (102) allows observation of the black-body hole in the rear face of the emitter.

This converter design allows extremely accurate measurement and control of spacing. Edge effects are virtually eliminated by the use of the active guard ring, which can be maintained at the same potential and temperature as the collector by use of the instrumentation which is discussed in Chapter IV.

## B.    CONVERTER DEVELOPMENT

### 1.    Emitter Assembly

The first converter uses a rhenium emitter. This emitter consists of a solid rhenium disc, as shown in Figure III-2 (part 9). The disc was fabricated by electrical-discharge machining (EDM) and grinding from flat rhenium stock. After being cut to its final shape, the emitter disc was fitted to a rhenium sleeve (part 26). This step completed all machining and grinding operations on the emitter itself. The final preparation of the emitter surface was carried out by the metallurgist and is described in Chapter V. Following the metallurgical

preparation, the emitter and its sleeve were assembled and electron-beam welded. The choice of rhenium as the emitter sleeve material was dictated by the fact that rhenium forms brittle intermetallics with almost all the refractory metals. Any weld, therefore, of the rhenium disc to any other refractory sleeve tends to form a brittle weld, and, even though such welds have been made successfully in the past, the risk involved was felt to be too great. An additional advantage of using a rhenium emitter sleeve is that this material is far more inert to impurities and much less subject to crystal growth than tantalum, which was used heretofore. Investigation revealed that the Rembar Division of Chase Copper and Brass (Dobbs Ferry, N. Y. ) is able to seam-weld rhenium sheet into a tube of the appropriate size for use as an emitter sleeve. A length of several inches of such tubing was obtained and checked for vacuum-tightness as received and after firing. The seam weld was found to be sound at the conclusion of these tests. A weld of the emitter sleeve to the emitter disc was then developed. This was accomplished, after several experimental operations, in Thermo Electron's beam welder. The opposite end of the sleeve was then brazed with copper to the molybdenum support ring. The emitter assemblies prepared in the above manner have operated satisfactorily in the test vehicles.

2.    Collector Guard Ring

One of the principal objectives of the program was to obtain data from a device in which the conversion process is as one-dimensional as possible. Results obtained in this manner should be free of geometrical effects and will therefore be of general applicability. To achieve

this objective, an active-guard-ring design was used. The guard ring is designed to operate at the same temperature and electrical potential as the collector at all times. The gap between the collector and its guard ring is minimized, and the two are kept as coplanar as possible. The collector face, however, must be positioned slightly above the plane of the guard ring, so that the emitter can be shorted to it and the zero spacing point thus established. A design goal of half a mil was set for this step, and careful planning in the machining and selective fitting of these parts has accomplished this goal. The design goal of half a mil for the gap between the collector and guard ring was established. This value was considered a good compromise between the possibility of shorting of the two elements and the desire to keep the gap to a minimum. The sapphire ball race which separates collector and guard ring, as well as the sapphire ring that positions one element with respect to the other, proved to be successful design features, once the proper sequence of machining, and holding of the appropriate tolerances was accomplished. Both collector and guard-ring surfaces were kept flat to within 0.1 mil by grinding. The sequence of grinding the collectors is as follows:

The collector and guard are rough-machined, leaving 0.005" to 0.010" extra material on the face of the two elements and on that surface on the collector on which the spacing sapphire ring rests. Both parts are then vapor-degreased for 2 minutes, ultrasonically cleaned in a hot solution of 0.05% Igepal for 2 minutes, rinsed in hot and cold water, and finally rinsed twice in acetone. After cleaning, the parts are fired in vacuum at 1500 to 1600°C for two hours. This firing is done in order to

34

allow any dimensional changes to occur prior to final machining. The collector and guard faces are then surface-ground.* They are then assembled with the sapphire ring spacer. The flatness, and the height of the step between the two elements, are measured with an electronic height indicator whose sensitivity is 0.00005". The final machining of the collector surface supporting the sapphire ring is then performed, removing sufficient material to give the step between the two elements the desired height. The collector, guard and spacer are then re-assembled and the flatness and step height measurement repeated.

Figure III-3 shows the leadthrough which is used to seal between the collector and guard. Figure III-4 shows the face of the collector guard assembly after brazing and Figure III-5 shows another view of the assembly.

## 3.    Bellows Assembly

A flexible member was necessary to provide the variable-spacing feature of the converter. The readily available stainless steel bellows were rejected because stainless steel was considered to be too gassy for use in the interior of the converter. A number of bellows manufacturers were contacted in the search for a bellows made of less gassy materials, preferably of vacuum tube grade. In general, none of these manufacturers had such a bellows available, nor were any willing to attempt a custom design. Finally, a local manufacturer was found who was willing to manufacture bellows assemblies to our specifications. A nickel-iron alloy was selected as the bellows material because it could be obtained in the gas-free state. The first assemblies were made

---

*A SiC wheel is used for grinding these surfaces, and the lubricant is an oil-water emulsion.

Figure III-3.   Collector-Guard Leadthrough.

36
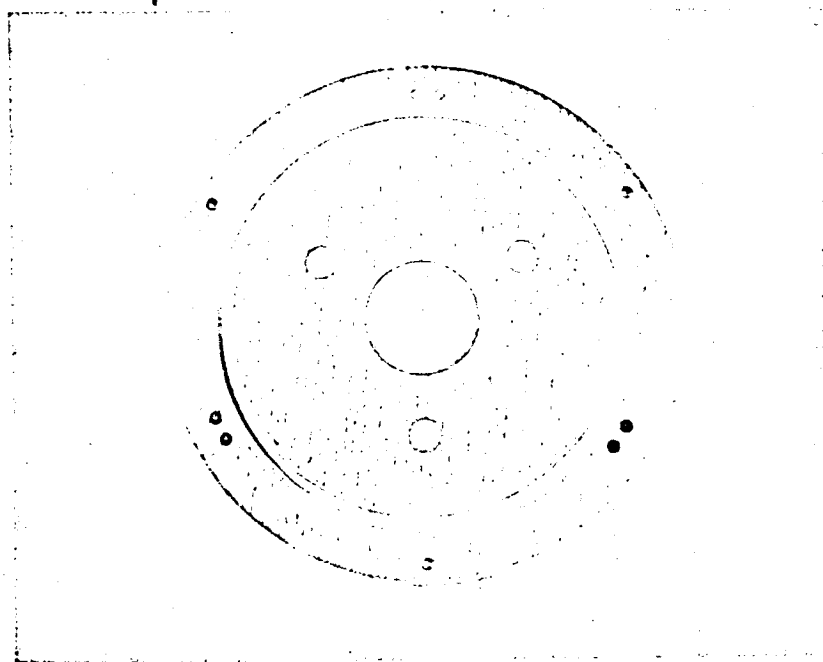
Figure III-4.   Collector-Guard Assembly Subsequent to Brazing.

37
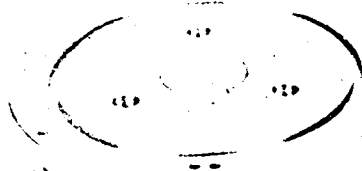
Figure III-5.   Collector-Guard Assembly Prior to Final Machining.

with Driver Harris 146 alloy. A number of satisfactory welds were obtained; however, the results were not always consistent. Occasionally blemishes, indicative of impurities, appeared on the welds. A better grade of this alloy was sought, and a gas-free vacuum-melted grade was obtained from Carpenter Steel. This new material gave consistently satisfactory welds.

The end pieces, part 20 of Figure III-2, were originally machined out of solid stock. However, after cycling, a number of these parts developed cracks, and upon close examination it became apparent that there were flaws in the original material. In view of this, provisions were made to stamp this part out of sheet which was of a satisfactory consistency. When assemblies were made with these new stamped parts the welds were consistently satisfactory. As shown in Figures III-2 and III-6, the emitter-collector-insulator (parts 24 and 25) is incorporated into this bellows assembly. This was done for the sake of compactness and because the ceramics that are used are compatible with the nickel-iron alloy used in the bellows. The leadthrough part of the bellows assembly presented no serious problems. The ceramic for this leadthrough is Wesco AL300, and it is metallized with moly-titanium.

Bellows insulator assemblies which showed no flaws in the weld areas were consistently leaktight. Several were cycled to temperatures exceeding their operating temperature by about 200°C several times, and also were mechanically cycled up to 1000 cycles in order to evaluate the soundness of these assemblies. The results were satisfactory, and these assemblies were incorporated in operating converters. A photo of the bellows-collector-seal subassembly is shown in Figure III-6.
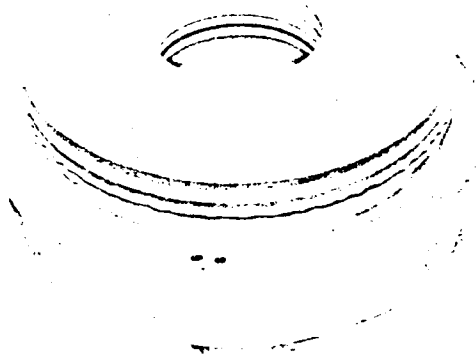
Figure III-6.   Assembly of Collectors to Bellows and Leadthroughs

40

This solution to the bellows problem was good for roughly 100 hours of converter operation, at which time cracks were found to develop in the joint between the molybdenum body of the guard ring (part 38) and the nickel-iron end piece of the bellows assembly (part 20).

To eliminate this failure, the material for part 20 was changed to molybdenum so that the difference in expansion could be taken up by the yielding of the thin nickel-iron flange (part 29). However, the yield strength of the nickel-iron flange was too high, and failures occurred in the braze between parts 20 and 29.

The next step was to change the flange material to pure nickel, which has a lower yield strength. This combination of materials (thin nickel flange brazed to heavier molybdenum section) had been used successfully in the past and is used in this converter for the seal between the collector and the guard (see parts 32, 33, 34).

The use of nickel flanges had been avoided in the basic design of this unit, because previous converters using nickel in flexible-seal assemblies had experienced failures due to either fatigue or creep of the nickel brought about by the stress-time-temperature characteristics of the component design. All such failures had occurred, however, in seal assemblies of the two-flange type, since bellows of the multiplane design used here had not been included in previous converters. The flanges used here are also of larger diameter and more flexible design than those previously used. These factors reduce the stress imposed on the flanges, and a decision was made to change to nickel with the hope that the lower-stress design of the bellows would eliminate the failures in the nickel experienced

41

with earlier designs. Also, it was hoped that the greater yield of the nickel would eliminate the failures in the nickel-to-molybdenum braze. This has been shown to be true, and the resulting converters have operated for longer periods of time than any previously built under this program, without any failure in these problem areas.

4.  Cesium Reservoir Design

The cesium reservoir is located above the emitter structure. This location was chosen because it allows the liquid cesium to be located as close as possible to the interelectrode space. At the same time, it avoids passing the tubulation through the collector heat flux measuring section. The original design of the reservoir is shown in Figure III-7. It consisted of two blind holes drilled into opposite ends of a molybdenum cylinder parallel to each other and a cross hole drilled in the upper section of the cylinder. This geometry resulted in an ink-well type reservoir. In the early stages of testing of the first converter, it became apparent that the reservoir was not able to provide control of the cesium pressure. Investigation showed that the following process was taking place: Inspection of Figure III-7 shows that the cooling strap at the top of the reservoir results in Areas A and A' being the coldest points in the reservoir and, therefore, in the whole converter. Cesium vapor from the interior of the converter first strikes Area A, and there it condenses, there being no driving force making it condense in Area A'. Once the cesium has condensed in Area A, however, gravity will force the liquid cesium to return back down the tube, and, once it reaches a sufficiently warm point, Area B, it then evaporates and keeps refluxing between Areas A and B. This refluxing action resulted
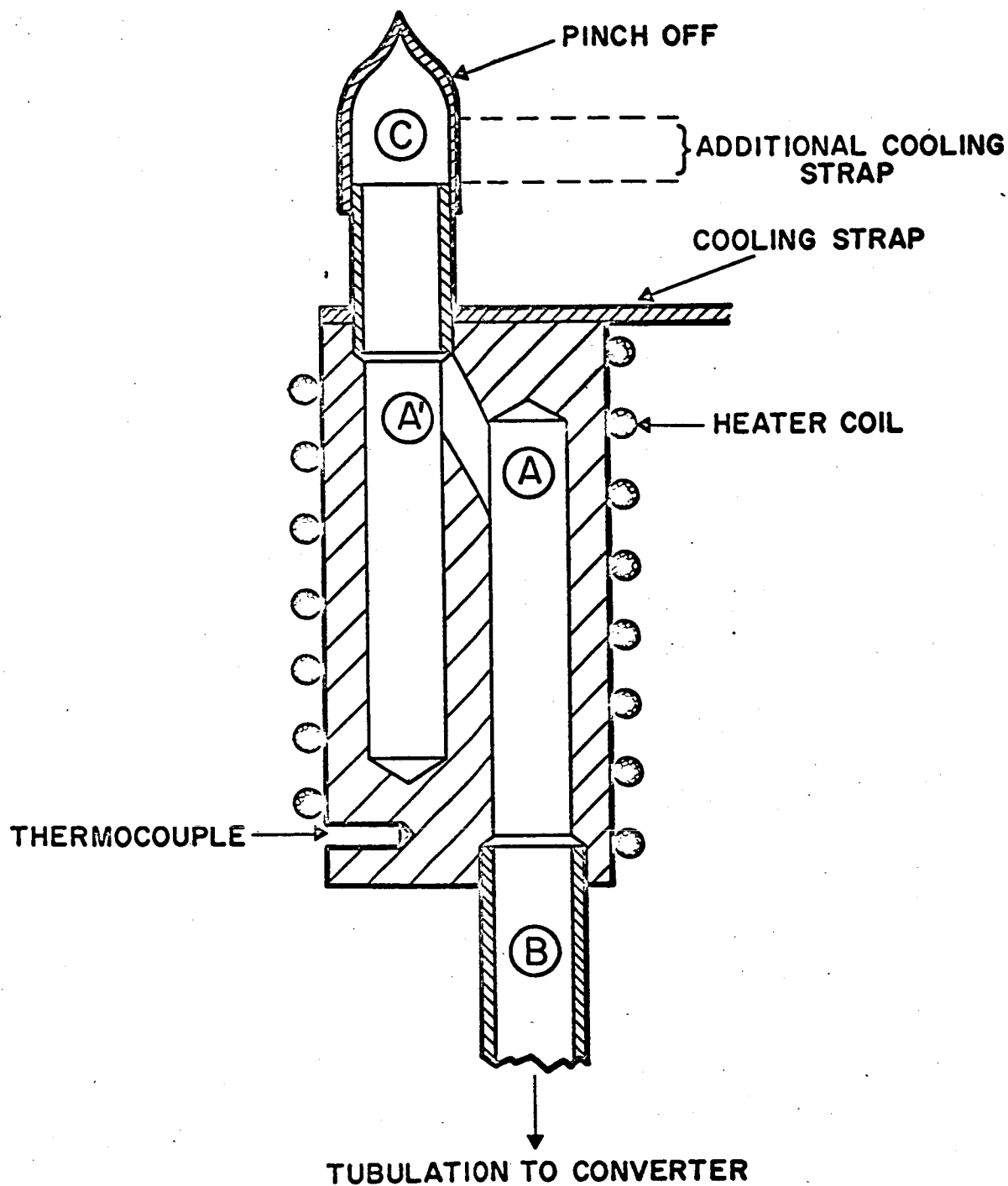
Figure III-7.   Original Cesium Reservoir.

in the cesium pressure fluctuating between two different levels at the rate of about 5 cycles per second. The cesium reservoir was redesigned, and the new configuration is shown in Figure III-8. Another inkwell-type configuration is used. The coldest area in this reservoir is Area A. Cesium striking this spot, however, cannot drip back down the tubulation and set up the refluxing mechanism. This reservoir design has resulted in satisfactory control of the cesium temperature over the entire range of investigations. A photograph of the reservoir and its appendages is shown in Figure III-9.

### 5. Spacing Mechanism

One of the areas considerably improved with the design of this converter is the control and measurement of interelectrode spacing. The spacing mechanism, described in Section A of this Chapter, is so designed as to permit an independent adjustment and measurement of interelectrode spacing. The adjustment is made by rotating three micrometer heads geared together and driven by a minimum-backlash mechanism. The measurement of the spacing is done independently by three dial indicators calibrated to 0.0001" and located in such a manner on the emitter assembly and guard-ring assembly as to insure direct reading of spacing independently of temperature changes. This spacing mechanism has been in use for a considerable period of time, and it has proven to be quite satisfactory. The sensitivity of the system is about 0.0001" and the reproducibility about 0.0002". Figure III-10 shows the precision gearing which is used to control the spacing mechanism.

44
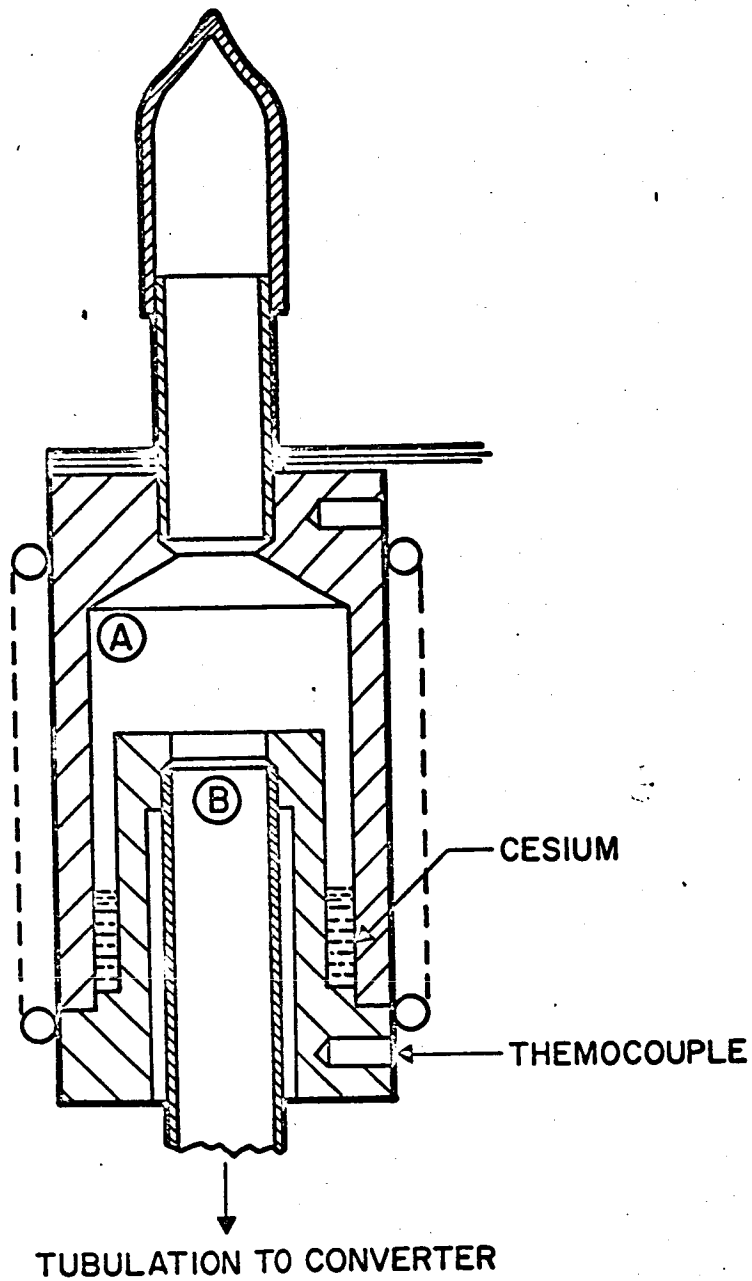
Figure III-8.   New Cesium Reservoir Design.
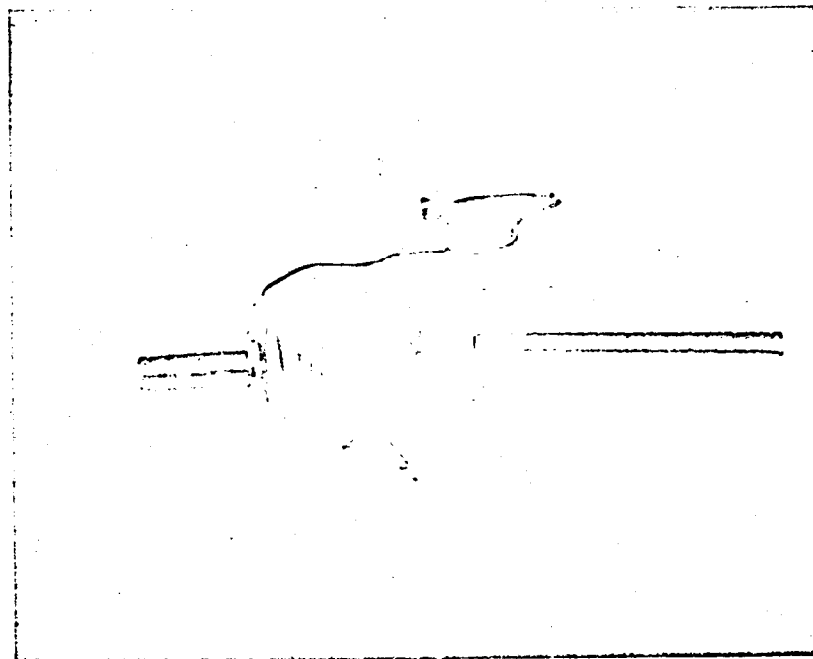
Figure III-9.   Cesium Reservoir with Heater and Cooling Strap
Subsequent to Brazing.

46
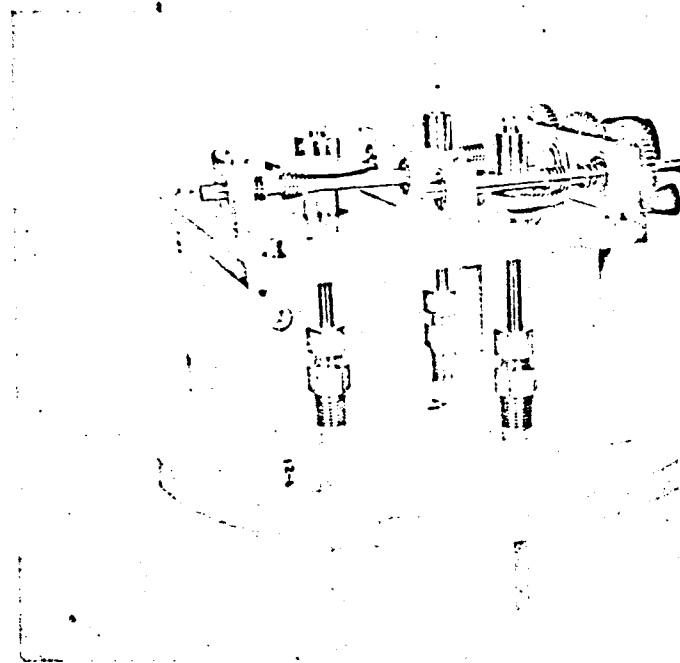
Figure III-10.   Assembled Gearing and Top Plate.

47

6.  Collector, Guard Ring and Cesium Reservoir Heater Requirements
    for Steady-State Operation

In order to cover the entire operating range of practical interest,
the following temperature limits had to be attainable during point-by-
point testing:

1.  Emitter temperature                1200°C to 1800°C
2.  Collector temperature               400°C to  800°C
3.  Guard temperature                   400°C to  800°C
4.  Cesium reservoir temperature         50°C to  420°C

These requirements had to be satisfied for various diode load conditions;
the limiting conditions are as follows:

1.  Maximum collector heat flux 250 watts/cm$^2$ of emitter area
2.  Maximum guard heat flux 250 watts/cm$^2$ of emitter area

To achieve the wide ranges of collector and guard temperatures,
a heating-cooling system was devised where a constant-temperature
water-cooled sink is used in conjunction with an electrically heated
variable-temperature heating section. The desired temperature may
be obtained by varying the power to the electrical heater without alter-
ing the water flow or water temperature.

To solve the general case of the heat transfer equation for these
conditions we may write

$$Q_i = \frac{k_i A_i (T_i - T_{ii})}{L_i}$$

48

where $\quad Q_i$ = heat flux, watts/cm$^2$

$\qquad k_i$ = thermal conductivity, watt cm$^2$/cm °C

$\qquad A_i$ = area for heat transfer, cm$^2$

$(T_i - T_{ii})$ = temperature difference across which $Q_i$ is transferred, °C

$\qquad L_i$ = length for heat transfer, cm

We shall also define, the quantity

$$R_i = \frac{L_i}{k_i A_i}$$

Examining the conditions for the collector, on Figure III-11, we may write the following equations:

$$Q_{C1} = \frac{T_{C1} - T_{C2}}{R_{C1}}$$

and

$$Q_{C1} + Q_{C2} = \frac{T_{C2} - T_3}{R_{C2}}$$

with the following boundary conditions:

when $\qquad Q_{C1}$ = 250 watts/cm$^2$

then $\qquad T_{C1}$ = 400°C

$\qquad\qquad Q_{C2} = 0$

$\qquad\qquad T_3$ = 20°C

49
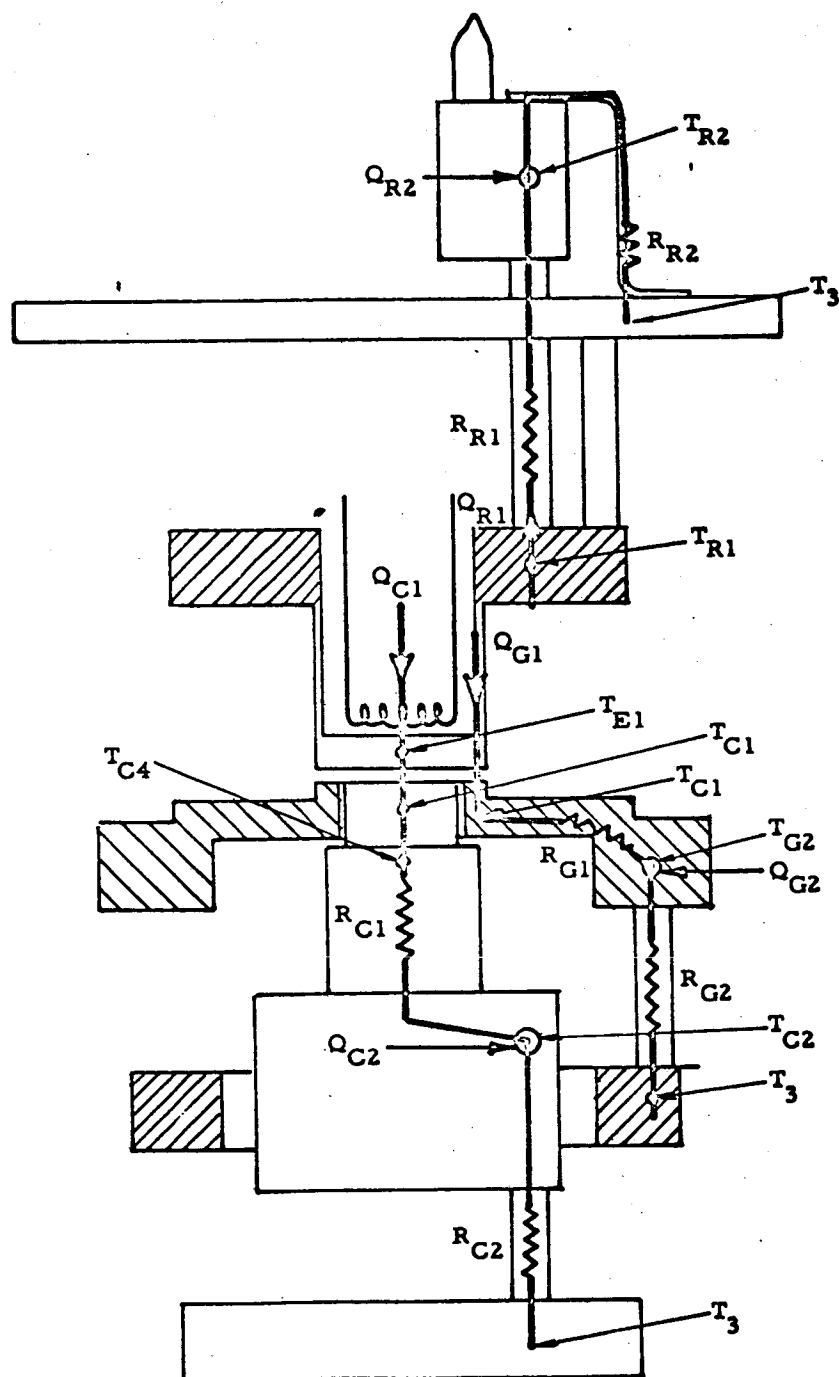
Figure III-11.   Schematic Diagram for Heat Transfer Computations.

and when $\quad Q_{C1} = 0 \text{ watt/cm}^2$

then $\quad T_{C1} = T_{C2} = 800°C$

Solving these equations with these boundary conditions, we find a relationship between $Q_{C1}$, $Q_{C2}$ and $T_{C1}$. This relationship has been plotted on Figure III-12. The dashed lines show the limits of various possible combinations of temperatures and heat fluxes available when the heat input at the electrical heater is 1000 watts/cm$^2$ of emitter area.

To compute the size of the various heat-flow members, the resistance values may be calculated with the aid of the relationships above.

$$R_{C1} = 0.74°C/\text{watt-cm}^2$$

$$R_{C2} = 0.78°C/\text{watt-cm}^2$$

For the guard ring we may write as follows:

$$Q_{G1} = \frac{T_{G1} - T_{G2}}{R_{G1}}$$

and

$$Q_{G1} + Q_{G2} = \frac{T_{G2} - T_3}{R_{G2}}$$

with the following boundary conditions:

when $\quad Q_{G1} = 250 \text{ watts/cm}^2$

then $\quad T_{G1} = 400°C$

$\quad Q_{G2} = 0$

$\quad T_3 = 20°C$
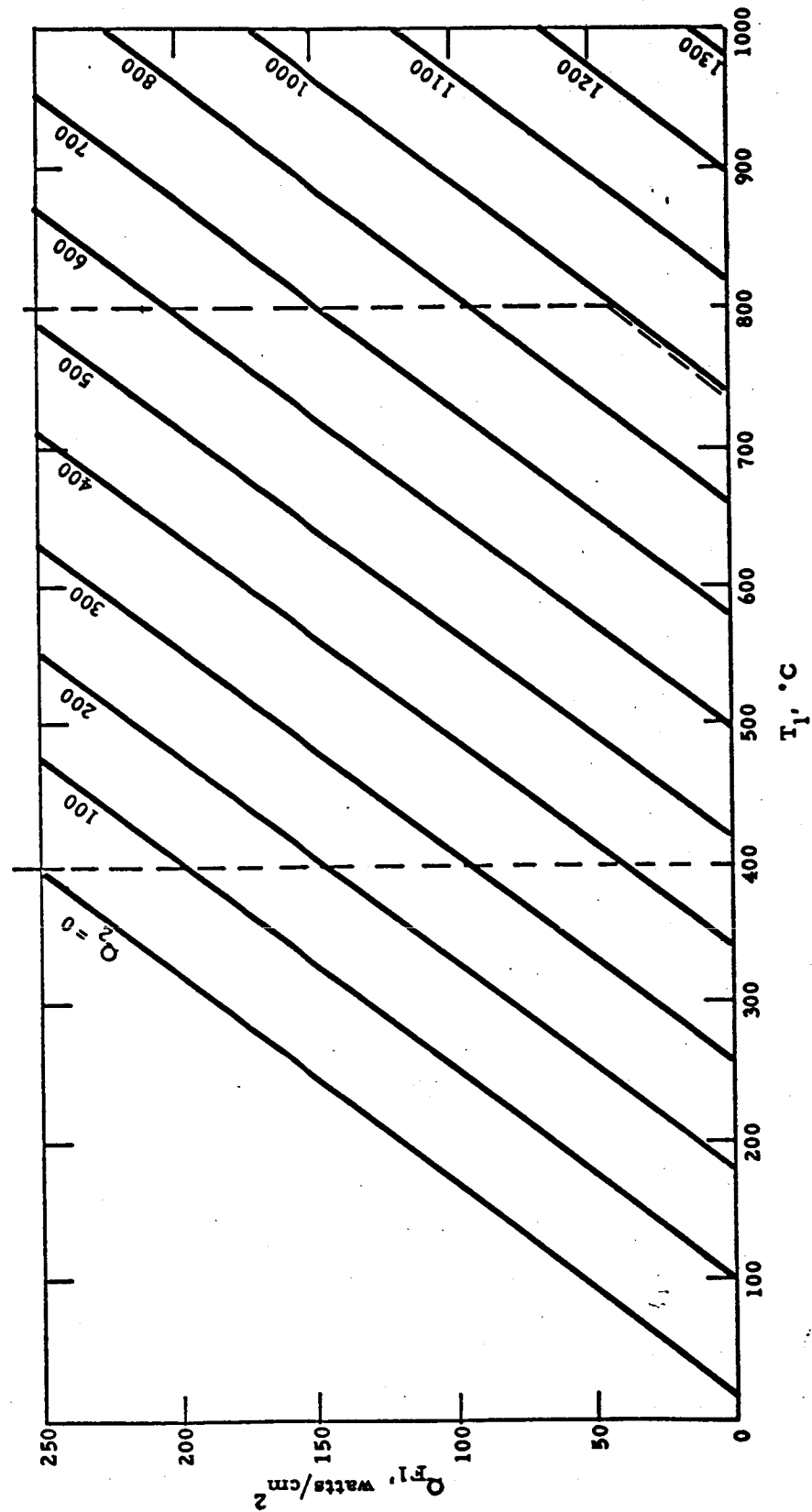
Figure III-12.   Collector Heater Design Chart.

and when $Q_{G1} = 0$ watt/cm$^2$

then $T_{G1} = T_{G2} = 800°C$

Solving these equations with the above boundary conditions, we find a relationship between $Q_{G1}$, $Q_{G2}$ and $T_{G1}$. This relationship has been plotted on Figure III-13. The dashed lines show the limits of the possible guard ring temperatures with a heater capable of supplying 60 watts input.

The resistances may be computed as follows:

$$R_{G1} = 0.25°C/\text{watt-cm}^2$$

$$R_{G2} = 1.27°C/\text{watt-cm}^2$$

To solve the case of the cesium reservoir, we may write

$$Q_{R1} = \frac{T_{R1} - T_{R2}}{R_{R1} + R_{R2}}$$

and

$$Q_{R2} = \frac{T_{R2} - T_3}{R_{R2}}$$

and the boundary conditions are as follows:

when $Q_{R1} = 0$

then $T_{R2} = 50°C$

$T_{R1} = 600°C$
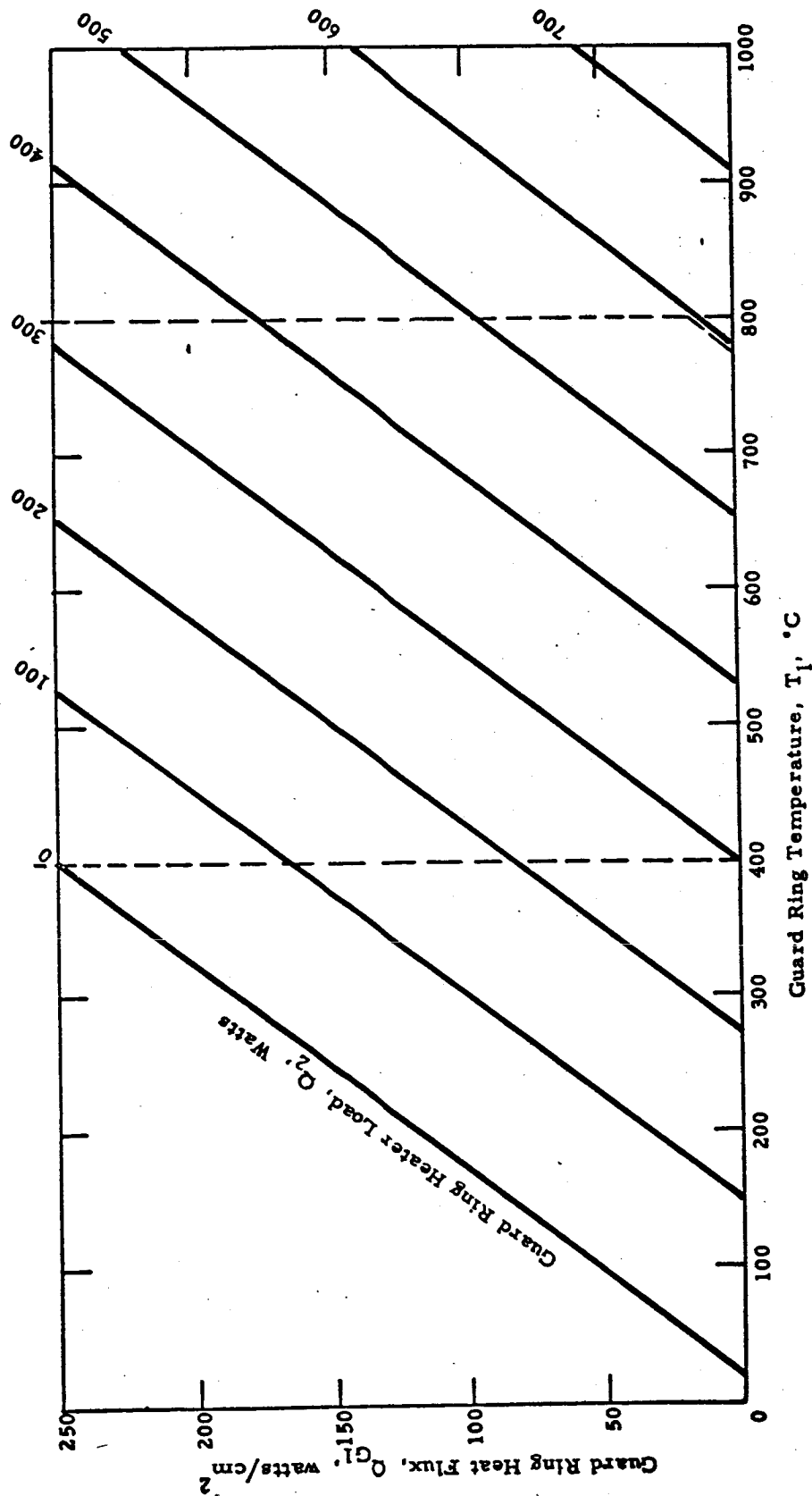
Figure III-13.  Guard Heater Design Chart.

when        $Q_{R1}$ = 100 watts

then        $T_{R2}$ = 420°C

$T_{R1}$ = 600°C

Solving these equations for a 100-watt heater, we find

$$R_{R1} = 75.1°C/watt\text{-}cm^2$$

$$R_{R2} = 4.1°C/watt\text{-}cm^2$$

The actual heater is designed as follows:

## Heaters - Collector and Guard

Maximum Power Requirements:

Guard     (1 cm$^2$) -   600 W

Collector (2 cm$^2$) - 2000 W

Heater Material - coaxial sheathed wire

Mechanical Sheath - Inconel

Wire - Nichrome V

Insulation - compressed MgO

Manufacturer - Aero Research

Electrical:

Power density with brazed sheath 100 W/in$^2$ of sheath area

Heater Body:

Area Calculation

With close-spaced turns, total effective surface area required is determined by the power density.
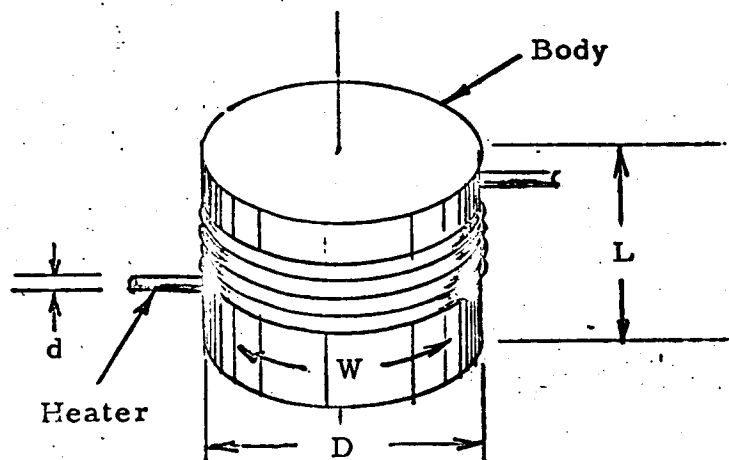
In a surface area w by L there are $\frac{L}{d}$ heater wires with length **w** for a total sheath area of $\pi wL$. The area necessary is thus independent of sheath diameter. Power density is thus $\pi \times 100$ or 314 W/in$^2$ on the heater body.

## Collector

$\frac{2000w}{314}$ = 6.38 in$^2$. Design diameter is 1.8 in., and a length of $\frac{6.38}{1.8 \times \pi}$ = 1.13 in. is required.

## Guard

$\frac{600}{314}$ = 1.9 in.$^2$               $\frac{1.9}{3.75 \times \pi}$ = 0.16 in. required

Wire Size Calculations

Voltage limited to 100 volts to reduce leakage currents during low-current testing.

Current limited to 25A by vacuum leadthrough and power supply capacities.

For current of 20A with 100 V input, wire resistance must be 5Ω. With 93-mil sheath diameter at 100 W/in$^2$ there are

III-33

56

$$100 \times \pi \times .093 \times 12 = 350 \text{ W/ft.} \quad \text{At 20 A, } R = \frac{350}{20^2} = .88\,\Omega \text{/ft, corre-}$$

sponding to #21 B & S Nichrome V heater wire.

## Power Supply

Collector - heater split into two windings to smooth control (main and auxiliary)

Main - 720 W, 0-36 V, 20 A, autotransformer regulated. Controlled by Honeywell R7161B

Schematic - Figure III-14

Auxiliary - 1500 W, 0-80 V, 25 A adjustable in steps with taps. Figure III-15.

Guard Heater - 720 W, same as main

## Heater - Cesium and Additive

Power required:

Cesium     120 W, 12 V at 10 A
Additive   240 W, 24 V at 10 A

Wire:

69-mil sheathed heater brazed to reservoir; wire #23 Nichrome
Maximum current 15 A

Length:

Cesium     12 in.
Additive   24 in.

Power Supply:

Autotransformer-regulated, Honeywell R7161B controlled
Schematic Figure III-16

Figure III-17 is a schematic showing the relationship between the converter and its various heaters and power supplies. The individual components and values are not shown here but may be identified in Figures III-14, -15 & -16.

57
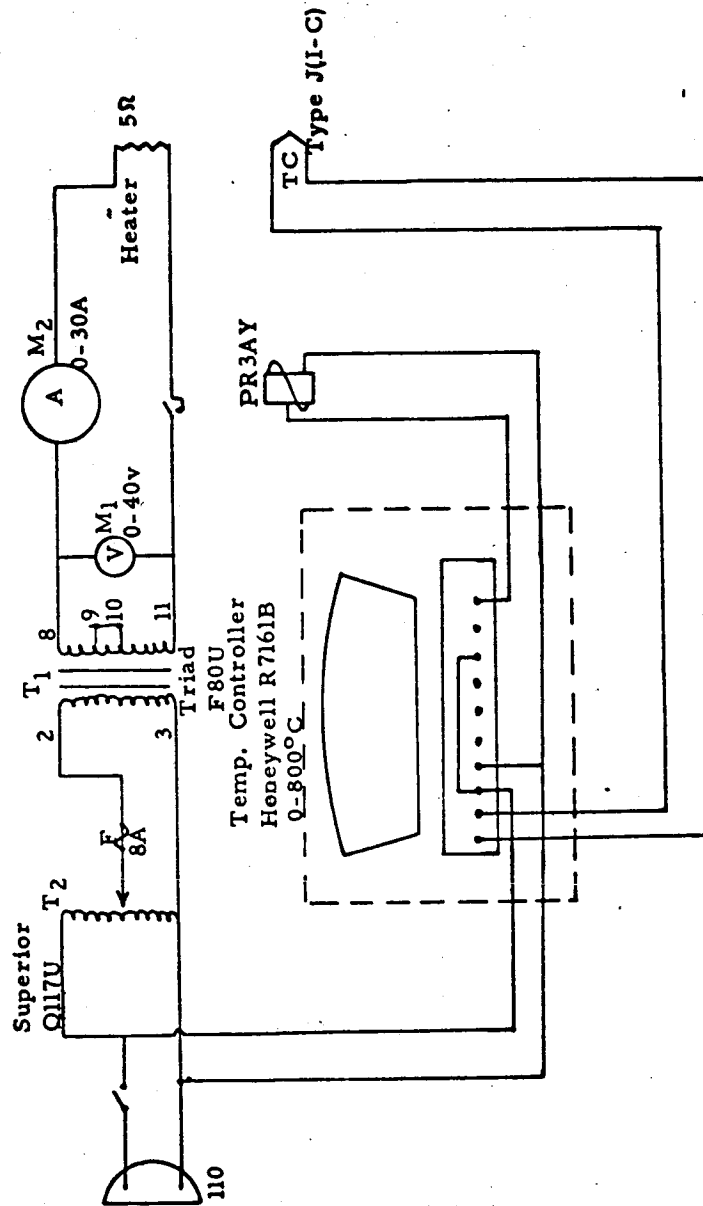
Figure III-14. Collector and Guard Heater Power Supplies and Controls.

58
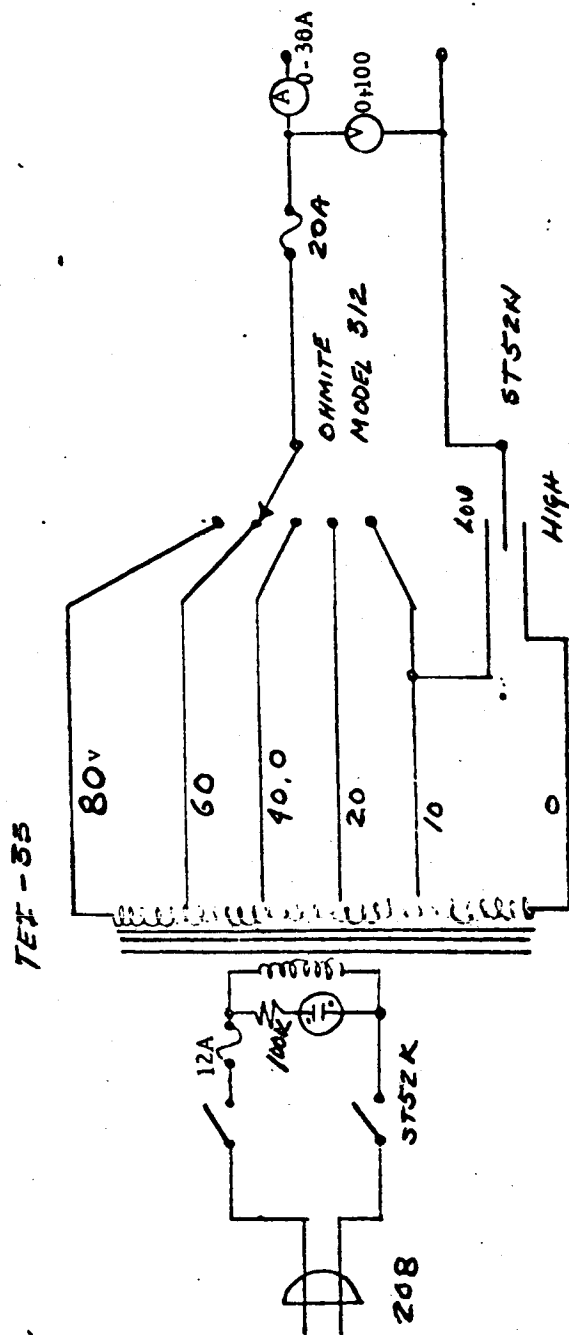
Figure III-15. Auxiliary Heater Power Supply, TEECO HS 8025.
Job # 8002-103.
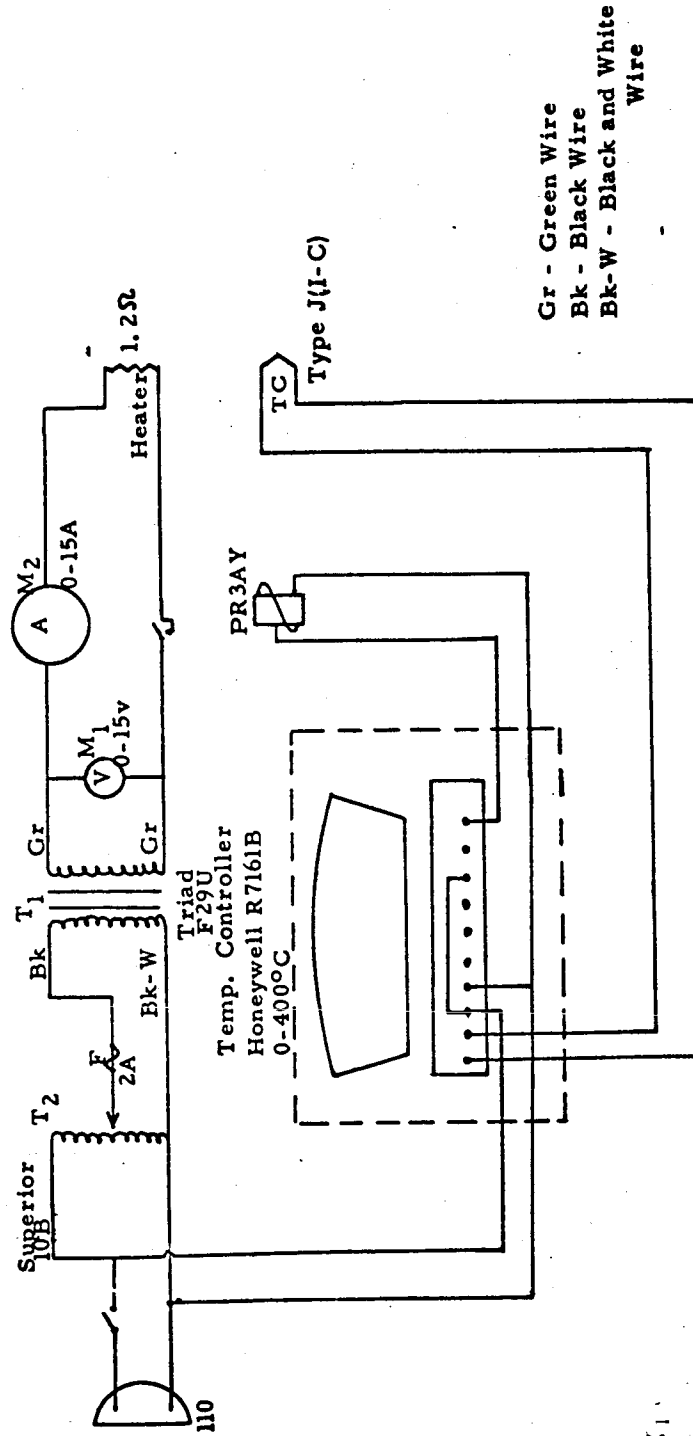
Figure III-16. Cesium Heater Power Supply and Control.

60

64-R-8-6
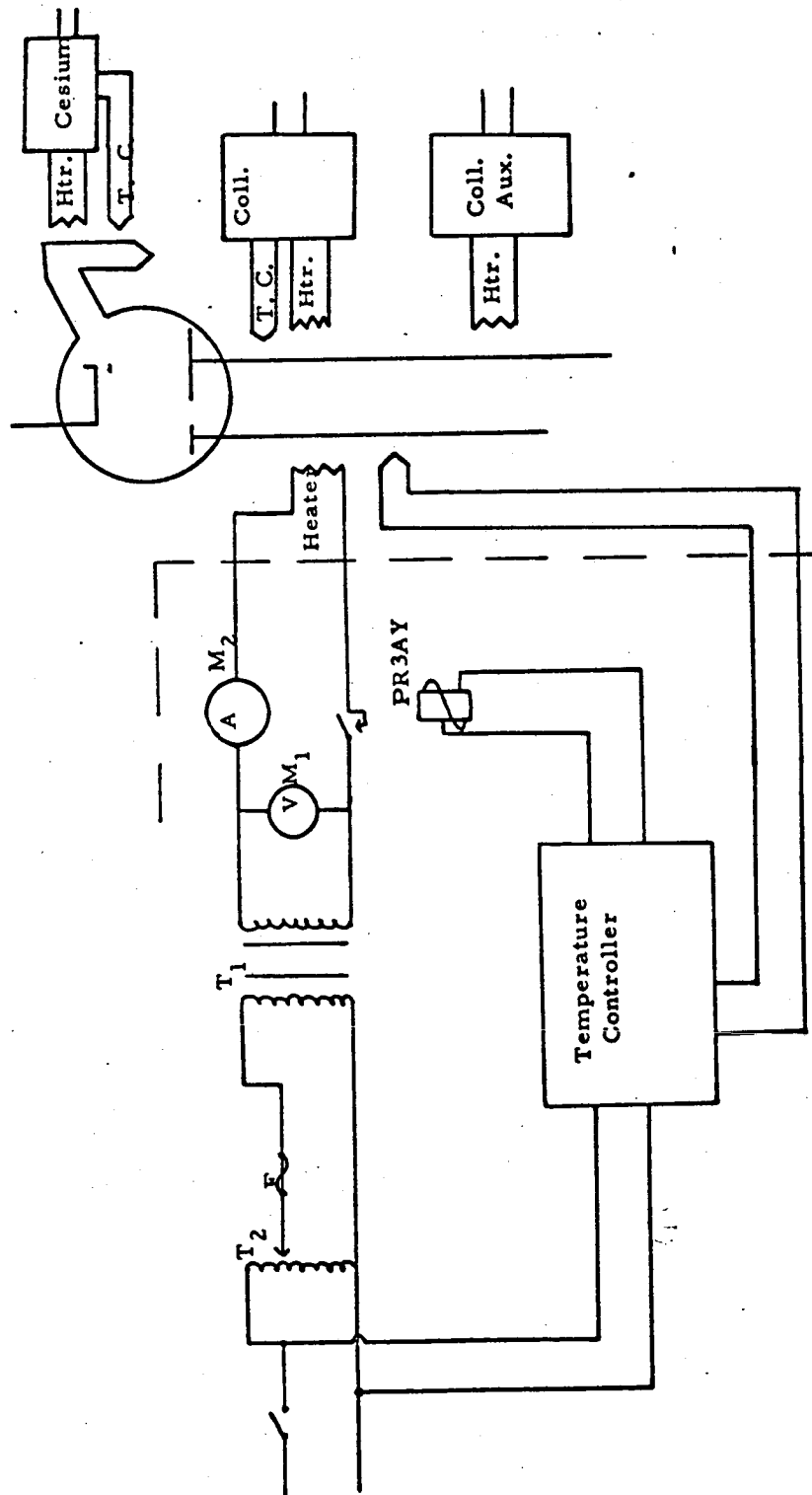


Figure III-17. Heater Power Supplies and Controls.

Development work on the collector and guard heaters revealed a serious fabrication difficulty. The inconel sheath of the heater wire did not braze well to the molybdenum heater body. Overheating resulted and the early heaters burned out at much lower power inputs than were calculated. Test heaters were then built from several types of sheathed wire. Burn-out values were established for each material, as was the upper temperature limit for continuous operation. A tantalum wire with MgO insulation and tantalum sheathing was finally chosen, and special lengths were ordered. This wire was then tested in the actual configuration used in the converter, and, once its operation proved satisfactory, the heating-cooling assemblies for the collector and guard ring were fabricated. The end connections to these heater elements proved to be another problem which had to be overcome. This was done by preparing special nickel members which accepted the wire in an opening at one end and were crimped over it. The heaters developed in this manner resulted in adequate temperature control when tested with the converters in actual operation.

## C. EMITTER TEMPERATURE CALIBRATION

Figure III-18 is a schematic of the diode portion of the test vehicle. The emitter is in the form of a cup, part No. 1, and opposite it are located the collector, No. 2, and the guard ring, No. 3. A black-body observation recess in the form of a cavity is provided. The exact cavity configuration had been calibrated earlier by direct comparison of pyrometer readings with Pt 10% Rh thermocouple readings. The calibration data are plotted in Figure III-19, and the resulting corrections are replotted in the form of a calibration curve, Figure III-20. These corrections include glass and prism losses, since the calibration is made under

T. C.

B. B.
Hole

④

①

③

②
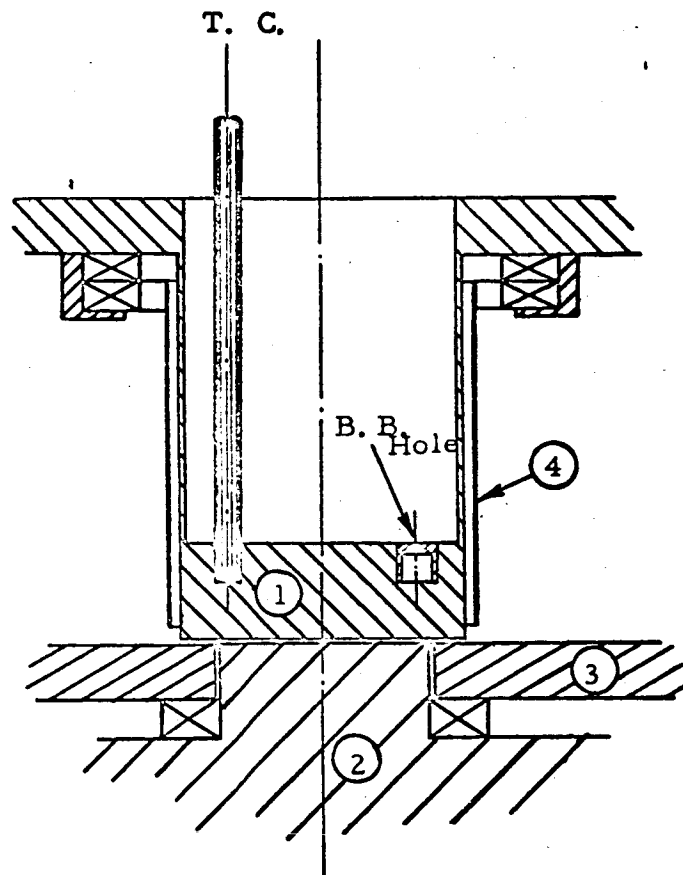
Figure III-18.   Schematic of Electrode Arrangements.

THERMO ELECTRON
ENGINEERING CORPORATION
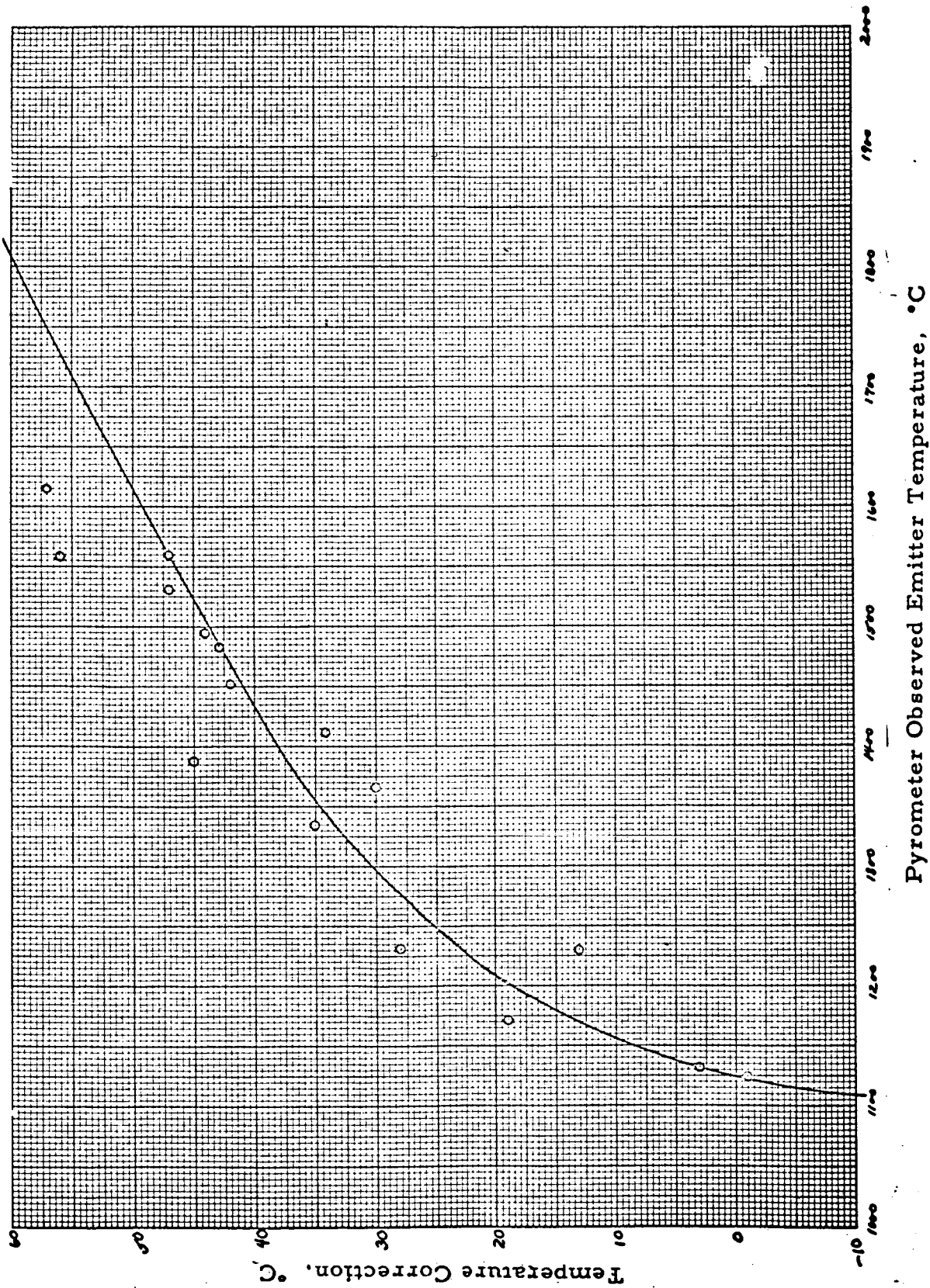


Figure III-19. Temperature Correction vs Observed Pyrometer Temperature.

.64
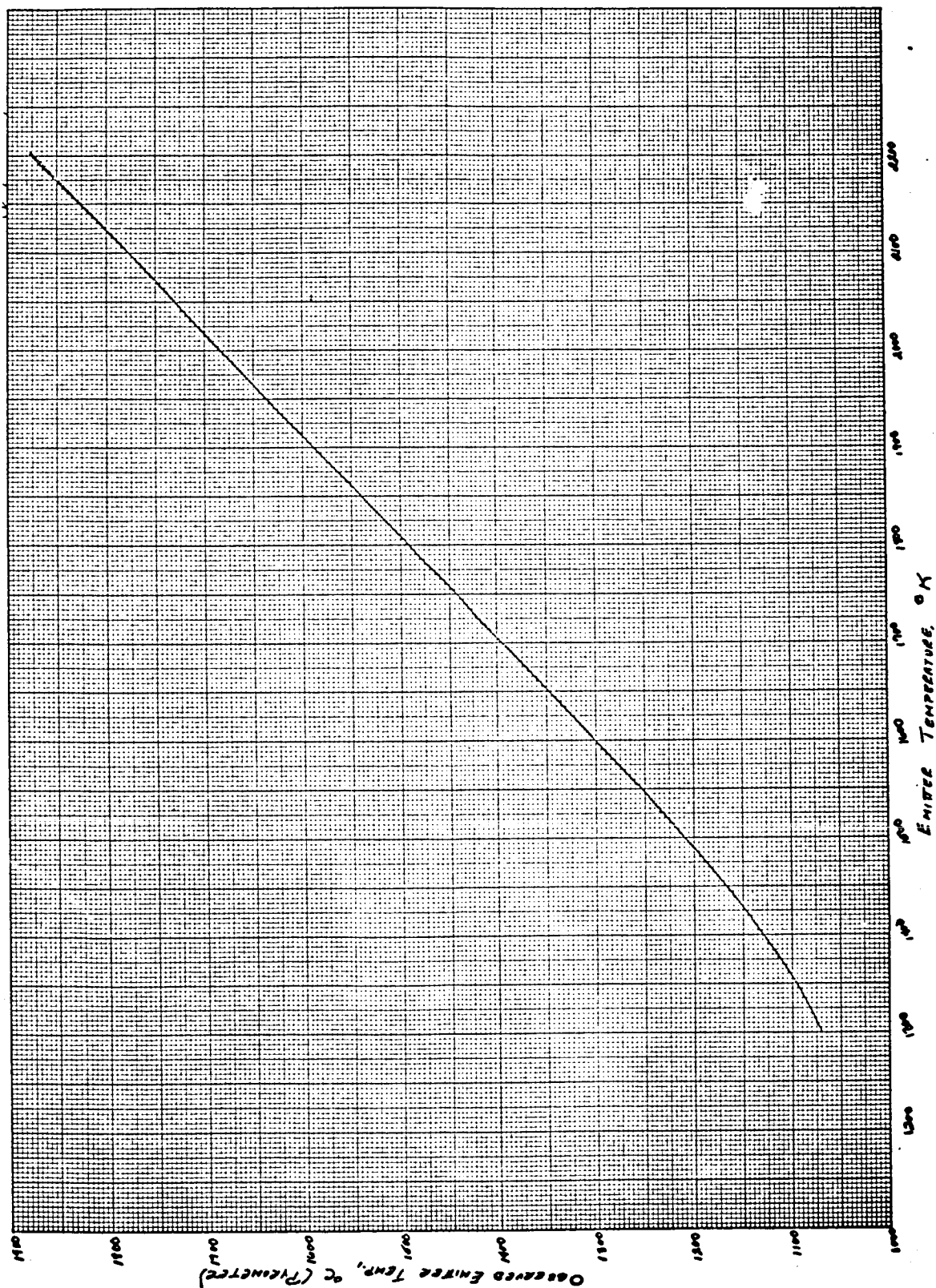
Figure III-20. Pyrometry Calibration Curve for JPL Test Vehicles.

actual test setup conditions. Figure III-20 is used for correcting all pyrometer readings taken on these converter test vehicles.

The corrected cavity temperature and surface temperature differ by the temperature drop required to sustain the heat flux. This difference, then, clearly depends on the level of heat flux and is proportional to it. To account for this temperature difference, the rhenium thermal conductivity must be known. The thermal conductivity values reported in the literature do not extend beyond 500°K. These values, as well as a recommended extrapolation to higher temperatures, are shown in Figure III-21, which is reproduced from Reference 1. In view of the fact that no experimental data are available, and the extrapolated values may be off by as much as 50%, the conductivity of the rhenium used in this program was measured at as high temperatures as possible.

The experimental method selected consisted of producing a given heat flux through two intimately joined pieces of material, one of known conductivity and the other unknown, and then using the temperature gradient through each material to compute the ratio of the unknown to the known conductivity.

Schematically the arrangement is shown in Figure III-22. The rhenium piece shown is identical to the pieces used as emitters. It is brazed with niobium to a molybdenum rod of the same diameter which is considerably longer. The other end of the molybdenum rod is connected to a heat sink. A series of ten black-body holes are located on the side of the composite rod, four in the rhenium and six in the molybdenum, at accurately measured intervals. Heat is supplied to the top

65-R-5-81
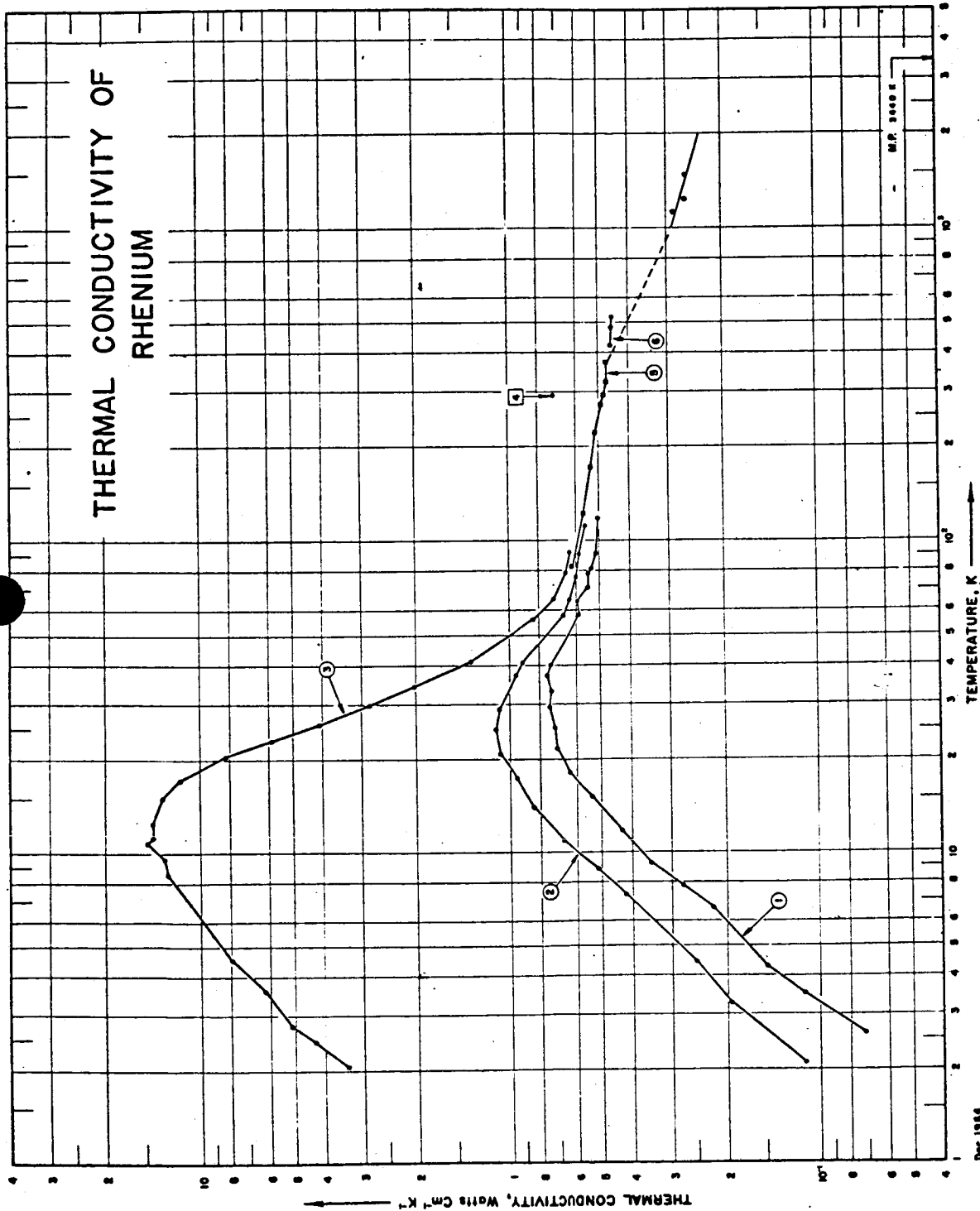


Figure III-21. Measured Thermal Conductivity of Rhenium.

III-44
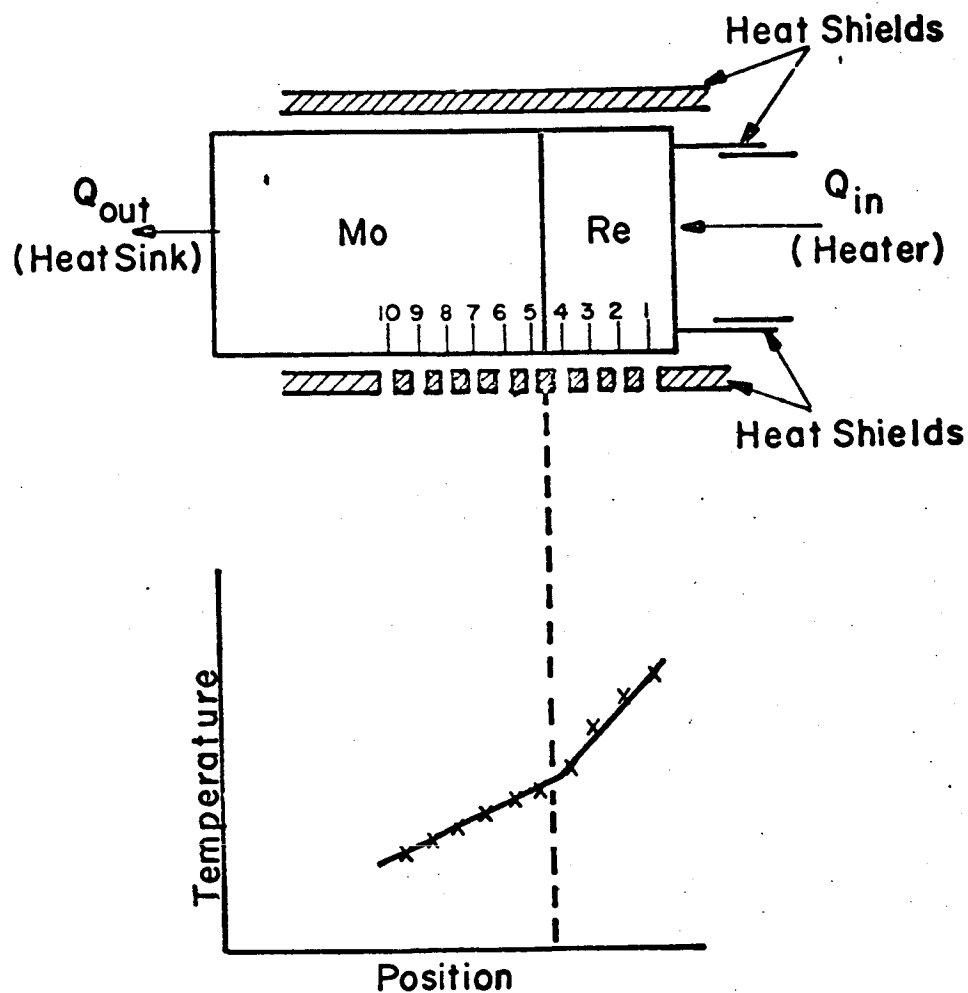
Figure III-22.  Schematic of Rhenium Thermal Conductivity
Measuring Apparatus.

of the rhenium disc by electron bombardment. Let us assume for the time being that no heat is lost through the cylindrical surfaces of the test piece. Then the temperature gradient in each material must be constant and the following relationship holds:

$$Q = k_{Re} A_{Re} \left(\frac{dT}{dx}\right)_{Re} = k_{Mo} A_{Mo} \left(\frac{dT}{dx}\right)_{Mo}$$

where: $k_{Re}$ is the thermal conductivity of rhenium

$k_{Mo}$ is the thermal conductivity of molybdenum

$A_{Re} = A_{Mo}$ is the cross-sectional area of the specimen

$\frac{dT}{dx}$ is the temperature gradient along the cylinder.

The above relationship reduces to:

$$k_{Re} \left(\frac{dT}{dx}\right)_{Re} = k_{Mo} \left(\frac{dT}{dx}\right)_{Mo}$$

The validity of the assumption that lateral heat losses are negligible compared with the axial heat flux $Q$ can readily be checked by observing the gradient $dT/dx$ as a function of x. If the assumption is correct $dT/dx$ will be constant. Figure III-23 is a plot of temperature versus position for a particular experimental run. Inspection of Figure III-23 shows that data can best fit two straight lines, one on either side of the interface. Figures III-24 and III-25 are additional runs at other temperature levels. All but four of the experimental points fit the straight lines to within $\pm 5\,°K$, the typical probable error for the micropyrometer used. The four points which show a larger error of $10 - 20\,°K$ are deviating always in the same direction and correspond to the same locations, indicating that the error is systematic.

THERMO ELECTRON
ENGINEERING CORPORATION
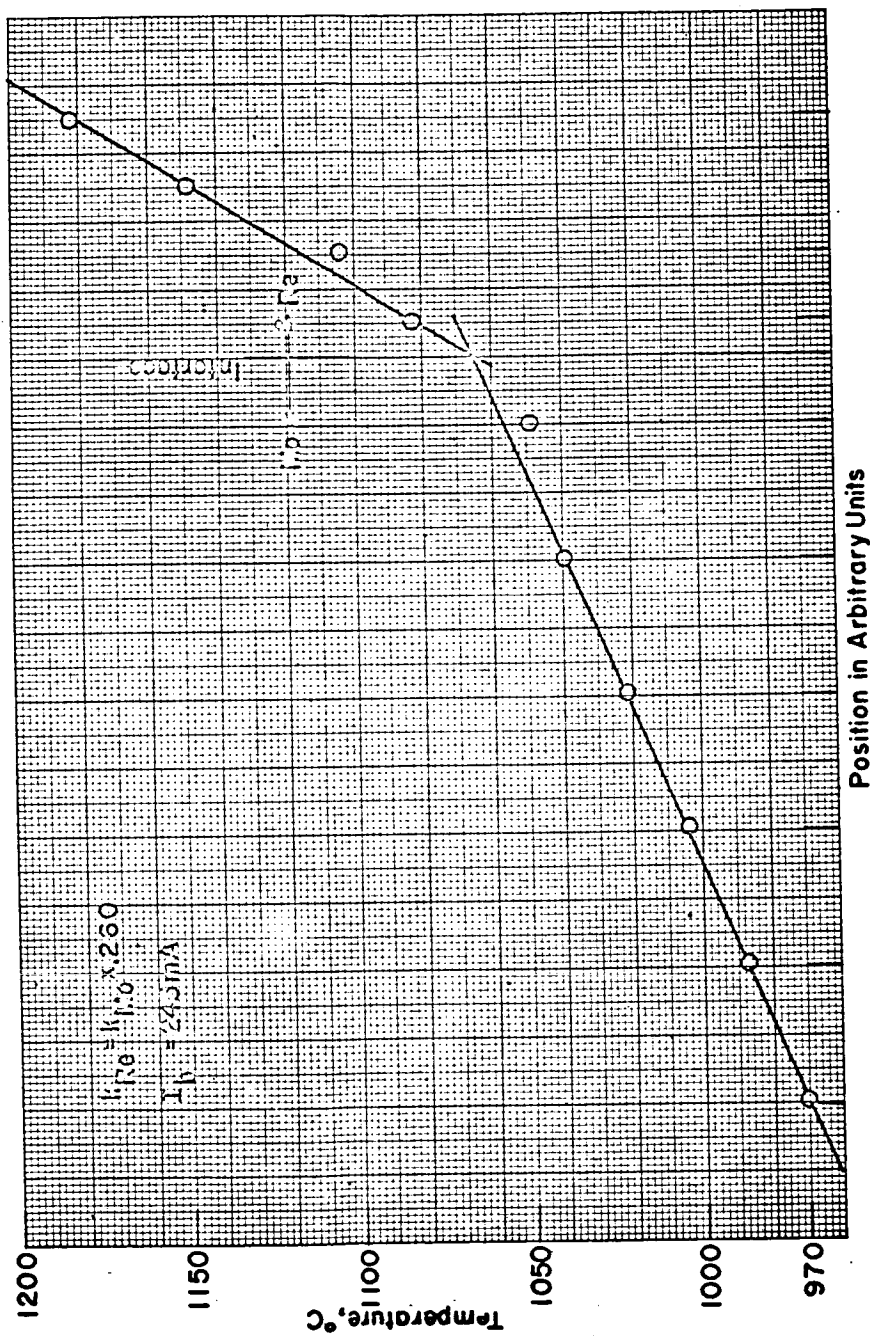


Figure III-23.  Temperature vs Length Plot of Experimental Results.
(Ion Bombardment Current = 245 mA.)
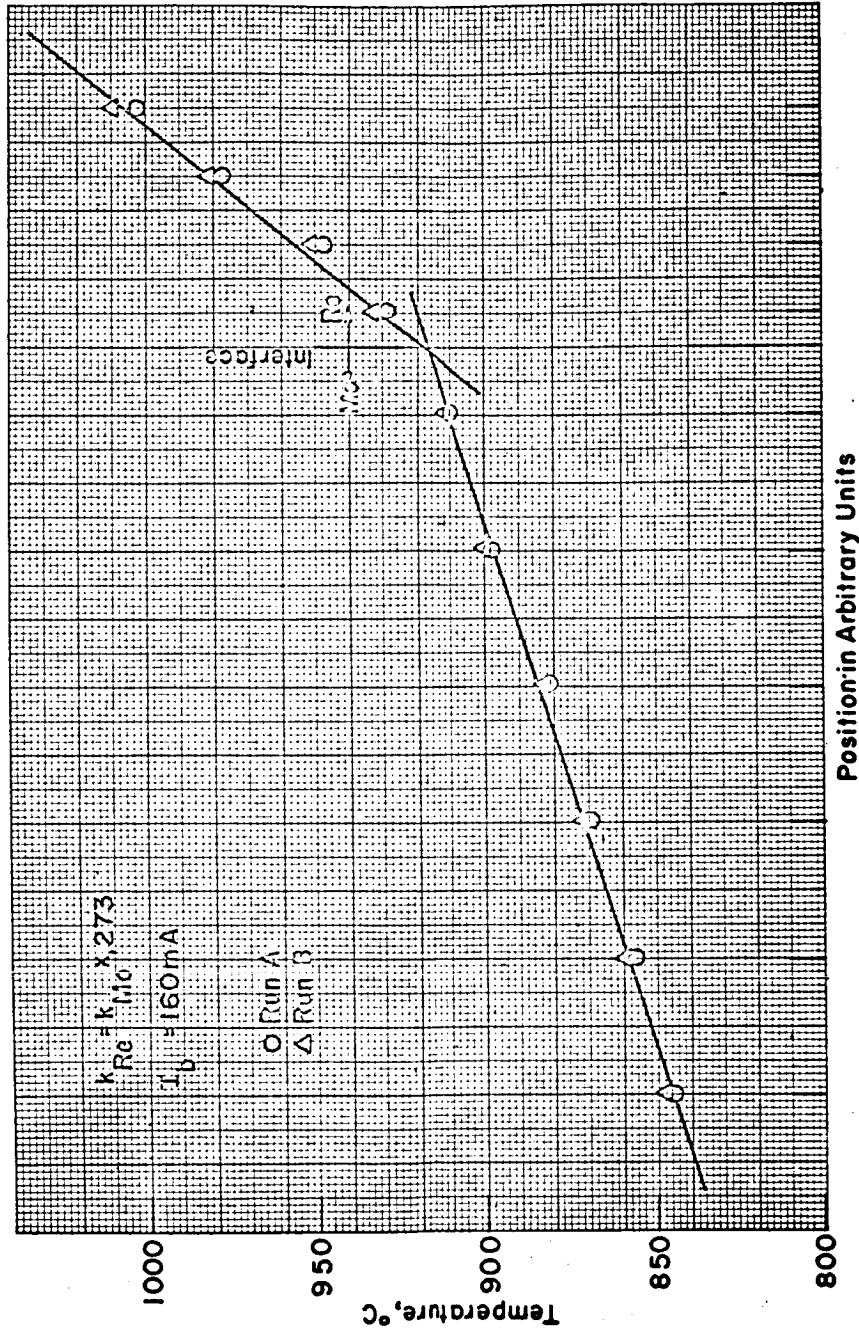
Figure III-24. Temperature vs Length Plot of Experimental Results.
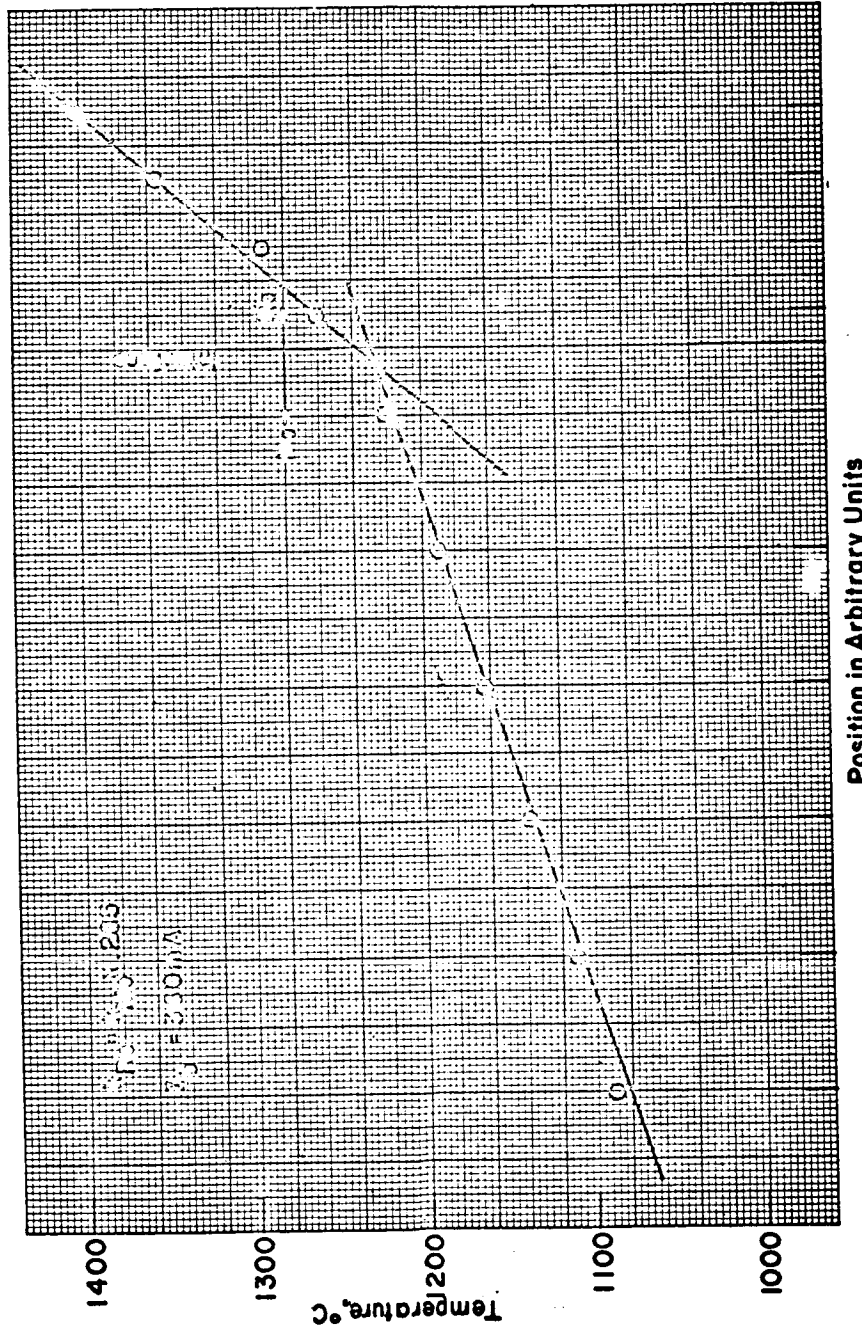
Figure III-25.  Temperature vs Length Plot of Experimental Results.
(Ion Bombardment Current = 260 mA.)

The values of $k_{Re}/k_{Mo}$ computed from the three runs are 0.260, 0.273 and 0.280. The highest temperature at which the experiment was performed is $1493^{\circ}K$. Attempts at measuring the conductivity at higher temperatures were unsuccessful because the error caused by stray lateral losses became significant and the temperature-vs-position lines were no longer straight.

To arrive at an absolute value for the conductivity of rhenium, a value for the conductivity of molybdenum is needed. Figure III-26 is a copy of the data given in Reference 1. The average values obtained for molybdenum from Figure III-26 at the temperatures in question are given in Table III-1. Also in Table III-1 are shown the rhenium conductivity values based on the experimental results and the reported molybdenum conductivity values. These values of rhenium conductivity are also plotted in Figure III-21. A line has been fitted to the data obtained and it has been used to extrapolate these values to $2000^{\circ}K$. In view of the small dependence on temperature in this range, the value of 0.25 watt/cm$^{\circ}$K has been chosen for the entire thermionic emitter temperature range. The corresponding difference in the temperatures of the black-body hole and the emitter surface is $1.52^{\circ}K$/watt.

$$T_S = T_{BB} - 1.52\,Q_E$$

where:

$T_S$ is the emitter surface temperature

$T_{BB}$ is the corrected observed temperature

$Q_E$ is the heat flowing through the emitter.
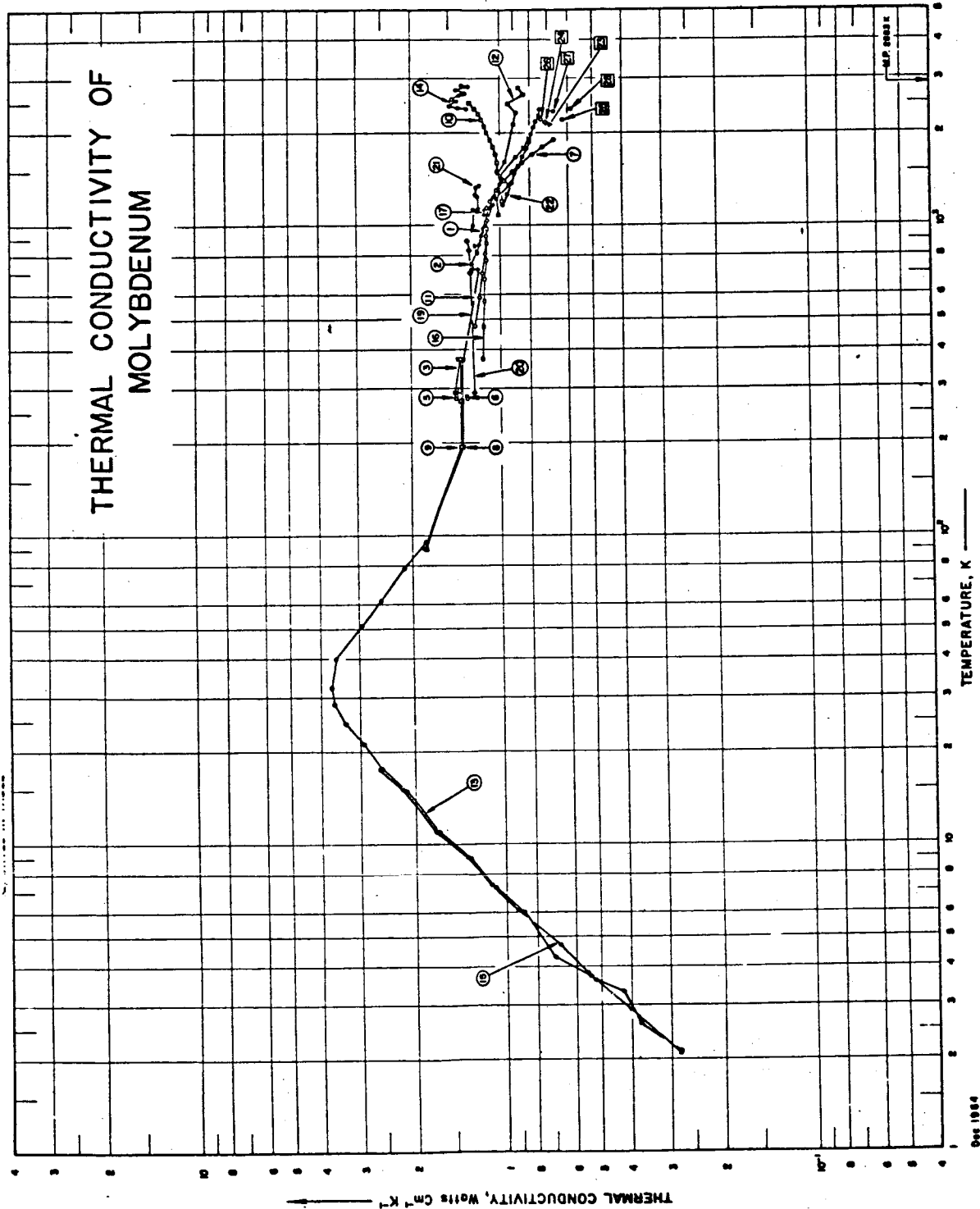
Figure III-26.   Measured Thermal Conductivity of Molybdenum.

TABLE III-1

CONDUCTIVITY OF RHENIUM AND MOLYBDENUM

| Temperature °K | $k_{Mo}$ W/cm°K | $k_{Re}$ W/cm°K |
|---|---|---|
| 1193 | 1.05 | 0.287 |
| 1303 | 0.98 | 0.255 |
| 1493 | 0.91 | 0.259 |

## D. THE CESIUM FLUORIDE CONVERTER

This converter is almost identical in design to the cesium-only converter that has been previously described in detail. The only difference is the fact that the additive converter has two reservoirs on the upper emitter structure and has a tungsten emitter. One of the reservoirs contains cesium fluoride, and the other contains cesium. The cesium reservoir is equipped with a 10-mil diameter orifice at one end of the tubulation leading from the reservoir to the converter. The purpose of this orifice is to prevent the condensation of cesium fluoride vapor in the cesium reservoir, since, under most conditions, the cesium reservoir operates colder than the cesium fluoride reservoir.

The experimental program started with cesium-fluoride-only tests. This was deemed necessary, since the presence of two vapors tends to confuse effects due to each. This, of course, necessitated a means of keeping the cesium in its reservoir without releasing it until the appropriate time arrives. To accomplish this, a metal cesium capsule was required, since retaining cesium in a glass capsule at the relatively high temperatures of the cesium reservoir for any prolonged period of time would result in reactions between the cesium and the glass. Such a capsule had been developed in the past. It consists of copper tubes fusion-brazed onto a molybdenum tube and pinched off at the ends after cesium has been introduced in the structure. Figure III-27 shows such a capsule. The capsule can be held indefinitely at temperatures of 200 to 300°C without any reaction and is contained in

76

Cu TUBE

FUSION
BRAZE

Mo TUBE

Cu TUBE
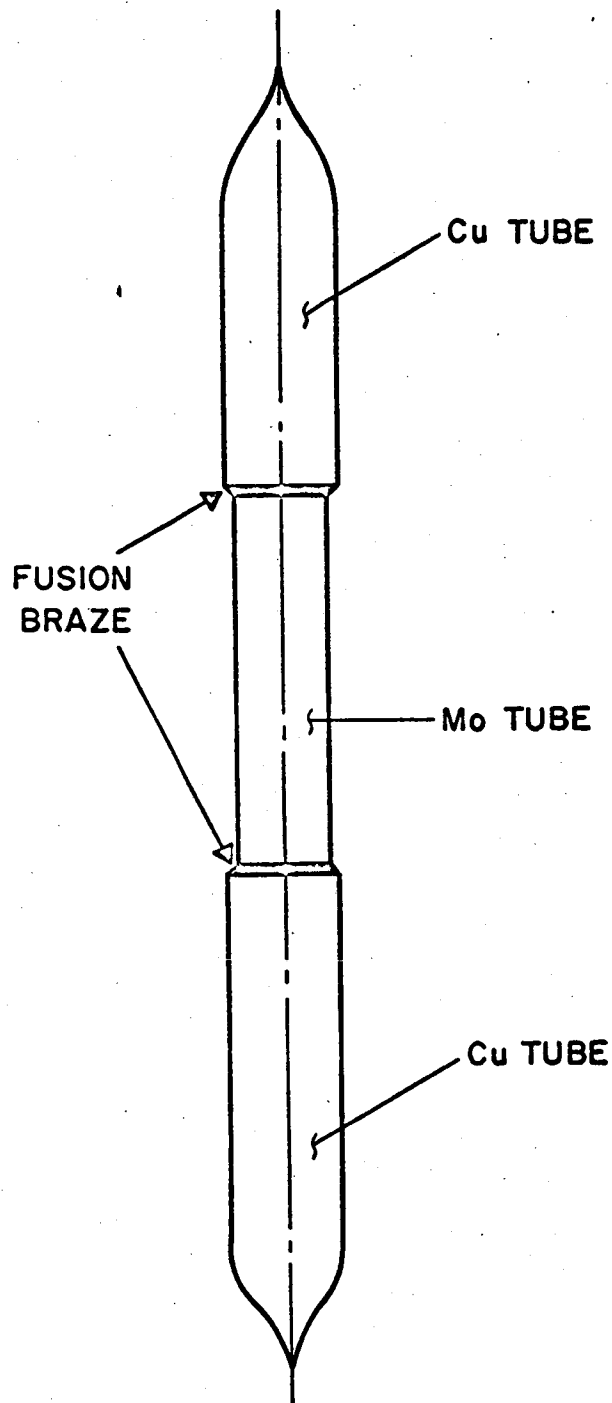
Figure III-27.   Metal Cesium Capsule.

the copper tube at the upper end of the cesium reservoir. When the cesium fluoride experiments have been concluded, this capsule is broken by squeezing the copper tube containing it and fracturing the molybdenum portion of the capsule. At this point, of course, the cesium is released into the device.

The procedure for preparing this capsule can be seen by following Figure III-28. A molybdenum tube which has been fired at about 1400°C in wet hydrogen is brazed in wet hydrogen at both ends to two copper tubes with fusion brazes of the copper to the molybdenum. A long copper tube and a short copper tube are used for this purpose. The short tube is pinched off, and the glass cesium capsule is inserted in the long tube. The other end of the long tube is attached to the vac-ion pump. The whole assembly is outgassed, the portion containing cesium at about 200°C and the portion which will result in the metal capsule, to the far right of Figure III-28, at 400°C. Once a sufficiently low pressure (about $10^{-8}$ mm Hg) is achieved, the glass capsule is cracked by collapsing the copper tube containing it, and any inert gases that may evolve are pumped out. Once the original pressure of the system is reached, the long copper tube is pinched at point B. The cesium is then distilled into the molybdenum tube portion of the assembly in the usual manner, and a second pinch-off is performed at point A. Since the cesium cannot be visually observed in the metal capsule, a method is required to insure that cesium has, in fact, been placed in this capsule. This is accomplished by weighing the whole assembly containing the glass capsule prior to attaching to the vac-ion pump. After the process is completed, all the components are weighed, and the portion of the copper tube between pinch-offs at points A and B is inspected for remnants of

79
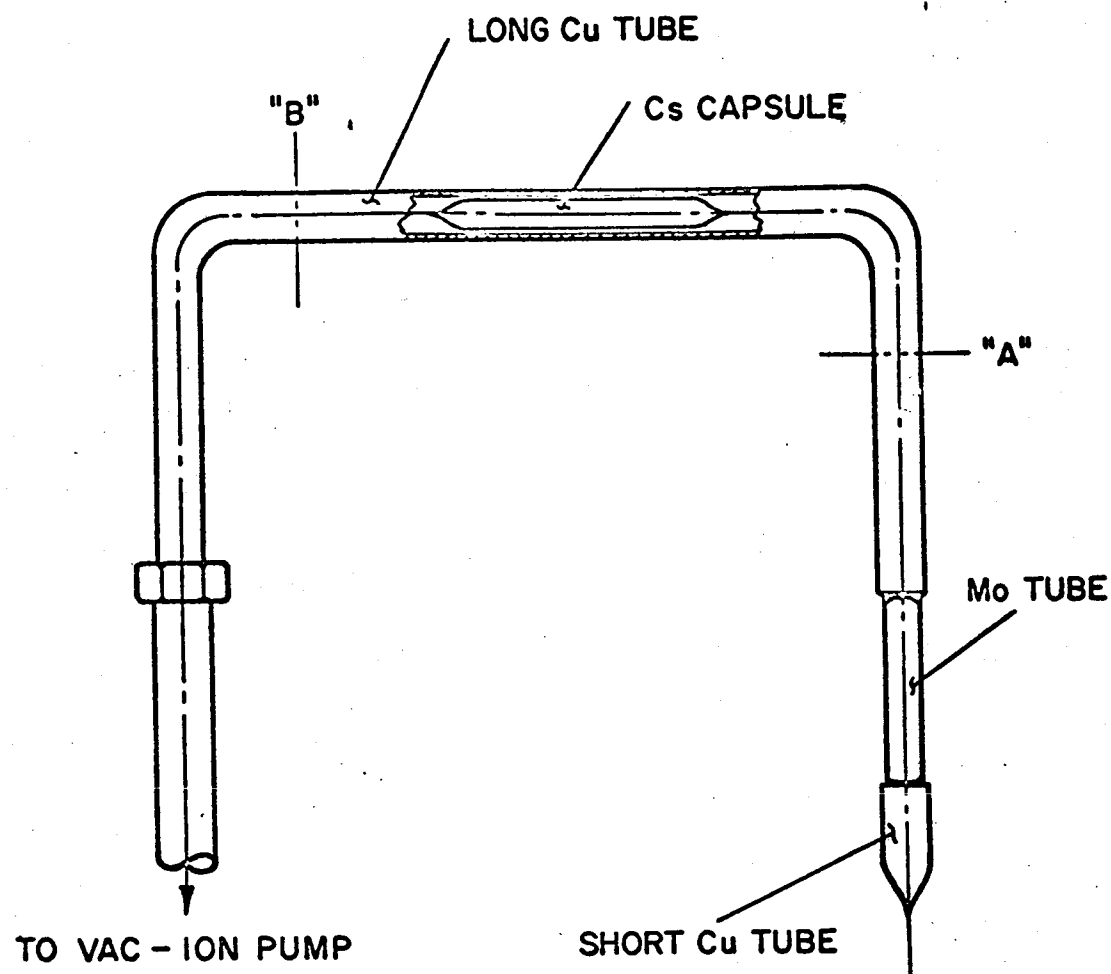
Figure III-28.  Preparation of Cesium Capsule.

cesium. If the weights at the beginning and the end are the same, and no cesium is observed in the portion containing the broken glass capsule, then the cesium must be in the metal capsule. In fact, the cesium can be heard if the capsule is shaken after being warmed to body temperature by holding it in one's hand.

Introduction of the cesium fluoride into the converter also presents problems. Cesium fluoride is a highly hygroscopic substance, and, if left exposed in the atmosphere, it will very quickly pick up moisture from the air and will become wet, until finally it all dissolves in a puddle of water. The problem is aggravated by the fact that cesium fluoride is received in a powder form, and a powder, having a very large surface area, will very quickly pick up large amounts of water. To counteract this tendency, the cesium fluoride was never exposed to the atmosphere, but was handled under argon during transferring. As a further precaution, a pellet-making press was used to compress the powdered cesium fluoride into pellets. These pellets were inserted in the device under dry argon,[*] and they were outgassed in place prior to any outgassing of the device.

To drive off the water vapor it is only necessary to raise the temperature of the cesium fluoride pellet slightly above 100°C. This does not result in any loss of cesium fluoride, since it has a low vapor pressure. As a matter of fact, inspection of Figure III-29 will reveal that the vapor pressure of cesium fluoride is about $10^{-4}$ at a temperature of slightly below 300°C. This is the level at which the cesium

---

[*] The argon is supplied by AIRCO and has the following specifications: oxygen, 0.5 ppm; hydrogen, 0 ppm; dew point, -110°F; purity, 99.999%.
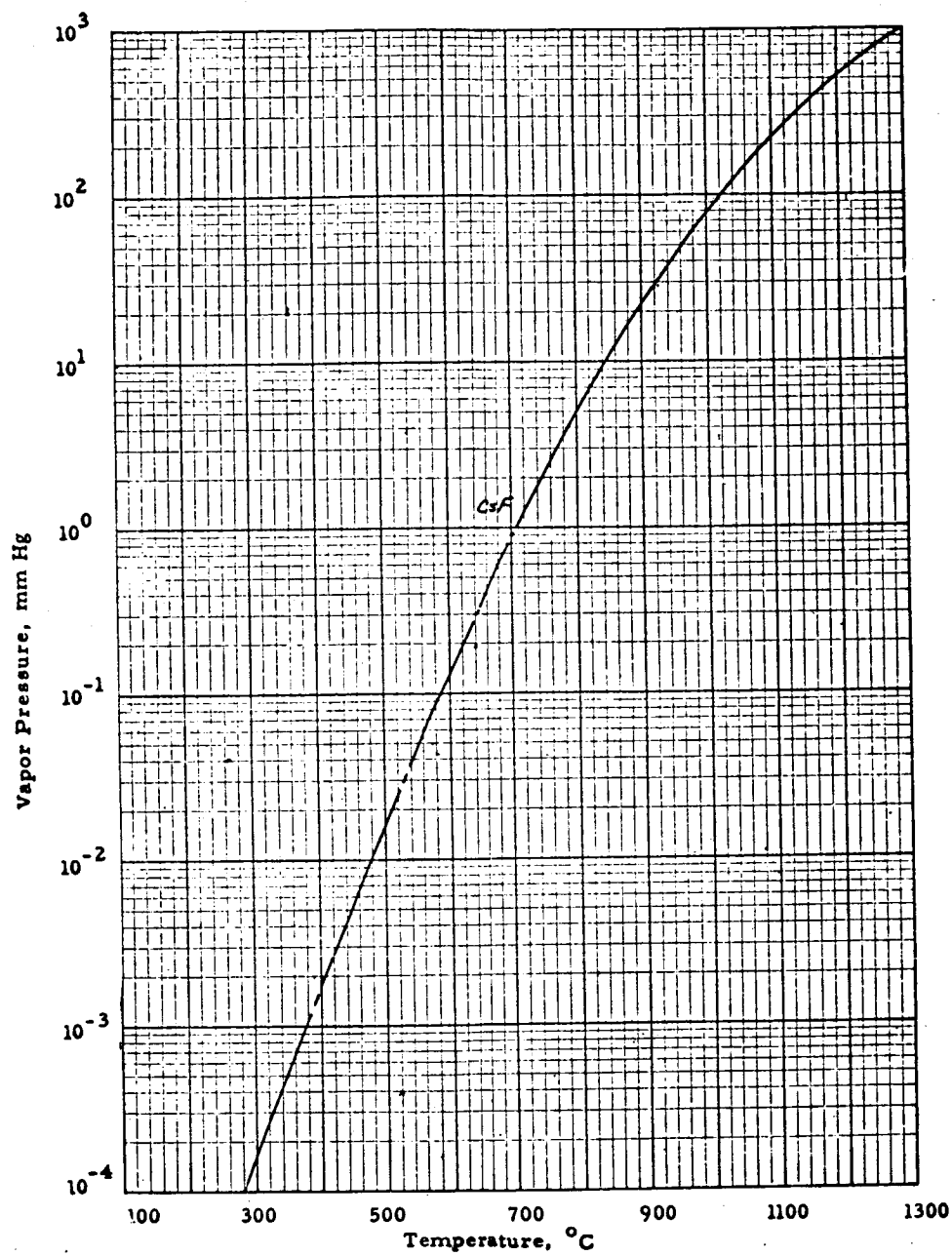
Figure III-29.  Cesium Fluoride Vapor Pressure.

fluoride reservoir was outgassed during outgassing of the device. This method of handling and pelletizing the cesium fluoride has proved quite satisfactory. Outgassing of the converter was begun by outgassing the additive reservoir. This was accomplished at about 150 °C, where the water vapor is rapidly driven off.

Hydrogen and oxygen are not expected to react with cesium fluoride based on thermodynamic considerations.* Water, however, is absorbed by cesium fluoride, and the wet cesium fluoride can attack metals and therefore have corrosive action on diode components.

---

*The free energy of formation for cesium fluoride is more than twice that of any other species that can be formed by reactions of cesium fluoride with hydrogen or oxygen.

## CHAPTER IV

## INSTRUMENTATION

### A. GENERAL

The instrumentation developed under this program represents a significant advance in the state of the art of testing thermionic converters. The most important feature incorporated is the virtually complete elimination of edge effeots. In other words, the data generated will be almost identical to that produced by a diode having plane parallel electrodes of infinite size. This is accomplished by use of a guard ring around the collector. The guard ring, however, to be effective, has to be maintained at the same temperature and electrical potential as the collector. The success of the experiments will depend on how closely the guard ring temperature and potential can follow the collector temperature and potential.

The temperature control requirements and their effects on diode geometry have been described in Chapter III of this report. The instrumentation arrangement is illustrated in the block diagram shown in Figure IV-1. Column A contains the power supplies, controllers, and chart recorder controlling and measuring the element temperatures in the converter test cell, Column B. In Columns C, D, and E is the output equipment required for electrical tests. The switching and shunt block, C5, provides the jacks, switches and measuring shunts to interconnect the power supplies, X-Y recorder, and oscilloscope for the various tests.

83
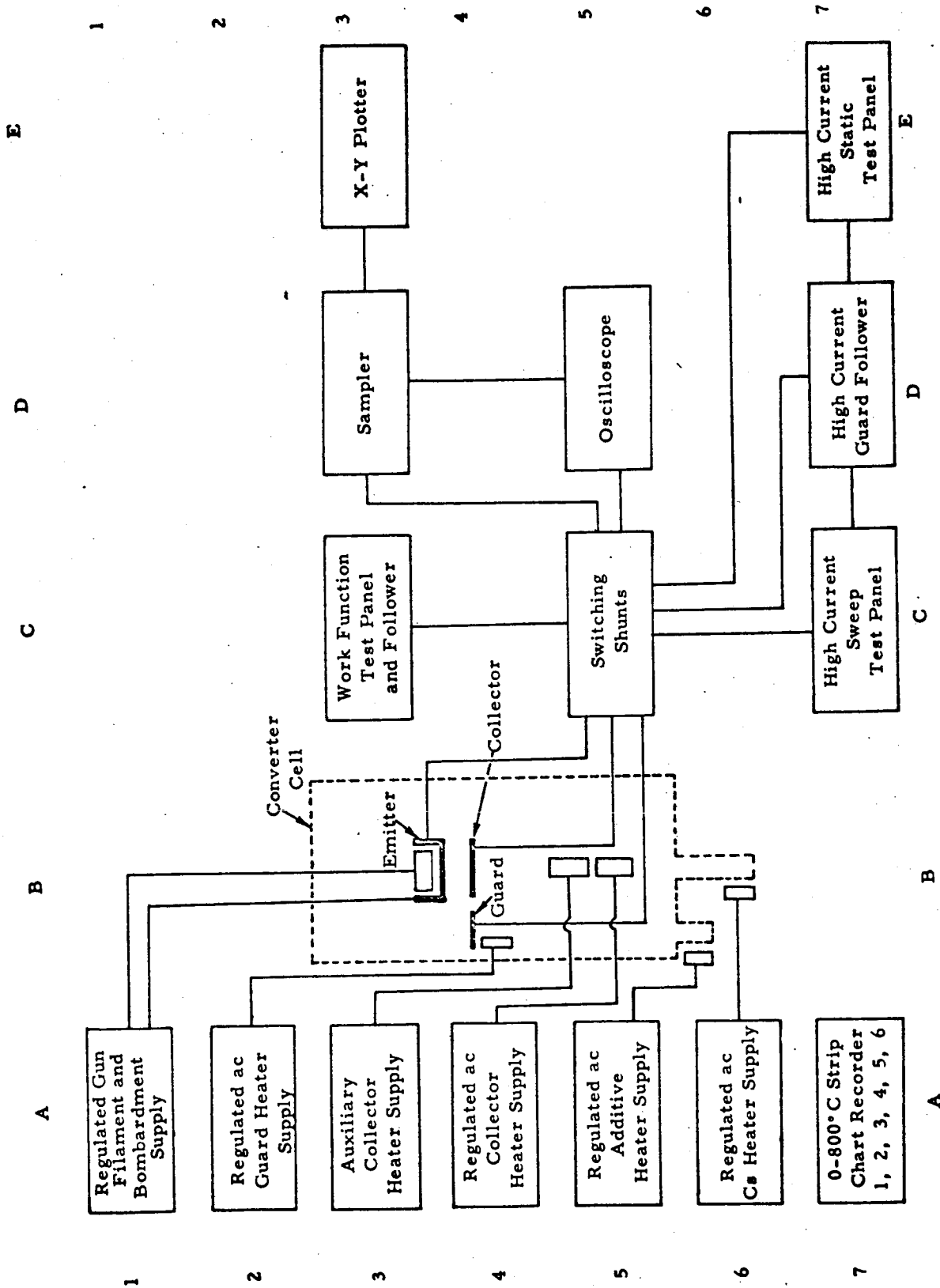
Figure IV-1. Block Diagram of Test Equipment

B.    TEMPERATURE CONTROL

The emitter is heated by an electron-bombardment power supply arranged for either internal constant power control or external control from a temperature sensor.  This system uses a servo-motor to regulate the filament power.  A block diagram of the unit is shown in Figure IV-2 and the detailed schematics are included in Appendix A.

The cesium reservoir, collector, and guard temperatures are controlled by a balance between the power input to their respective resistance heaters and the heat flow to a water-cooled sink.  The power supplies are low-voltage transformer-isolated units and include an on-off type of proportioning controller which responds to a thermocouple in the diode element.  These units maintain the required test cell conditions with only occasional manual adjustment.  Because of the high power input necessary for collector control, an auxiliary heater and step-adjustable power supply were designed to ease the controlling load.  The functional schematic for the controlling heater power supplies is shown in Figure IV-3, and the complete circuit diagrams are shown in Figures III-9, -10 and -11.

Actual temperatures in the test cell are monitored by the multipoint strip chart recorder, A7 of Figure IV-1.  This recorder is observed during testing, and any necessary adjustments are made to the heater supplies to produce the desired conditions.  In addition, this unit monitors the collector heat flow section and emitter ring structure to insure that there are no cold spots in the converter and to provide any required heat flow data.

THERMO ELECTRON
ENGINEERING CORPORATION
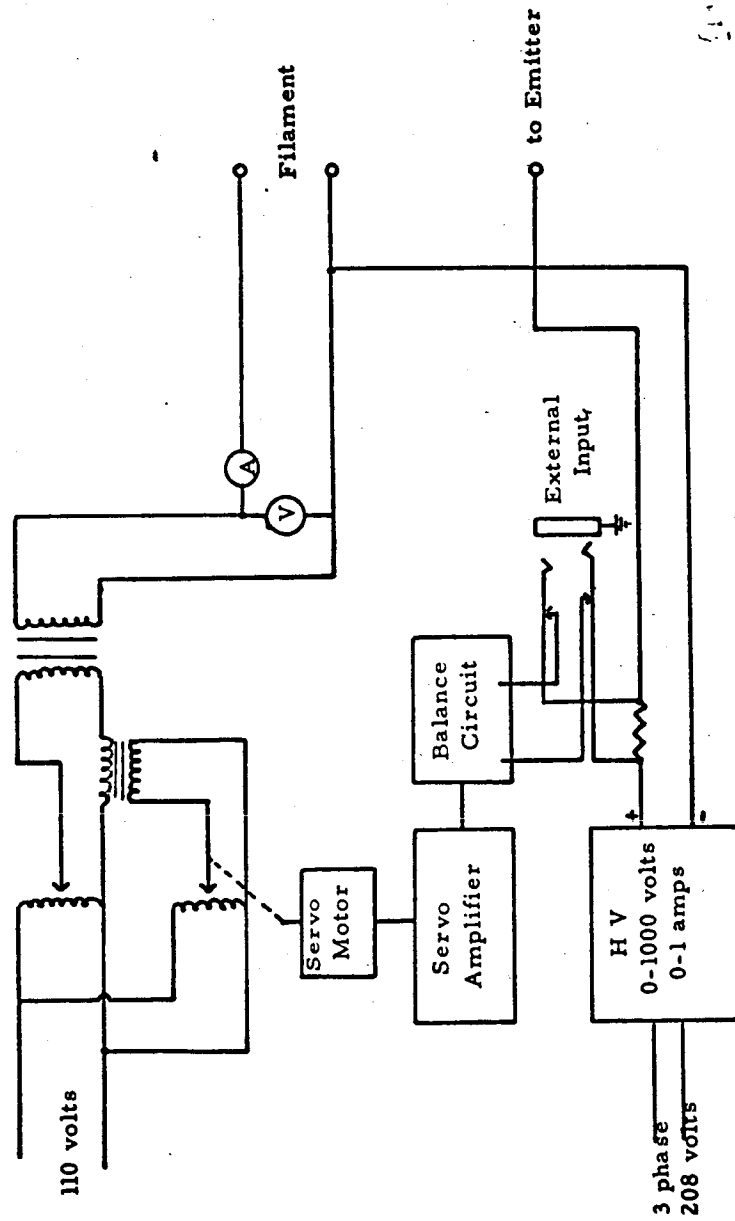
Figure IV-2. Regulated EB Supply Schematic, A1, A2.

86
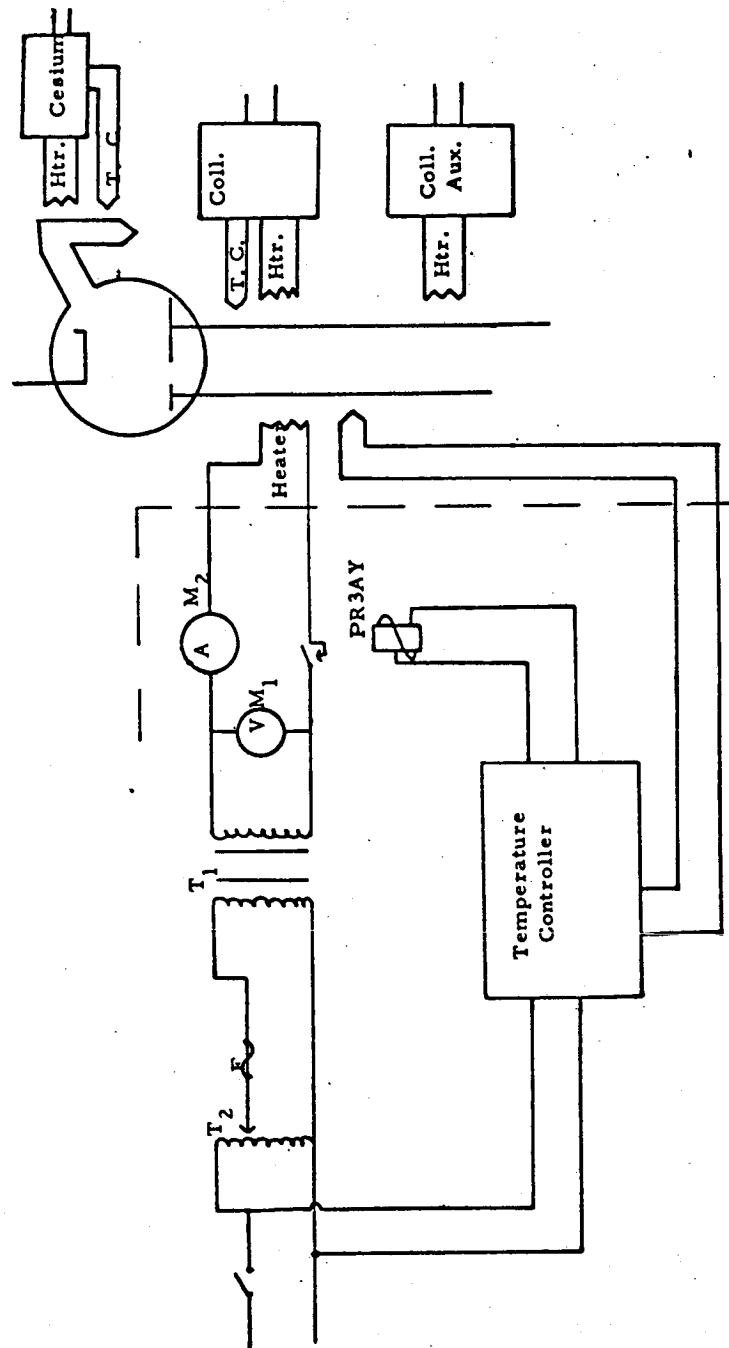
Figure IV-3. Heater Power Supplies and Controls.

Figure IV-4 shows the heater control cabinet with its power supplies and regulators. From top to bottom these units are: guard heater supply, cesium heater supply, collector heater supply, electron bombardment filament supply and control, collector auxiliary supply, and electron-bombardment high-voltage power supply.

## C. ELECTRICAL TESTS

The experiments performed in this study may be conveniently divided into three main groups, each of which requires a specific set of equipment and is designed to produce a given type of output data. These groups are:

1. High-power output static tests, including electron cooling and heat transfer measurements.

2. Low-power quasi-static or manually traced J-V curves.

3. Dynamic parametric tests.

A typical high-power static test is conducted at a single point on the J-V characteristic and can involve emitter currents in the range from 10 to 300 amperes, where the converter element temperatures are very dependent upon the operating point chosen. To produce reliable electron cooling and heat transfer measurements, static equilibrium conditions must be established at each point, and the test system must thus provide means to select and maintain the desired current and voltage for both guard and collector.

Low-power quasi-static tests are used in the emitter current range under 10 amperes, where current-dependent heating or cooling is negligible. Once the desired electrode conditions in the converter have been established, an entire J-V characteristic may be traced out without introducing temperature variations. This method of testing differs from
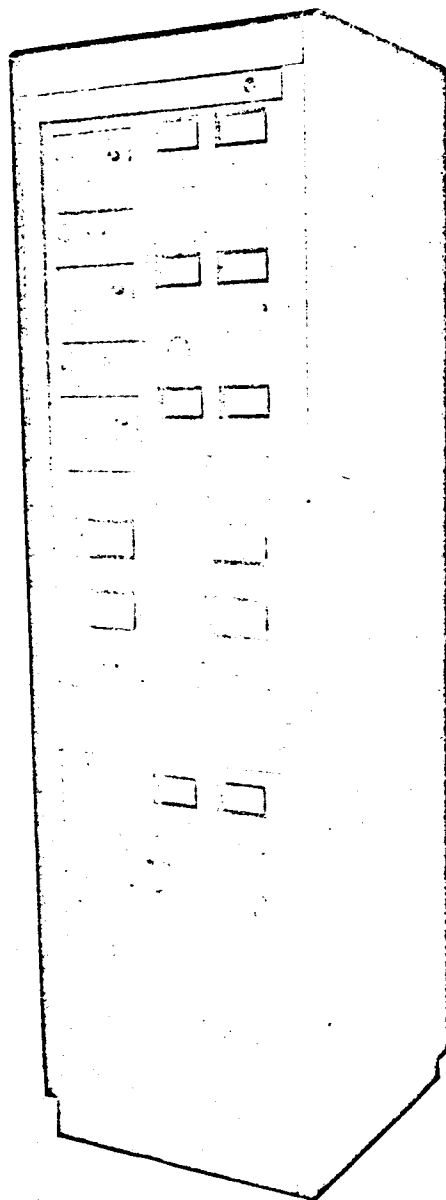
Figure IV-4.  Data Control Cabinet.

89

true static testing in that the voltage and current parameters are changed while all other parameters are assumed to remain constant. The assumption is justified because the imbalance due to the additional current drawn is very small.

Because these tests can be made with slow variations in current, a high degree of balance between collector and guard potential can be achieved, thereby eliminating edge effects and greatly reducing leakage currents between emitter and collector. With an imbalance of 1 milli-volt it was possible to measure currents of less than 1 micro-ampere. This is facilitated by the configuration of the diode, where all the ceram-ics which are the principal sources of leakage currents are isolated from the collector by the guard ring structure. This group of tests thus pro-duces a complete J-V characteristic on an X-Y plotter in a form suitable for work function and other low-current analyses.

The dynamic parametric tests trace out a complete J-V character-istic over a current range similar to that of the high-power static tests. In this case, however, the characteristic is swept at a 60-Hz rate so that the temperatures remain constant even though the current varies over a wide range. Furthermore, because of the low duty cycle, the average electrical power to the elements is small enough to simplify temperature control. The entire J-V curve produced is displayed on an oscilloscope for monitoring purposes and may be recorded on an X-Y plotter using a sampling technique. These curves form parameter families which are the major output of the converter testing procedures and indicate the device performance over a wide range of conditions.

1.  Static Tests — High-Power Equipment

The static testing circuit with manual balancing is shown in Figure IV-5. It uses two adjustable low-voltage high-current power supplies called static load controls, with water-cooled resistances to control the operating point in the converter. The voltages on the collector and guard are balanced manually. Figure IV-6 shows the same circuit with the addition of the guard balance control for dynamic testing. A shunt in the collector lead provides for current measurement, and voltage taps on the emitter and collector electrodes provide a potential output which bypasses IR drops in the current leads. This set-up allows the converter to operate at high power output conditions with all parameters fixed at predetermined values. The device is therefore at static equilibrium. The circuits for the guard and collector static load control are shown in Figures IV-7 and IV-8, respectively.

The guard circuit uses a six-phase star rectifier arrangement with three transformers. These are Y-connected to three similarly connected mechanically coupled variable autotransformers. A neutral wire provides a path for the third harmonic current produced by the nonlinear behavior of the iron cores and rectifiers.

The collector circuit, because of its high currents (200 amperes), uses a double-Y rectifier connection, with an interphase reactor for balancing. In this arrangement two rectifiers at a time conduct, thereby reducing the peak currents and improving transformer utilization. This is a single transformer with a delta-connected primary, eliminating the neutral wire requirement. The variable autotransformer control is similar to that for the guard.

THERMO ELECTRON
ENGINEERING CORPORATION
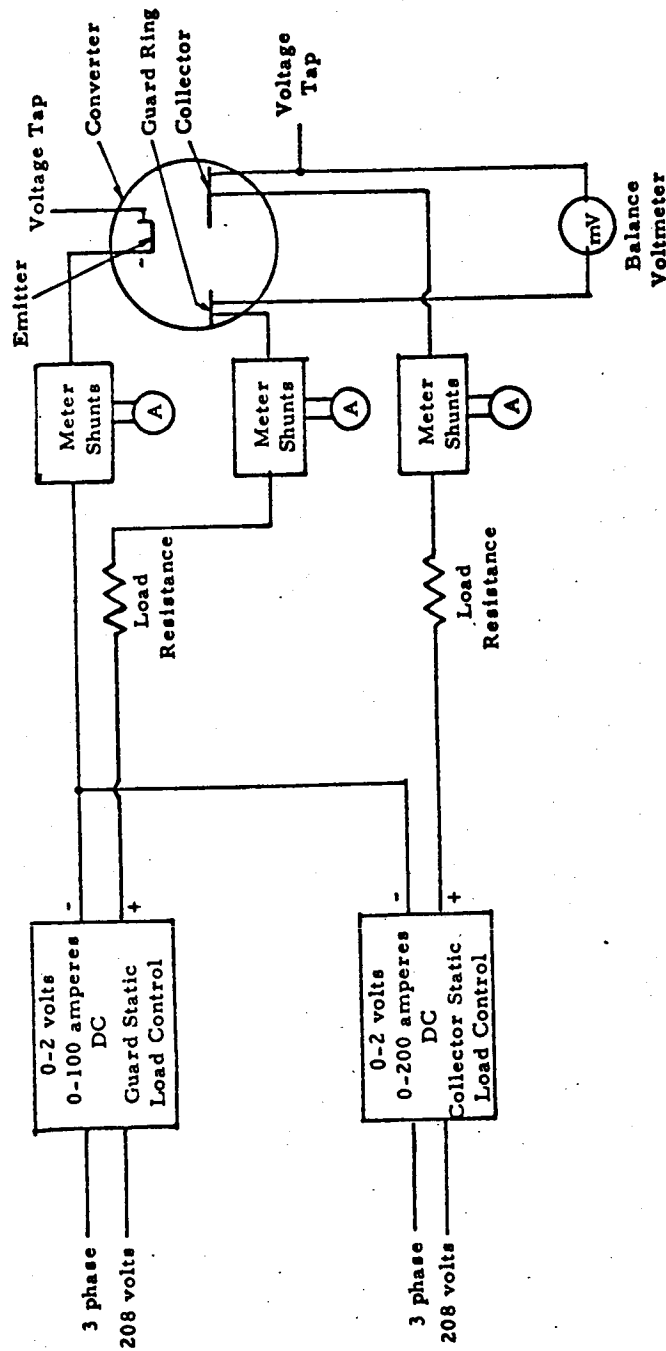


Figure IV-5.  Manually Balanced High-Power Static Testing Circuit, D7.
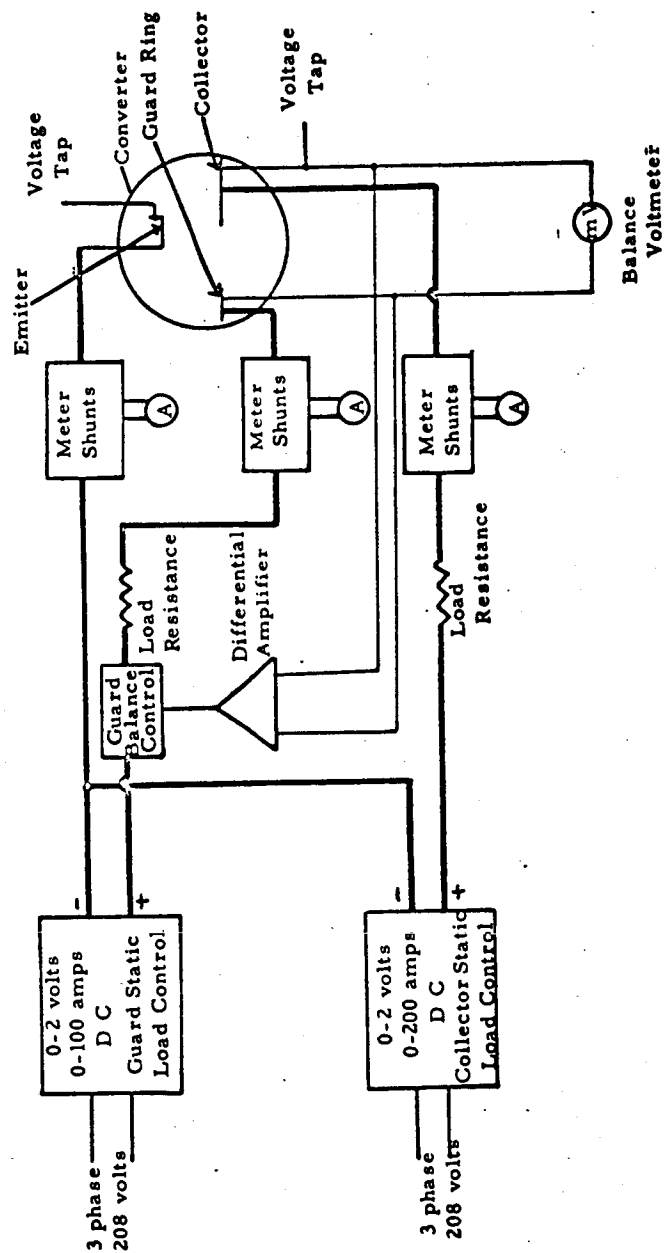
Figure IV-6. Automatically Balanced High-Power Static Testing Circuit, E7, D7.

93

THERMO ELECTRON
ENGINEERING CORPORATION

1N1183A
Diodes

Output

3 P6468
Transformers

CB Trip Coils

10B-3
Poverstat

CB

3PH
208 v
60
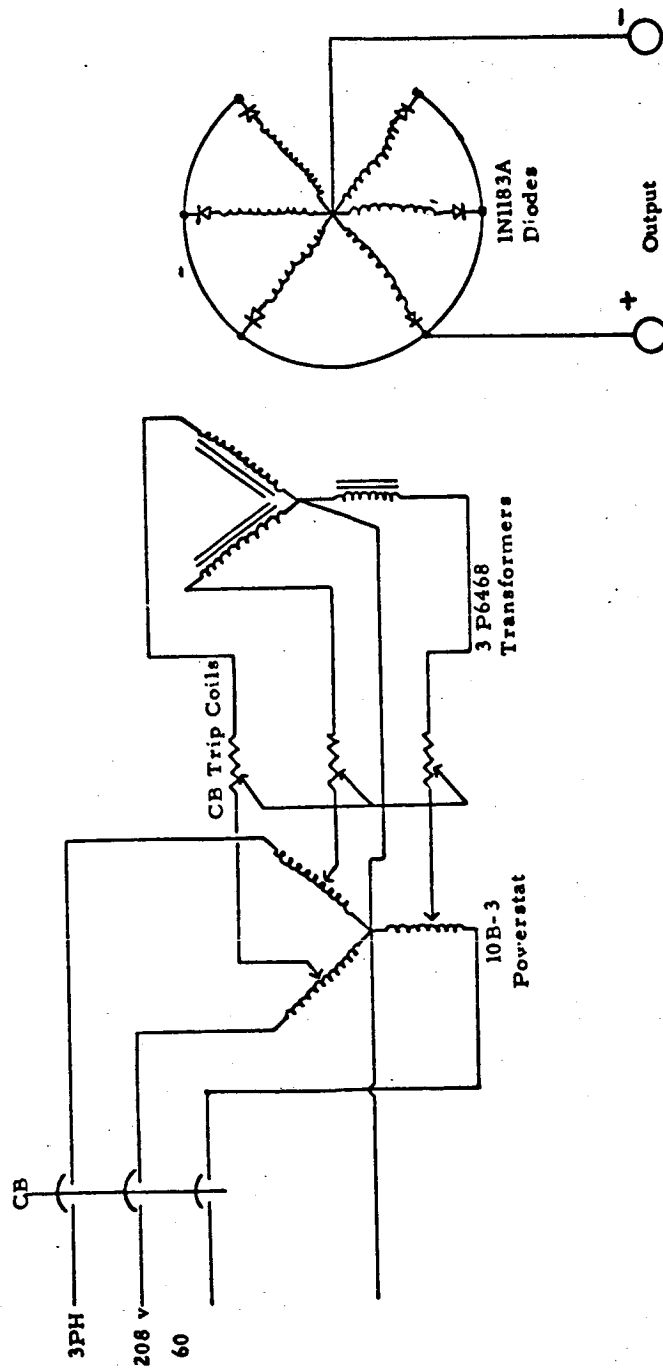
Figure IV-7. Guard Static Load Control.

94
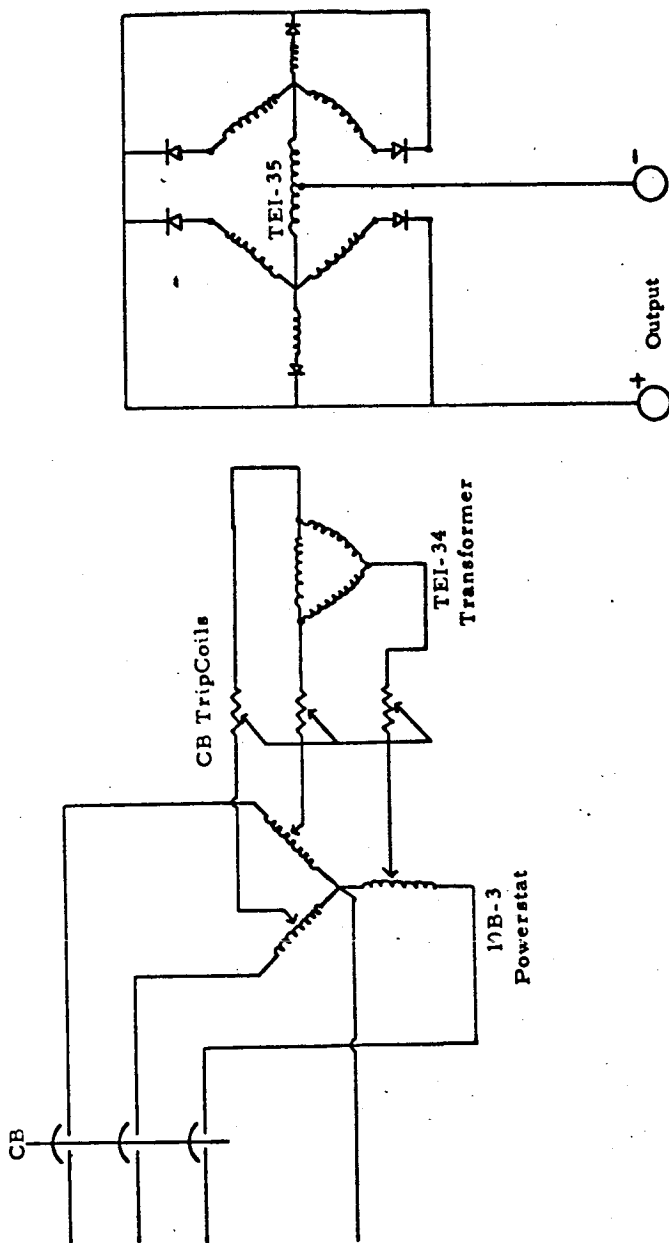
Figure IV-8. Collector Static Load Control.

These supplies were not filtered, since tests showed that the small amount of ripple present did not affect the static D'Arsonval current and voltage meters. It was found that the X-Y plotter, in addition to indicating the actual static point on the J-V characteristic, also, through the sampler, showed the slope of the actual curve at that point, thereby furnishing additional information on any deviations from the dynamic performance curve.

2.   Quasi-Static Panel

This unit, shown at position 3C of Figure IV-1, is used for the low-current J-V characteristic measurements, where it is desirable to cover the entire range from forward to reverse saturation. Referring to the typical curve shown in Figure IV-9, it can be seen that the converter has two power-absorbing regions separated by a power source area. In order to trace this curve, the test equipment must be able to control positive and negative voltage and current. To avoid discontinuities in the plot it is desirable that a single control sweep the entire curve without the use of reversing switches. Over the entire J-V curve the collector and guard must be maintained as an equipotential surface if valid data, independent of edge effects and leakage, is to be produced.

A block diagram of the panel is shown in Figure IV-10 and a schematic in Figure IV-11. $P_1$ is the main power supply, whose output is varied to plot the curve. $P_2$ continually senses the collector-guard imbalance and adjusts its output to reduce this imbalance to a minimum. Separate current and voltage leads to the converter minimize any effects of lead drop which may become important at the higher currents. Collector current is measured across a set of 1% four-wire shunts whose values
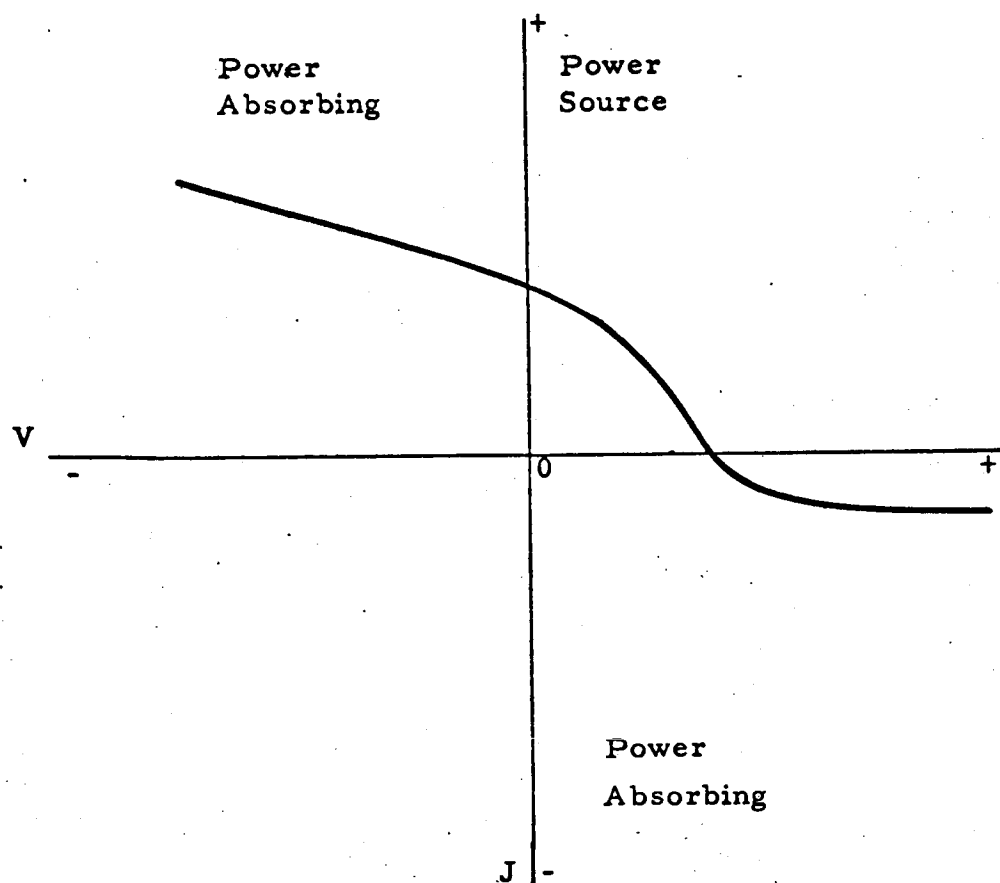
Figure IV-9.   Typical Low-Current J-V Characteristic.
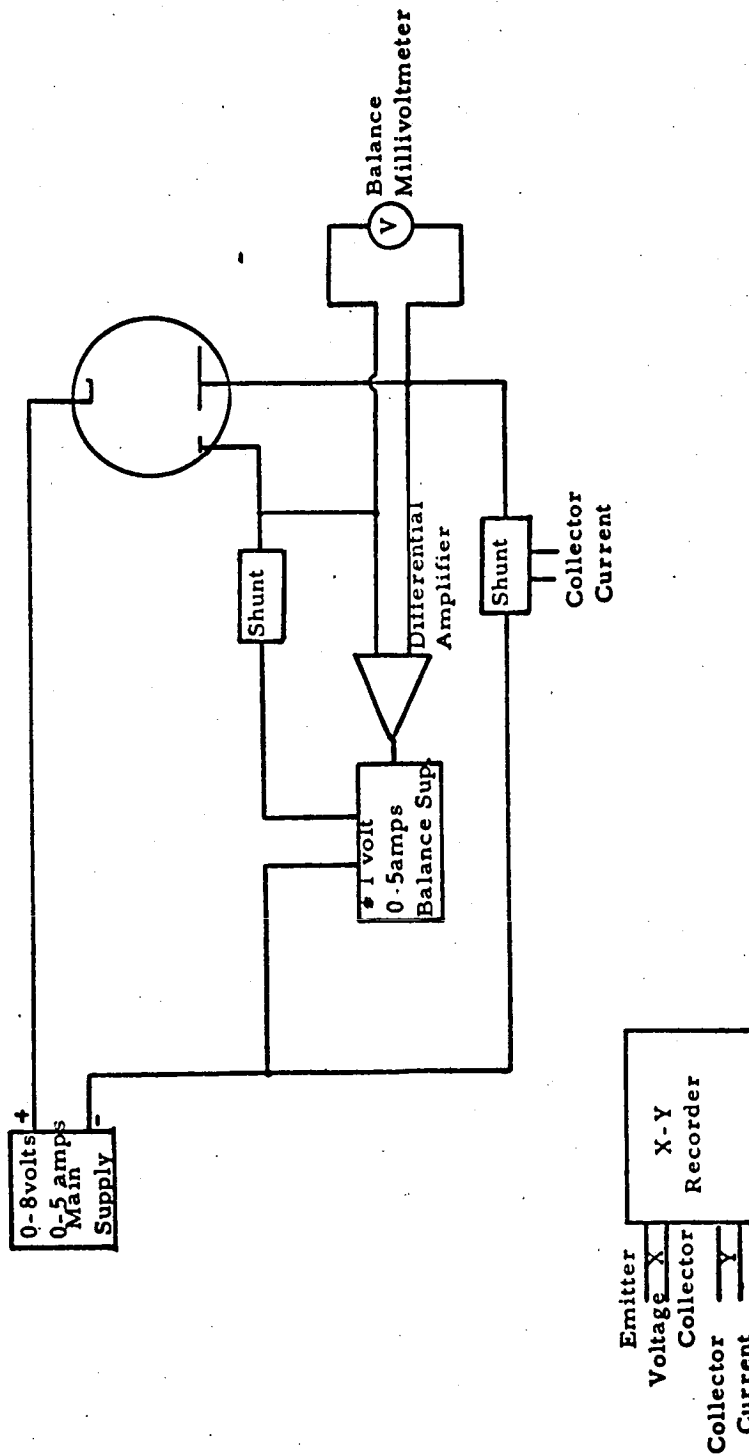
Figure IV-10. Low-Power Quasi-Static Circuit C3.

98
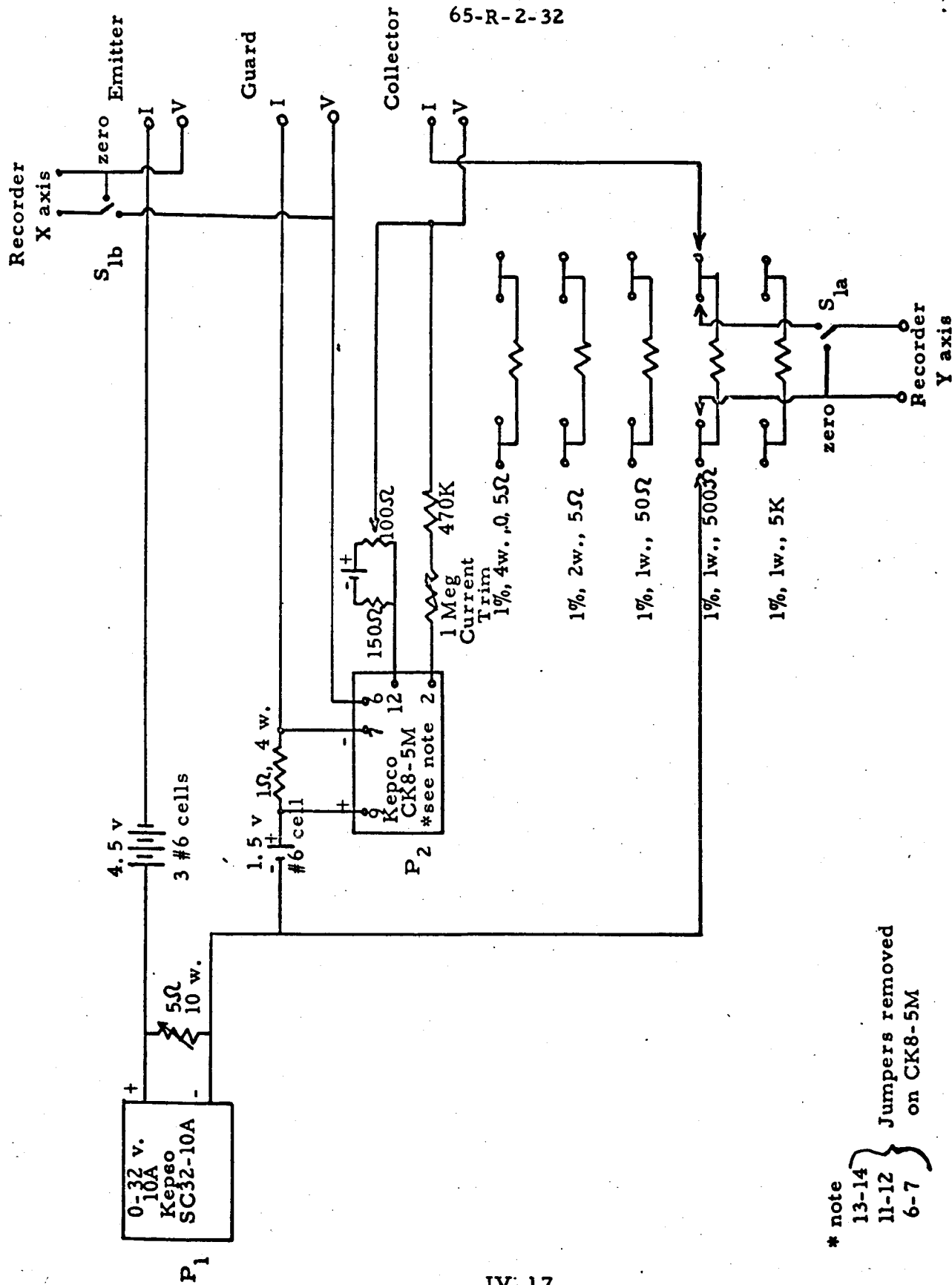
Figure IV-11. Schematic of Quasi-Static Test Panel.

are selected to match the currents expected. Collector-emitter voltage is measured from the guard and emitter voltage lead, thereby eliminating recorder currents from the collector shunt. The construction of the converter is such that all leakage currents, except those through the water cooling and the sheath heater, are to guard potential and therefore negligible. The sense current for $P_2$ is trimmed to about 1 $\mu$A from a negative source internal to $P_2$. An adjustable voltage in series with the sense lead provides a balance adjustment for the guard collector voltage. This balance may be monitored by a high-impedance voltmeter connected to the voltage taps. Primary batteries in series opposition with $P_1$ and $P_2$ provide for both positive and negative voltage output without switches. However, since these supplies will not absorb power, swamping resistors are connected across the output of $P_1$ and $P_2$ and adjusted to keep the power supply current in the proper direction on all portions of the J-V curve.

The performance of this panel was tested both with the converter and with a dummy resistive load and showed less than 2 mV imbalance with collector currents up to 2 amperes. It was capable of balancing with leakage resistances as low as 1000 ohms. With a leakage resistance of the order of 20 ohms, motorboating in $P_2$ was observed due to the high loop gain and increased load currents. This performance was considered acceptable, since this poor a leakage is unreasonable in the operation of the diode.

3. Dynamic Test Equipment

During dynamic testing the converter is driven into the high-current region by a low-voltage transformer controlled by a variable autotransformer (see Figure IV-13). To maintain effective guarding, the potentials of the collector and guard must be matched. A differential amplifier, connected between the collector and the guard voltage taps, continually senses
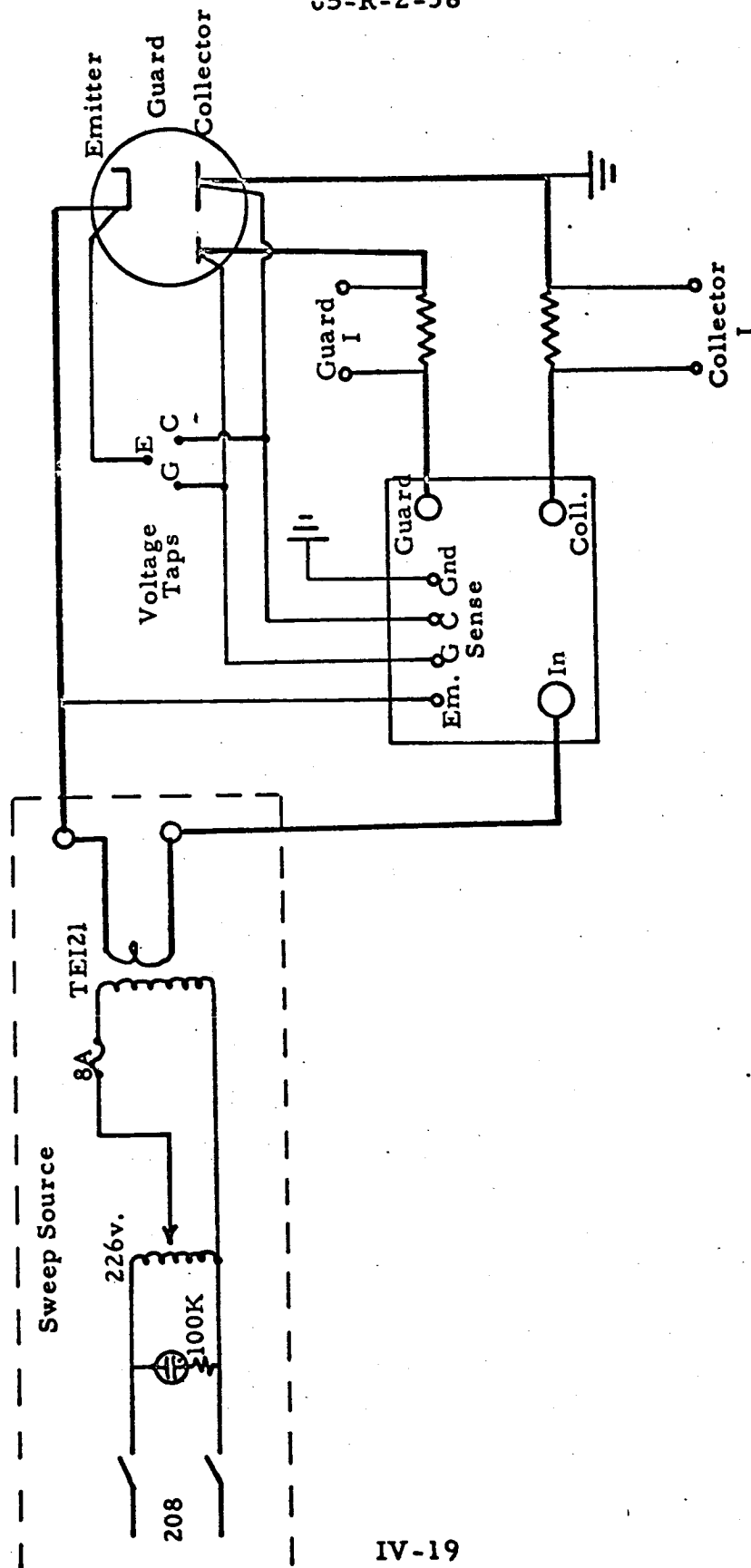
Figure IV-12.  Dynamic Testing Circuit.

the error between the two and, during the sweep, automatically drives a transistor series element in the guard lead, to balance out the potential difference. These components are contained in the guard balance control. The converter J-V characteristic, as obtained from the current shunt and the voltage taps, is monitored by the oscilloscope and recorded on the X-Y plotter after passing through the sampler. Balance between collector and guard can also be monitored on the oscilloscope.

The guard balance control functions with both the dynamic and the static test equipment. It is capable of controlling currents of up to 100 amperes in the guard circuit and 200 amperes in the collector circuit. In dynamic testing the 60-Hz variations in voltage must be matched, and a 2-kHz frequency response is required to balance at this rate. However, in this region the diode has low sensitivity to small variations in the guarding potential, and leakage resistances appear relatively unimportant, so that the balance requirements may be relaxed.

A schematic of the control is shown in Figure IV-13. The three pass transistors $Q_1$ control the voltage drop in the guard lead to balance that in the collector lead. Diode $D_1$ in the collector circuit provides that sufficient voltage be available across the $Q_1$ transistors to keep them out of saturation. $Q_1$ and $D_1$ also block the reverse-current portion of the sweep and are mounted on a water-cooled heat sink to allow greater power dissipation. $Q_2$ is a driver transistor with the sweep voltage as a power source. The differential amplifier P65 senses the imbalance at the voltage leads and, after the amplification of $Q_4$ and the isolation provided by $Q_3$ (a common base stage), it drives $Q_2$ to control the guard voltage. The phase-correction network ($R_1 C_1$) and feedback ($R_2 C_2$) at the input to P65 reduce oscillations due to the feedback from the guard voltage sense.

/02
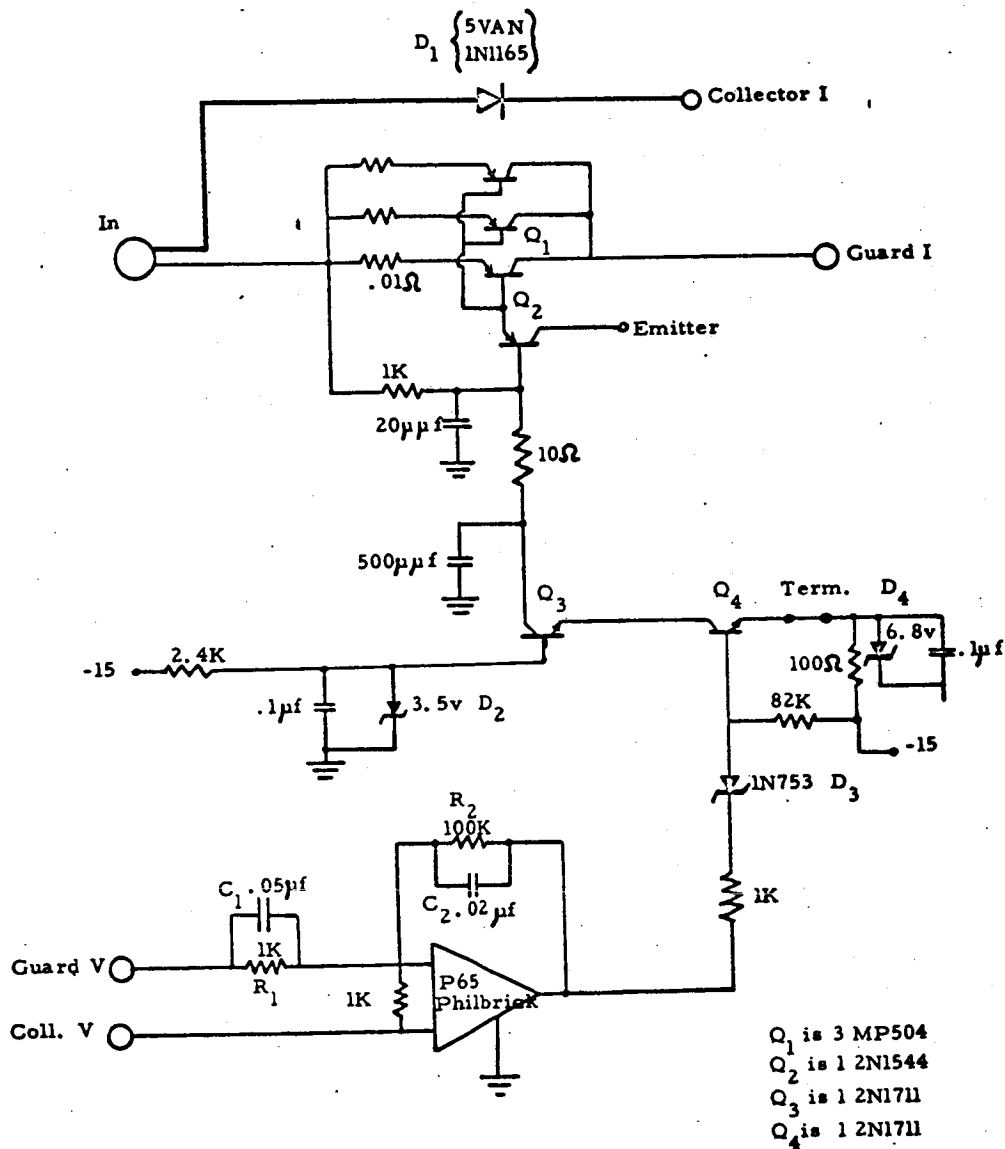
Figure IV-13. Schematic of the Guard Balance Control.

The performance of the subassembly containing the pass transistor $Q_1$, the driver $Q_2$, $Q_3$, $Q_4$, and the diode $D_1$ was evaluated quasi-statically with dc control currents and a resistive load which simulated the converter. With a 60-Hz ac input the characteristics shown in Figure IV-14 were obtained. In this figure the current scales have been chosen to simulate the actual current density in both the guard and collector circuits. Proper control action will be in that region where the "collector" curve is to the right of the "guard" curve. As the drive current is varied, the guard voltage may be shifted to match the collector voltage. With the differential amplifier connected and the panel patched through the switching panel to the converter, the composite performance characteristic shown in the oscillograph of Figure IV-15 was obtained. In this figure are shown the collector and guard J-V characteristics and the collector-to-guard voltage as a function of guard current. The oscillations observed near the start of the curve are the result of transients occurring near ignition and are too small to be significant in the portion of the J-V curve of interest for power measurements. In fact, on the J-V characteristic the oscillations are barely visible. At higher currents the system is very stable and no oscillations are observed.

4.    Switching Panel

To facilitate interconnection between the test vehicle and the various test panels, a patch or switching panel has been designed and fabricated. This unit is located at position 5C in Figure IV-1. The panel face is shown in Figure IV-16, and the TEECO identification number on the panel is SS 303.

104
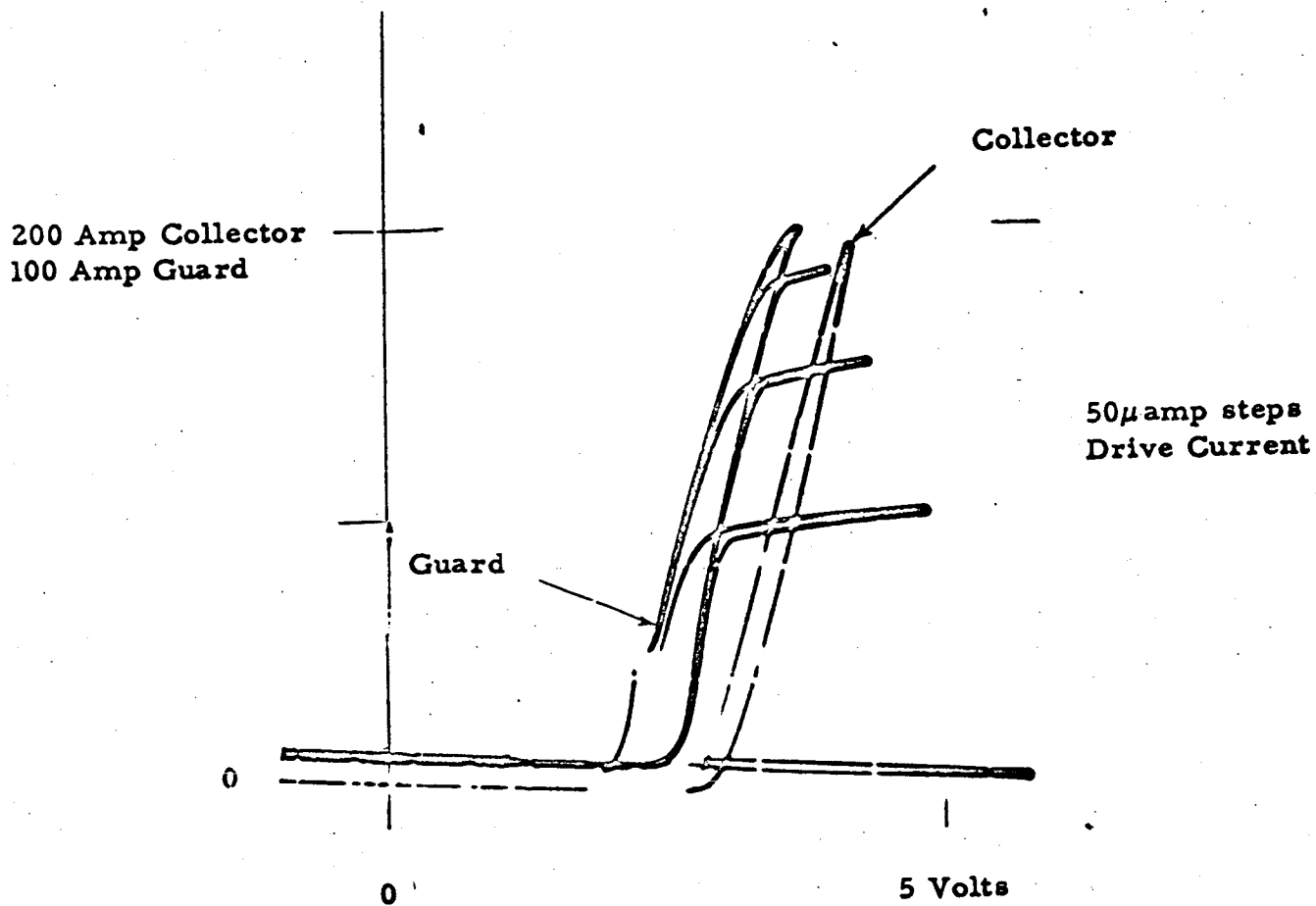
Figure IV-14.   Static Control Characteristics.

65-R-2-39
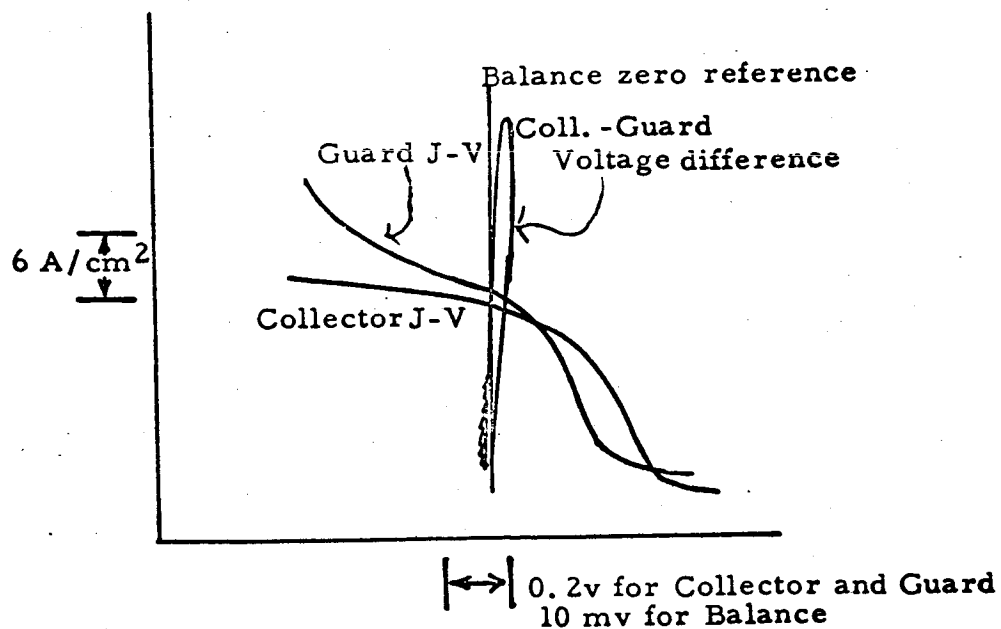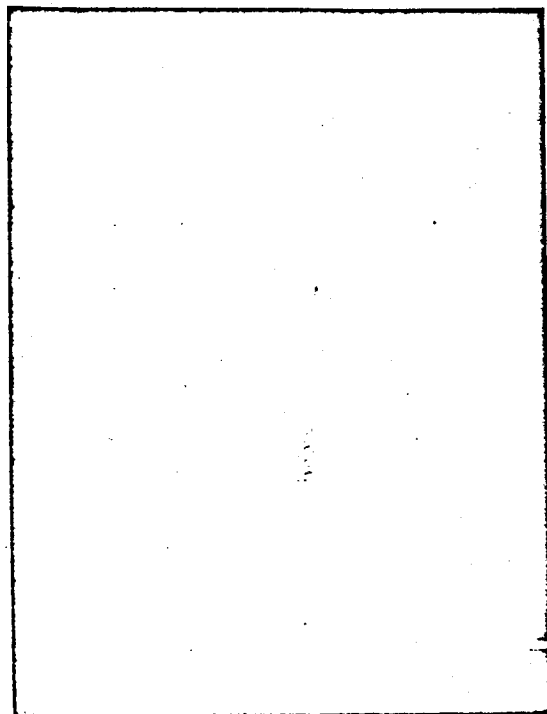


Figure IV-15.   Composite Performance Characteristic.

106
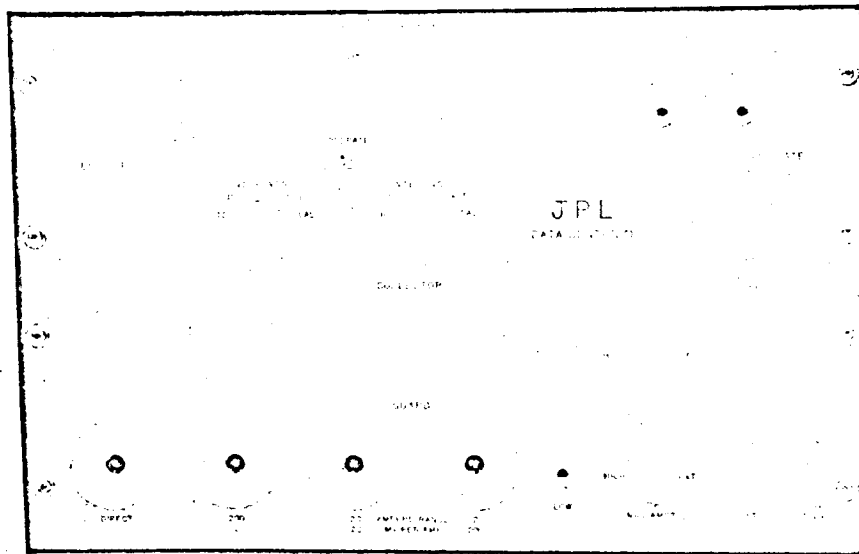
Figure IV-16. Switching Panel.

107

This panel contains the jacks, switches and shunts required to operate the test vehicle. The converter electrodes are connected directly to the 250-ampere connectors, which make up the left-hand column of connectors on the panel face.

A series of calibrated shunts made from water-cooled constantan tubing, as well as six additional 250-A collector and guard connectors, are provided so that a wide variety of current ranges can be accurately metered. The high-current shunts have been calibrated to within 2% using a standard shunt and precision voltmeter. To the right of the high-current connectors are a pair of low-current connectors followed by two switches for additional ranges of the shunts in the collector and guard circuits. The four plugs at the extreme lower right are the meter connections. Figure IV-17(A) is a schematic of the shunt and plug-in connections. This circuit provides resistances from two milliohms to two kilohms.

A built-in calibrator furnishes precise voltages to simplify calibration of the X-Y recorder. It has been adjusted to 2% accuracy using a precision voltmeter. The circuitry, which is shown in Figure IV-17(B), makes use of a temperature-compensated Zener diode supply and matched wire-wound resistors. In Figure IV-16 the terminals of the calibrator appear near the middle right-hand edge.

The signal switching circuits shown in Figure IV-17(C) provide output connection from the shunts and voltage taps. The two switches, shown near the center of IV-16, allow the two pairs of output terminals to monitor selected currents or voltage. A zero switch and "calibrate" position simplify calibration set-up time.
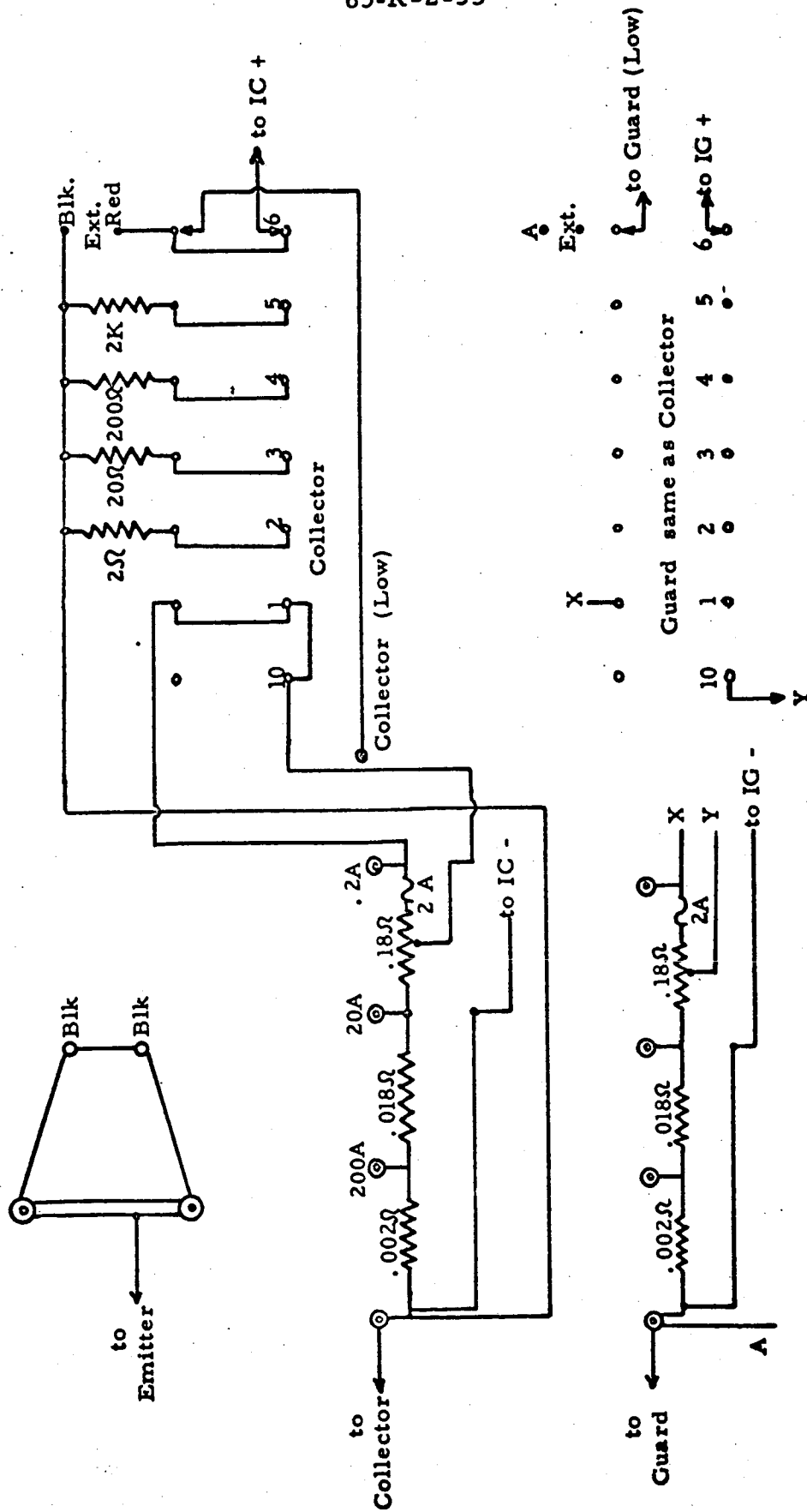
Figure IV-17(A). Current Shunts and Plug-In Connections.
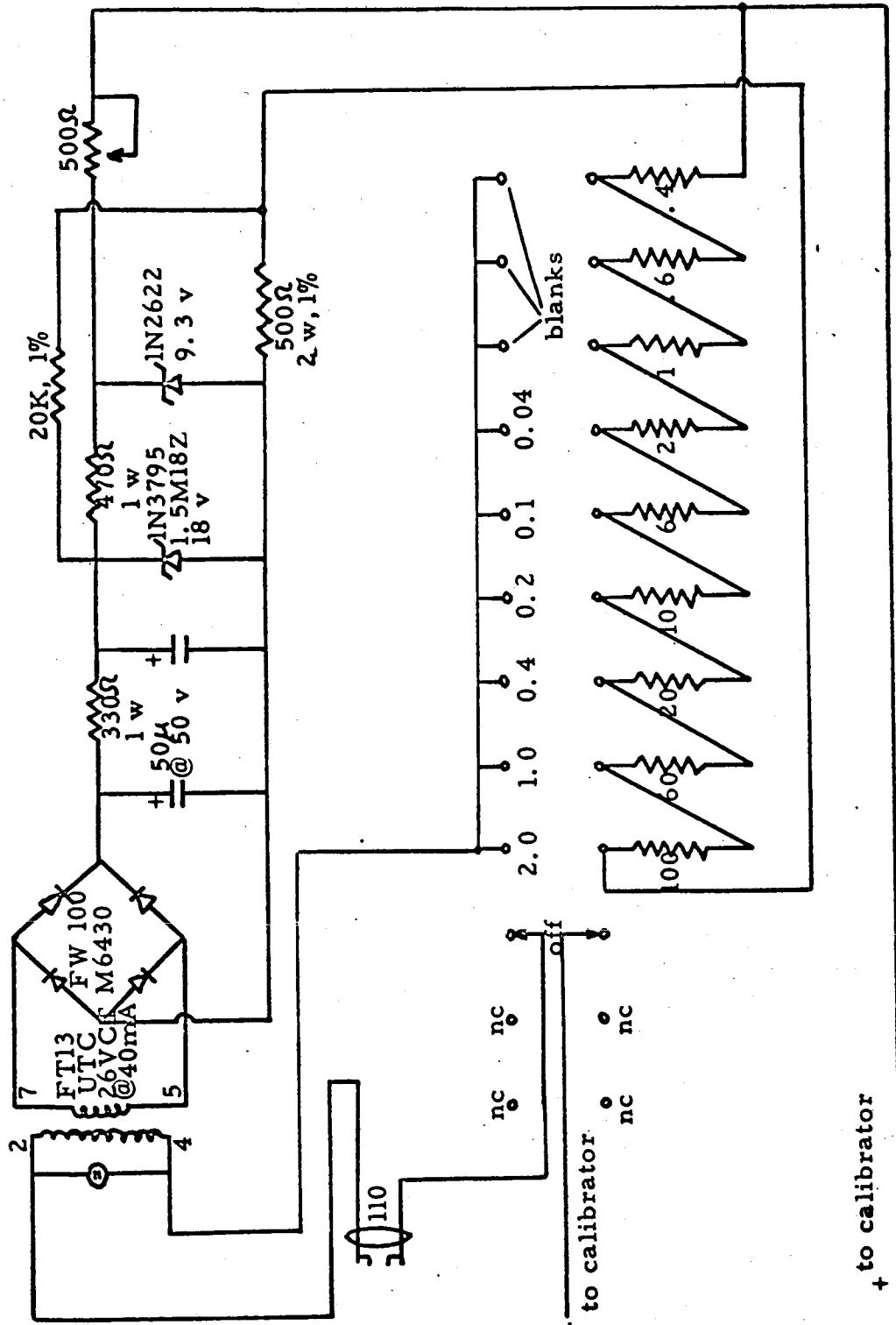
Figure IV-17(B). Calibrator Circuit.
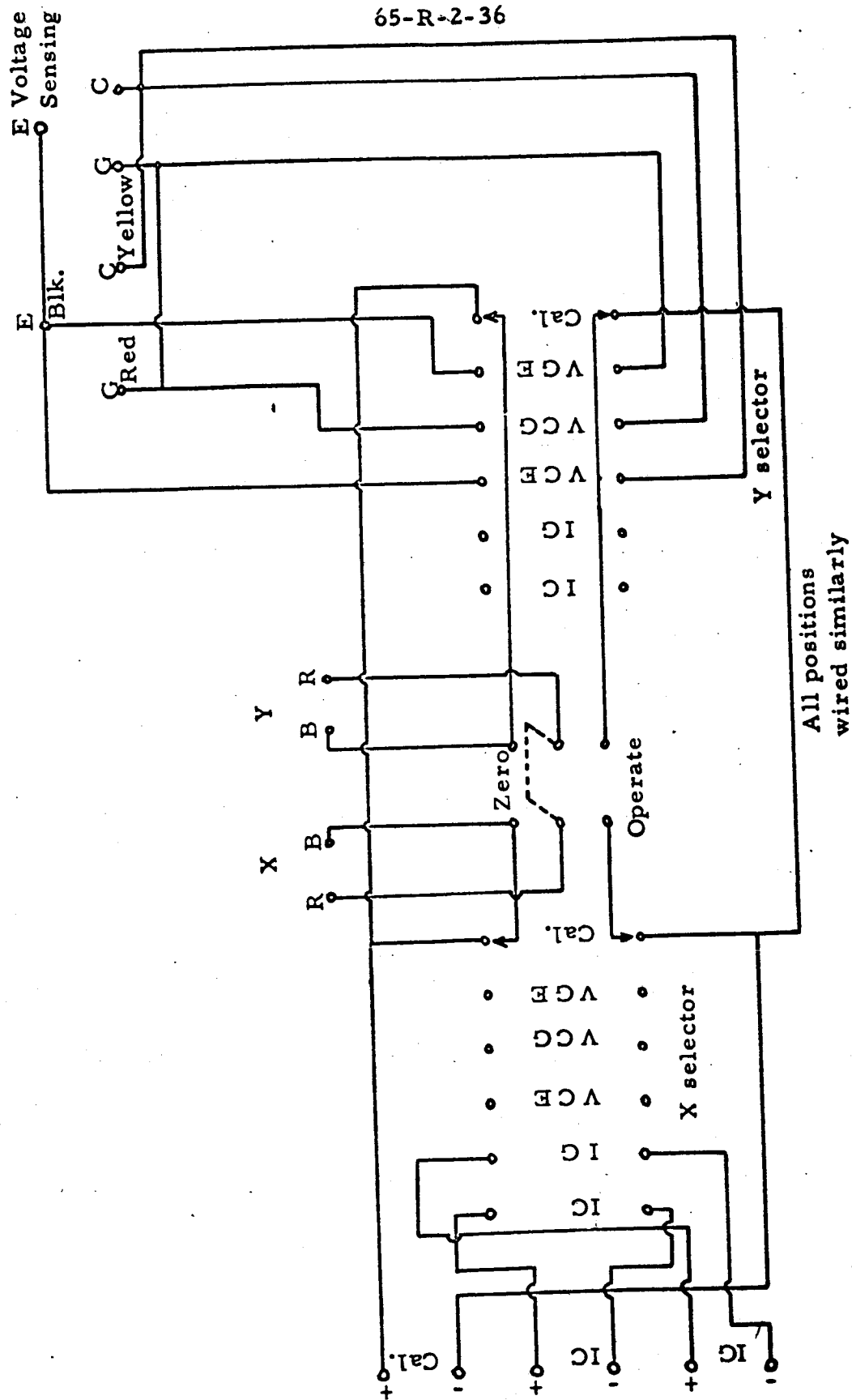
Figure IV-17 (C).   Signal Circuit

5.   Test Equipment Cabinet

Figure IV-18 shows the output test cabinet.   In the photograph the following units may be seen starting from the top:   guard static load control, collector static load control, oscilloscope, sampler, X-Y recorder on shelf, guard balance control, switching and shunt panel, and dynamic sweep source.
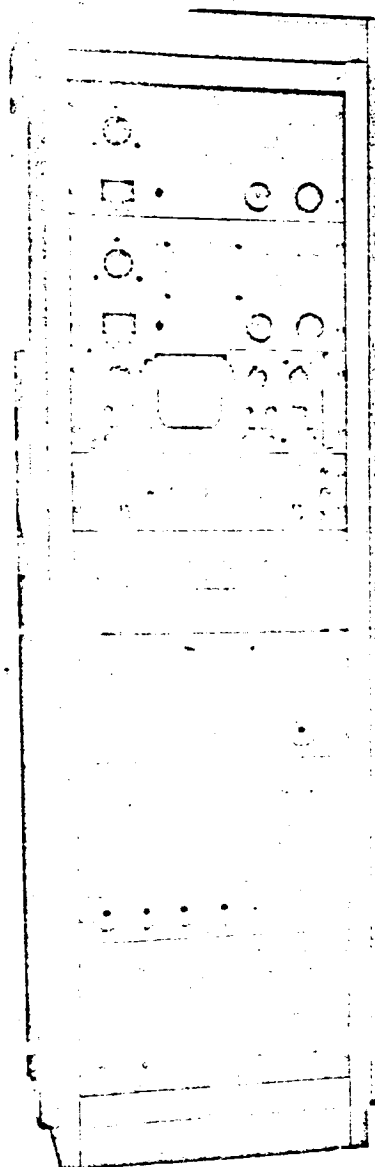
Figure IV-18.   Test Equipment Mounted in Cabinet.

113

# CHAPTER V
## EMITTER PREPARATION

### A. INTRODUCTION

Three emitters (two rhenium and one tungsten) were prepared for this program. The techniques used were chosen to provide a well characterized thermally stable surface for each emitter, and to be as far as possible reproducible.

This chapter contains details of the starting materials, the techniques used, and the microscopic appearance of the resulting surfaces.

### B. RHENIUM EMITTER PREPARATION AND CHARACTERIZATION

The procedure for each emitter included the following general steps:

1. Grain stabilization anneal.
2. Electrolytic polishing of emitter surface.
3. Surface stabilization anneal, well above diode operating temperature.

Square slugs of high-purity cold-wrought powder-metallurgy rhenium 0. 8" x 0. 8" x 0. 2" were obtained from Rembar Sales Corporation, a division of Chase Brass and Copper Company. The spectroscopic analysis of the batch from which this material was taken is as follows — all unit parts per million:

| | | | | | | | | |
|-----|------|-----|-----|-----|-----|-----|-----|-----|
| Al  | < 1  | | | | | | | |
| Cu  | < 1  | Ag  | B   | Be  | Mn  | Mo  | Na  | Nb  |
| Fe  | 43   | Pb  | Sn  | Th  | Ta  | V   | Zr  | W   |
| Mg  | < 1  | | | not detected | | | | |
| Si  | < 1  | | | | | | | |

114

Extensive work has been done on the chemical and metallurgical properties of rhenium emitters for thermionic diodes. Since much of this is relevant to the interpretation of data reported here, there follows a summary of the methods and results.

The type of cold-wrought powder metallurgy material used here has a strong preferred orientation, even after annealing. X-ray diffraction data, tabulated below, show unusually high intensities for certain lines, as compared with the, NBS random sample.

X-RAY DIFFRACTION LINE INTENSITIES
FROM RANDOM AND TWO OTHER RHENIUM SPECIMENS

| hkl | Random | Wrought |
|------|--------|---------|
| 100 | 32 | 120 |
| 002 | 34 | 26,496 |
| 101 | 100 | 100 |
| 102 | 11 | 1,200 |
| 110 | 22 | 112 |
| 103 | 16 | 1,256 |
| 200 | 3 | 32 |
| 112 | 20 | -- |
| 201 | 15 | 224 |
| 004 | 2 | 864 |
| 202 | 3 | 40 |
| 104 | 2 | 208 |
| 203 | 7 | 40 |
|  | NBS Sample | Annealed 8.8 hrs at 1910°C and 164 hrs at 1800°C |

These imply a strong tendency for basal planes to be parallel to the emitter surfaces. This is presumably a consequence of the fabrication technique used, and will affect the thermionic emission from the surface.

A Laue back-reflection x-ray photograph of a typical sample was taken, and is reproduced as Figure V-1. The presence of well defined rings on the photograph confirms the preferred basal plane orientation, and indicates the lack of a preferred orientation of secondary axes <u>within</u> the plane of the specimen. Had there been any preferred orientation of <u>secondary</u> axes, the rings of Figure V-1 would show variations in intensity around their circumference. (This supports the manufacturer's claim of isotropic mechanical properties in sheet specimens.) No randomly oriented material has been examined.

Two chemical analytical techniques were applied to this type of wrought rhenium specimen, in addition to the emission spectroscopy used by the manufacturer. The electron beam microprobe was used to seek concentrations of Fe, W and Mo caused by segregation, for instance at grain boundaries. These three elements were chosen after first establishing that no elements were present in concentrations above 0.1 w/o. The detectability limit for tungsten in about 0.05 w/o, and the only evidence of segregation found was a tungsten concentration just perceptibly above the detectability limit, at the grain boundaries.

This technique samples a very small area, $\sim 10^{-6}$ mm$^2$. The next technique used was mass-spectrometric analysis of ions sputtered from an area of about $10^{-1}$ mm$^2$ by a beam of 10-kV argon$^+$ ions. This novel and powerful technique[*] still suffers from the problem of relating output data to the impurity concentration causing them, but it has the advantages of very low detectability limits (parts per billion for some elements) and sensitivity to atoms and isotopes which the microprobe cannot detect. Data is presented in the form of a plot of log of ion beam intensity versus mass/charge ratio. A typical unit of output data is reproduced as Figure V-2. This was obtained from below the surface of a wrought rhenium

---

[*]Developed and applied by GCA Corporation, Bedford, Mass.

116
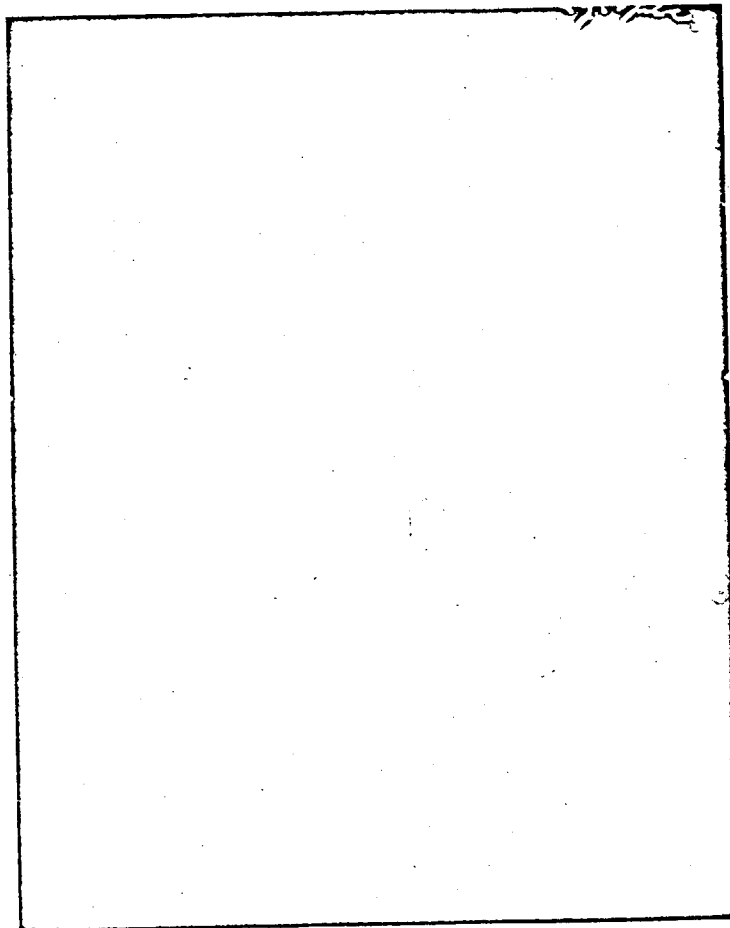
Figure V-1. Laue Back-Reflection X-Ray Photograph of Wrought Rhenium Sheet.

117

THERMO ELECTRON
ENGINEERING CORPORATION
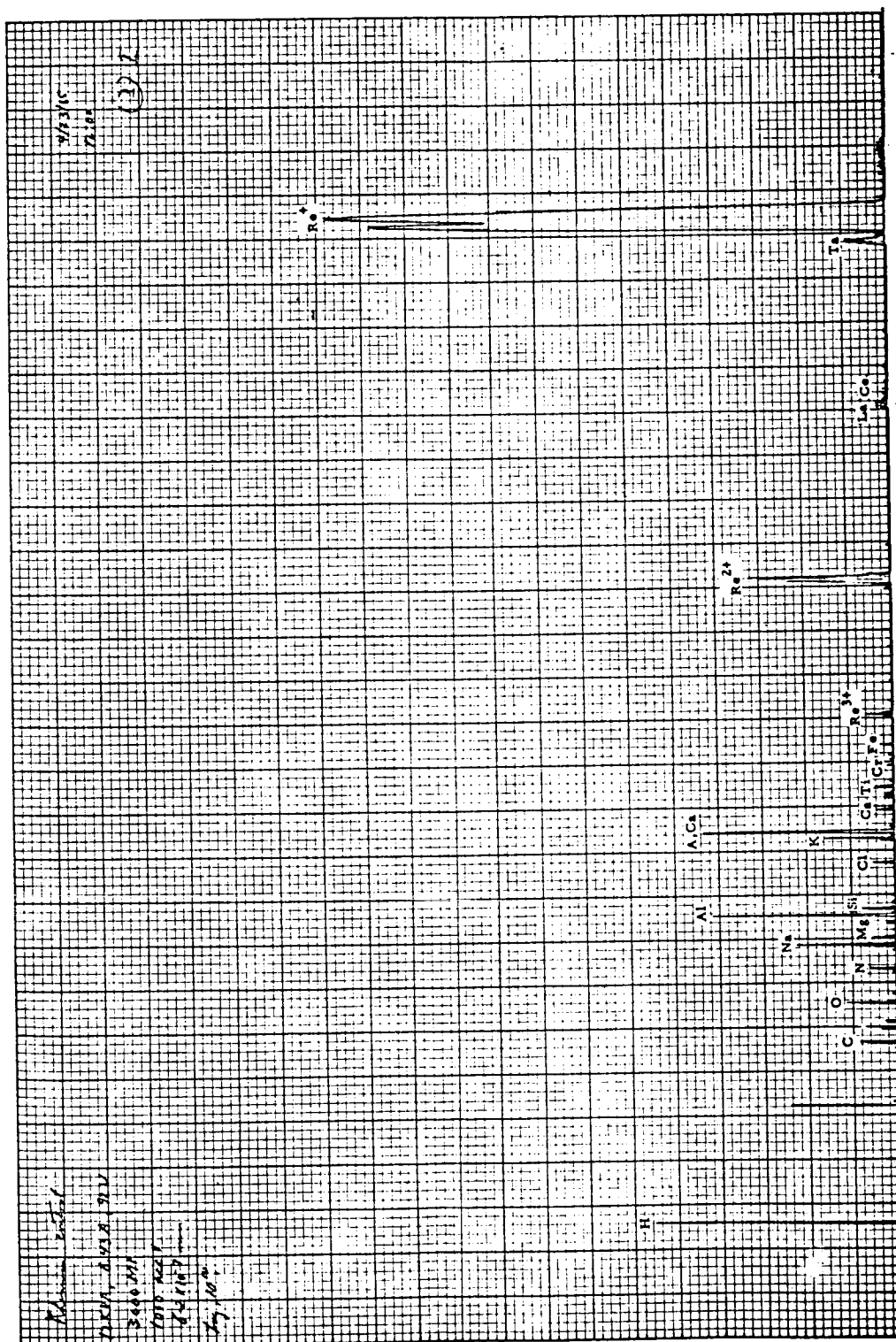


Figure V-2. Mass Spectrum of Sputtered Ions — Intensity vs
Mass/Charge Ratio. Intensity Scale is Logarithmic.
Wrought Rhenium Control Sample — Below Surface.

118

sample. Figure V-3 was obtained from vapor-deposited rhenium, near the interface between deposit and tungsten/rhenium alloy substrate. This figure was chosen to show the extent of contamination present on the alloy substrate, even at a temperature of about 1200°C, which prevailed when the rhenium was being deposited onto it. Similar contamination is found on the surfaces of wrought rhenium emitters. From the data obtained with this technique we draw the following conclusions:

1.  The specimen on which W was detected with the microprobe showed no W with this technique, presumably owing to the much smaller average W concentration over the larger area studied.

2.  The spectroscopic analysis fails to give a complete picture of the impurities in Re. In particular, it does not detect H, Ba, CE, and Ta which are indubitably present at a low level.

3.  Even severe heat treatments will not remove from Re the H which is dissolved in it. All data taken using this technique showed large $H^+$ peaks.

4.  The surfaces of emitters always show contamination which is not present in the bulk material.

5.  In summary, the rhenium is not as clean as it is reported to be, although there is no reason to believe that the specimens used as emitters in this work are in any way untypical of the available material.
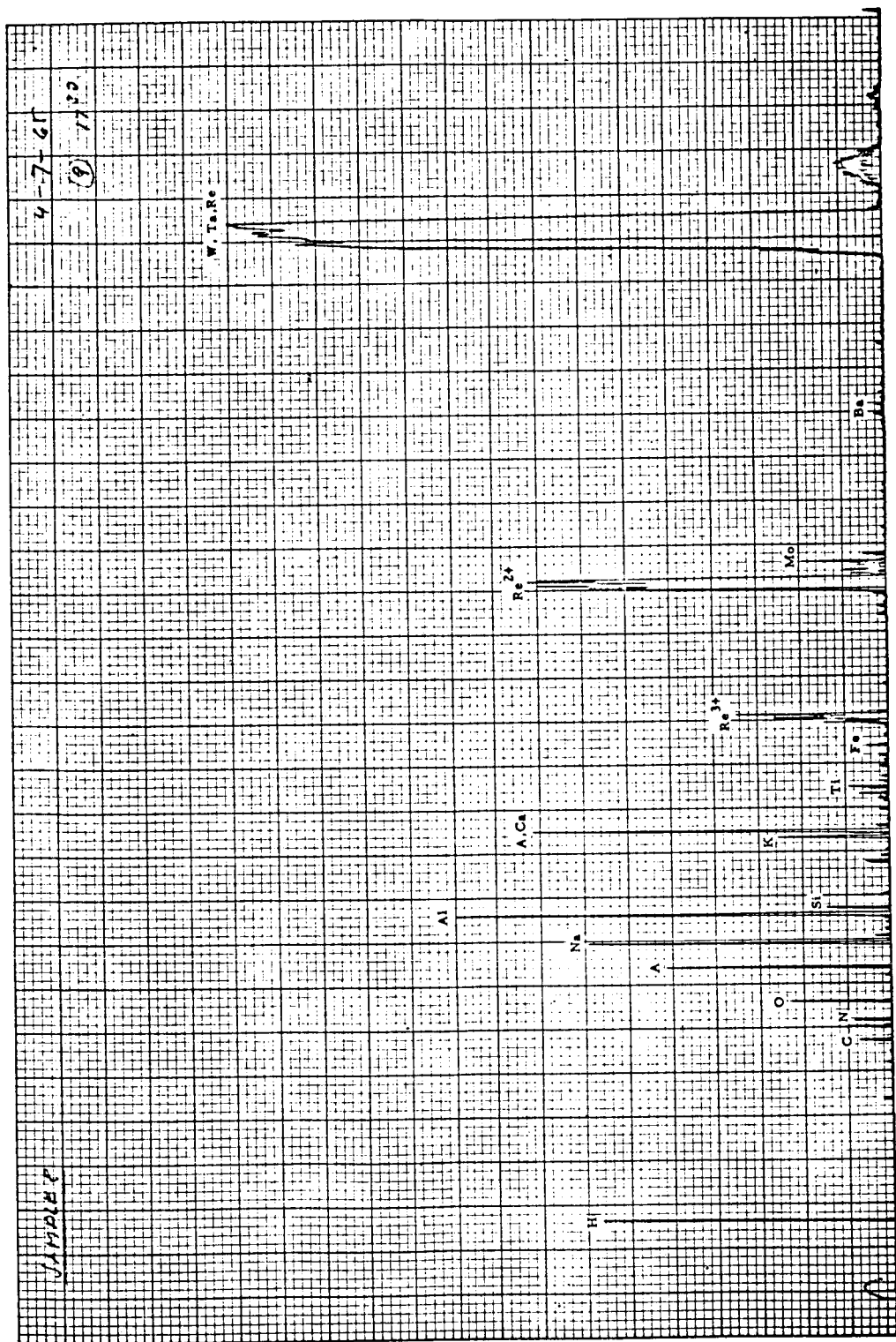
Figure V-3. Similar Data from Vapor Deposit, sufficiently Far Below Surface to Detect Impurities at Interface of Deposit and W26Re Substrate.

Grain stabilization was carried out by firing in a vacuum of $2 \times 10^{-7}$ torr at 2300°C ± 30° for 23 hours. A cold-walled electron-bombardment furnace was used. The effect of this treatment is to induce a grain structure in the bulk of the material which will not change at diode operating temperatures.

An emitter was cut from each slug of rhenium, by electrical-discharge machining, to produce a disc 0.770" in diameter with a black-body hole and a thermocouple hole on the back. The emitting surface was ground flat to less than 0.0003" across its diameter, with a surface finish of better than 40 microinches rms. The resulting emitters were given TEECO designations Re15 and Re16.

Electropolishing of each emitter was attempted, using the perchloric acid recipe described by Geach et al, in "Rhenium," Ed. Gonser, Elsevier, N.Y., 1962, p. 85. This electrolyte had been used successfully in the past, but would not produce acceptable results on these specimens, for reasons which remain elusive. Pronounced local pitting occurred, which was exacerbated by further polishing. This electrolyte was therefore abandoned, and each emitter surface was reground to remove the pits, and then polished on a metallographic wheel using fine-mesh SiC and $Al_2O_3$ powders. At this stage the emitters were flat to less than 0.0002" to within 0.05" of the edge. Given the guard-ring design of the diode, this was felt to be an acceptable flatness.

The next step was a stress-relief anneal of 30 minutes at 2250°C in vacuum, to reduce the mechanical damage on the reground surface. This was followed by electropolishing at the following conditions:

1 vol. conc. sulphuric acid

1 vol. butanol

2 vols. methanol                Time: about 30 secs.

21 ± 1 volt, 0.3 ± 0.1 A/cm$^2$, Temperature < 5°C

The electrolyte was contained in a stainless steel beaker, which functioned as the cathode. The results of this were quite satisfactory, judged by our extensive experience in electropolishing rhenium surfaces. The surfaces were photographed at this stage and are discussed below.

Figures V-4 and V-5, taken together, show an area which has responded to electropolishing in a homogeneous manner, but which appears heterogeneous under polarized light. Contrast in polarized light is a function of orientation of the surface with respect to the incident and reflected light; in this case both light beams are perpendicular to the gross emitter surface. We know from independent experiments[6] that this sort of material has a strong preferred orientation, with basal planes parallel to the surface, and the homogeneously polished area probably represents a group of grains, each of which exposes basal planes of the lattice on the specimen surface. This would account for the uniformity in electropolishing behavior. However, we also know that the grains of this material lack preferred orientation of their secondary axes along particular directions in the specimen. In other words, though basal planes tend to be parallel to the surface, prism planes are randomly distributed in the material. The varied distribution of secondary axes will not necessarily affect the electropolishing behavior, but will affect the appearance under polarized light. Thus the

64-R-10-3
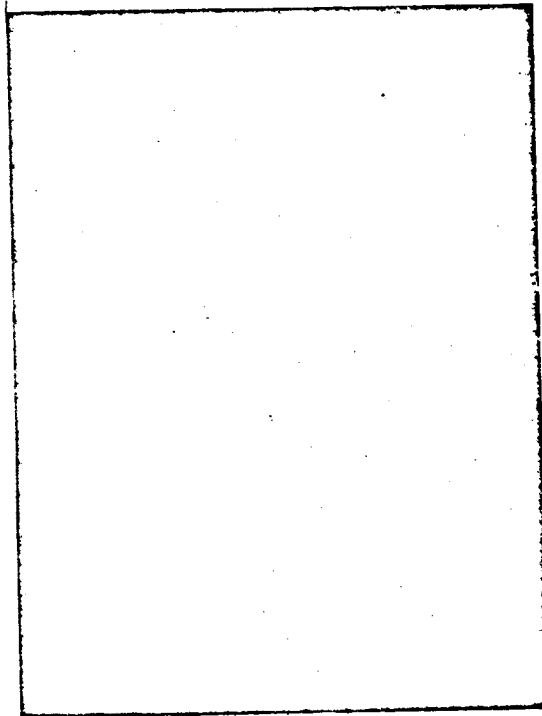


Figure V-4.   Emitter Re15 — Surface after Electropolishing and
before Final Anneal.   White Light, 310x.

123
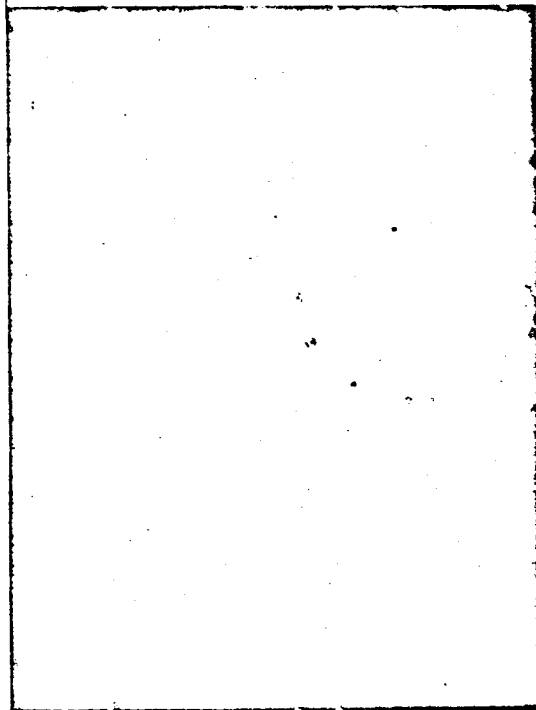
Figure V-5. Emitter Re15 — Same as Figure V-4 but in Polarized Light, 310x. Note contrast within

nature of the preferred orientation accounts for the observed appearance of the metallographs.

The interference fringe pattern of Figure V-6 is in effect a contour map of the surface — dark fringes are spaced with a vertical interval of half a wavelength, or about 0.3 $\mu$ for sodium yellow light. Inspection of this photomicrograph shows that there is no overall slope of the surface; that is, it is flat over distances of the order of 1-2 mm. This confirms the measurements made on the overall flatness before electropolishing. It also shows that there is some roughness on a scale smaller than that of the grains. This is caused by the combination of electropolishing action and the very orientation-sensitive etching of rhenium in the preparation of this emitter. Individual grains are mostly fairly flat, but grain boundaries have etched fast, and there are steps between many adjacent grains. It is interesting to compare this figure with V-9, which uses the same interference technique on the rather better-polished surface of Re16. Here the steps between grains are almost always less than 0.3 $\mu$ high, while the same observations about overall flatness and flatness within grains apply.

Figures V-7 and V-8 are a pair of photos of Re16 corresponding to Figures V-4 and V-5 from Re15. The similarity between the pairs of photos is obvious, while the differences are discussed below.

Final surface-stabilization anneals were carried out on Re15 and Re16 for 3 and 3.2 hours, respectively, at 2380 $\pm$ 30°C and a pressure $< 10^{-6}$ torr.

These produced the expected grain boundary grooving, and some grain growth, because this temperature was higher than that used for

THERMO ELECTRONENGINEERING CORPORATION
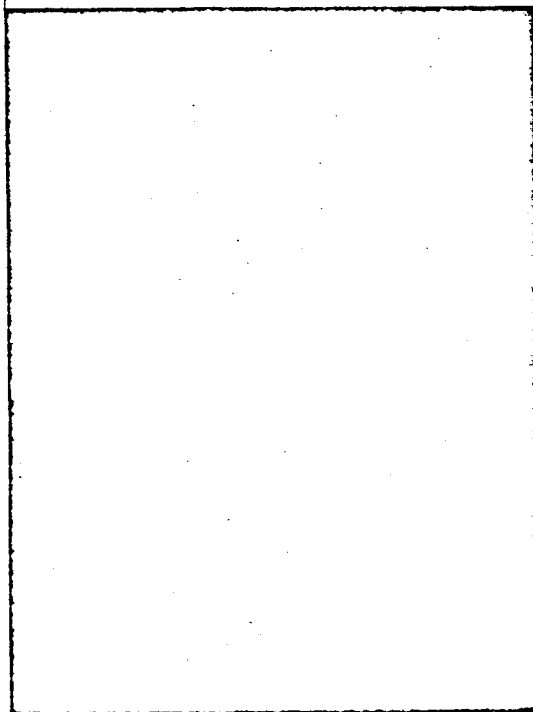
64-R-10-5



Figure V-6. Emitter Re15 — Typical Area with Sodium Yellow Light
Interference Fringe Pattern — 150x.
Shows uneven polishing between grains,
but overall flatness.

V-13
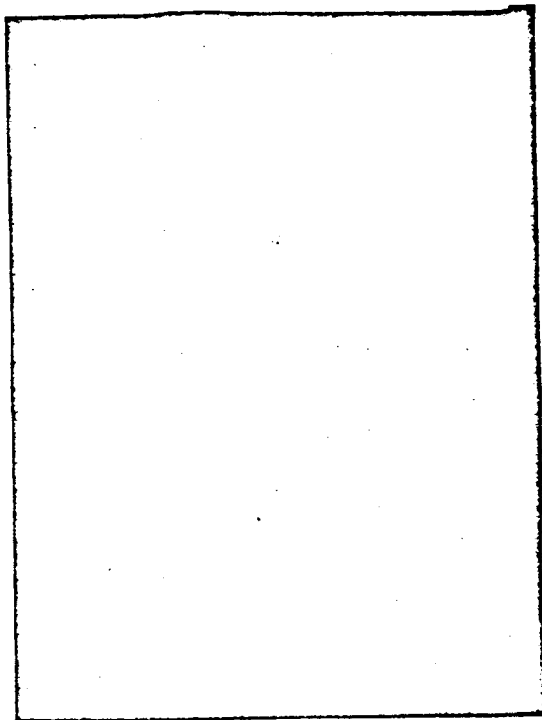
Figure V-7. Emitter Re16 — Surface after Electropolishing and before Final Anneal. White Light, 310x. Compare with Figure V-4.
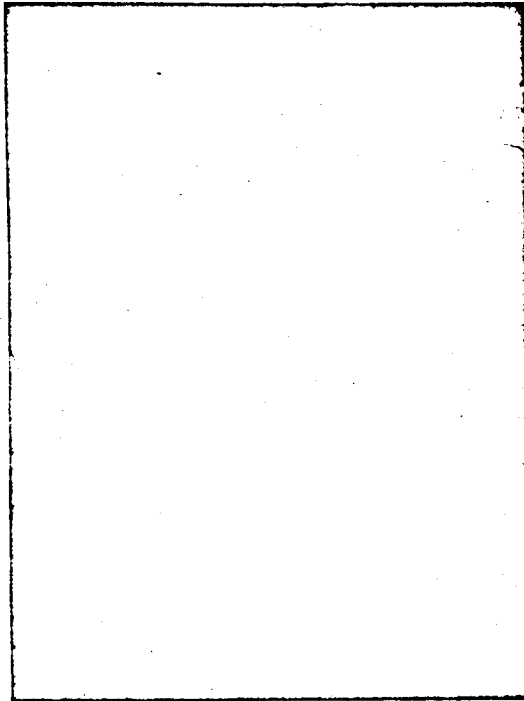
Figure V-8.   Emitter Re16 — Same as Figure V-7 but in Polarized
Light, 310x.   Compare with Figure V-5.

128
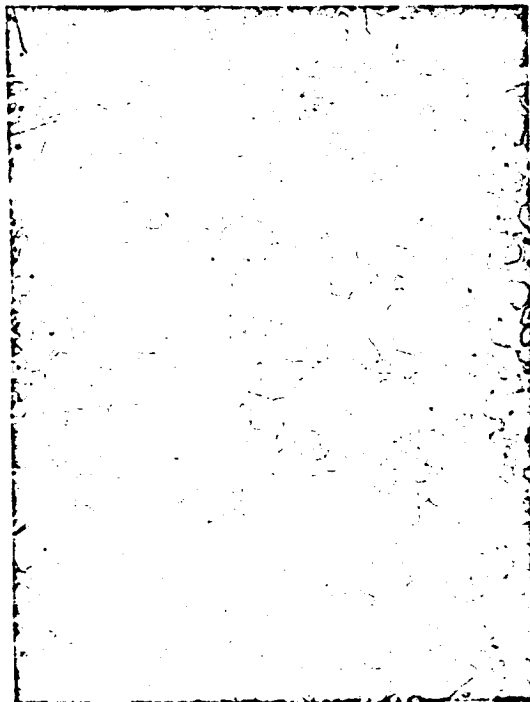
Figure V-9.   Emitter Re16 — Typical Area with Sodium Yellow Light
Interference Fringe Pattern — 150x.
Compare with Figure V-6.

previous annealing. The strong dependence of grain growth on annealing temperature is due to the fact that the rate controlling process, volume diffusion, has a very high activation energy ~100 k cal/mole. It also produced various forms of thermal etching.

A comparison of Figures V-4 and V-7 shows that the electropolishing of Re15 had left it with a large number of small pits, which are not present on Re16. The effect of these becomes more pronounced during heat treatment.

Under polarized light, Figure V-10, we can distinguish three types of features. Many pits appear as cruciform dark areas in a bright ring. This is a feature of hemispherical pits in anisotropic materials such as rhenium and is explained[7] in terms of reflections, and interferences between them, from the curved surfaces. Other pits are manifestly polygonal, rather than hemispherical. This can be seen more clearly under the higher magnification of Figure V-11. Here we can observe the polygonal pits as darkly outlined shapes, and the hemispherical ones as bright spots in a circular pattern which gives a cruciform-like appearance under the lower magnification of Figure V-10. A third feature is the mass of flat terraces with curved boundaries, shown more clearly in Figure V-12. The corresponding interference fringe pattern, Figure V-13, shows that within each grain the terraces are flat and uniformly sloping. Adjacent grains in Figures V-12 and V-13 have differently shaped terraces with different slopes.

The following interpretation for the terraces is proposed: At elevated temperatures the atoms of the metal gain mobility, and tend to rearrange themselves in the lowest-energy configuration. Since the surface energy of close-packed basal planes is a minimum, the development of these planes is favored. In grains where the basal plane is

<div align="center">V-17</div>
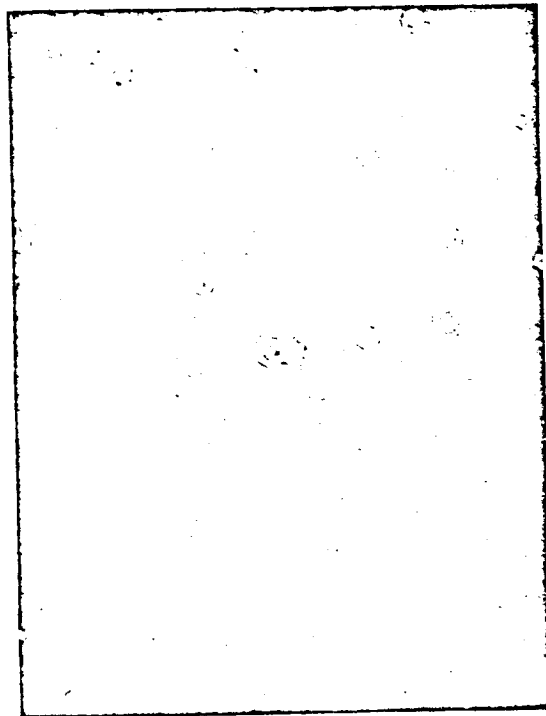
Figure V-10. Emitter Re15 — Another Typical Area after Final
Anneal, 310x. Polarized Light.

131
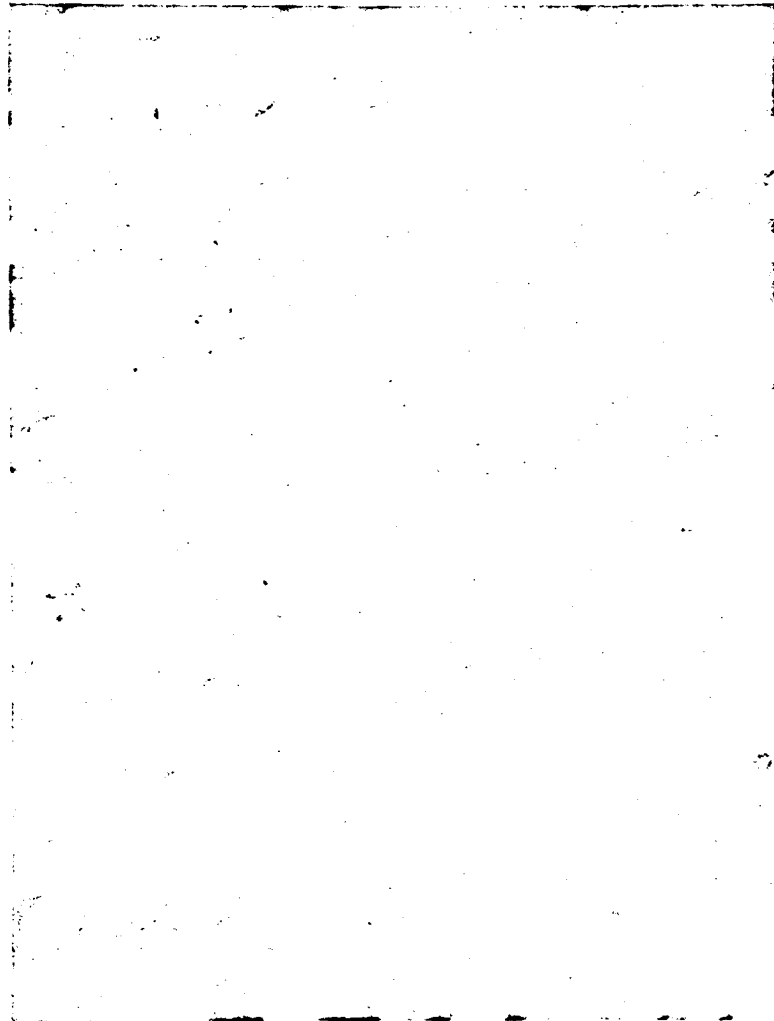
Figure V-11. Emitter Re15 — Another Typical Area after Final
Anneal, 740x. Polarized Light.
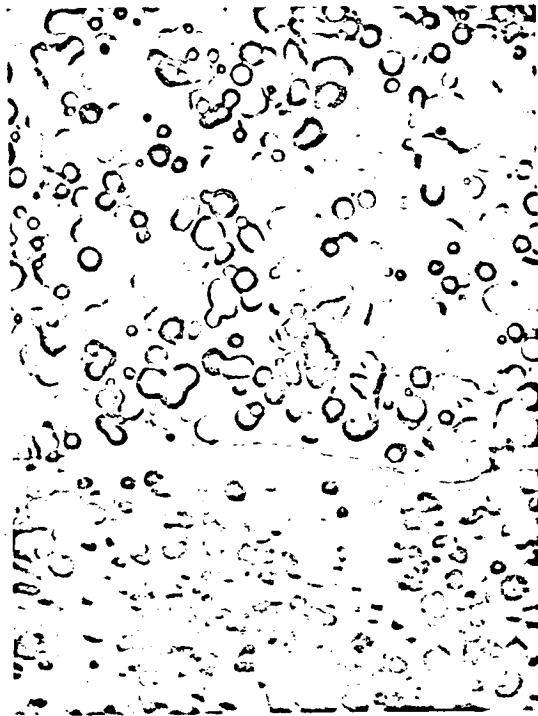
Figure V-12. Emitter Re15 — Typical Area after Final Anneal, 310x, White Light. Grain boundary can be seen.

Figure V-13. Emitter Re15 — Interference Fringe Pattern at 280x.

parallel to the gross specimen surface, a grain surface consisting of a multitude of basal plane terraces develops. These strongly reflect light back down the microscope, and so this grain appears bright on photomicrographs. Similar changes occur on other grains, but if the terraces develop at an angle to the surface, and so do not reflect strongly in the microscope, they have a different appearance. A striking example of this effect is seen in Figure V-14, in which the different surface appearances of the various grains are clearly visible.

The electropolishing of Re16 resulted in a better surface than had that of Re15, in that fewer small pits developed and the steps at grain boundaries were smaller. The final anneal again developed thermal etch pits as can be seen from Figure V-15, although they are fewer in number than those of Re15. The etch pits had varying shapes from grain to grain but infrequently showed distinguishable terraces or hemispherical pits as had Re15. This is seen by comparing the interference fringe patterns of Figure V-16 with those of V-13. Even though V-13 is at lower magnification, the terracing is much more prevalent than on V-16. The differences between Re15 and Re16 are presumed to result from the difference after polishing. Apparently the rougher pitted surface of Re15 broke up more easily to give terraces and polygonal pits than did the more uniform surface of Re16. It is noteworthy that there is no significant difference in the thermionic performance of Re15 and Re16.

Grain growth and grain boundary grooving also occurred (Figure V-17). These invariably accompany high-temperature annealing. Grain growth occurs in order to minimize the amount of grain boundary in the specimen, and thereby lower its free energy. This process continues until a metastable limiting array of grain boundaries is reached. Grain

Figure V-14.  Emitter Re15 — After Final Anneal, showing Different Surfaces Developed on Different Grains. 75x.

136

64-R-11-49
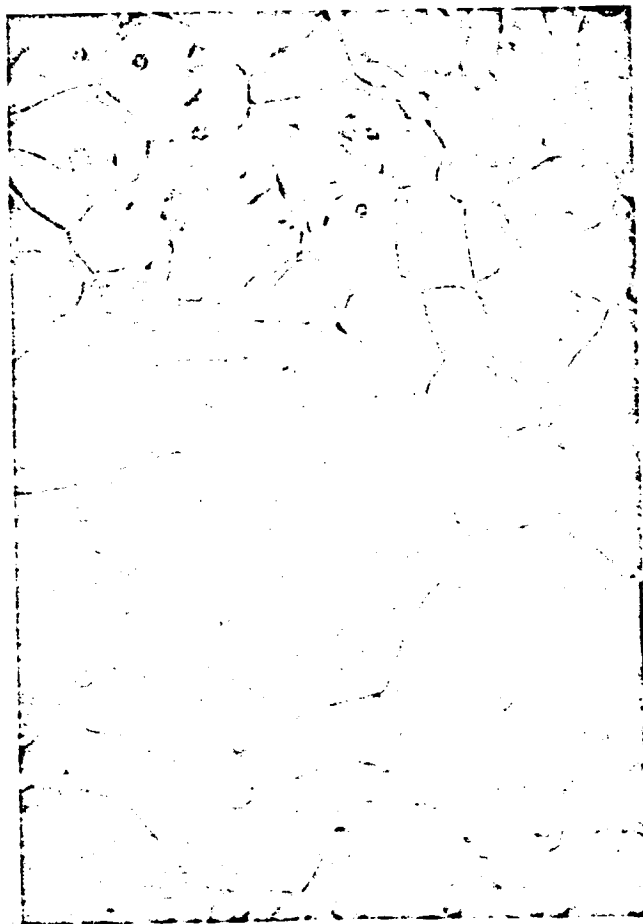


Figure V-15. Emitter Re16 — After Final Anneal, 460x. Shows grain boundary grooving and etch pits.

137

THERMO ELECTRON
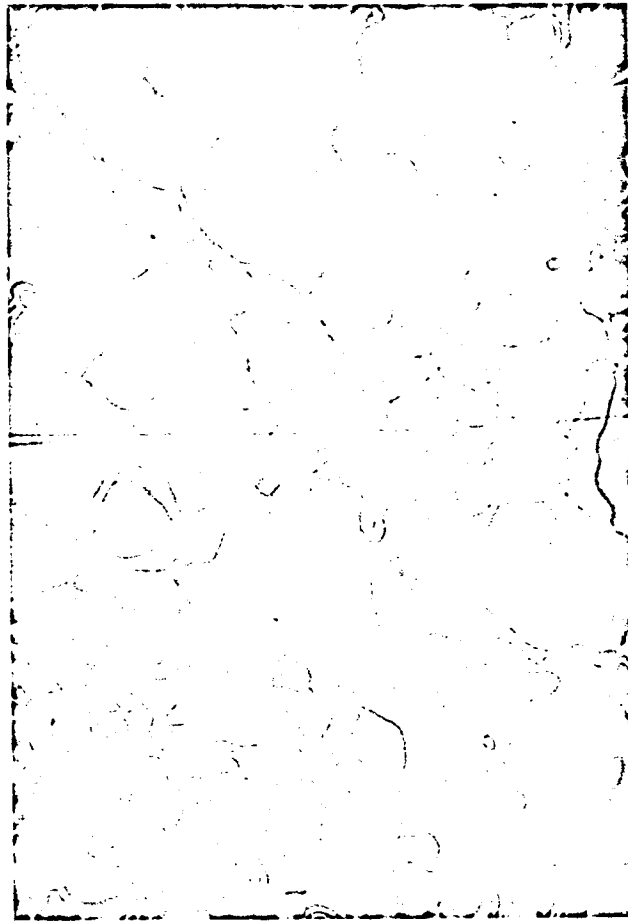
64-R-11-50



Figure V-16. Emitter Re16 — Sodium Yellow Interference Fringe

138
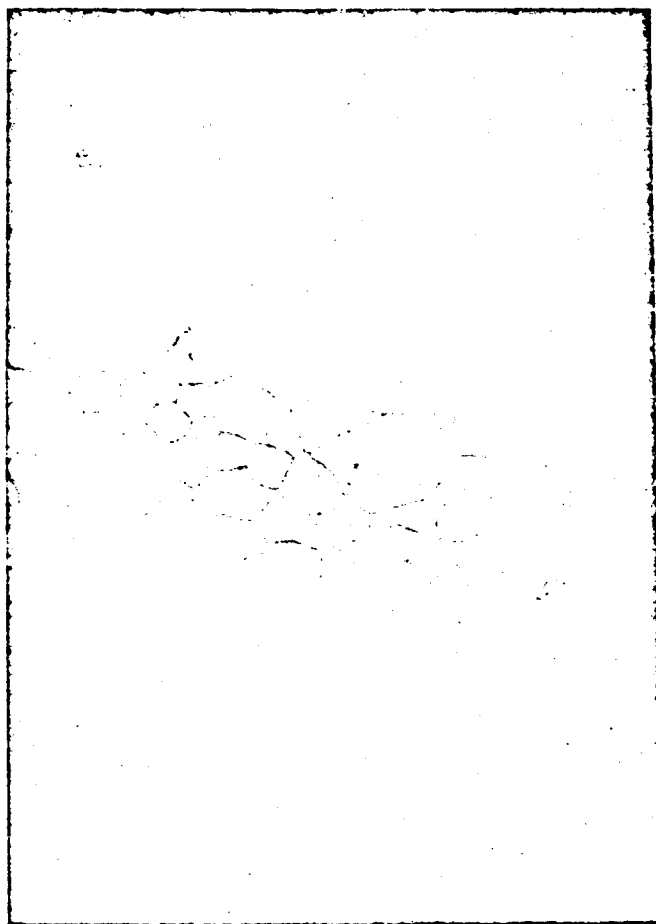
Figure V-17.  Emitter Re16 — Central Area under Polarized
Light, 225x.  Extensive grain
boundary grooving.

139

boundary grooving occurs as a result of the incessant interplay of surface energy forces and sharp edge forces, as explained by Mullins.[8] This process continues indefinitely, though at a decreasing rate.

Note that any straight line seen on an interference pattern metallograph and extending over more than one grain may be assumed to be a scratch on the half-silvered mirror, which is in contact with the specimen when these patterns are made.

## C. TUNGSTEN EMITTER PREPARATION

This emitter, designated W4, was prepared from wrought sheet stock with the following spectroscopic analysis (all units parts per million):

| | | | | | | | |
|-----|-----|-----|-----|-----|-----|-----|-----|
| Al | < 6 | Fe | 13 | Mn | < 6 | Mo | 30 |
| Ca | < 3 | Ni | 8 | Mg | < 3 | Co | 29 |
| Si | 50 | Cu | < 3 | Sn | < 6 | Zr | < 3 |

This stock had a good ground surface, and was flat to within 0.00025" on the stock slug. It was electropolished lightly in 2% aqueous sodium hydroxide, contained in a stainless steel beaker, acting as a cathode at a potential of $10 \pm 1$ volts, for about 30 secs. This is a very satisfactory electrolyte, and the resulting surface is so uniform as to be practically featureless. The emitter was cut from the stock slug by electrical-discharge machining, to the same design as the rhenium ones. This was done <u>after</u> polishing in order to minimize edge effects on the actual emitter. A different route had been chosen for the rhenium emitters because of the high power density requirements of the perchloric and electrolyte; it was felt that the smaller emitter would be easier to

polish than the whole 0.8" square slug.

Surface stabilization was carried out on the polished and machined W4 for 65 minutes at 2300 ± 30°C and a pressure less than $2 \times 10^{-6}$ torr. These conditions were chosen to duplicate preparation of an earlier tungsten emitter, for which extensive data were available. After this, a set of metallographs was taken. Interference fringe measurements showed that the surface was flat to within thirty fringes of sodium yellow light, or 0.00036 inch.

White light photomicrographs at 150 X are shown in Figures V-18 and V-19. Each photo is of a different area of the surface. Both areas were chosen at random; thus the similarity is a good indication of the surface uniformity.

These photomicrographs, taken after stabilization, show slight traces of grain growth, and the inevitable grain boundary grooving. The orientations of the grains are probably fairly random, and some grains show traces of thermal etching and development of fine pits.

Two other areas of the surface were used to produce Figures V-20 and V-21, which are sodium yellow interference fringe patterns. The interference fringes are notably broad and diffuse, compared with those on rhenium. This indicates that the surface is much smoother and more gently sloping, which is consistent with previous experience in electropolishing tungsten, a much easier material to handle than rhenium.

D.  CONCLUSIONS

During this program three emitters were prepared and examined in preparation for use in the test vehicles. They were prepared from commercially available materials of acceptable purity, and the results of
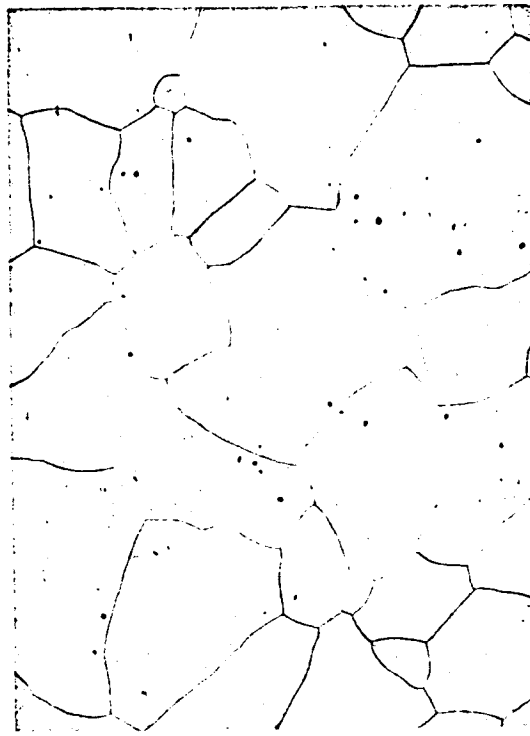
Figure V-18.  Emitter W4 in White Light at 150x after
Electropolishing and Final Anneal.

Figure V-19. Another Area of W4 in White Light at 150x after Electropolishing and Final Anneal.

143
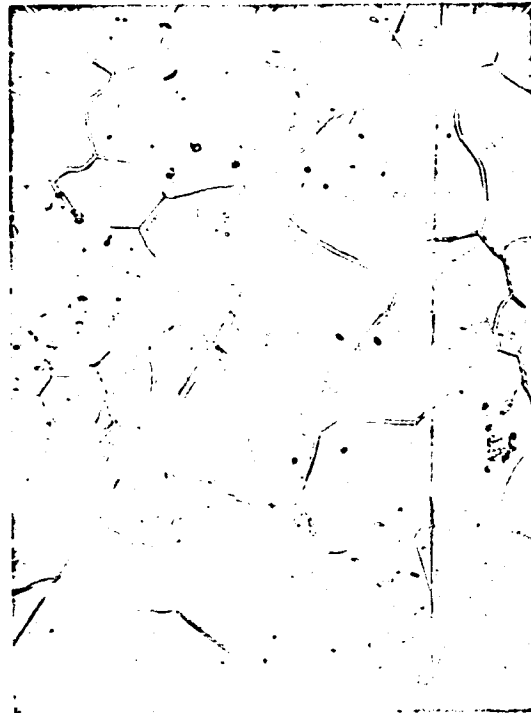
Figure V-20. Sodium Yellow Interference Fringe Pattern of
Surface of W4 after Electropolishing and
Final Anneal, 150x.

144
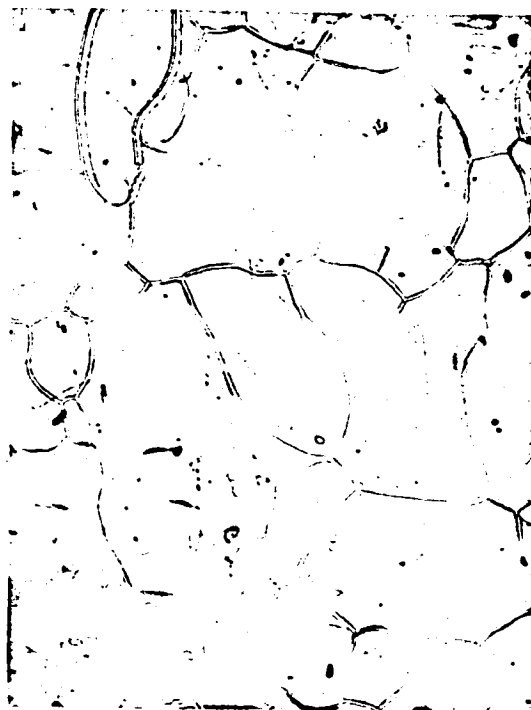
Figure V-21.  Another Area of W4 after Electropolishing and
Final Anneal, Interference Fringe Pattern, 150x.

electropolishing and heat treatment produced surfaces of reasonable flatness and stability which were well characterized by careful microphotography.

The small pits present on both tungsten and rhenium surfaces are a normal feature of such surfaces, and are presumably due to small heterogeneities in the materials of either a chemical or a physical nature.

146

## CHAPTER VI

## ELECTRODE WORK FUNCTION MEASUREMENTS

### A. GENERAL

The first experimental task of the program was the definition of the emitter and collector surfaces in terms of their work functions. This serves two objectives: 1) The values of the work functions of the electrodes are available for use in the correlation of the subsequent output data; and 2) work function values are monitored at intervals during the experimental program. Any changes observed during this periodic monitoring are signs of contamination or change in the structure of the electrode surfaces and provide an immediate clue to any change in converter performance. This chapter describes the procedures used in measuring the work functions of the surfaces and the limitations inherent in these procedures. Finally, the experimental results are shown in summary form. The raw data are presented in Appendix B.

### B. EMITTER WORK FUNCTION

### 1. Experimental Procedure

The emitter work function, $\phi_E$, is determined from the emitter saturation current $J_s$ obtained at a given emitter temperature $T_E$ by substituting these values in the Richardson equation,

$$\phi_E = -kT_E \ln [J_s/AT_E^2]$$

where k is the Boltzmann constant and A is the Richardson constant.

The validity of the results is strongly dependent upon the measurement of the true value of saturation current density. A necessary condition is that contact potential be such that electrons are accelerated

147

toward the collector. This condition is not sufficient, however, since an electron space charge barrier may exist which can replace the emitter work function as the barrier controlling the electron current. In this case, the potential energy diagram has the shape shown in Figure VI-1.

Under these conditions the measured current density J is not equal to $J_s$, even though it may show little variation as V is made more and more negative, thus giving the impression of saturated emission. In fact, the observed current J will have the value:

$$J = J_s \exp(-\delta / kT_E)$$

where $\delta$ is defined as the space-charge barrier.

To avoid the presence of a space-charge barrier, the electron current density $J_s$ must be neutralized by positive ions generated by surface ionization. This is the condition referred to as ion-rich. In this case the potential energy diagram has the shape shown in Figure VI-2. Uner these conditions, no electron space-charge barrier exists that can inhibit the flow of electrons.

There is another process, however, which may prevent the collection of the total saturation current density. This is the scattering of electrons in the interelectrode space.

This back-scattering of electrons under ion-rich conditions has been previously documented.[9] The ratio of the actual output current density J to the saturation current density $J_s$ has been found to depend on the pressure-spacing product Pd and the relative ion-richness $\beta$. This dependence is shown in Figure VI-3. At $\beta = 1$ the ion current emitted is that required to neutralize the electron current emitted.

148
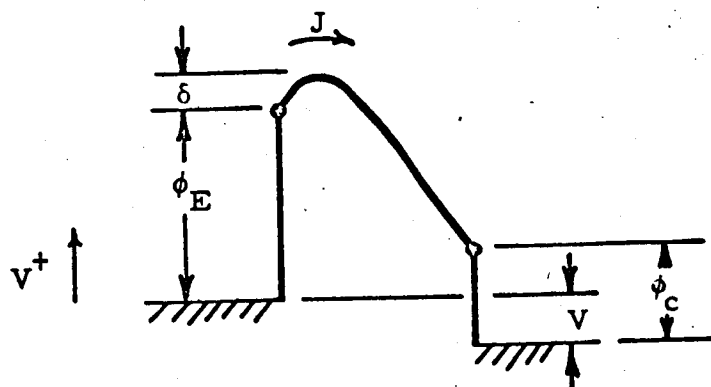
Figure VI-1.  Motive Diagram — Electron Space Charge Limited Operation.
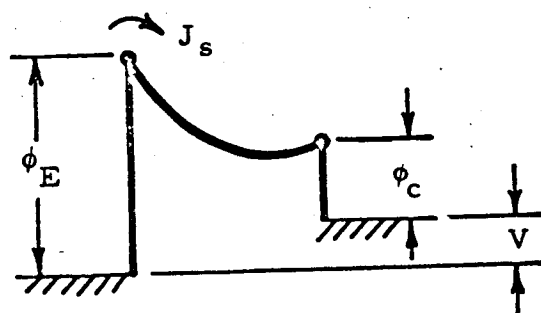


Figure VI-2.  Motive Diagram — Ion-Rich Operation.
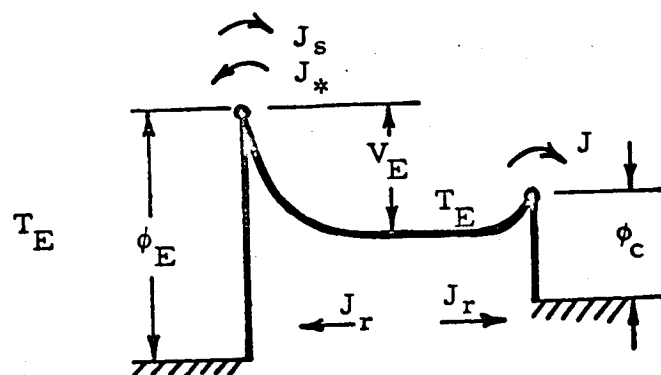


Figure VI-3.  Ion-Rich Motive Diagram Showing Current Components.

*149*

When $\beta < 1$ the emission is electron-rich, and when $\beta > 1$ it is ion-rich. However, as Pd gets smaller $J_a/J_s$ approaches 1 regardless of ion-richness. Clearly, then, saturation current measurements should be made with Pd as small as possible. Since the value of cesium pressure is fixed by the range that needs to be covered, the only means available for minimizing Pd is the reduction of spacing to the smallest possible values.

The above experimental technique is useful for the determination of work function under ion-rich conditions, i. e. , work function values above 2. 8 - 2. 9 eV. Several methods are available for work function measurement under these conditions and have the common characteristic that they in some way overcome the electron-space-charge barrier existing at the emitter. The most direct way of doing this is to operate in the ignited mode, where ions produced in the volume eliminate the barrier. The measurement of current, however, is hampered by the fact that scattering is extensive under these conditions. To avoid the use of large corrections associated with current measurements in the ignited mode, the following technique was developed.

Families of J-V curves were generated by varying the emitter temperature and keeping all other variables constant. Such a family is shown in Figure VI-4. The only difference from curve to curve is the change of the emitter work function. The knee of the J-V curve corresponds to the motive diagram shown in Figure VI-5. The emitter work function is given by:

$$\phi_E = V + \phi_c + V_d$$
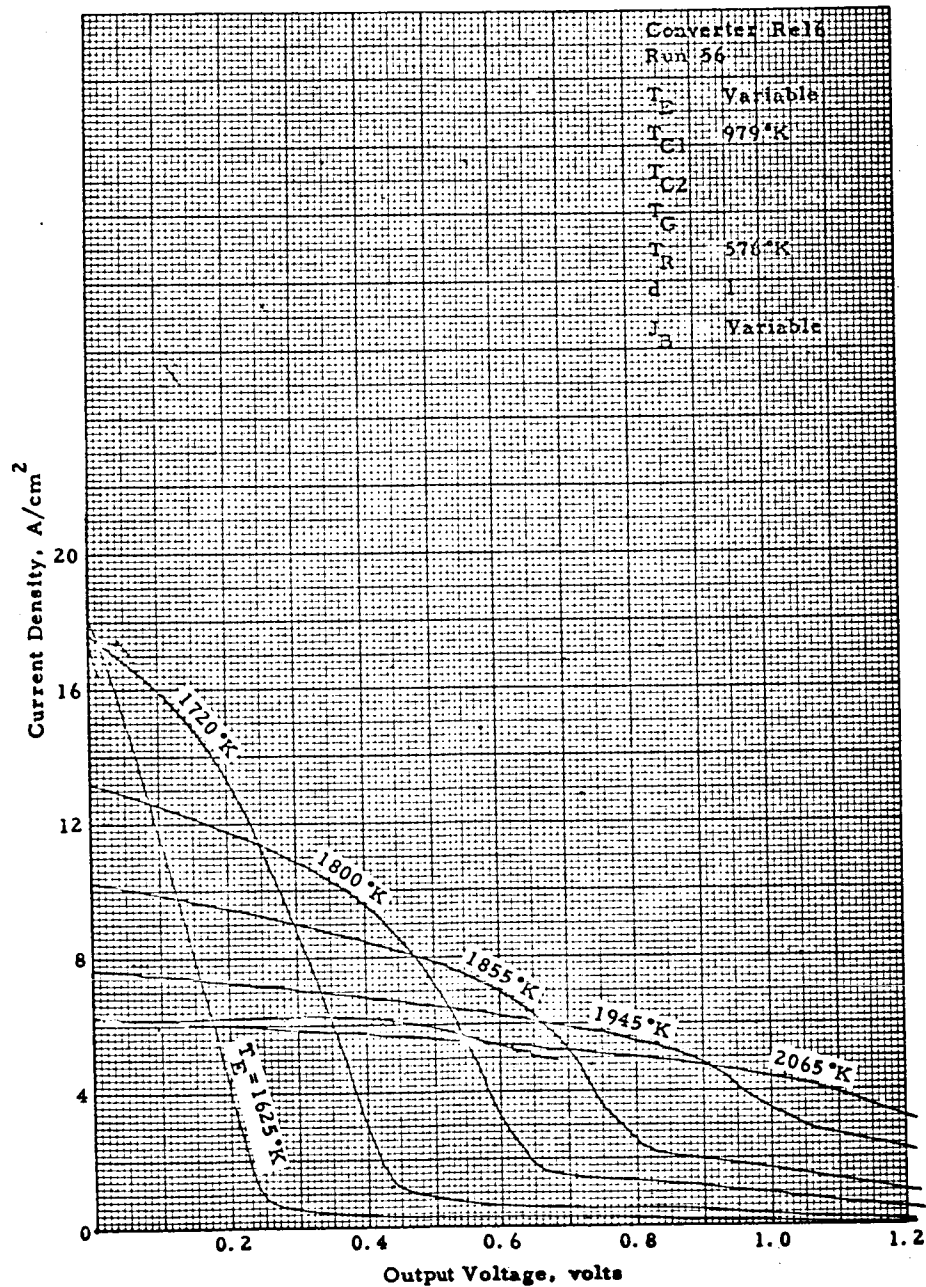
Figure VI-4.   Variable Emitter Temperature Family.
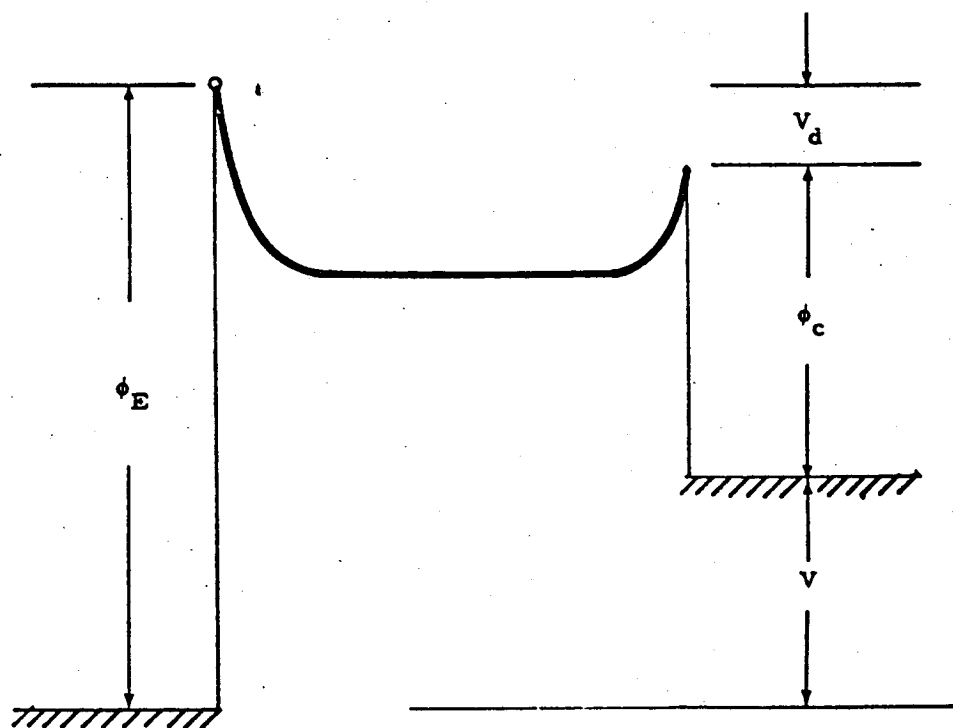
Figure VI-5.  Motive Diagram for Voltages Corresponding to the Knee of the J-V Curve.

$V_d$ is a function of the pressure-spacing product only, and $\phi_c$ is a function of the pressure and collector temperature only, so that $\phi_c$ and $V_d$ are independent of emitter temperature. Any change in $\phi_E$ results in a direct change in V, the output voltage. In this manner differences in work function are measured for a group of J-V curves such as those shown in Figure VI-4, but the absolute value is not determined. If, however, one of the curves is taken at such an emitter temperature that the emitter work function is above 2.9 eV, then this work function can be determined by the previously described method which is valid for $\phi_e > 2.9$. Once one of the work function values associated with one of the J-V curves in such a family is known, the rest are determined by difference. This technique was successfully employed in determining work function values down to 2 eV.

## 2. Results

### a. Bare Work Function Measurements

The work function of the rhenium emitter surface was measured prior to the introduction of cesium vapor. This operation was performed at the conclusion of outgassing. The spacing was fixed at its minimum value and the vacuum characteristic of the converter recorded at various emitter temperatures.

Figure VI-6 is a typical run used in this experiment. The curve consists of an exponential and a saturation region. The saturation region has been used for the determination of the bare work function by substituting the current density value in the Richardson equation.

Log-J-versus-V curves are shown in Figure VI-7 for the eight runs compiled. The work function values computed for these runs are tabulated in Table VI-1. Figure VI-8 is a plot of work function versus

*153*

THERMO ELECTRON
ENGINEERING CORPORATION
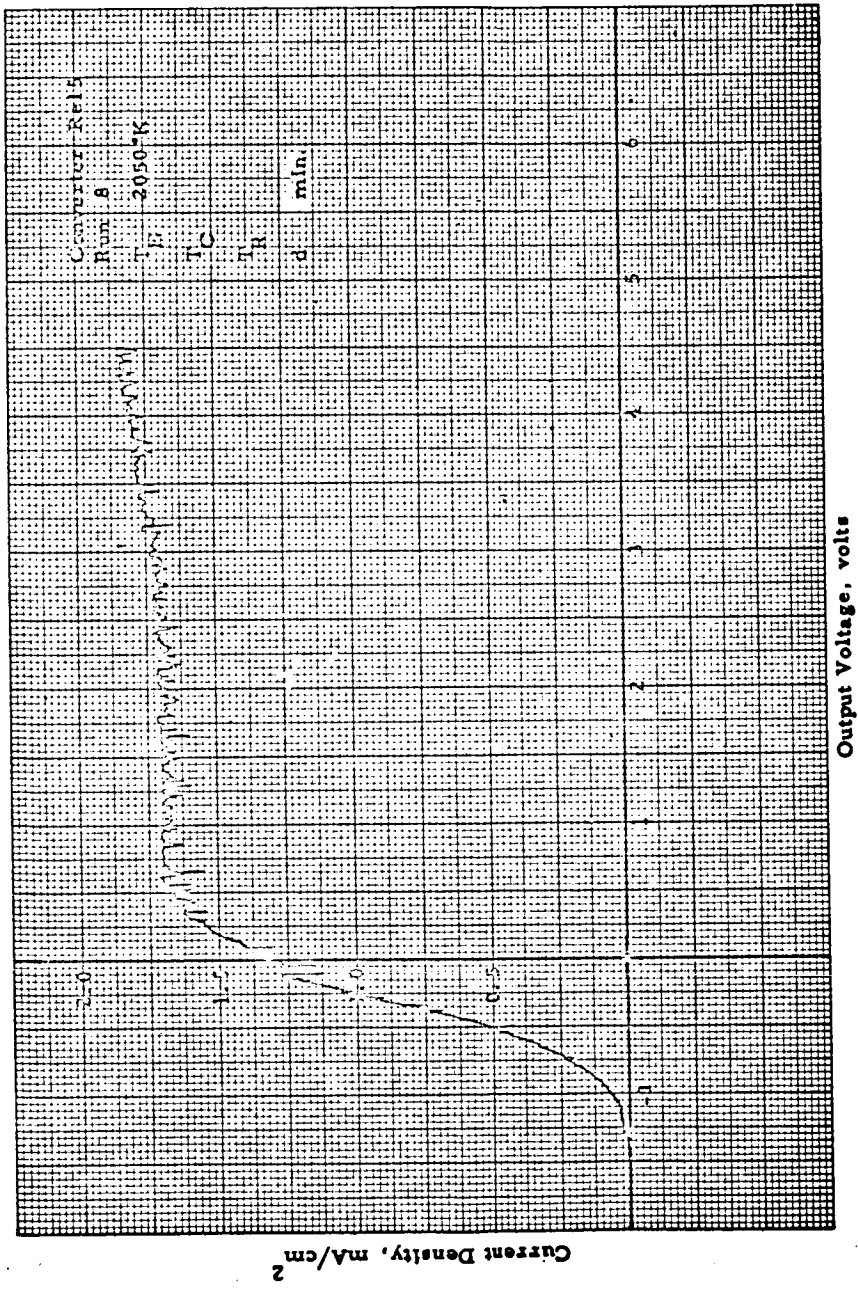


Figure VI-6. Typical J-V Curve for Bare Work Function.
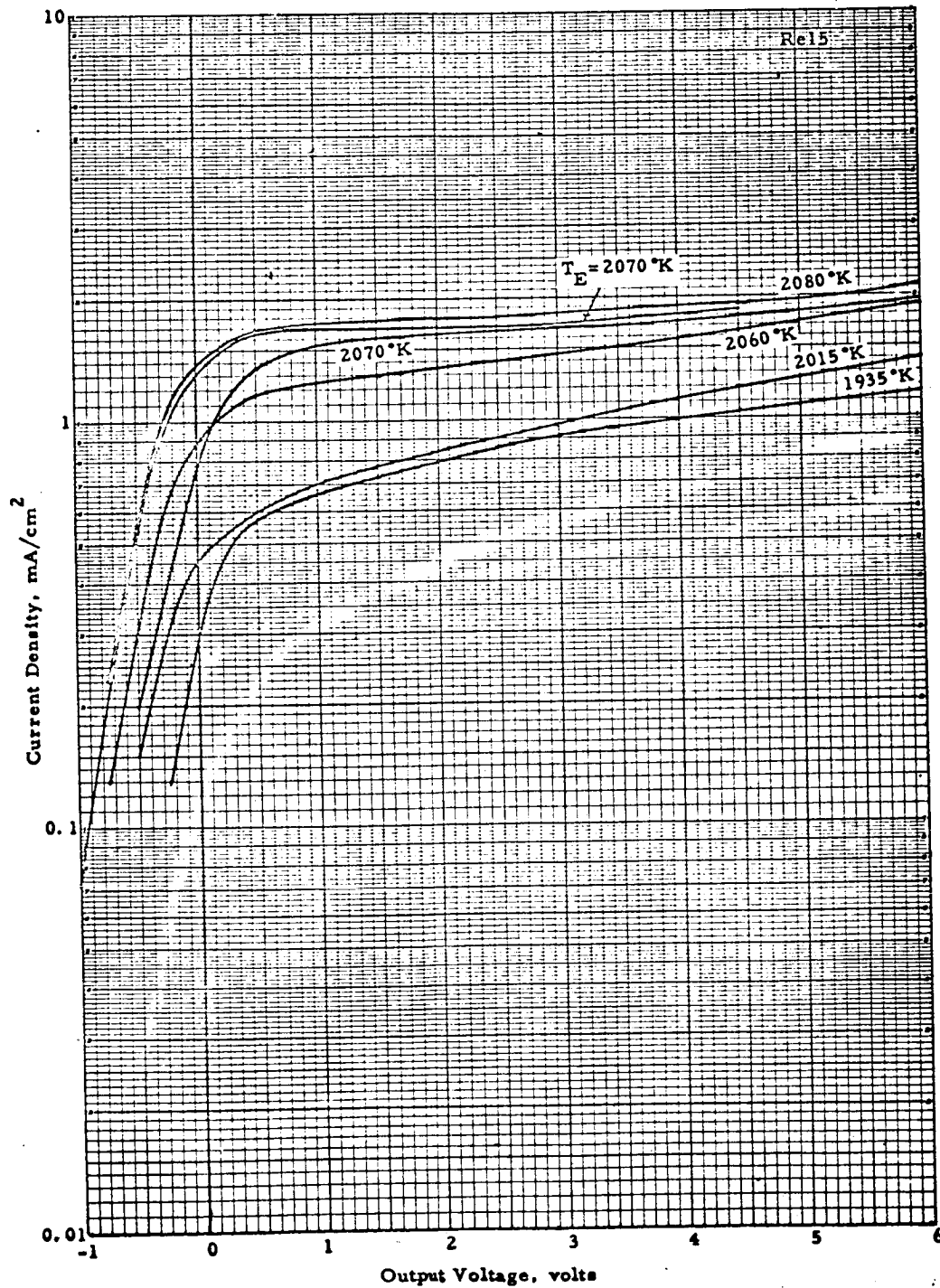
Figure VI-7.  Log Plots of J-V Curves.

## TABLE VI-1

### COMPUTED EMITTER WORK FUNCTION VALUES

| $T_E$ °K | $I_s$ mA | $J_s$ mA/cm$^2$ | $\phi$ |
|---|---|---|---|
| 2015 | 1.20 | .60 | 4.77 |
| 1935 | 1.25 | .625 | 4.65 |
| 2035 | 1.5 | .75 | 4.795 |
| 2060 | 2.35 | 1.175 | 4.77 |
| 2070 | 3.35 | 1.675 | 4.73 |
| 2070 | 3.1 | 1.505 | 4.75 |
| 2080 | 3.4 | 1.7 | 4.75 |
| 1950 | .5 | .25 | 4.76 |

156
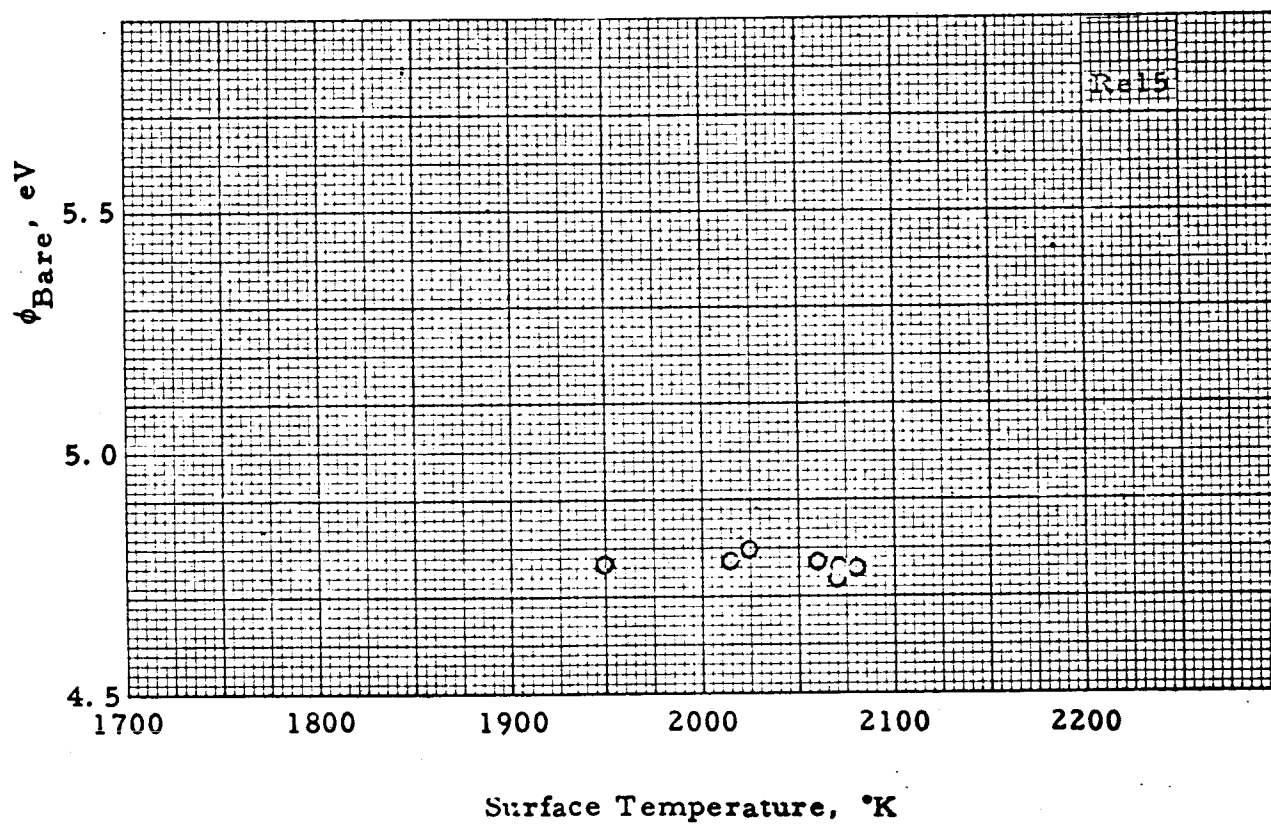
Figure VI-8.  Bare Work Function versus Temperature.

157

temperature. Inspection of Figure VI-8 reveals no significant change in work function with temperature over this temperature range.

The average value of 4.75 eV is in line with previously obtained values.

b. Cesiated Re Work Function

The experimental techniques described above were used to compile 167 runs from which the cesiated work function of the Re emitter could be determined. The range of temperature covered extended, for the emitter, from 1550° to 2075°K and, for the reservoir, from 377° to 635°K. These results are presented in Figure VI-9 in the form of a plot of work function versus the ratio of surface temperature to reservoir temperature. On this plot the data correlate along a single line.

A curve was fitted to these points and the mean deviation, defined as

$$S = \sqrt{\frac{\sum_{i=1}^{n} (x_i - \bar{x})^2}{n}}$$

was calculated,

where S is the mean deviation

$x_i$ experimental value

$\bar{x}$ mean value

n the number of experimental points

The calculated mean deviation of the data points of Figure VI-9 from the curve shown was found to be 32 mV. Conversely, 90% of the experimental points are within 53 mV of the value predicted by the fitted curve.

VI-12
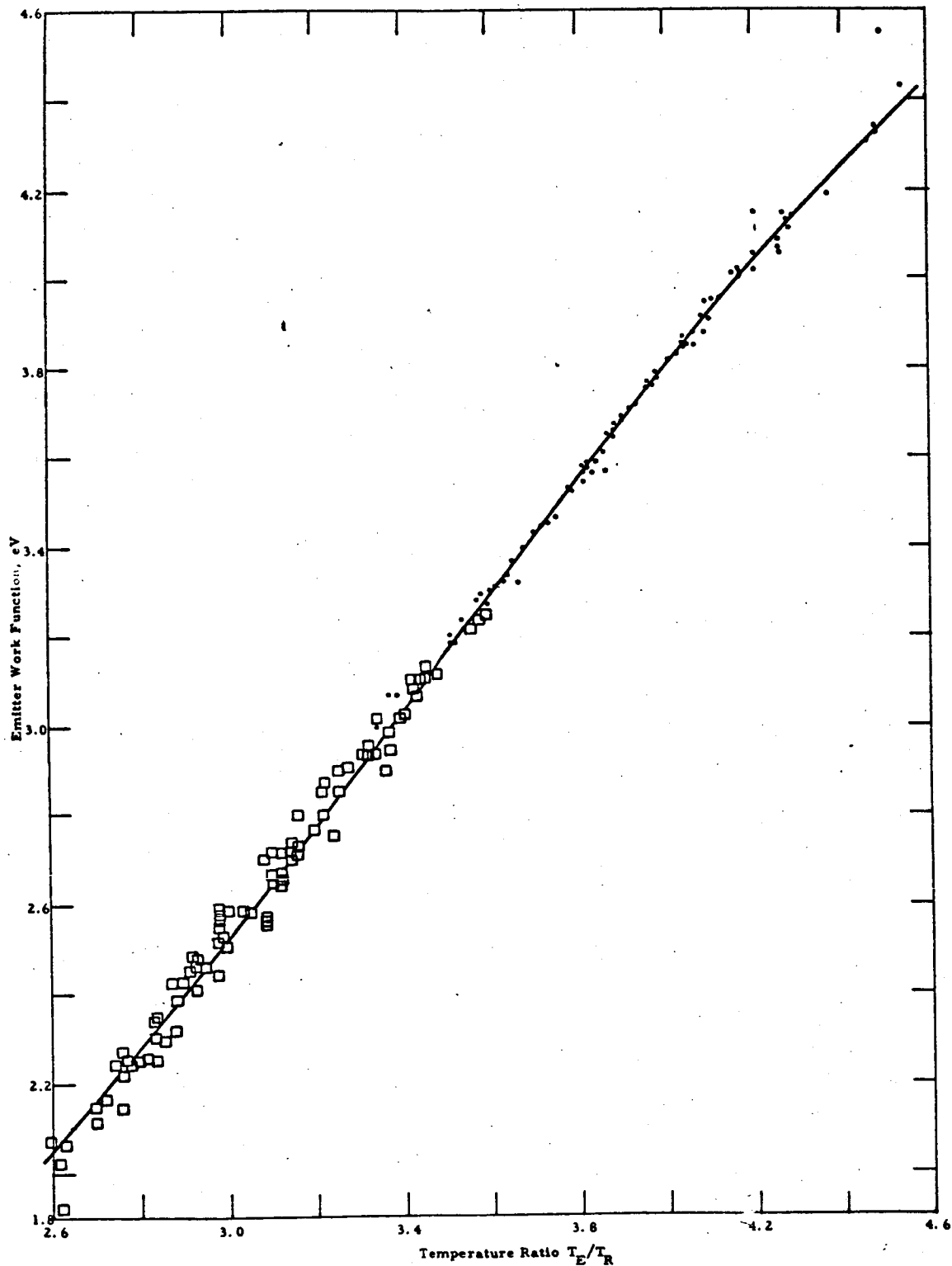
Figure VI-9. Rhenium Emitter Work Function Dependence on the Ratio of Emitter Surface Temperature to Cesium Reservoir Temperature.

An alternate method of presenting these work function data is shown in Figure VI-10. In this figure constant-work-function lines are plotted in the plane of reservoir temperature versus surface temperature. Constant-saturation-current lines are shown also. This plot is more useful for predicting work function and saturation current values than Figure VI-9. On the other hand, Figure VI-9 is far more useful for correlation purposes.

The data of Figure VI-9 can be expressed analytically for the range of work function from 2.2 to 3.3 by the following equation:

$$\phi_E = 1.29 \, T_E/T_R - 1.33$$

## C. COLLECTOR WORK FUNCTION

### 1. Experimental Procedure

The most useful method of measuring collector work function is the retarding plot. In principle this is a very simple and direct method. Let us consider the idealized diode, in which electron space charge is absent and ion current, back emission from the collector and back scattering are negligible. The J-V characteristic for such a diode is shown in Figure VI-11. This characteristic is made up of two curves; the first is given by:

$$J = J_s \qquad\qquad\qquad \text{for } V < V_c$$

and the second by:

$$J = AT_E^2 \exp\left[-(\phi_c + V/kT_E)\right] \qquad \text{for } V > V_c$$

Any point on the exponential part of the characteristic can be used to compute collector work function by substituting J, V and $T_E$ in the
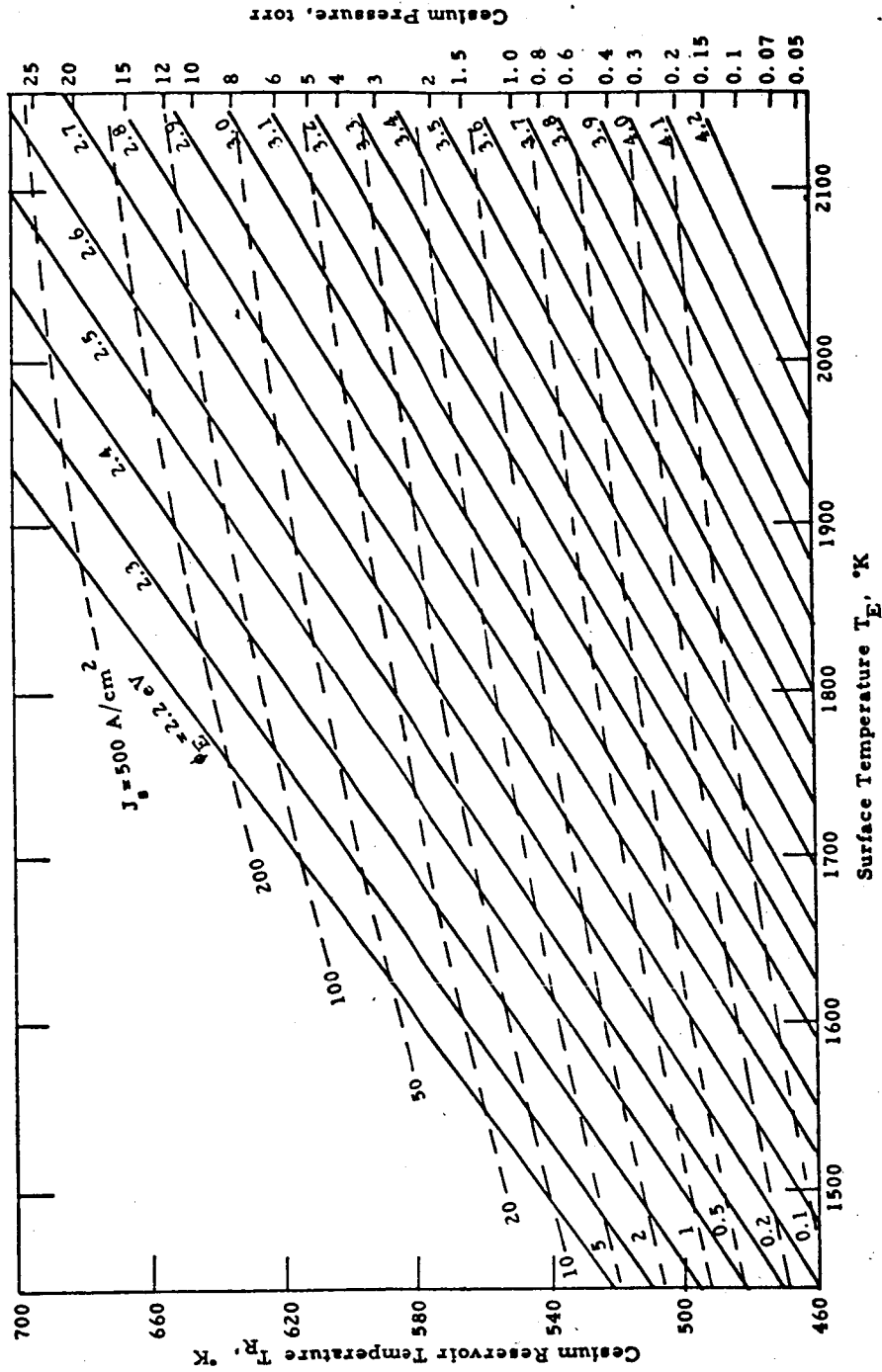
Figure VI-10. Rhenium Emitter Work Function and Saturation Emission as a Function of Surface and Cesium Temperatures.

161

second equation. In reality, the conditions postulated for the curve never do exist, so that the interpretation of actual data must take into account the presence of ion currents and back emission. In Figure VI-12 the curve of Figure VI-11 is shown, but in addition the ion current and back emission are shown. Note that both the forward current and the ion and back emission currents have a cut-off at the same point, $V_c$, which is the voltage equal to the difference of the emitter work function and the collector work function.

The actual characteristic of the converter, postulated in Figure VI-11, is curve No. 3, which is a sum of curves Nos. 1 and 2. Already the presence of this ion current and back emission has altered the resulting characteristic, and, if No. 3 were to be used to compute the collector work function, an error would result approximately equal to the shift of curve No. 3 from curve No. 1. Clearly, then, the object of the experimenter will have to be the reduction of curve No. 2 so that its effect on curve No. 1 can be minimized. To do this, the back emission has to be made as low as possible, which can be accomplished by keeping the collector temperature low. The ion current is somewhat more difficult to control. This can be accomplished by keeping the emitter temperature low, or, more generally, by keeping the number of ions generated at the emitter surface as low as possible. A point that should be made is that one should not compare the saturation ion current with the saturation electron emission from the emitter, but rather compare the saturation ion emission with the kind of electron current magnitudes that are used when the Boltzmann line is plotted. In practical terms, this means that the maximum tolerable ion current is of the order of one milliampere, since the straight portion of the Boltzmann line usually occurs within 1 to 50 milliamperes. This ion current is sufficient to neutralize 1/2 ampere of

64-R-12-59
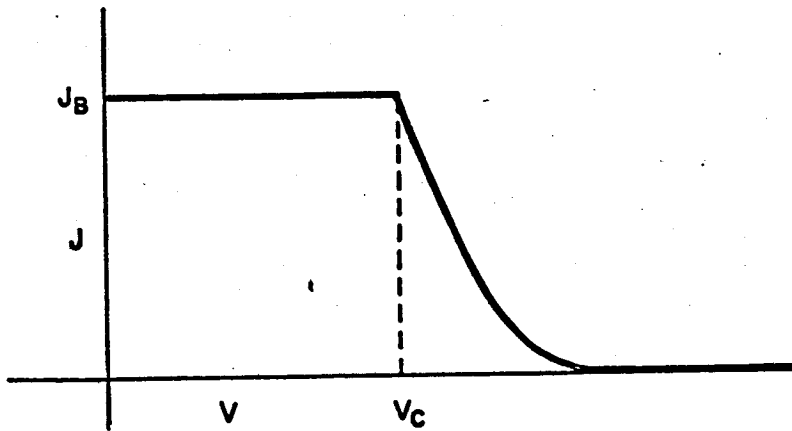


Figure VI-11.  Ideal J-V Characteristic.

64-R-12-60



① FORWARD ELECTRON EMISSION

③ SUM OF ① + ②

② ION CURRENT AND BACK EMISSION
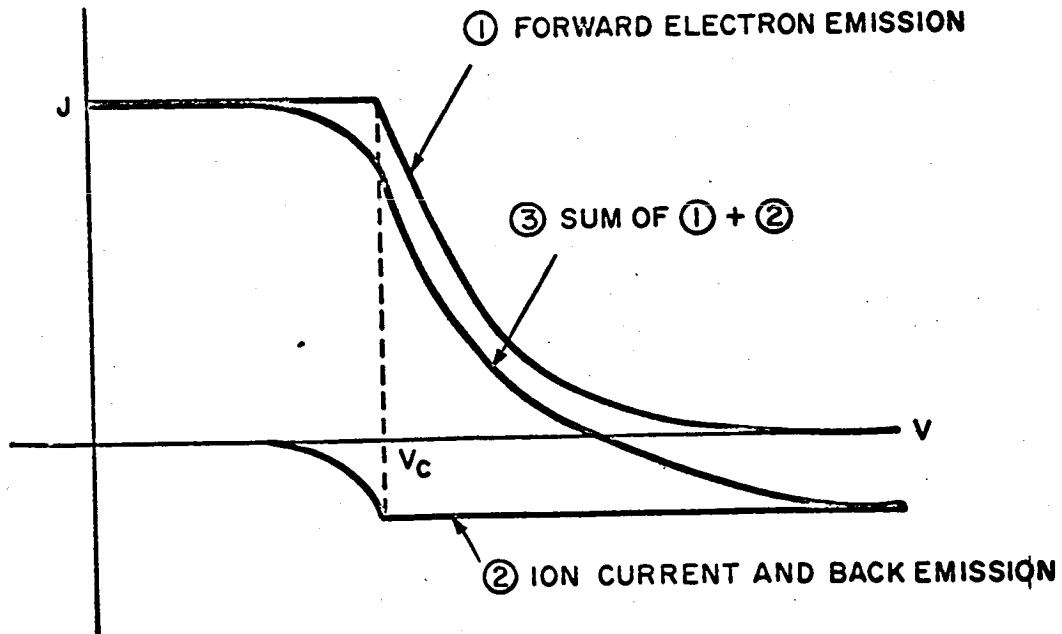
Figure VI-12.  Actual J-V Characteristic.

forward electron emission.

Figure VI-13 is a plot of a current-voltage characteristic used in determining collector work function. Note that three different scales have been used on the current axis, so that, as the current values become smaller, greater accuracy can be achieved in their measurement. Also note that the back current, as evidenced by the saturation past open circuit, is very, very small, in fact less than 1% of the forward current. This curve is replotted in the form of a logarithm of the current density versus the voltage in Figure VI-14, which was used to identify the collector work function. A great number of such curves have been taken, and many of them are not suitable for collector work function measurements and have been so identified. In fact, before the region of validity of these measurements could be defined, a great deal of data had to be accumulated.

An alternate method of determining collector work function is the measurement of the saturation emission from the collector. This back-emitted current $J_B$ can be used to compute the collector work function $\phi_c$ by substitution in the Richardson equation:

$$\phi_c = -kT_C \ln [J_B/AT_C^2]$$

The technique, of course, requires accurate measurement of collector temperature and back-emitted current. The back current measurement is performed by making the emitter positive with respect to the collector and collecting at the emitter the electrons emitted by the collector. At the same time any ion current generated at the emitter will flow to the collector and add to the electron current arriving at the emitter. It is necessary, therefore, for the surface-generated ion current to be
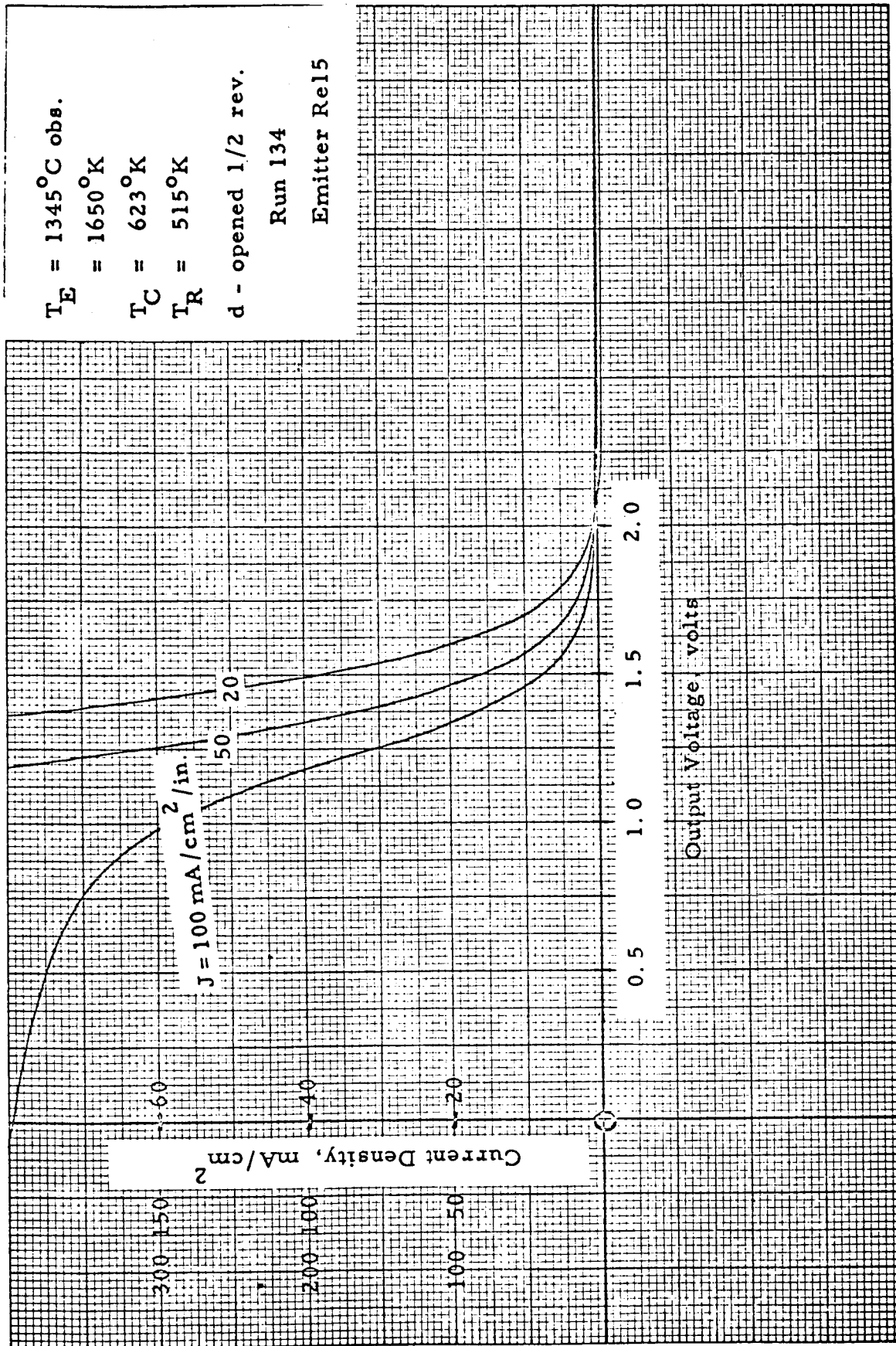
Figure VI-13. Characteristic for Collector Work Function Determination

$T_E$ = 1345°C obs.

= 1650°K

$T_C$ = 623°K

$T_R$ = 515°K

d - opened 1/2 rev.

Run 134

Emitter Re15

J = 100 mA/cm²/in.

Output Voltage, volts

Current Density, mA/cm²
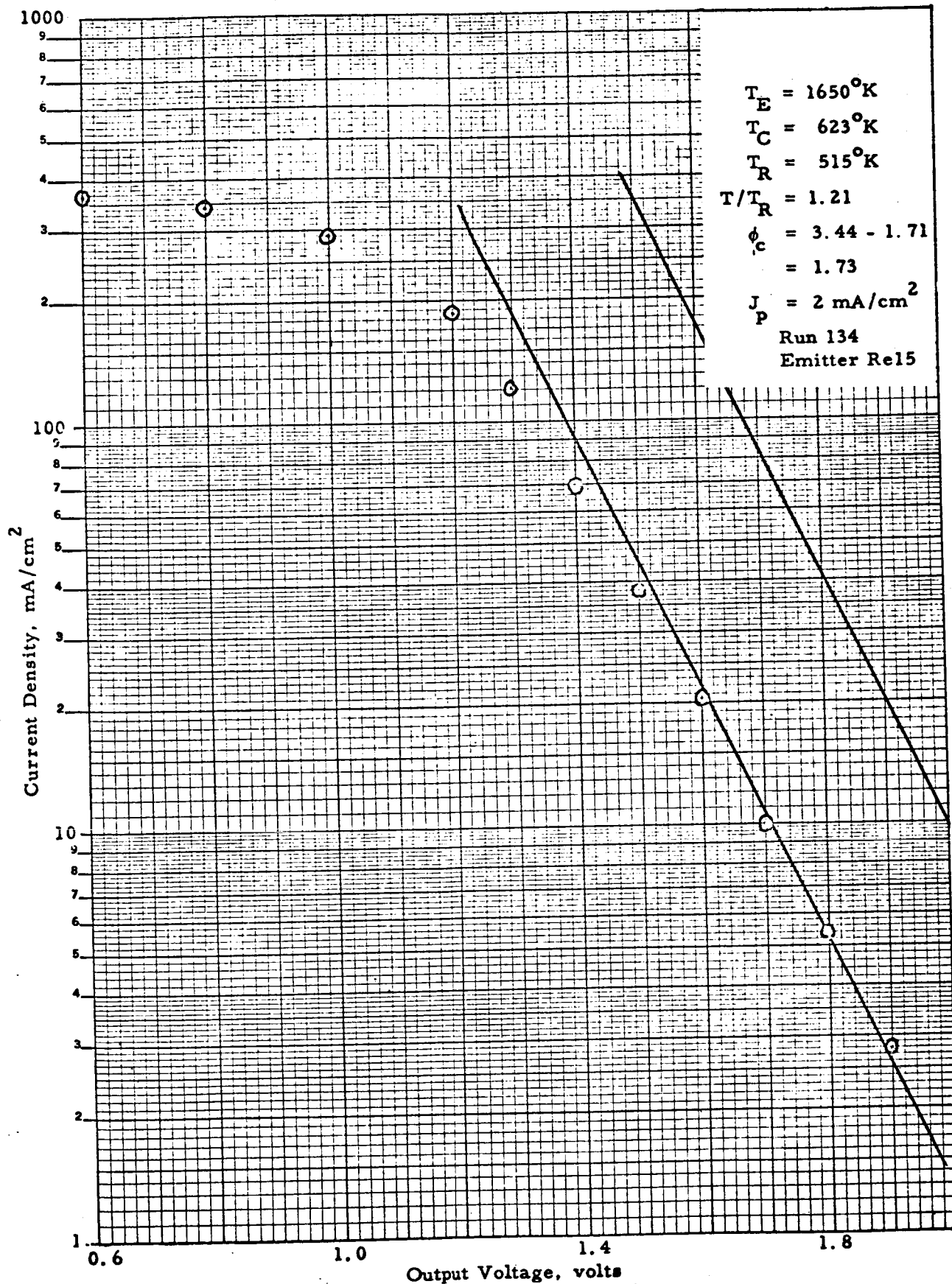
Figure VI-14. Log J-V for Collector Work Function Determination.

negligible compared with the back-emitted current.

## 2.    Effect of Spacing on Retarding Plots

In the preceding discussion it was assumed that, in the Boltzmann portion of the characteristic, the emitter saturation current density is modulated by the collector barrier only. On this basis the conclusion was drawn that, in the absence of ion current and back emission, the collector work function can be correctly determined from any point on the Boltzmann line. This hypothesis does not take into account any scattering in the interelectrode space. Scattering is a function of the number of collisions suffered by electrons, which in turn depends on the product of pressure and spacing.

To investigate the effect of scattering, the following experiment was performed: A series of J-V characteristics was generated under conditions yielding good retarding plots, keeping all parameters constant, except spacing. These runs are shown in Figures VI-15, -16, -17 and -18.[*] The corresponding retarding plots are shown in Figures VI-19, -20, -21, and -22. Inspection of Figures VI-19 through VI-22 shows that the resulting Boltzmann lines are straight over a sufficient range, and their slopes agree with the emitter temperature. Ln-J-vs-V plots for all four curves are shown in Figure VI-23. Two effects can be observed in this figure. The straight portions of Boltzmann lines are displaced to the left as spacing is increased, and the characteristic deviated from a straight line at lower currents as the spacing was increased. The collector work functions calculated from the straight portion of the retarding plots are shown in Table VI-2.

---

[*] Note that the total back current is about 1 mA, and should not have any significant effect on the Boltzmann line above 3 mA.

167
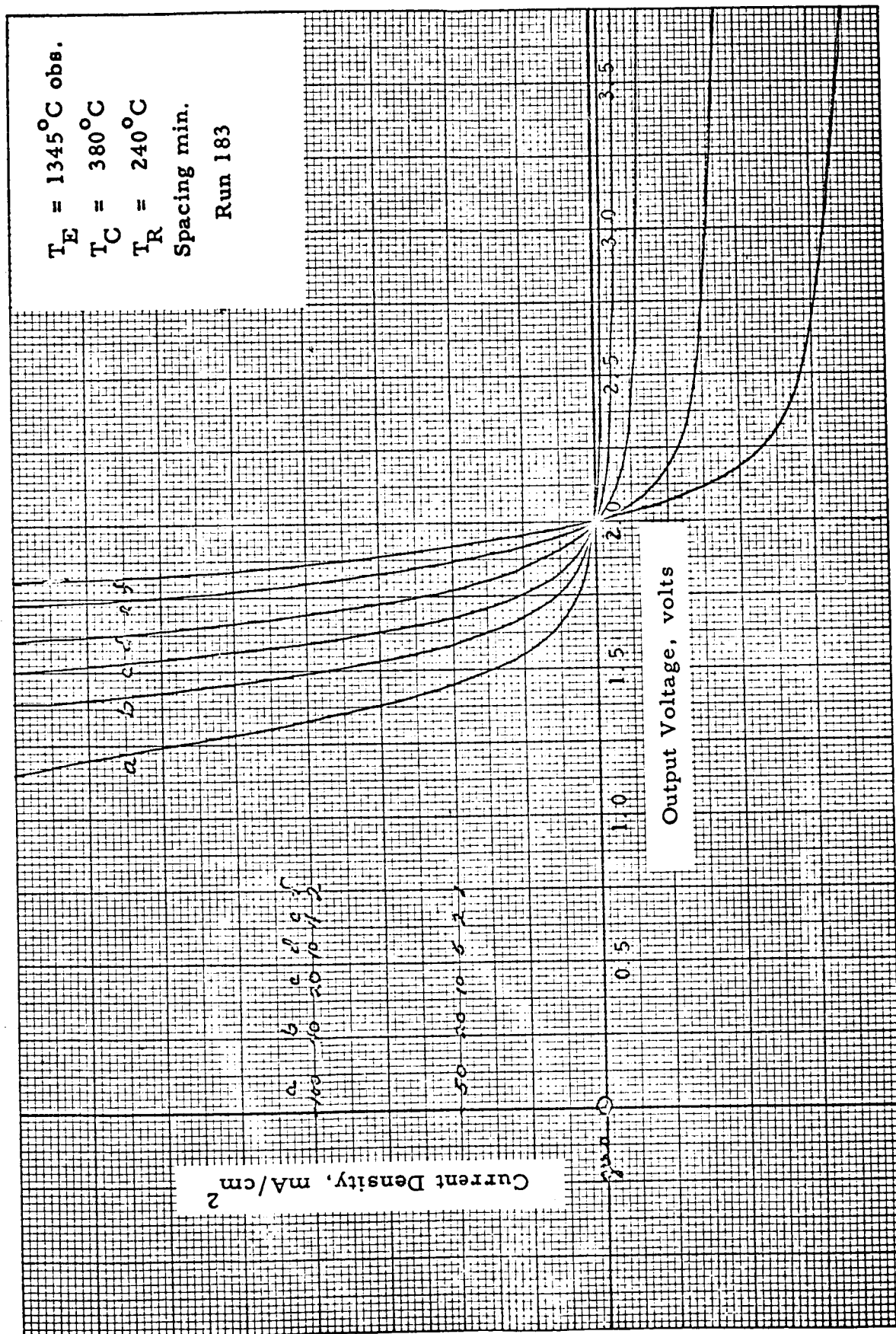
Figure VI-15. Current-Voltage Curve — Retarding Range.
Spacing: Minimum.

T_E = 1345°C obs.
T_C = 380°C
T_R = 240°C
d = 1 + min.

Run 184

Output Voltage, volts

Current Density, mA/cm$^2$
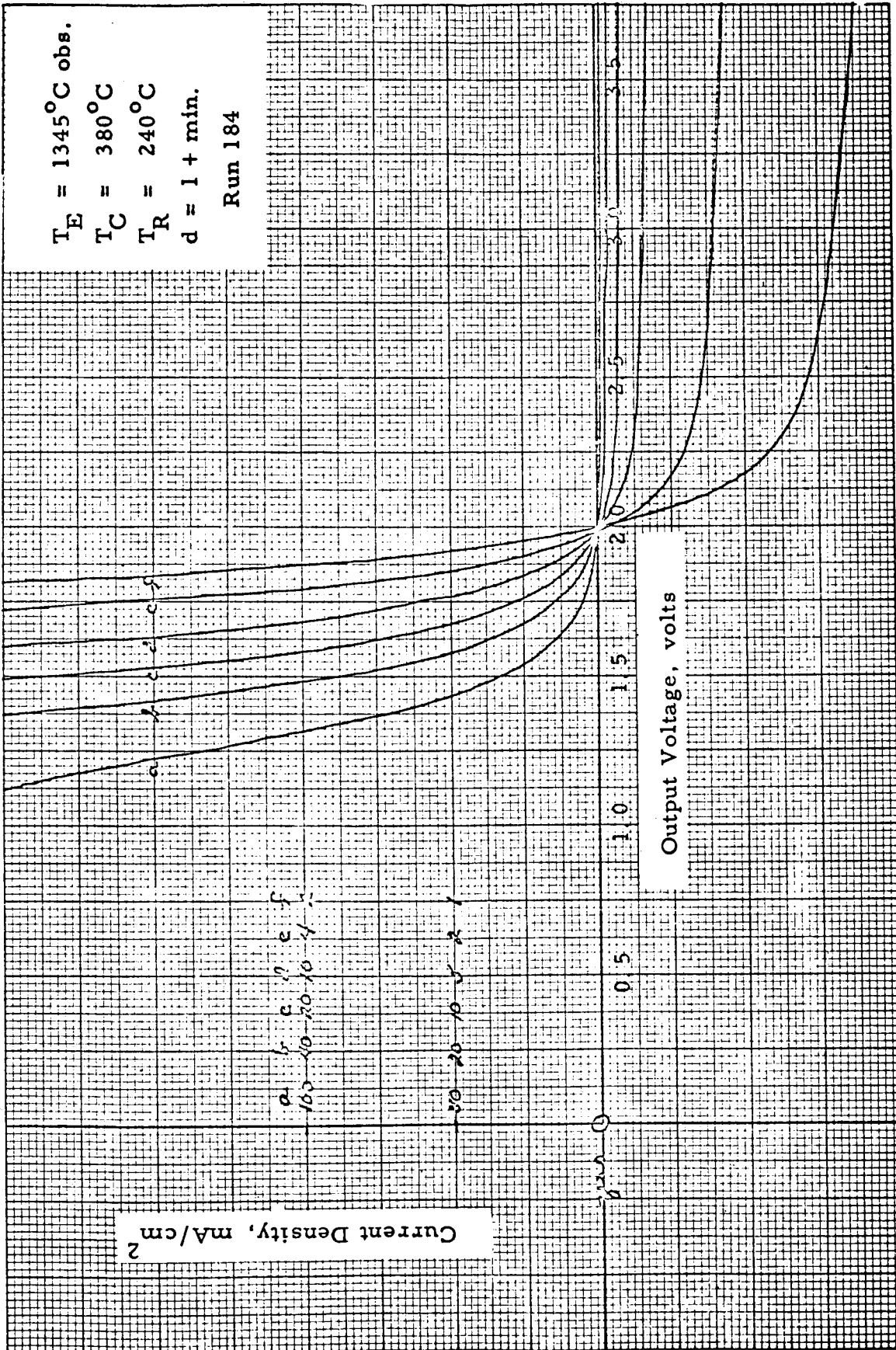
Figure VI-16.   Current-Voltage Curve — Retarding Range.
Spacing:  1 + Minimum.

169

$T_E$ = 1345°C obs.

$T_C$ = 380°C

$T_R$ = 240°C

d = 2 + min.

Run 185

Output Voltage, volts

Current Density, mA/cm$^2$
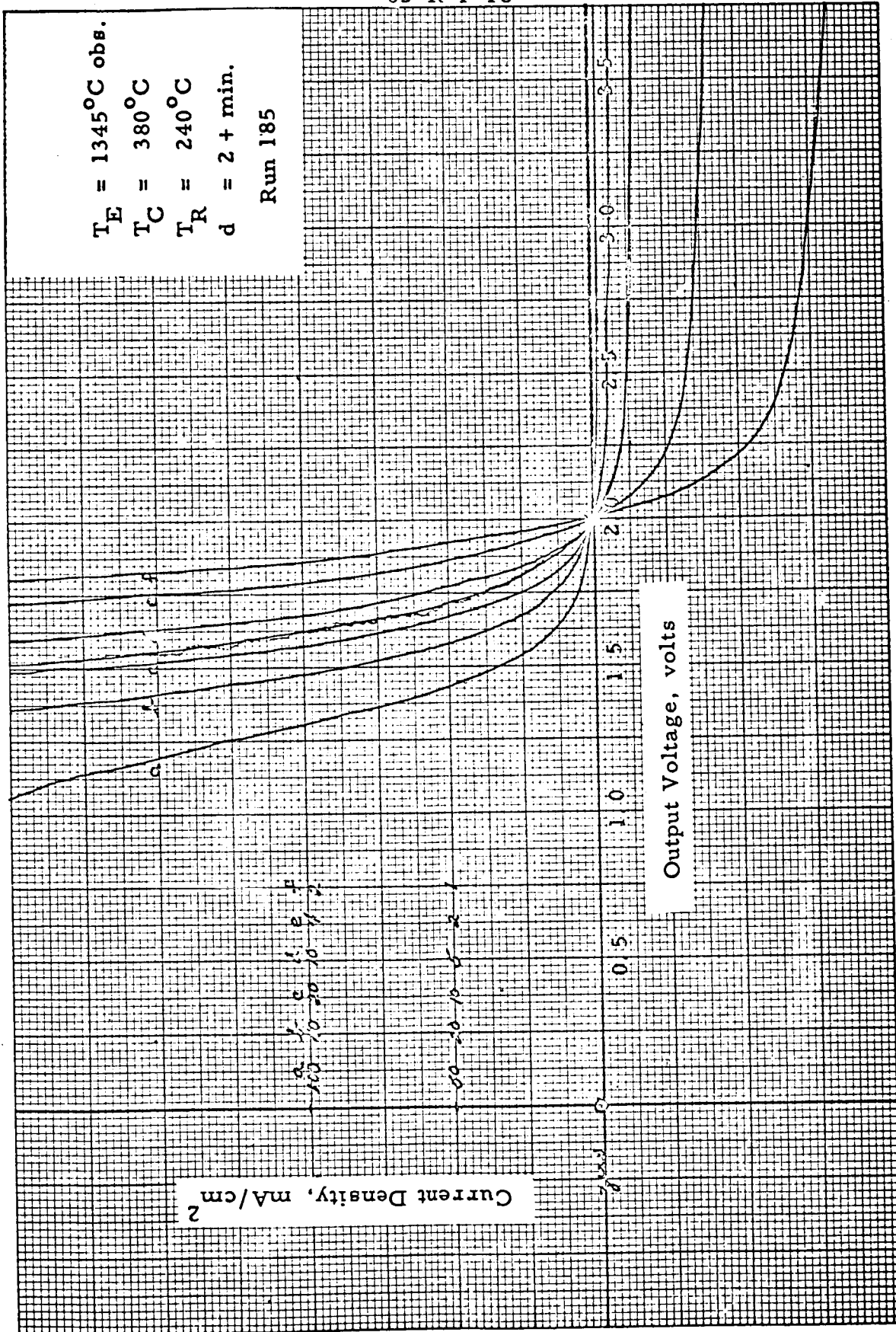
Figure VI-17.   Current-Voltage Curve — Retarding Range.
Spacing:  2 + Minimum.

170
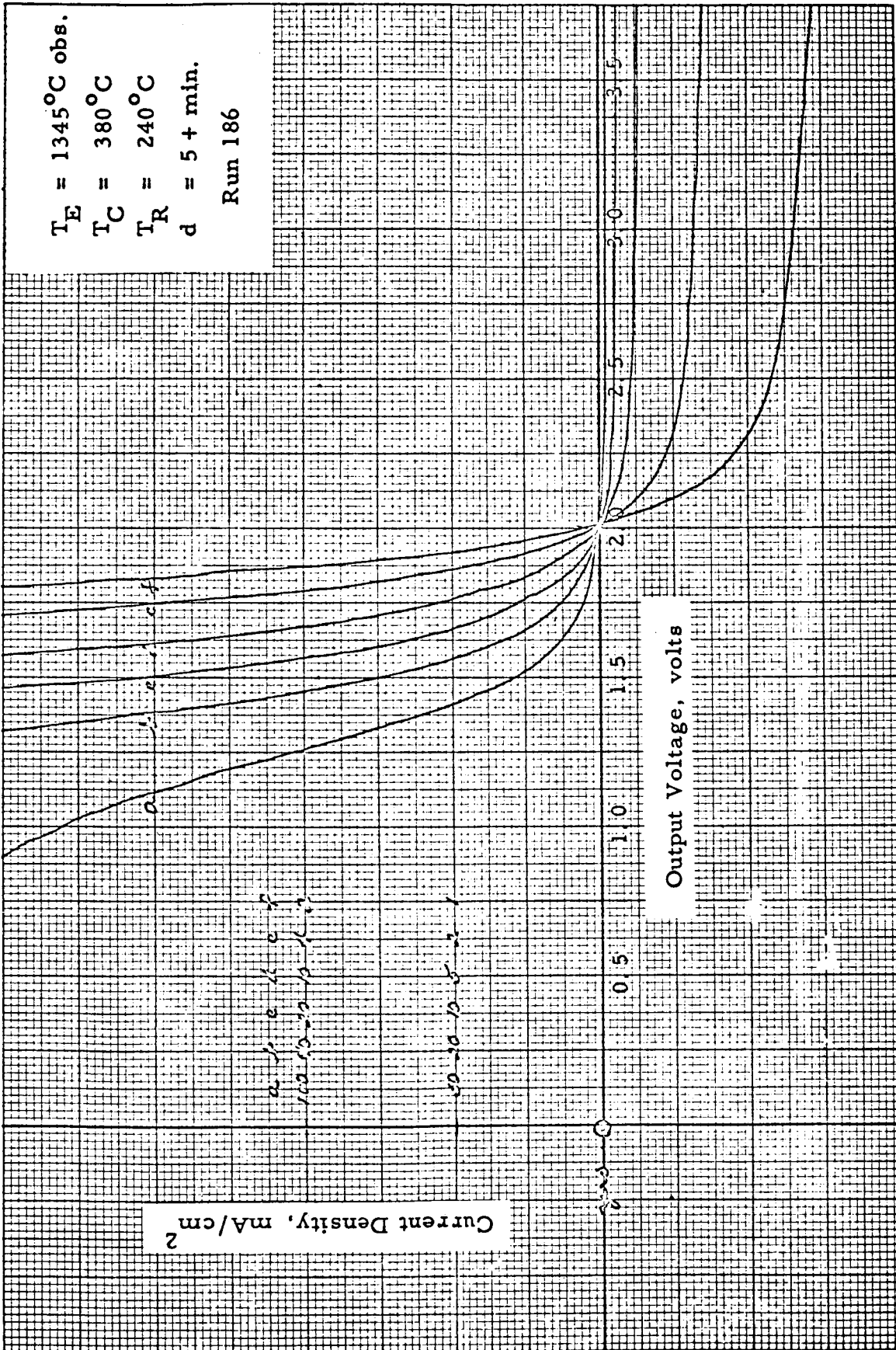
Figure VI-18. Current-Voltage Curve — Retarding Range
Spacing: 5 + Minimum.

$T_E$ = 1345°C obs.
$T_C$ = 380°C
$T_R$ = 240°C
d = 5 + min.

Run 186

Output Voltage, volts

Current Density, mA/cm$^2$

$$T_E = 1650°K$$
$$T_C = 653°K$$
$$T_R = 513°K$$
$$T/T_R = 1.27$$
$$d = min.$$
$$\phi_c = 3.435 - 1.705$$
$$\phi_c = 1.73$$
$$J_p = 3 \text{ mA}$$

Run 183
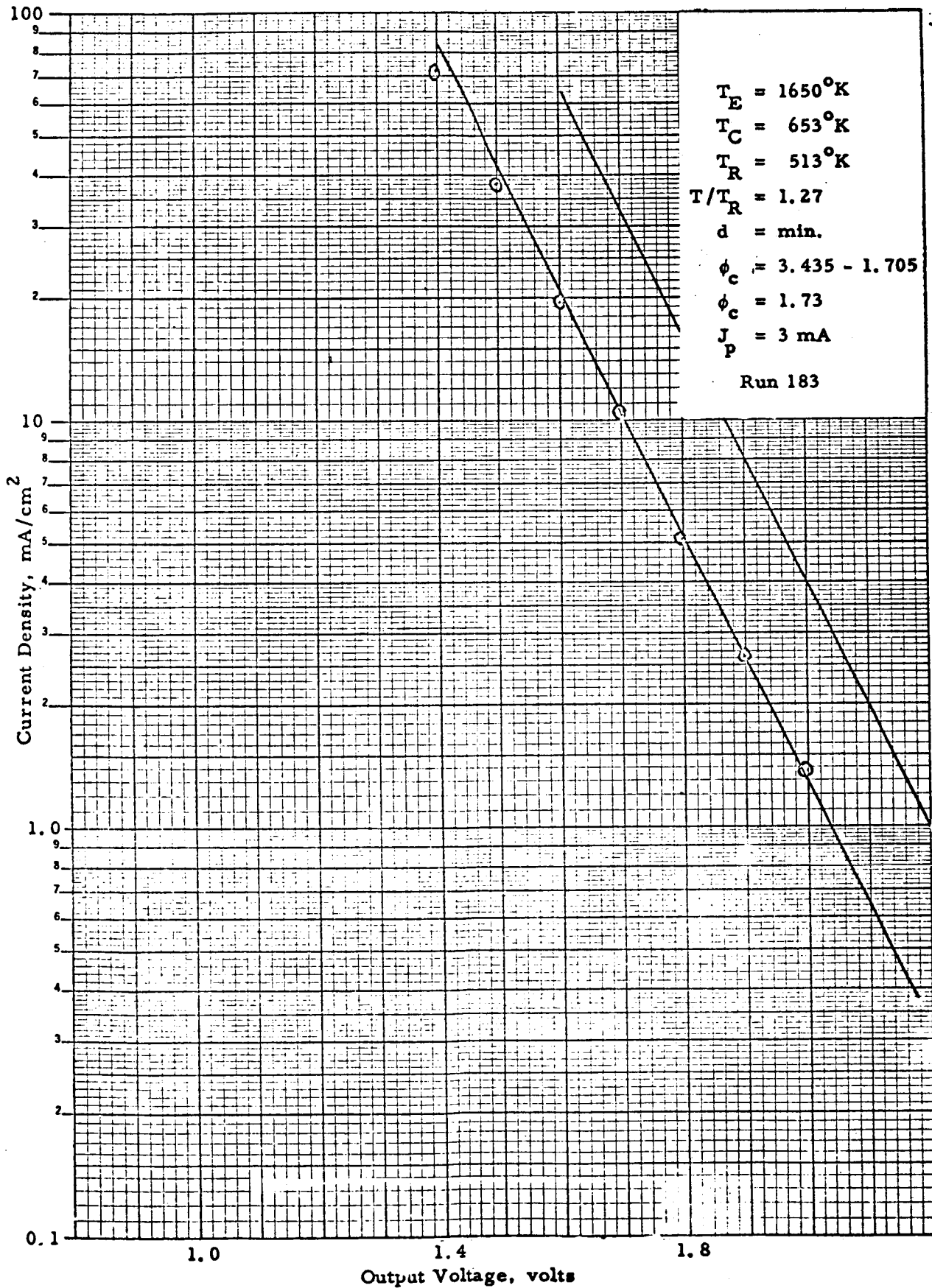
Figure VI-19.   Log J-V for Minimum Spacing.

$T_E$ = 1650°K

$T_C$ = 653°K

$T_R$ = 513°K

$T/T_R$ = 1.27

d = 1 + min.

$\phi_c$ ≐ 3.435 - 1.70

= 1.735

$J_p$ = 3 mA

Run 184

Current Density, mA/cm²

Output Voltage, volts
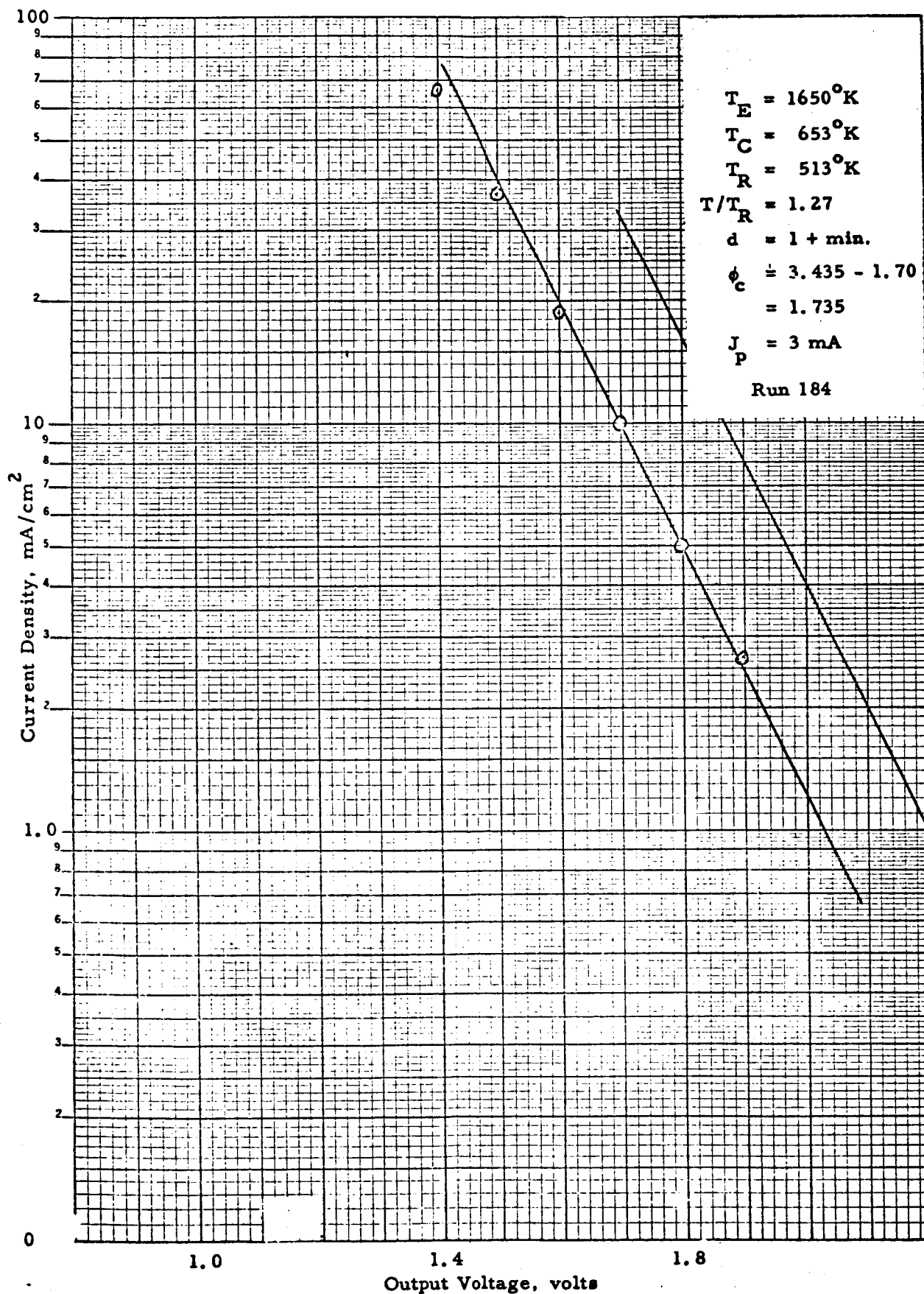
Figure VI-20. Log J-V for Spacing = 1 + Minimum

173

$T_E = 1650°K$
$T_C = 653°K$
$T_R = 513°K$
$T/T_R = 1.27$
$d = 2 + min.$
$\phi_c = 3.435 - 1.695$
$= 1.74$
$J_P = 3 mA$

Run 185

Current Density, mA/cm²

Output Voltage, volts
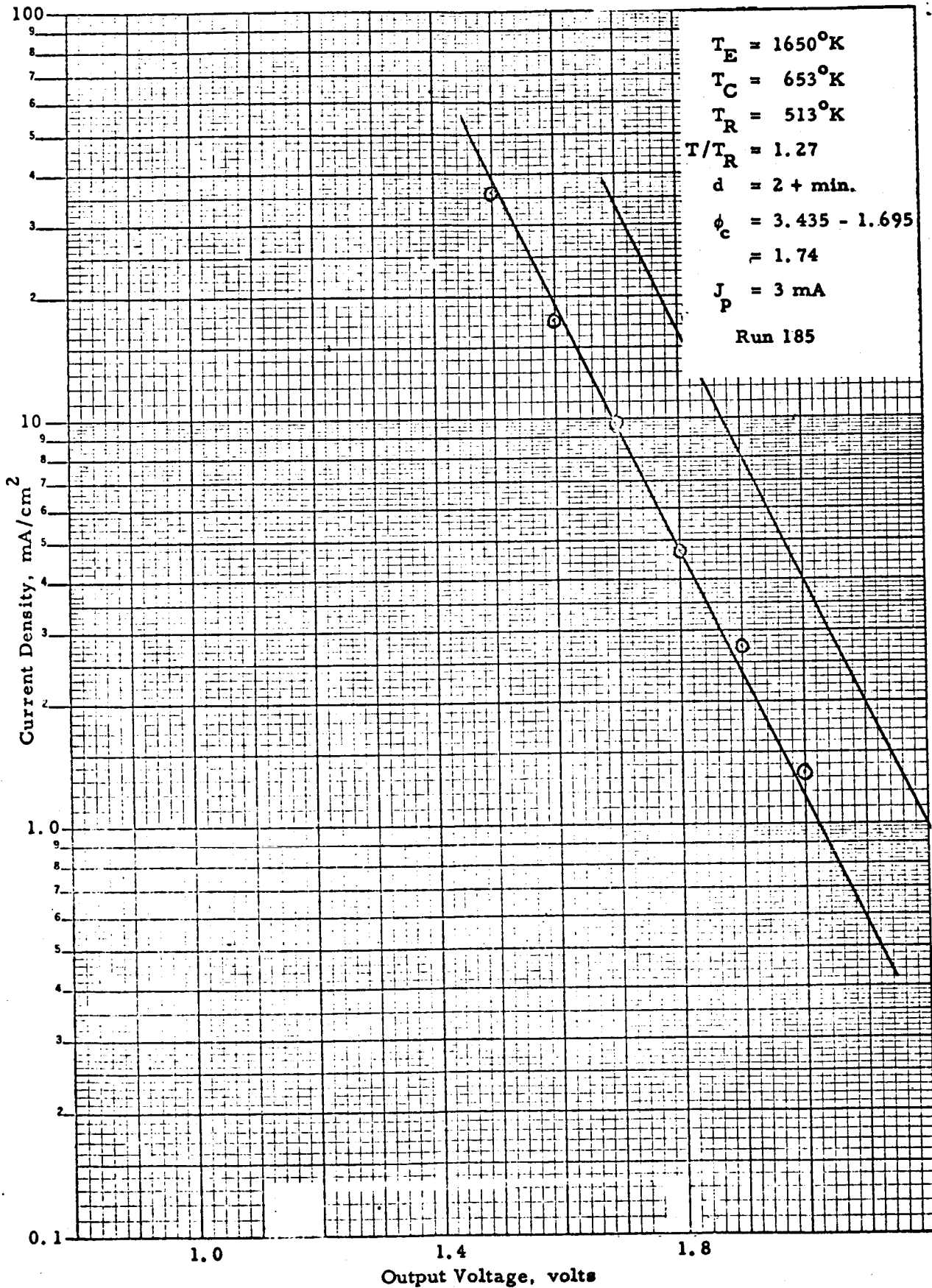
Figure VI-21. Log J-V for Spacing = 2 + Minimum.

$T_E$ = 1650°K

$T_C$ = 653°K

$T_R$ = 513°K

$T/T_R$ = 1.27

d = 5 + min.

$\phi_c$ = 3.435 - 1.69

= 1.745

$J_P$ = 3 mA

Run 186

Current Density, mA/cm$^2$

Output Voltage, volts
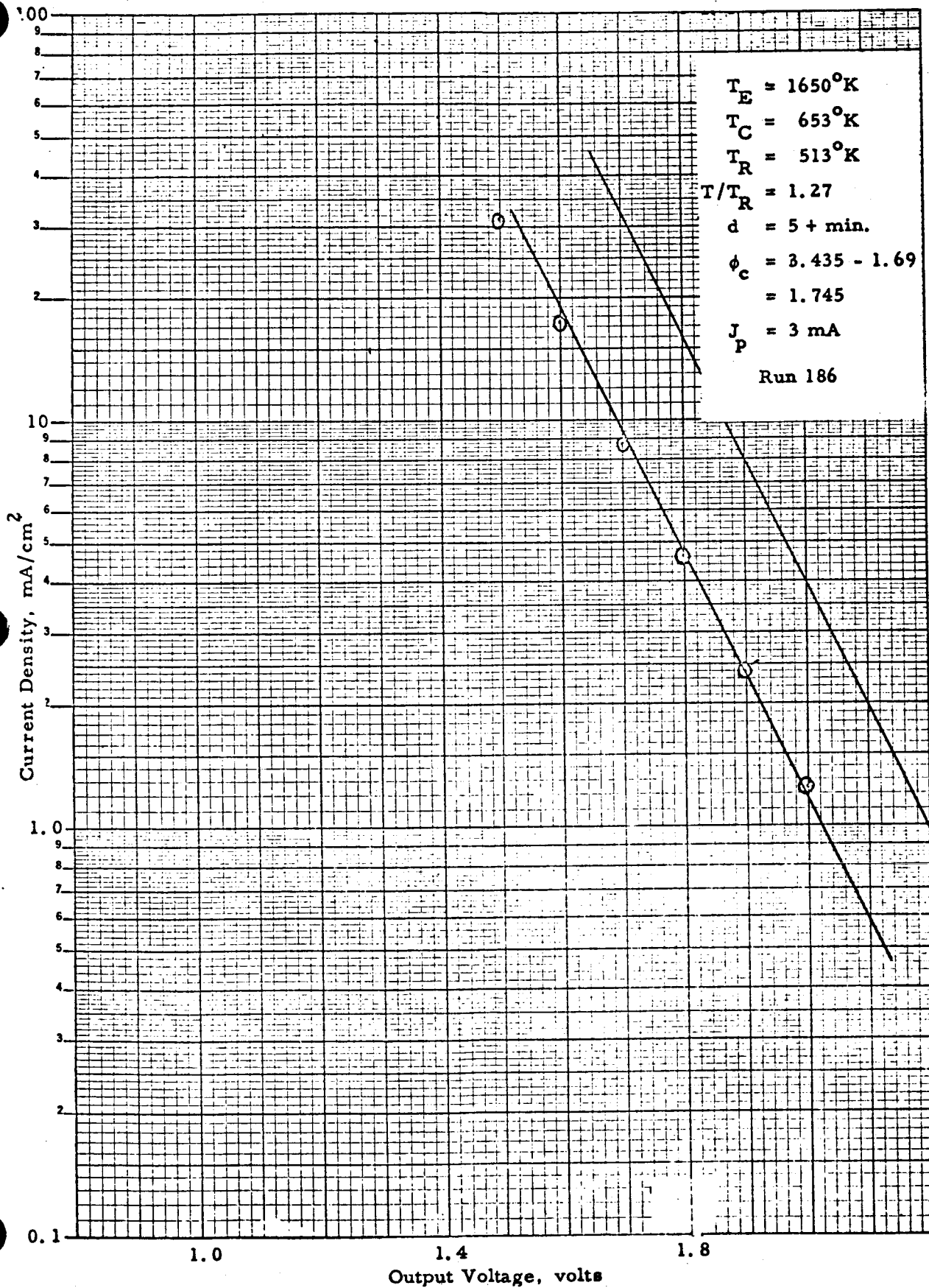
Figure VI-22. Log J-V for Spacing = 5 + Minimum.

THERMO ELECTRON

T_E = 1650°K
T_C = 653°K
T_R = 513°K
T/T_R = 1.27

Current Density, mA/cm²

Output Voltage, volts
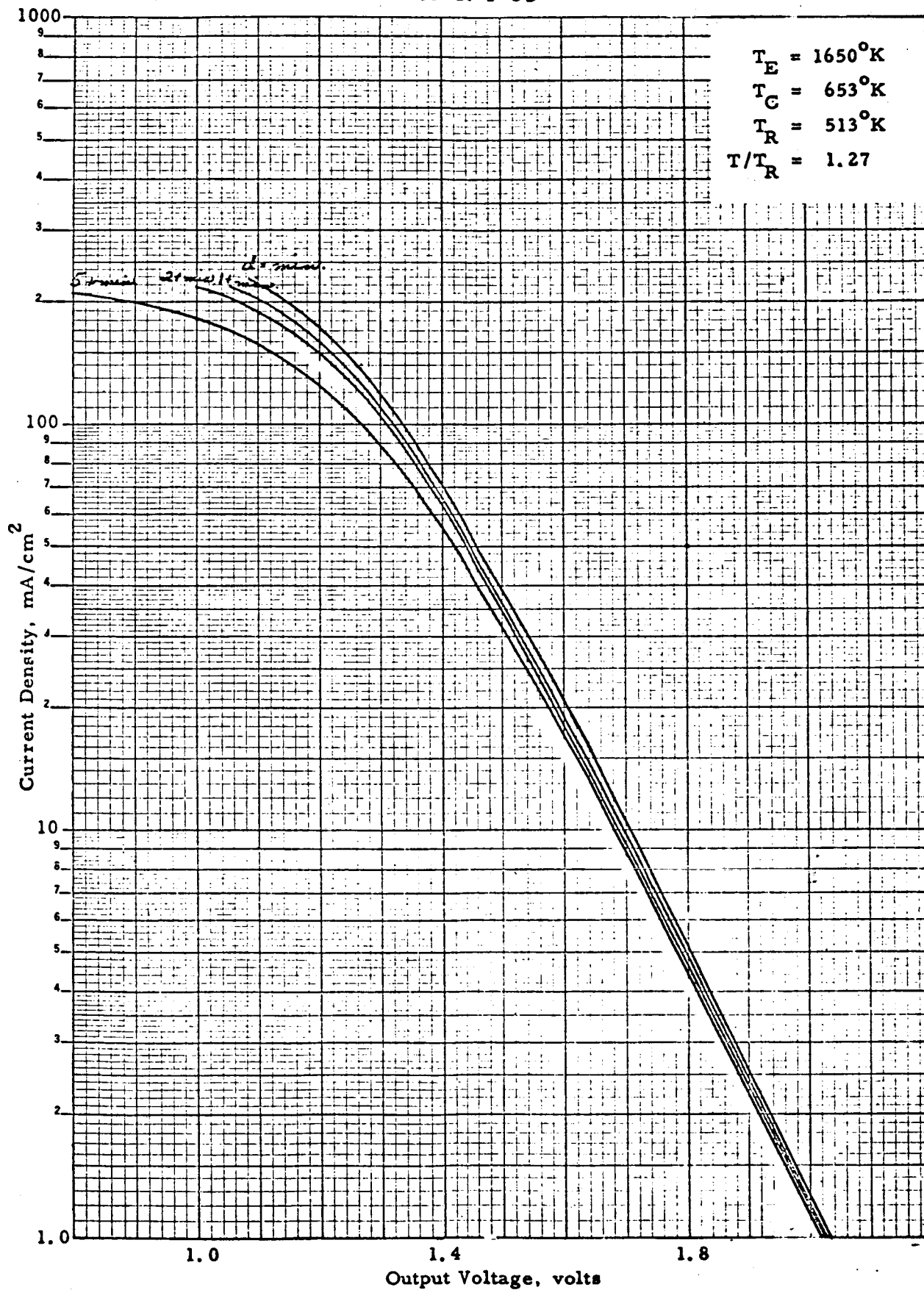
Figure VI-23. Ln J vs V for Entire Range of Retarding Plots.

## TABLE VI-2

### COMPUTED COLLECTOR WORK FUNCTION VALUES

| Run No. | Spacing | Pressure | Pd | Collector Work Function | $\Delta\phi_c$ |
|---------|---------|----------|------|-------------------------|------|
| 183 | 0.5 | 0.3 | 0.15 | 1.730 | 0 |
| 184 | 1.5 | 0.3 | 0.45 | 1.735 | 0.005 |
| 185 | 2.5 | 0.3 | 0.75 | 1.740 | 0.010 |
| 186 | 5.5 | 0.3 | 1.65 | 1.745 | 0.015 |

It is interesting to note that the total spread in collector work function is 0.015 volt, while the spacing, and therefore Pd, vary by an order of magnitude.

These results can be used to obtain a very accurate value for the collector work function. Clearly, the effect of scattering disappears at zero spacing. A plot was made of the change in apparent collector work function as a function of spacing, and this plot is shown in Figure VI-24. The minimum spacing is defined as $\epsilon$ and is known to be between 0 and 0.5 mil. Let us suppose that the uncertainty in spacing is equal to $\epsilon$; then, extrapolating the $\Delta\phi_c$-versus-spacing line to zero, we have an uncertainty in $\phi_c$ of 0.004 volt. In fact, assuming that the collector work function value calculated from the minimum-spacing curve is the true value results in a maximum error of 4 millivolts. This result is considered very satis-factory and, in fact, quite an improvement over previous measurements.

The experiment is of value from an analytical standpoint and results, as well, in greater confidence in our collector work function measurement. The scattering effects are important in high-temperature (2000-2100°K) close-spacing operation in the lower mode, which has possibilities for high efficiency. This kind of experiment is a direct measure of scattering and will be of significant value in the analysis.

177

THERMO ELECTRON
ENGINEERING CORPORATION
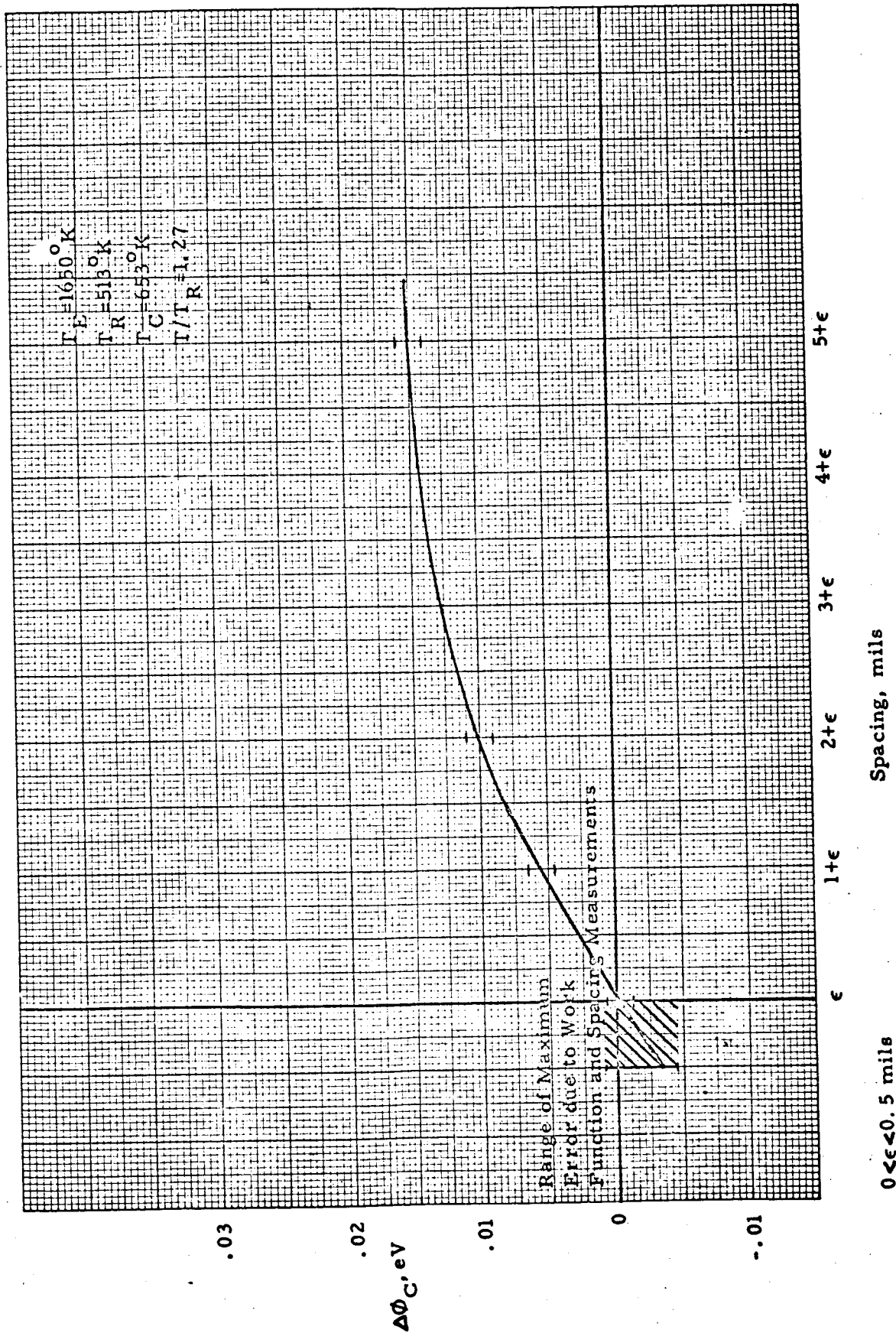


Figure VI-24.  Collector Work Function Change vs Spacing.

$0 < \epsilon < 0.5$ mils

Spacing, mils

$\Delta \phi_C$, eV

$T_E = 1650 \,^\circ K$
$T_R = 513 \,^\circ K$
$T_C = 653 \,^\circ K$
$T/T_R = 1.27$

Range of Maximum
Error due to Work
Function and Spacing Measurements

178

3.    Results

In the preceding two sections the conditions necessary for the acquisition of valid collector work function data were stated.   The ranges of emitter, collector and Cs reservoir temperature which satisfied these conditions had to be determined experimentally, however, and as a result a great number of J-V curves obtained were of no value in determining collector work function.   The valid runs are identified in Table VI-3, and the actual J-V curves are shown in Appendix B.

The collector work function measurements that satisfied the conditions of validity are summarized on a $\phi_c$-versus-$T_C/T_R$ plot in Figure VI-25.   The data show a unique dependence on $T_C/T_R$.   Good agreement is observed between the retarding-plot measurements (open circles) and the back-emission measurements (crosses).   A curve has been fitted to the data, and the mean deviation of the data from this curve, defined as:

$$S = \sqrt{\frac{\sum\limits_{i=1}^{n} (\phi_i - \overline{\phi})^2}{n}} \, ,$$

was calculated,

where    S    = mean deviation

   $\phi_i$   = experimental value of work function

   $\overline{\phi}$   = value from the curve at the same $T/T_R$ as $\phi_i$

   n    = number of experimental points

The mean deviation obtained was 0.025 volt.   Ninety percent of the data points are within 0.041 volt of the fitted line.

179
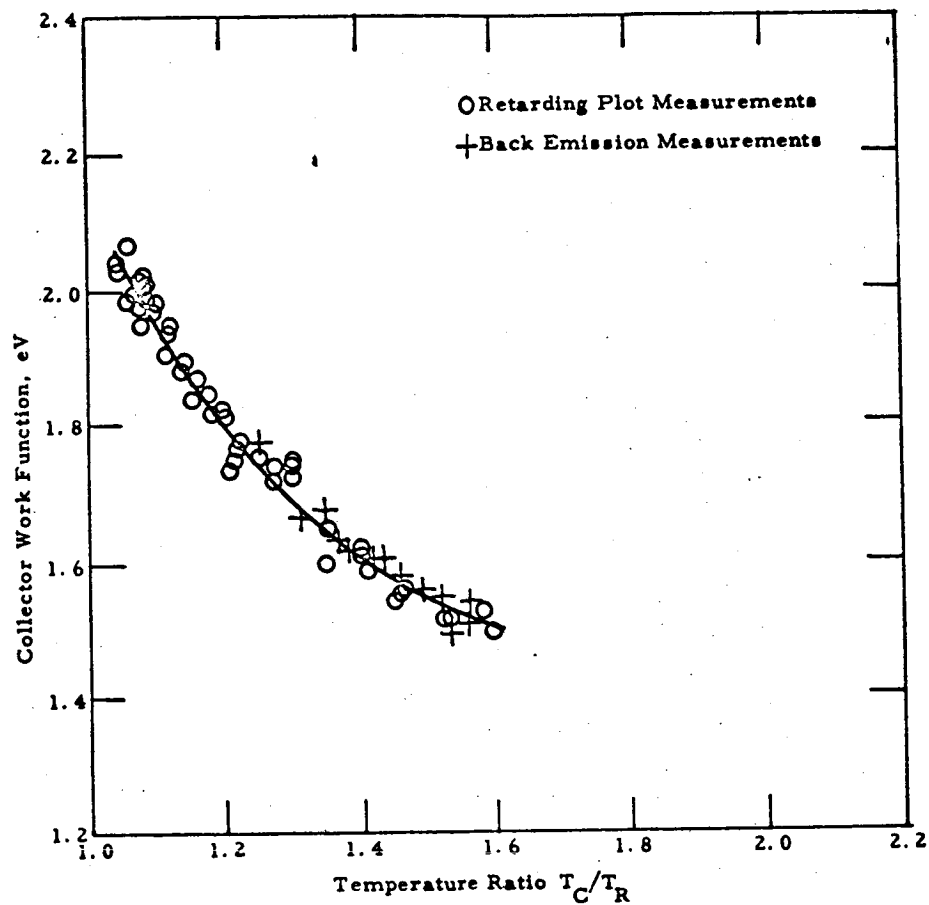
Figure VI-25. Molybdenum Collector Work Function Dependence on the Ratio of Collector Surface Temperature to Cesium Reservoir Temperature.

## TABLE VI-3

### EMITTER WORK FUNCTION RUNS

| Run | $T_E$ °K | $T_R$ °K | | Run | $T_E$ °K | $T_R$ °K |
|-----|----------|----------|---|-----|----------|----------|
| Re 15 | | | | | | |
| 28 | 1975 | 483 | | 67 | 1870 | 493 |
| 29 | | 473 | | 68 | | 513 |
| 30 | | 463 | | 69 | | 503 |
| 32 | | 483 | | 70 | | 493 |
| 33 | | 473 | | 71 | | 483 |
| 34 | | 463 | | 72 | | 473 |
| 36 | | 483 | | 72a | | 473 |
| 37 | | 473 | | 73 | | 463 |
| 38 | 2027 | 533 | | 74 | 1868 | 503 |
| 39 | | 523 | | 75 | | 503 |
| 40 | | 513 | | 76 | 1813 | 503 |
| 41 | | 503 | | 104 | 1800 | 534 |
| 42 | | 533 | | 105 | | 522 |
| 43 | | 524 | | 106 | | 513 |
| 44 | | 523 | | 107 | | 502 |
| 45 | | 513 | | 108 | | 493 |
| 46 | | 503 | | 109 | | 484 |
| 47 | | 493 | | 110 | | 473 |
| 48 | | 483 | | 111 | | 463 |
| 49 | | 473 | | 112 | 1848 | 535 |
| 50 | | 464 | | 113 | | 522 |
| 51 | 1975 | 503 | | 114 | | 513 |
| 52 | | 493 | | 115 | | 503 |
| 53 | | 483 | | 116 | | 493 |
| 54 | | 473 | | 117 | | 482 |
| 55 | | 463 | | 118 | | 473 |
| 57 | 1922 | 503 | | 119 | 1800 | 533 |
| 58 | | 493 | | 120 | | 522 |
| 59 | | 483 | | 121 | | 512 |
| 60 | | 473 | | 123 | 1900 | 523 |
| 61 | | 503 | | 124 | | 513 |
| 62 | | 483 | | 125 | | 503 |
| 63 | | 464 | | 126 | | 493 |
| 64 | | 473 | | 127 | | 473 |
| 65 | 1870 | 513 | | 129 | 1950 | 523 |

181

## TABLE VI-3 (continued)

### EMITTER WORK FUNCTION RUNS

| Run | $T_E$ °K | $T_R$ °K | | Run | $T_E$ °K | $T_R$ °K |
|---|---|---|---|---|---|---|
| 130 | 1950 | 503 | | 55 | 1780 | 576 |
| 131 | | 483 | | | 1685 | |
| 204 | 1800 | 504 | | | 1625 | |
| 205 | | 480 | | 56 | 2060 | 576 |
| 206 | | 459 | | | 1950 | |
| 207 | | 439 | | | 1855 | |
| 208 | | 421 | | | 1795 | |
| 209 | | 402 | | | 1715 | |
| 210 | | 379 | | | 1635 | |
| 211 | 1700 | 377 | | 57 | 2065 | 576 |
| 212 | | 398 | | | 2000 | |
| 213 | | 444 | | | 1925 | |
| 214 | | 485 | | | 1785 | |
| 215 | | 404 | | | 1710 | |
| 216 | | 419 | | | 1635 | |
| 217 | | 448 | | 59 | 1930 | 577 |
| 218 | | 467 | | | 1875 | |
| 219 | | 398 | | | 1810 | |
| 220 | 1800 | 404 | | | 1725 | |
| 221 | 1550 | 402 | | | 645 | |
| 222 | | 424 | | | 1615 | |
| 223 | | 444 | | 60 | 1930 | 577 |
| 224 | | 465 | | | 1860 | |
| 225 | | 484 | | | 1810 | |
| 226 | | 505 | | | 1730 | |
| 227 | 1900 | 399 | | | 1650 | |
| 228 | | 424 | | | 1590 | |
| 229 | | 443 | | 61 | 1965 | 605 |
| 230 | | 462 | | | 1900 | |
| 231 | | 480 | | | 1810 | |
| | | | | | 1750 | |
| Re 16 | | | | | 1690 | |
| 55 | 2050 | 576 | | | 1695 | |
| | 1985 | | | | 1635 | |
| | 1940 | | | | 1585 | |
| | 1865 | | | 62 | 1935 | 605 |

## TABLE VI-3 (continued)

### EMITTER WORK FUNCTION RUNS

| Run | $T_E$ °K | $T_R$ °K | | Run | $T_E$ °K | $T_R$ °K |
|-----|----------|----------|---|-----|----------|----------|
| 62 | 1875 | 605 | | 69 | 1980 | 634 |
| | 1800 | | | | 1925 | |
| | 1735 | | | | 1860 | |
| | 1680 | | | | 1800 | |
| | 1565 | | | | 1715 | |
| 64 | 2075 | 605 | | 73 | 1865 | 543 |
| | 2040 | | | | 1795 | |
| | 1940 | | | | 1685 | |
| | 1875 | | | 74 | 1875 | 543 |
| | 1805 | | | | 1800 | |
| | 1755 | | | | 1700 | |
| | 1665 | | | 75 | 1875 | 543 |
| 65 | 2050 | 605 | | | 1800 | |
| | 2035 | | | | 1715 | |
| | 1910 | | | 76 | 1855 | 543 |
| | 1860 | | | | 1775 | |
| | 1805 | | | | 1710 | |
| | 1765 | | | 77 | 1860 | 543 |
| | 1665 | | | | 1805 | |
| 66 | 2000 | 635 | | | 1710 | |
| | 1935 | | | | | |
| | 1860 | | | | | |
| | 1760 | | | | | |
| | 1670 | | | | | |
| 67 | 2010 | 635 | | | | |
| | 1960 | | | | | |
| | 1860 | | | | | |
| | 1800 | | | | | |
| | 1730 | | | | | |
| | 1665 | | | | | |
| 68 | 2030 | 635 | | | | |
| | 1975 | | | | | |
| | 1890 | | | | | |
| | 1830 | | | | | |
| | 1755 | | | | | |

183

The results are presented in the form of a chart in Figure VI-26. In this chart contant-work function lines are plotted in the plane of Cs reservoir temperature versus collector surface temperature. In addition, constant back-emission lines are shown (dashed lines). This chart is derived from Figure VI-25, and, as pointed out in the case of the emitter work function, it is far more convenient to use than Figure VI-25.

Finally, the results have been fitted with an algebraic expression

$$\phi_c = 5.38 - 4.625 \, (T_C/T_R) + 1.375 \, (T_C/T_R)^2 \, .$$
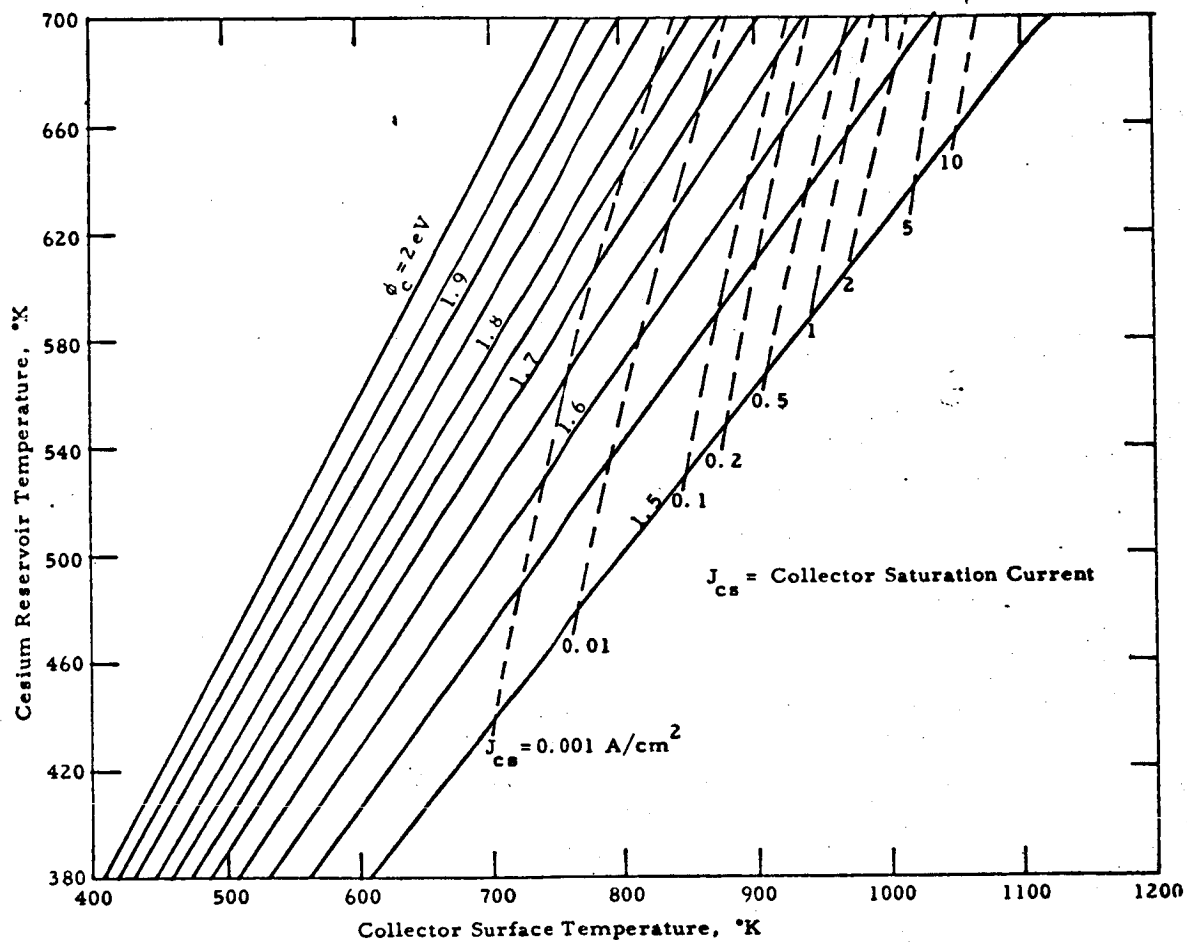
Figure VI-26. Molybdenum Collector Work Function and Saturation Emission as a Function of Surface and Cesium Temperatures.

## CHAPTER VII

## PARAMETRIC DATA

### A. GENERAL

The term parametric data is used here to describe sets of current-voltage characteristics generated through the systematic variation of parameters. In past work[2,3,4] such sets, or families of curves, were generated by keeping all parameters constant except the cesium reservoir temperature. In the present work, families have been generated by using as the variable parameters emitter temperature, spacing, and collector temperature, in addition to cesium reservoir temperature.

In general, the range of variation covered includes the region of interest for power production. Thus the emitter temperature range extends from 1600 to 2050°K, the spacing from 0.2 to 22 mils, the collector temperature from 700 to 1050°K, and the Cs reservoir temperature 540 to 700°K.

The parametric data generated have served two functions. They have furnished a starting point for the analytical work and have provided material with which to check the validity of the mathematical models derived. They have also resulted in a detailed set of design data.

This chapter describes the experimental procedure used in generating these data. Summaries of the results, such as performance maps, are given for each type of experiment as well as typical data. Additional original data are shown in Appendix C.

## B. VARIABLE Cs RESERVOIR TEMPERATURE FAMILIES

The greatest number of families of J-V curves are of this type. The reason for this preference is that the variable $T_R$ family is especially useful for hardware design. The Cs reservoir temperature, $T_R$, is usually the only variable about which the hardware designer has complete freedom of choice. It is, therefore, very convenient for him to have design data available in this form.

The experimental procedure used consisted of selecting emitter temperature, spacing and collector temperature values and then recording J-V curves at 10-15°K intervals of Cs reservoir temperature. The choice of emitter temperature and spacing was arbitrary within the ranges stated above. The collector temperature was chosen at or near the optimum for power generation. Figure VII-1 is a typical family generated by varying the Cs reservoir temperature. The first recorded curve is at $T_R = 575°K$, resulting in current levels considered to be at the lower limit of interest. The last recorded curve at $T_R = 645°K$ is almost vertical and at the upper limit of interest. The family exhibits a property that is very significant in summarizing experimental results obtained in this manner. This property is the existence of an envelope tangent to all curves in the family (the solid line in Figure VII-1). The envelope of the J-V family is also the locus of the maximum current obtainable at any given voltage for the condition under which the family was generated. A dashed line is also shown in Figure VII-1. This dashed line is the envelope (solid line) corrected for the voltage drop along the emitter sleeve. It represents the output at the electrodes. The correction necessary is 3 mV/ampere.
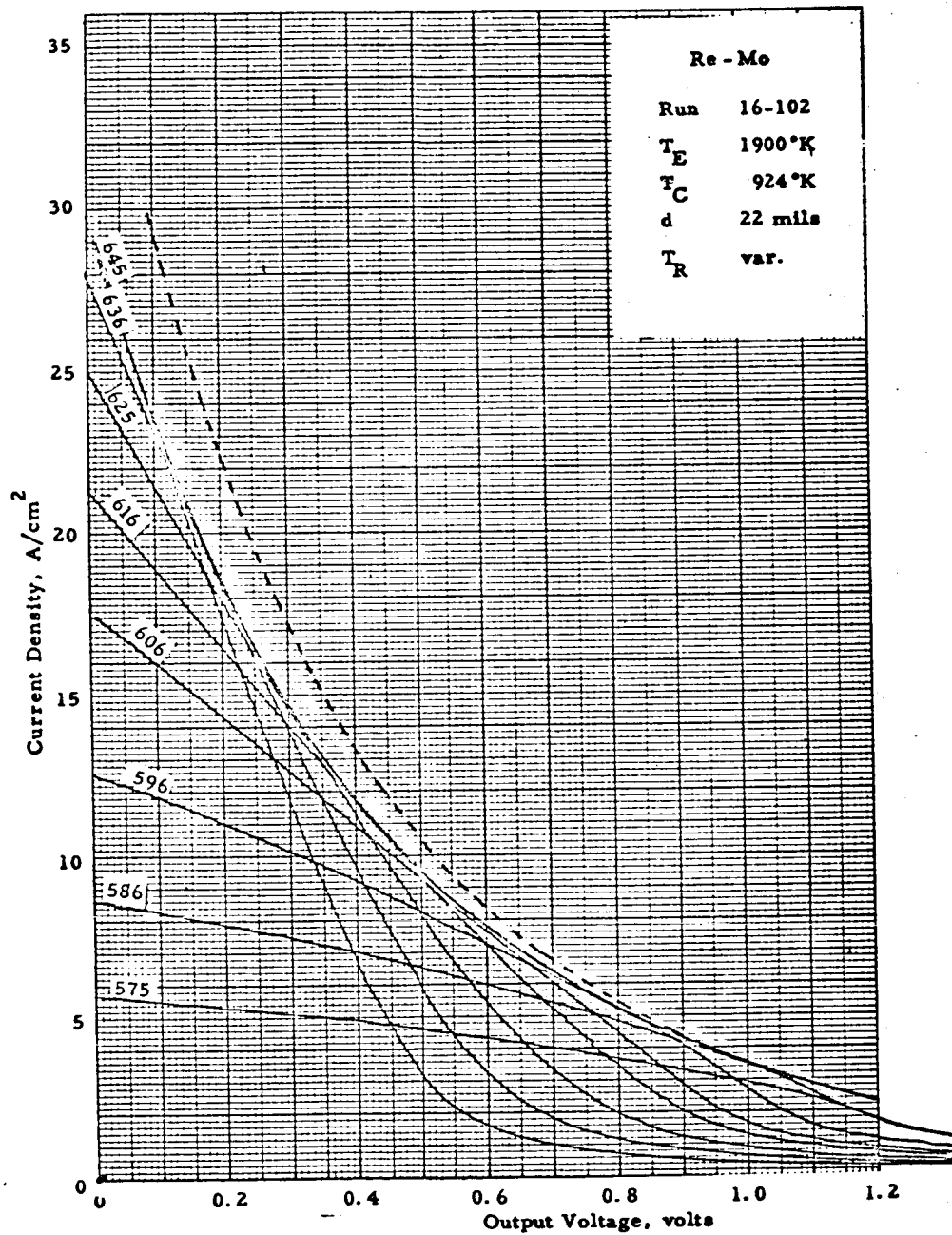
Figure VII-1.  A Typical Family of Current-Voltage Curves.

The actual system used in generating the $T_R$ families consisted of obtaining a family for each combination of a given emitter temperature with six selected spacing values and repeating this procedure for each emitter temperature. All families obtained in this manner are shown in Appendix C. The envelopes for all spacings at each emitter temperature are shown superimposed in Figures VII-2 to VII-7. Inspection of Figures VII-2 to VII-7 will reveal that the envelopes corresponding to families generated at different spacings intersect, especially at the lower emitter temperatures. This fact leads to the conclusion that a new envelope can be drawn which represents the maximum current obtainable at a given voltage and emitter temperature after the cesium reservoir temperature and interelectrode spacing have been fully optimized. A series of such envelopes, one for each emitter temperature, are shown in Figure VII-8. This figure represents the maximum performance map for the electrode materials under test. It should be pointed out, however, that a considerable portion of the envelopes of Figure VII-8 has been contributed by the minimum-spacing families. This is especially true of the lower-voltage, higher-current portion of the envelopes. The implication here is that, had the device been capable of achieving spacings smaller than 0.2 - 0.5 mil, even higher performance levels could have been obtained. Although such data would be of considerable analytical interest, it is doubtful that they would be of any practical value.

The power map corresponding to the maximum performance map of Figure VII-8 is shown in Figure VII-9. This map shows the maximum power that could be obtained at the various temperature levels after optimizing the Cs reservoir temperature and interelectrode spacing,
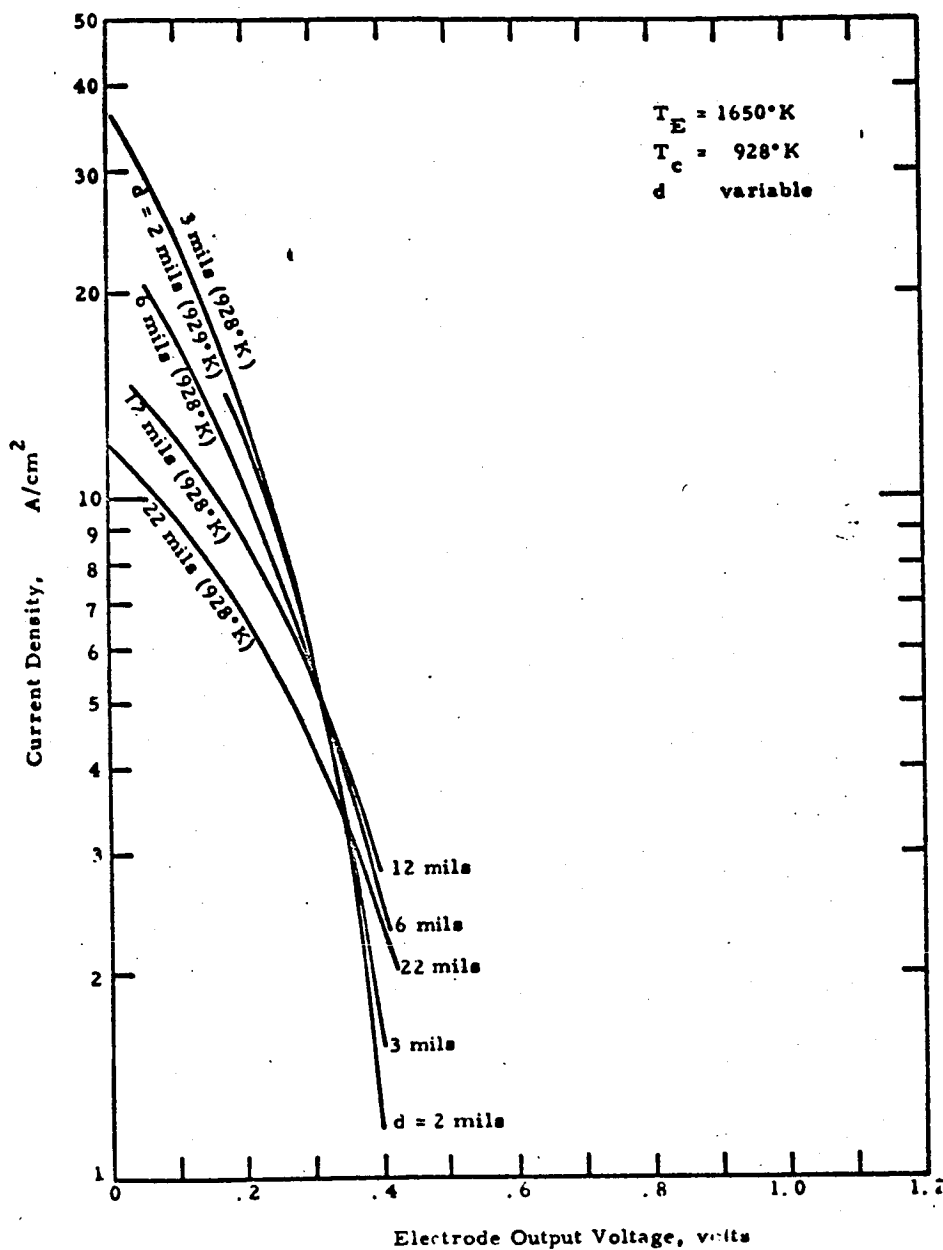
Figure VII-2. Envelopes at $T_E = 1650°K$ and Several Spacings.

*190*
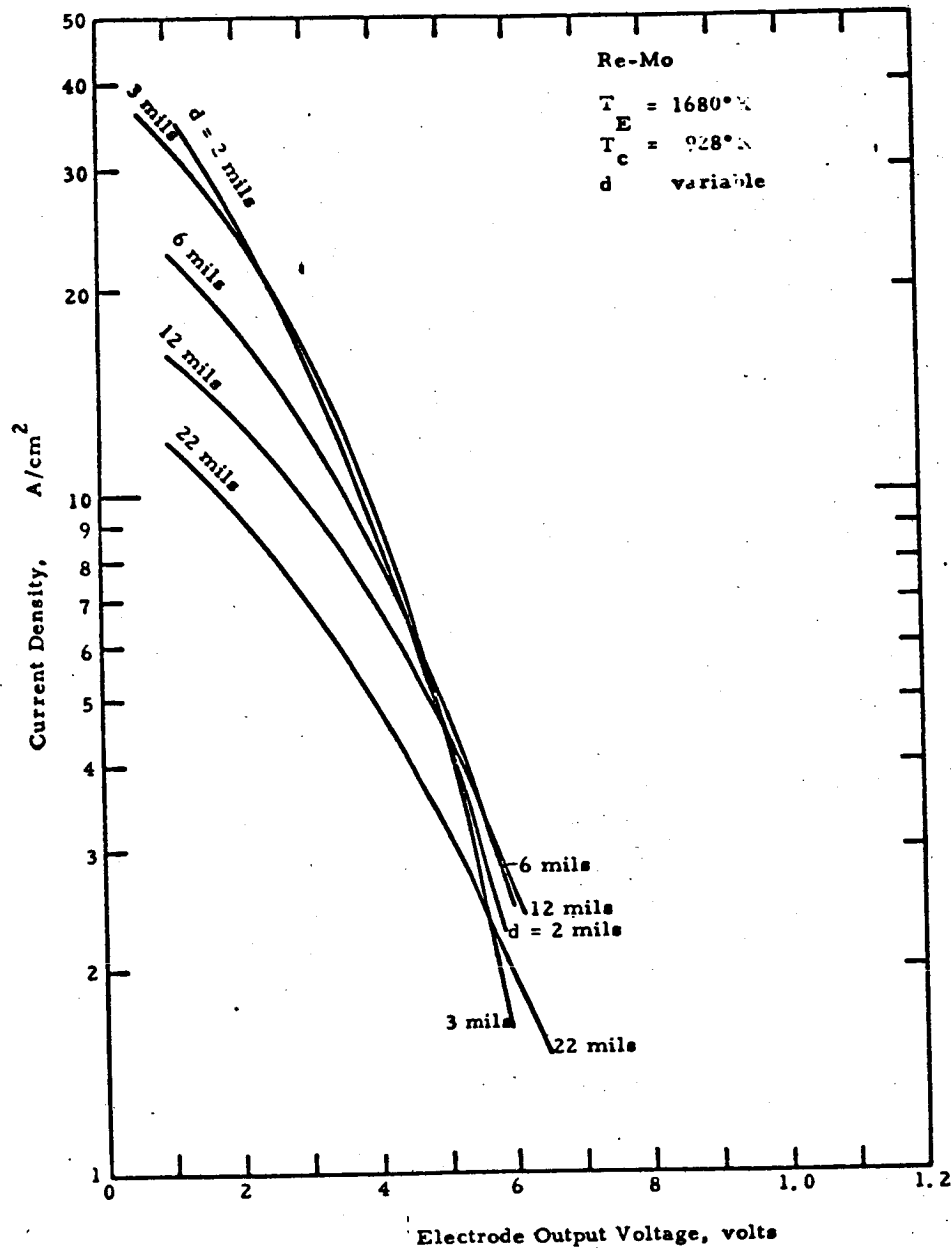
Figure VII-3. Envelopes at $T_E = 1680\,°K$ and Several Spacings.

65-R-7-52

Re-Mo

$T_E = 1750°K$

$T_C = 928°K$

d    variable
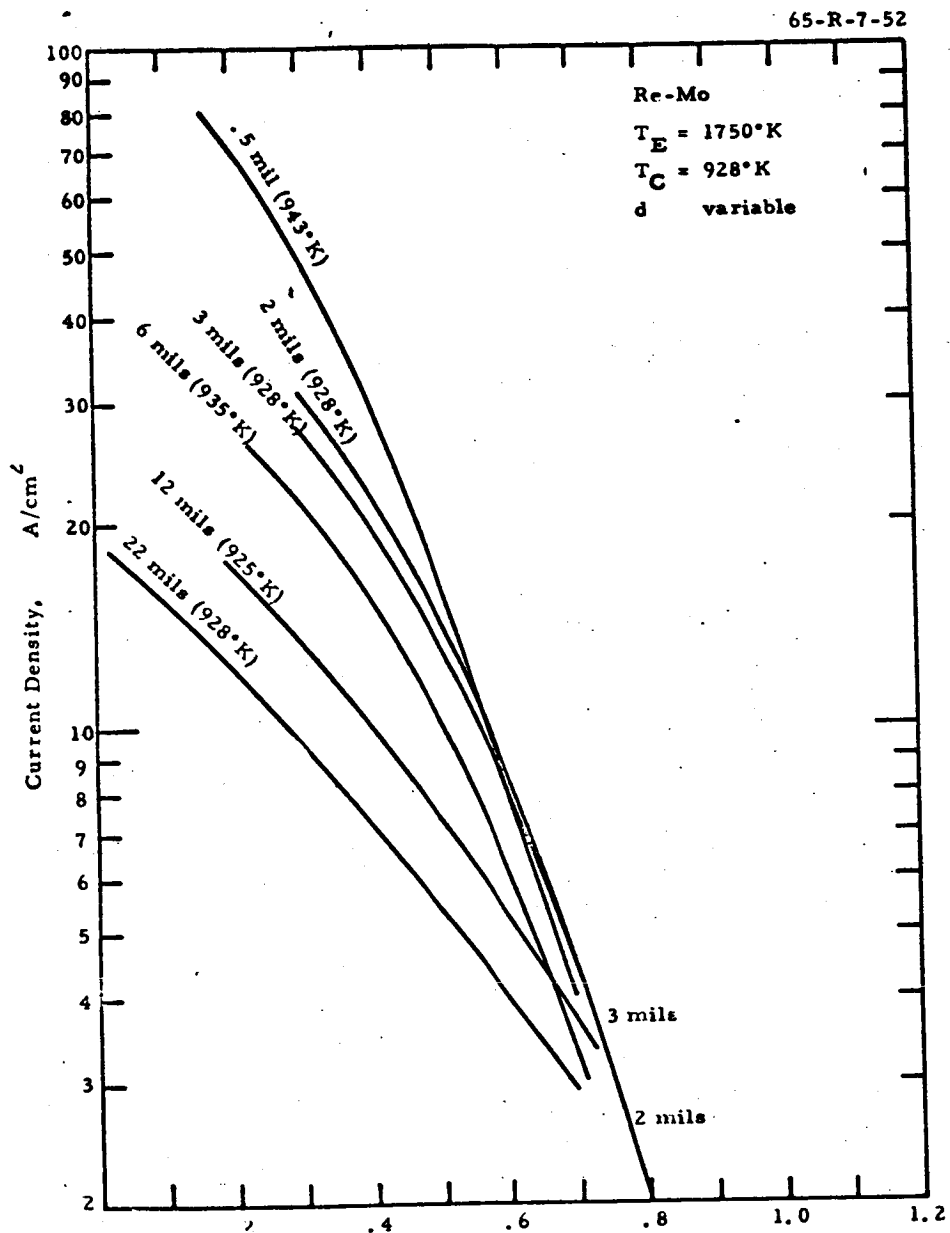
Figure VII-4.   Envelopes at $T_E = 1750°K$ and Several Spacings.
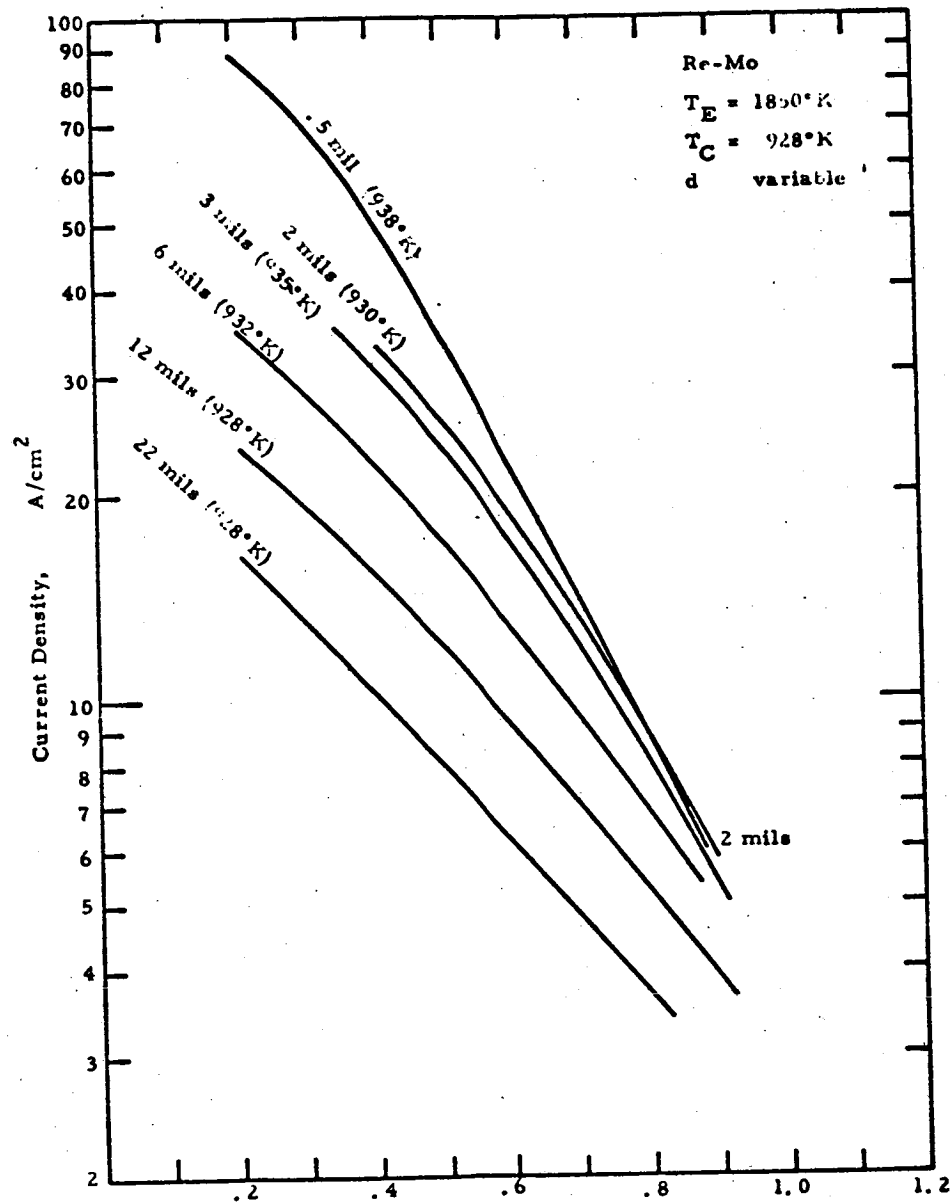
Figure VII-5. Envelopes at $T_E = 1850\,°K$ and Several Spacings.

193
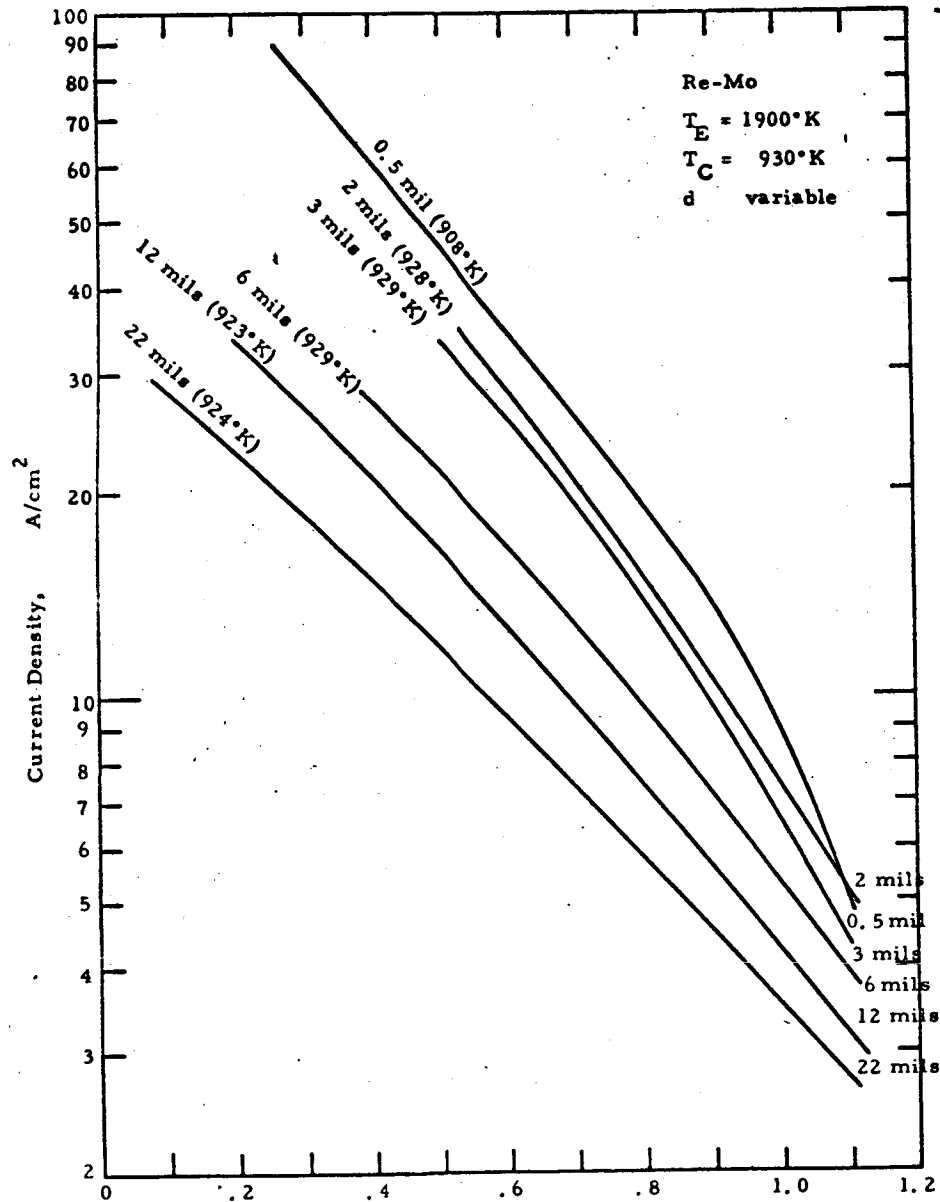
Figure VII-6. Envelopes at $T_E = 1900\,°K$ and Several Spacings
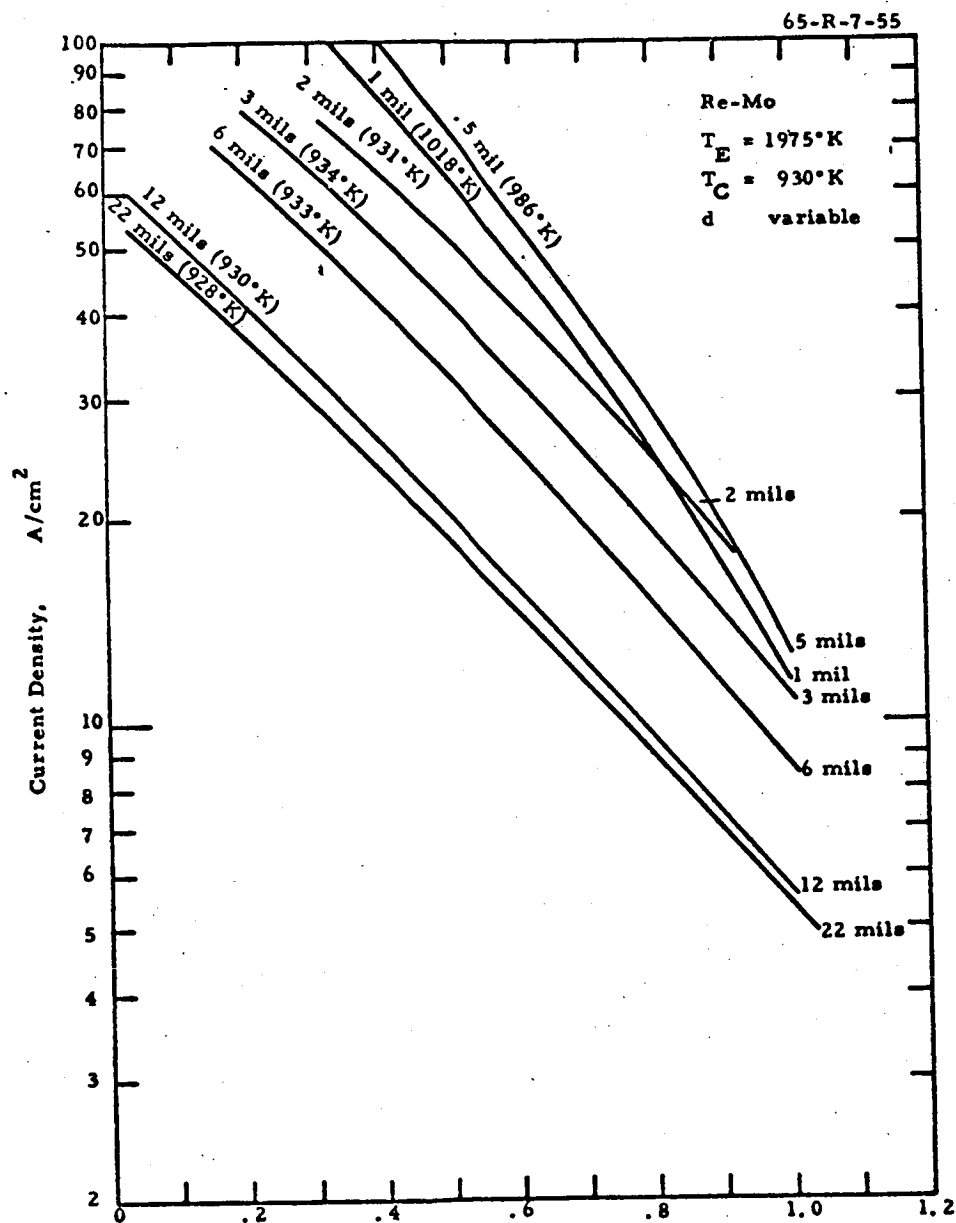
Figure VII-7.   Envelopes at $T_E = 1975°K$ and Several Spacings.
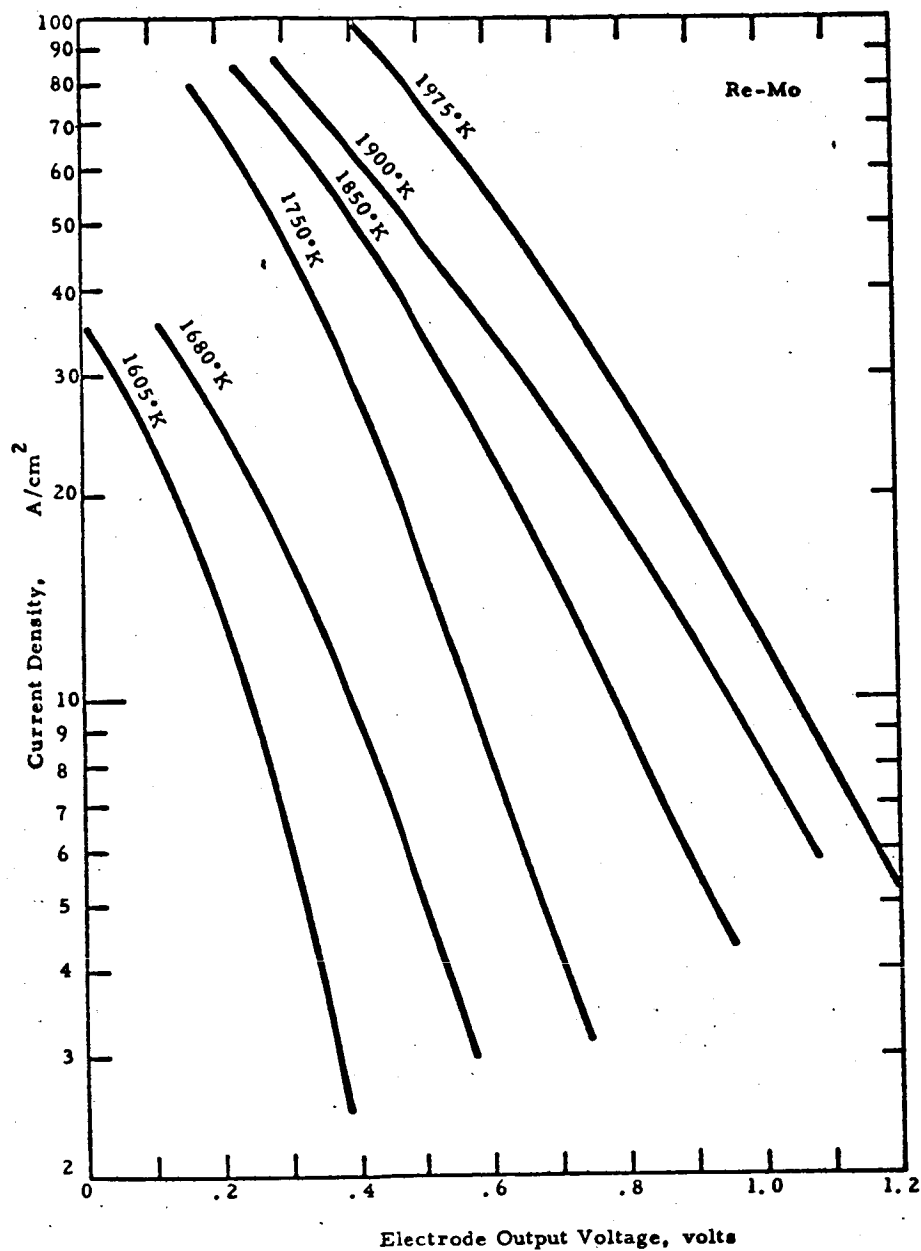
Figure VII-8.   Fully Optimized Envelopes at Various Emitter Temperatures.
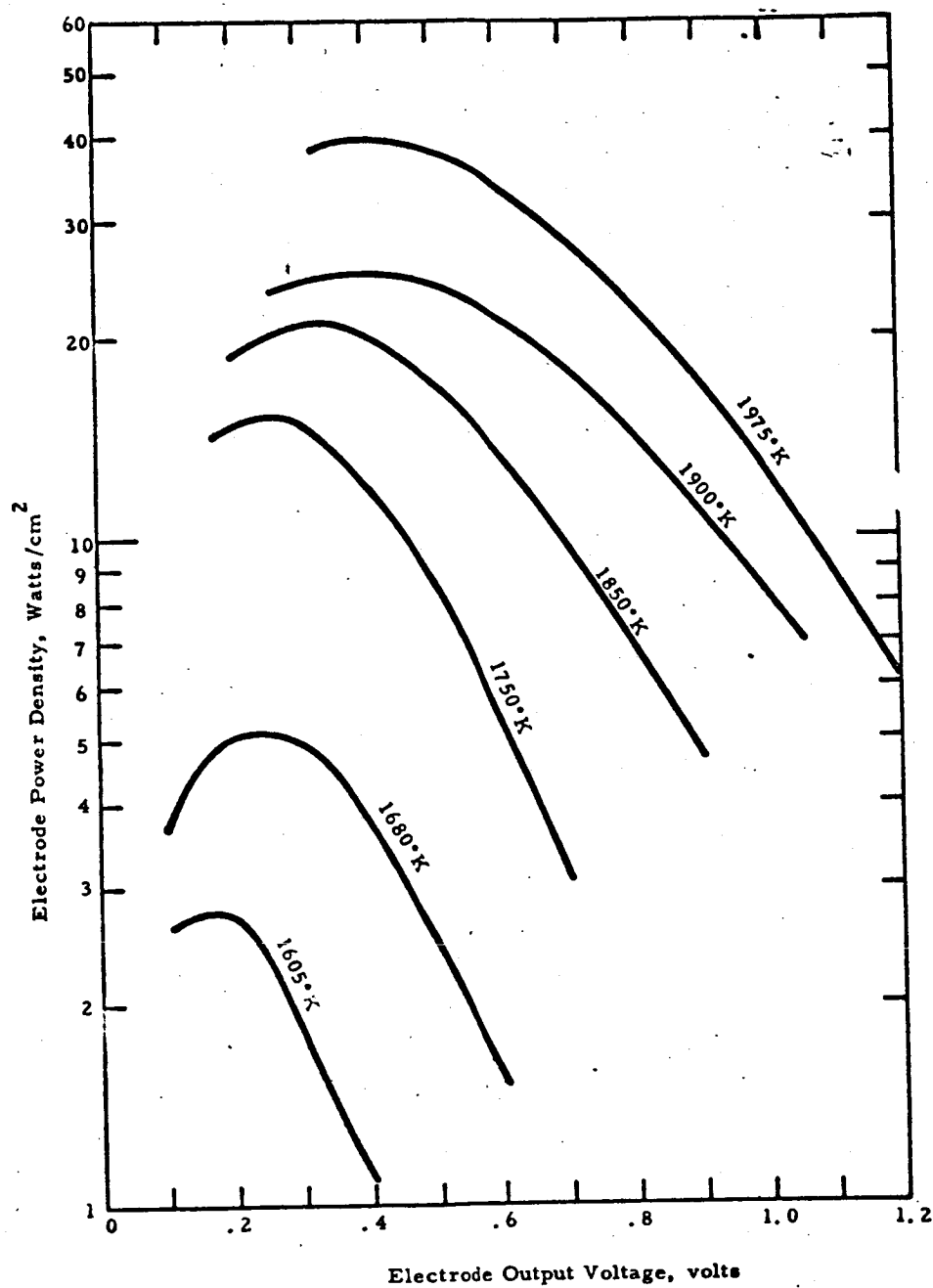
Figure VII-9.  Electrode Power Output Corresponding to
Fully Optimized Envelopes.

197

again subject to the limitation of a minimum spacing value of 0.2 to 0.5 mil.

## C.    VARIABLE-SPACING FAMILIES

This type of experimental result is particularly suited to analytical work and has, in fact, formed the foundation of that work in this program.   The analytical value of the variable-spacing family derives from the fact that, when spacing is changed, all other parameters remain constant.   To illustrate this point, consider a change in Cs reservoir temperature.   Such a change results in changes in both electrode work functions, which affect output voltage, and the emission level, which affects output current.   Similarly, a change in emitter temperature would result in both current and voltage changes.   On the other hand, changes in spacing do not affect the electrode work functions nor the emission.   Their sole effect is to alter the "thickness" of the plasma.

The experimental procedure used to generate these families was to set all parameters at selected values and reach equilibrium at some small value of spacing (approximately 1-2 mils).   The spacing was reduced until the emitter shorted to the collector, and was then increased by an amount just enough to avoid shorting.   The interelectrode spacing under these circumstances is estimated to be between 0.2 and 0.5 mil.   At that point the first J-V curve was recorded.   The spacing was then varied in a geometric progression and a J-V curve recorded at each value of spacing.   The actual values used were 0.5, 1, 2, 4, 8, 16 and 32 mils.

A typical family is shown in Figure VII-10.   In qualitative terms, the following observations can be made:

198
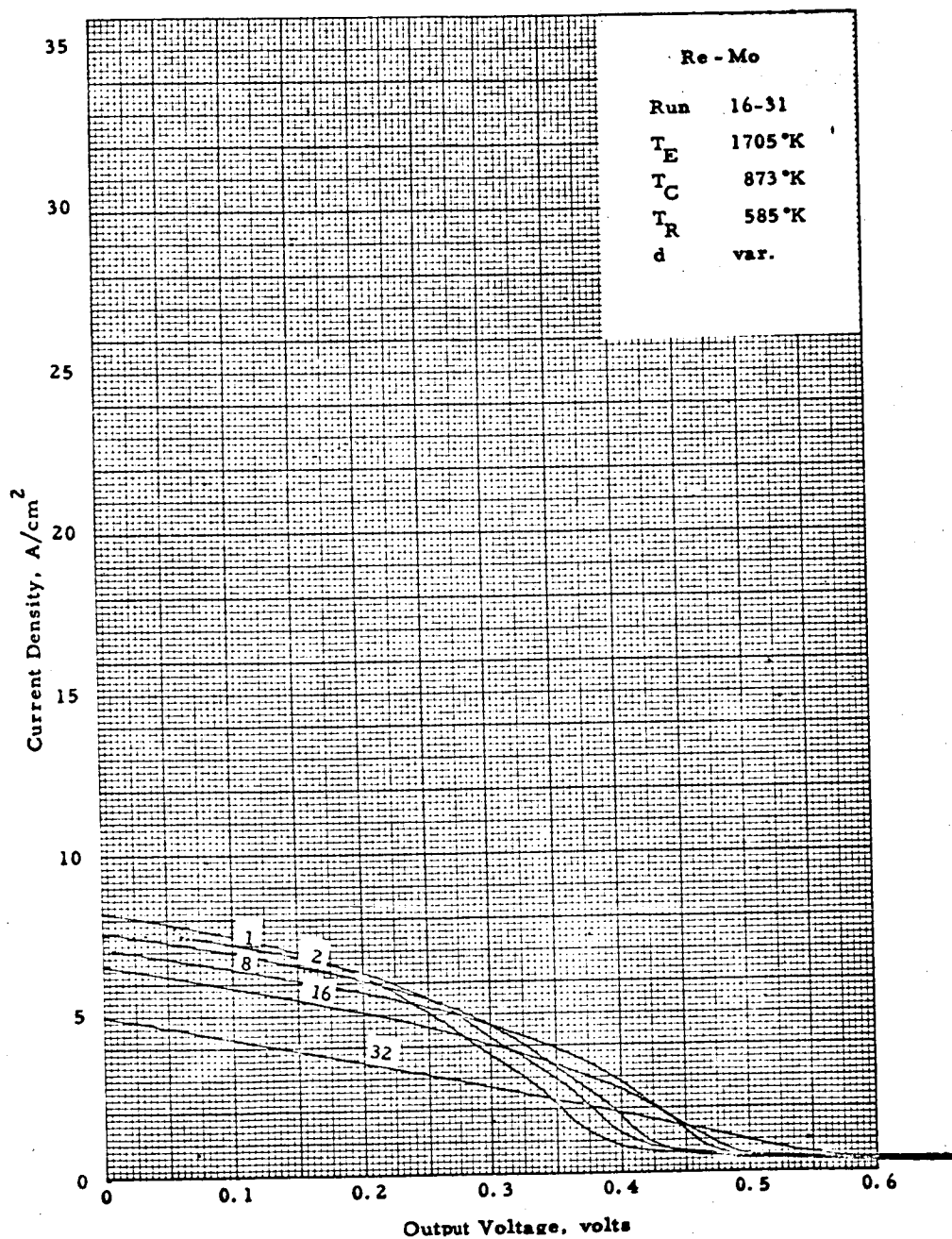
Figure VII-10. A Typical Variable-Spacing Family Showing
Overlap of J-V Curves.

199

a)   As spacing is reduced the current is increasing in the
"saturation-like" portion of the characteristic.   This behavior
is due to the reduced scattering at smaller spacing.

b)   The voltage increases in the exponential portion of the char-
acteristic as spacing is reduced in some of the families,
such as in the case of Figure VII-11.   In other families the
J-V curves intersect, such as in Figure VII-10.   The reasons
for this behavior will be discussed in detail in Chapter IX.
Suffice it to say, at this point, that in the former case the
optimum spacing is smaller than the 0.5 mil, the smallest
value recorded.   In the latter case it is greater than 0.5.
It is evident that an optimum spacing exists for each output
voltage value.   In Figure VII-10, for example, the 0.5-mil
curve shows the highest current values for voltages between
0 and 0.18.   The 1-mil curve shows the highest currents
between 0.18 and 0.26 volt, the 2-mil line between 0.26 and
0.30, and so on at higher voltages.

The original data of this type is shown in Appendix C.

D.   VARIABLE-EMITTER-TEMPERATURE FAMILIES

Changes in emitter temperature result in changes in the emitter
work function.   In the range of emitter work function which is of interest
for power production (2-3 eV) the change in work function is linear with
emitter temperature for constant Cs pressure.   This proportionality
of work function to emitter temperature implies that the branch of the
J-V curve at voltages higher than the "knee" will be translated to higher

| Re - Mo | |
|---|---|
| Run | 16-10 |
| $T_E$ | 1995 °K |
| $T_C$ | 973 °K |
| $T_R$ | 633 °K |
| d | var. |
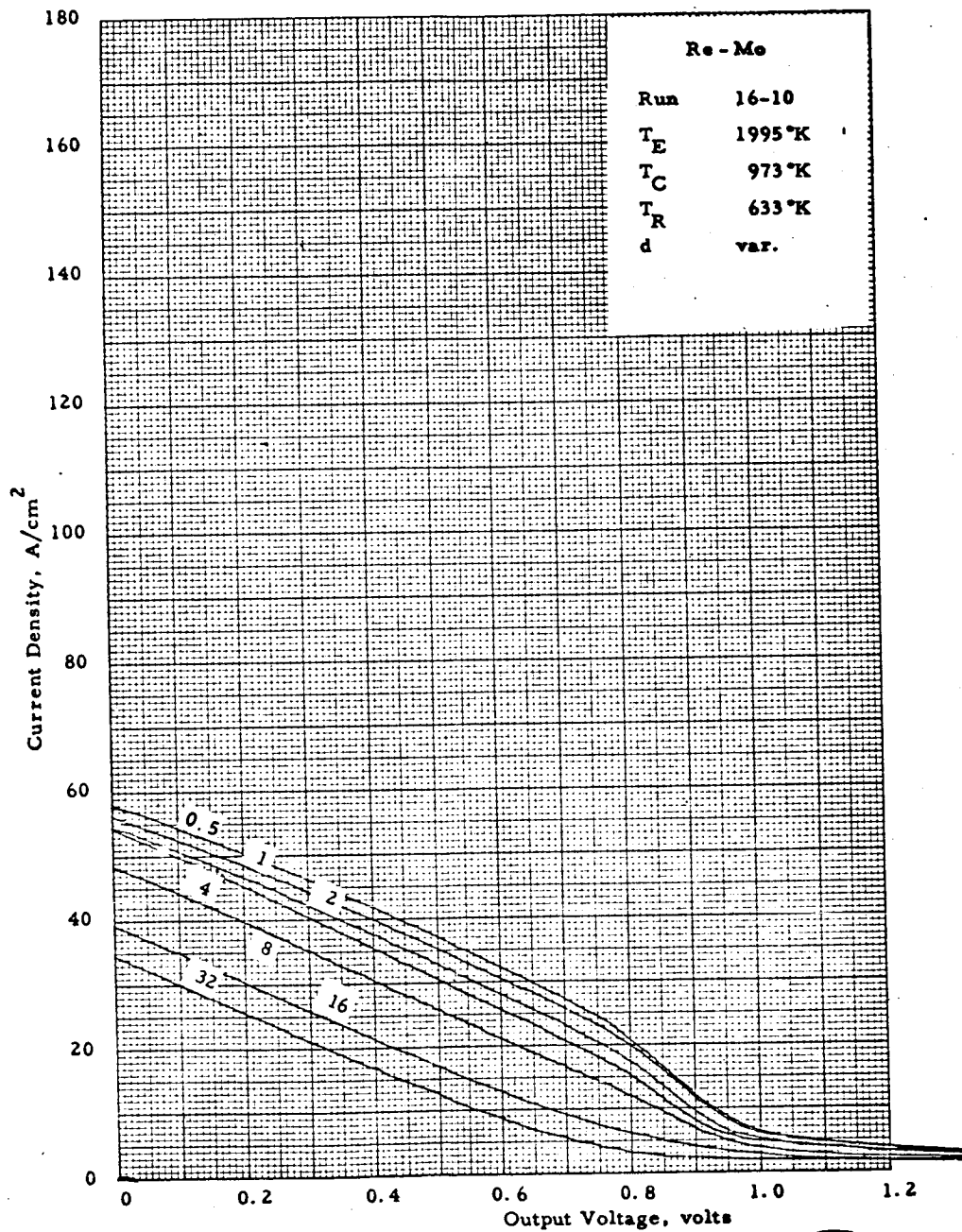
Figure VII-11.  A Typical Variable-Spacing Family Without Overlap of J-V Curves.

voltages as the emitter temperature is increased. Note that the internal voltage drop ($V_d$) will not change since it is a function of the pressure-spacing product (Pd) only. The collector work function will not change either, since it is a function of collector temperature and Cs pressure. Thus, voltage changes will be a direct reflection of emitter work function changes. The saturatiation current of the emitter will be affected both by the change in temperature and by the change in work function. The net result can be seen in Figure VI-10 of Chapter VI to be a decrease of saturation current with increasing emitter temperature at constant reservoir temperature. Thus, the "saturation-like" portion of the J-V curve will move to higher current with decreasing temperature. The combined effect of these current and voltage changes is that J-V curves belonging to a family generated by varying the emitter temperature intersect each other, each curve exhibiting the highest current for a given voltage. Figure VII-12 shows this effect.

The experimental procedure used in generating these families was the following: Starting with a low emitter temperature (about 1600°K), the desired values of cesium reservoir temperature, interelectrode spacing and collector temperature were set. The first J-V curve was then recorded. The heat input to the emitter was then changed to a higher level, and equilibrium was established at a new emitter temperature. The values of the remaining parameters were checked to establish that no change had taken place. The second J-V curve was then recorded. After a certain amount of trial and error the amount of change in heat input necessary for a 75°K change in emitter temperature could be estimated. Approximately 75°K intervals were used for
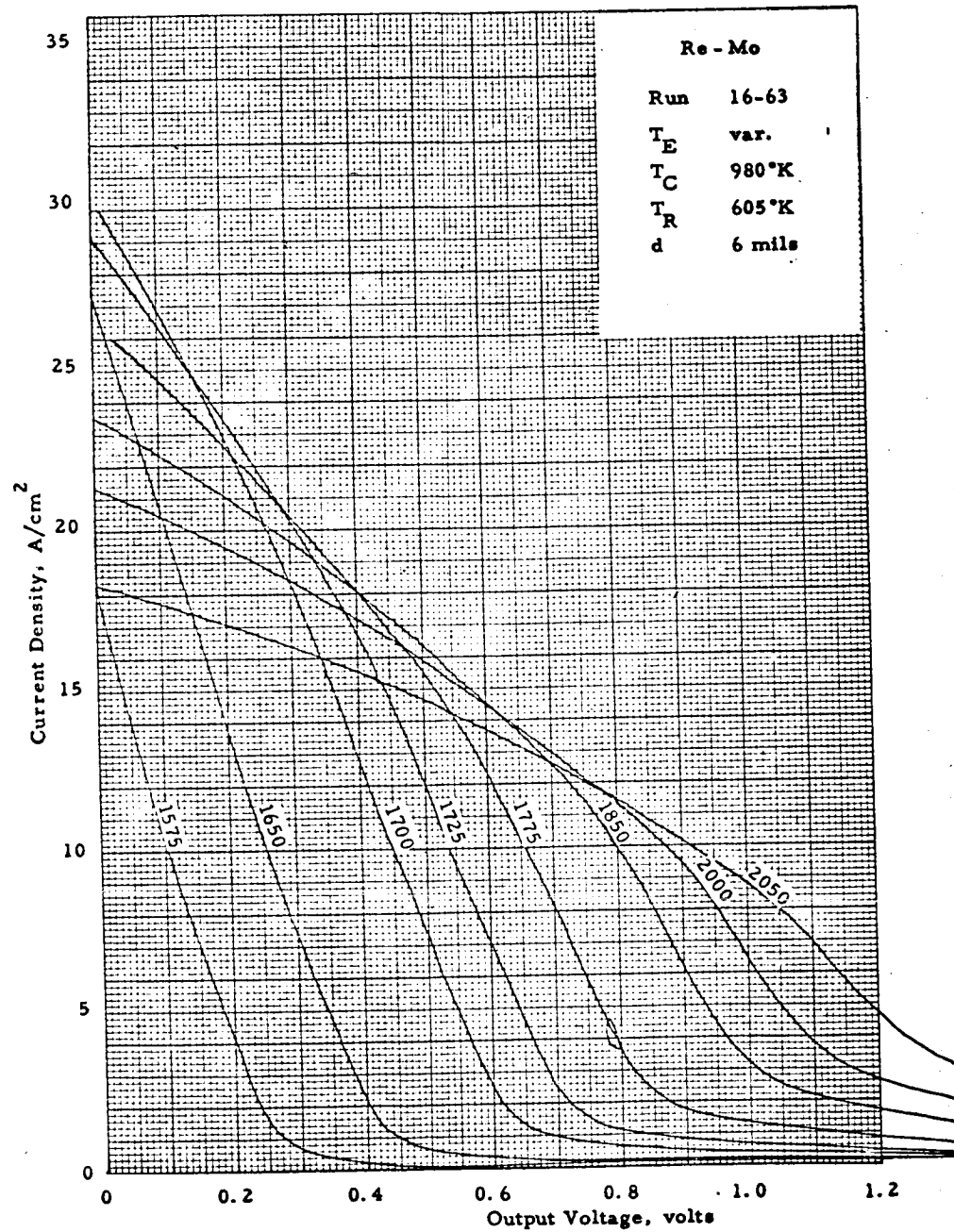
Figure VII-12.   A Typical Variable-Emitter-Temperature Family.

all the variable-emitter-temperature families. The process described above was repeated until an emitter temperature of about 2000°K was reached. A new family was then started. The range of spacing covered was 2 to 22 mils. The range of cesium reservoir temperature covered was 543 to 635°K.

The consistency of these parametric data with the rest is discussed in section G. All original data are shown in Appendix C.

E.    EFFECT OF COLLECTOR TEMPERATURE VARIATION

The effect of collector temperature variation is probably the least well documented aspect of converter performance. For this reason, special attention was given to the documentation and correlation of this variable in the course of the present work. The first step in this effort was the study of the molybdenum collector surface work function through retarding plots and back emission measurements. Those results are presented and discussed in Chapter VI.

The work discussed in this section aimed at relating performance data to the work function dependence derived in Chapter VI. The first step in that attempt consisted of generating families of curves with collector temperature as the variable parameter. Previous experience had shown that an optimum collector temperature existed, and it was planned to vary the collector temperature through this optimum.

The families of curves were generated by varying the collector temperature from about 770 to 1020°K and recording J-V curves at 50°K intervals of collector temperature. The emitter temperature was varied from 1575 to 1875°K and cesium reservoir temperature from 543 to 623°K. Interelectrode spacing settings of 4 and 16 mils were used.

VII-19

204

Figure VII-13 is typical of the families generated. The J-V curve corresponding to the lowest collector temperature recorded (773°K) is below the others at all voltages. As the collector temperature is increased the curves move to higher voltage and begin to intersect each other. The result is that, for every current level, the maximum voltage is obtained at a different collector temperature. Strictly speaking, therefore, before an optimum collector temperature can be defined for even a single J-V curve (at specified $T_E$, $T_R$, d) the current or voltage has to be specified.

To investigate this dependence of optimum collector temperature on current level, Table VII-1 was constructed from the available variable-collector families. The first four columns list the run number, emitter temperature, reservoir temperature, and spacing, respectively. The next two columns list a collector temperature and current density. The collector temperature is that which resulted in the highest voltage at the corresponding current density. Since the variation of collector temperature was incremental, each J-V curve gave the highest voltage over a range of current density. The current density noted in Table VII-I was taken at the middle of this range. The last column in the Table shows the ratio of collector to reservoir temperature. The only dependence found among the parameters was between current density and $T_C/T_R$. No dependence was found on emitter temperature or spacing. This result is shown in Figure VII-14.

Further attempts at matching the displacement of the J-V curves due to collector temperature changes with the collector work function results of Chapter VI gave erratic results. To resolve these inconsistencies the following experiment was devised: The output voltage at
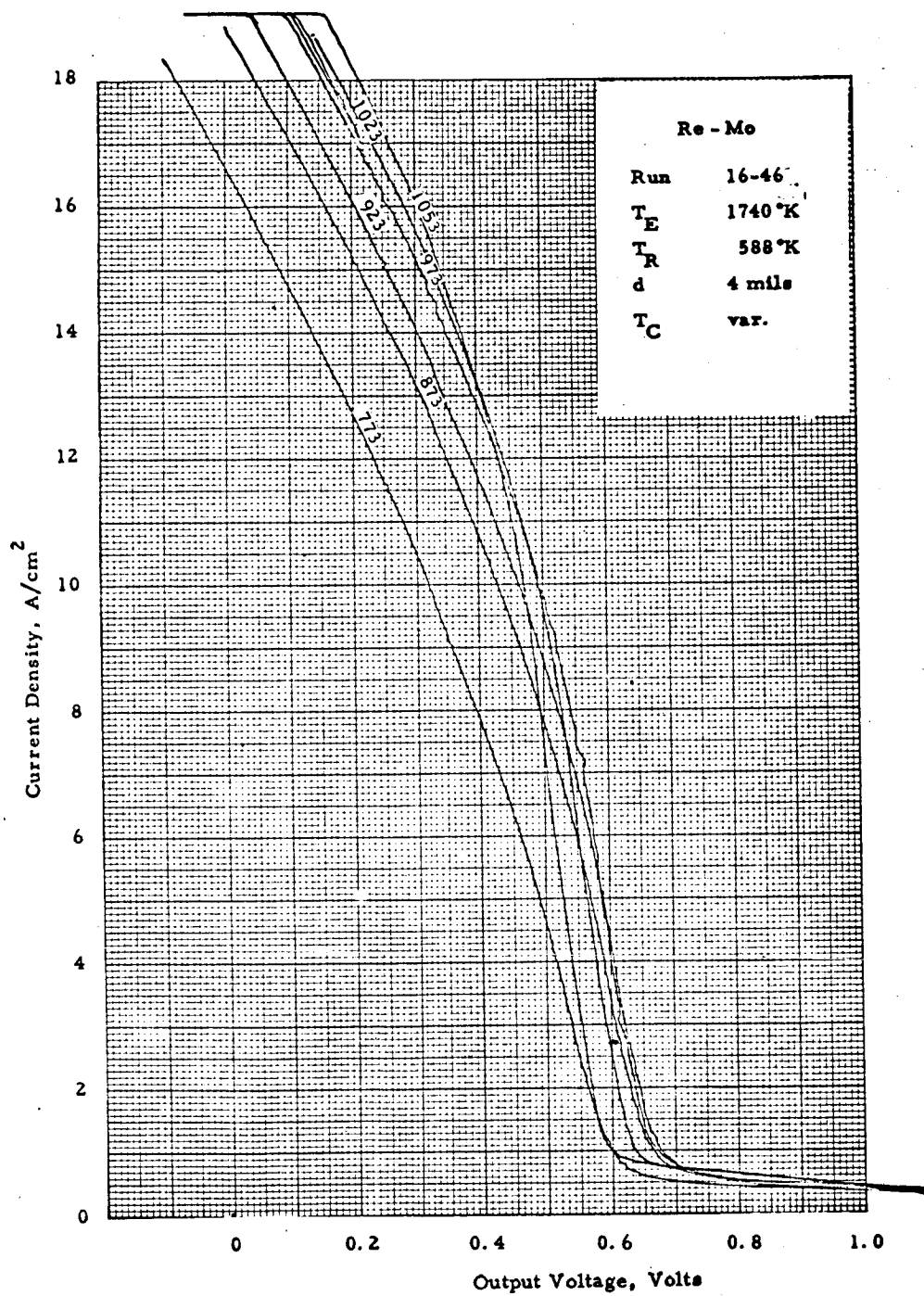
Figure VII-13. A Typical Variable-Collector-Temperature Family.

206

## TABLE VII-1

### VARIABLE-COLLECTOR-TEMPERATURE RUNS

| Run | $T_E$ °K | $T_R$ °K | d mils | $T_C$ °K | $J_s$ Amps/Cm$^2$ | $T_C/T_R$ |
|-----|----------|----------|--------|----------|---------|-----------|
| 46 | 1740 | 588 | 4 | 1053 | 18 | 1.79 |
|    |      |     |   | 1023 | 12 | 1.74 |
|    |      |     |   | 973  | 8  | 1.66 |
|    |      |     |   | 923  | 2  | 1.57 |
| 48 | 1750 | 559 | 4 | 973  | 6  | 1.71 |
|    |      |     |   | 923  | 2  | 1.65 |
| 49 | 1875 | 584 | 4 | 973  | 4  | 1.665 |
| 53 | 1850 | 605 | 16 | 1068 | 18 | 1.77 |
|    |      |     |   | 1027 | 6  | 1.70 |
|    |      |     |   | 979  | 2  | 1.62 |
| 54 | 1875 | 583 | 16 | 999  | 5  | 1.71 |
|    |      |     |   | 1073 | 14 | 1.84 |
| 37 | 1625 | 573 | 4 | 1023 | 14 | 1.79 |
|    |      |     |   | 973  | 8  | 1.70 |
|    |      |     |   | 923  | 2  | 1.61 |
| 38 | 1625 | 573 | 16 | 923  | 2  | 1.61 |
|    |      |     |   | 973  | 10 | 1.70 |
| 39 | 1575 | 558 | 4 | 923  | 6  | 1.65 |
|    |      |     |   | 873  | 1.5 | 1.57 |
| 41 | 1625 | 543 | 16 | 873  | 2  | 1.61 |
|    |      |     |   | 923  | 5  | 1.70 |
| 42 | 1575 | 558 | 16 | 973  | 8  | 1.74 |
|    |      |     |   | 923  | 5  | 1.65 |
|    |      |     |   | 873  | 2  | 1.57 |
| 45 | 1740 | 588 | 16 | 1053 | 14 | 1.79 |
|    |      |     |   | 1023 | 10 | 1.74 |
|    |      |     |   | 973  | 4  | 1.65 |

207
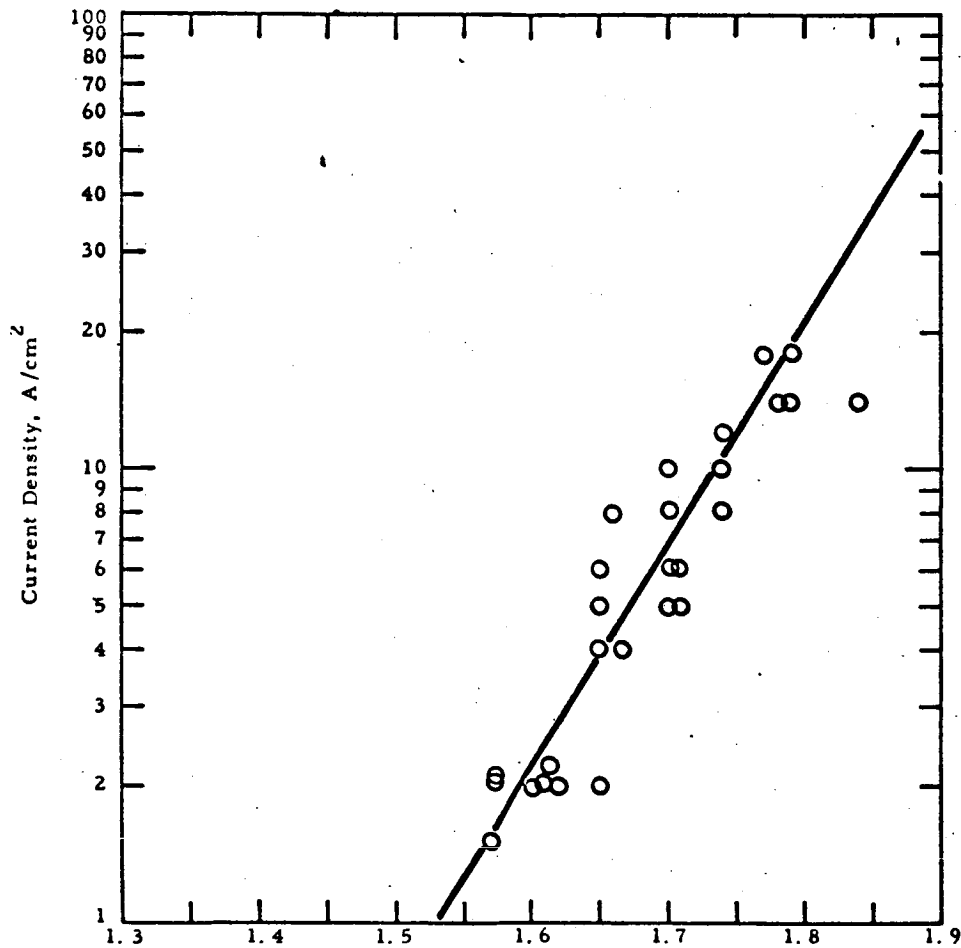
Figure VII-14. Optimum $T_C/T_R$ Ratio as a Function of Current Density.

a fixed current value was plotted as a function of collector temperature, all other parameters being constant. This procedure can be illustrated by inspection of Figure VII-15. A J-V curve is shown schematically in this figure, and three points are identified on it. The starting conditions of the experiment consisted of setting $T_C$ at a high enough value so that the output voltage at current $J_1$ had gone through a maximum. A constant-current power supply was used as the diode load so that the output current throughout the run was kept at the value $J_1$. The voltage $V_1$ was recorded on the Y-axis of an X-Y plotter. The output of the collector thermocouple was connected to the X axis of the X-Y plotter. Thus, a direct plot of output voltage versus collector temperature was generated. Figure VII-16 is a typical run. The run started at a collector temperature of 1007° K and an output voltage of 0.63 volt. As the collector temperature was reduced, a maximum output voltage of 0.72 volt was reached at a collector temperature of 839° K. Further decrease in collector temperature resulted in a decrease in output voltage. Finally the collector temperature became equal to the Cs reservoir temperature at 560° K and an output voltage of .37 volt. At that point a sharp break occurred in the curve since the Cs temperature was no longer constant; the run was terminated here. The procedure was then repeated at the next two higher current levels ($J_2$ and $J_3$ in Figure VII-15). Such runs were taken at emitter temperatures of 1750 and 1850° K, spacings of 2, 4, 10 and 20 mils, Cs reservoir temperatures of 553, 573, 593, and .613° K, and current densities of 2.5, 5 and 15 amperes per $cm^2$.

The variation in voltage of Figure VII-16 is the result of the change in collector work function brought about by the change in collector temperature. A change in collector work function can affect the

209
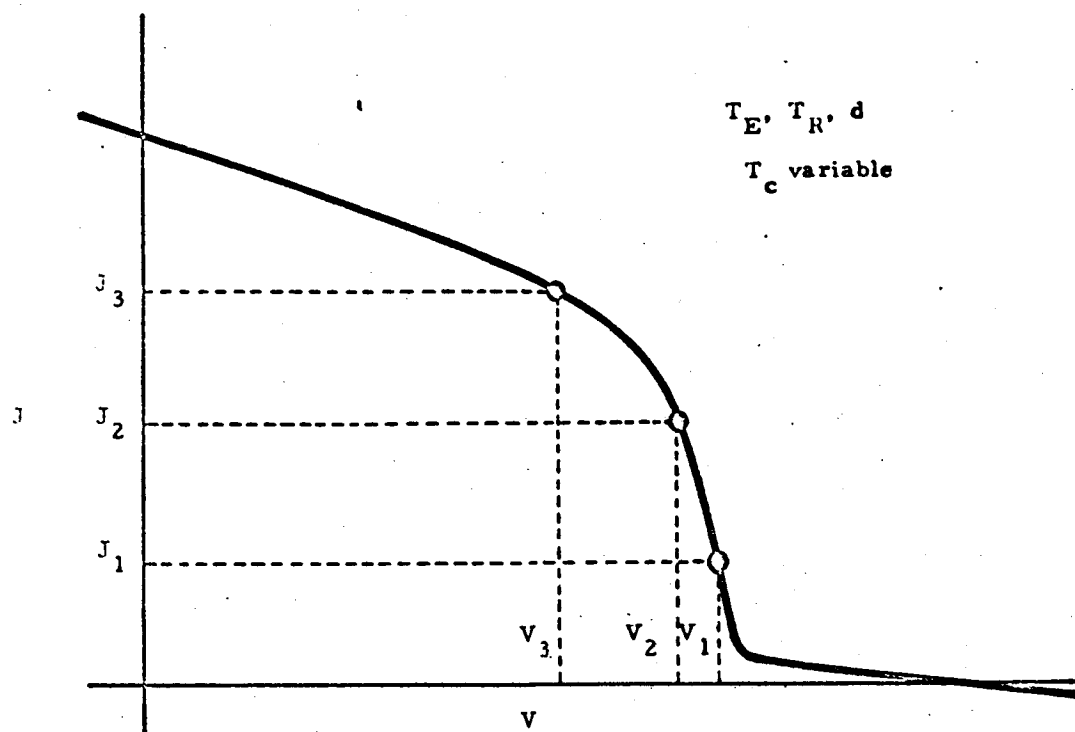
Figure VII-15. Schematic of Static Measurement Points on J-V Curve.

THERMO ELECTRON
ENGINEERING CORPORATION
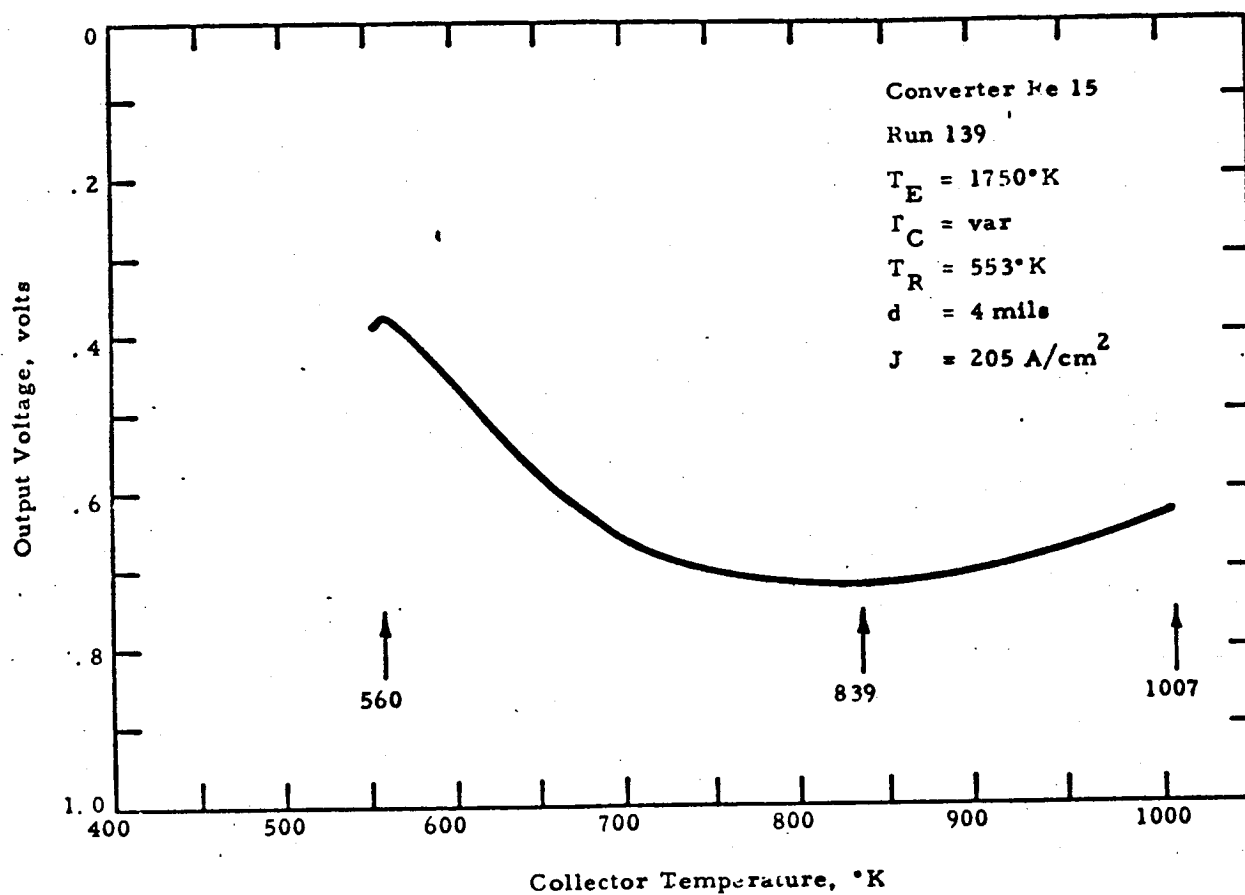


Figure VII-16.  A Typical Run Illustrating the Dependence of
Output Voltage on Collector Temperature.

performance of the converter in two ways. First, the output voltage
changes in the following sense:

$$\Delta V = -\Delta \phi_C$$

Second, the electron emission from the collector changes. The effect
of this second change is not clearly understood. Nevertheless, if the
level of back emission is negligibly small, then one can assume that
only the effect of the collector work function on voltage is present.
This is indeed the case in the neighborhood of $T_C/T_R = 1$. This assump-
tion leads to the conclusion that changes in voltage reflect changes in
collector work function. The effect of back emission then can be investi-
gated by replotting the curve of Figure VII-16 in terms of V versus
$T_C/T_R$ and comparing it to the plot of $\phi_C$ versus $T_C/T_R$ by matching
the two plots at $T_C/T_R = 1$. Figure VII-21 was constructed using this
procedure as outlined below.

Table VII-2 is a tabulation of all the runs generated. The run
number and conditions of each run are indicated and the change in
voltage from the break point in the V-versus-$T_C$ curve ($T_C/T_R = 1$)
to the maximum voltage point is noted as $\Delta V_m$. Inspection of Table
VII-2 reveals a small dependence of $\Delta V_m$ on J; $\Delta V_m$ increasing with
increasing J in runs which differ only in the value of J used. However,
there are inconsistencies in this trend, and it appears that the experi-
mental error obscures this dependence. The only strong dependence is
that of $\Delta V_m$ on $T_R$. This observation prompted the plotting of all
curves having a common Cs reservoir temperature on a single plot.
The coordinates used were 2.09 - $\Delta V$ and $T_C/T_R$. The 2.09 - $\Delta V$
coordinate was used so that the output voltage and collector work
function curves would coincide at $T_C/T_R = 1$. Four such plots were

## TABLE VII-2

### TABULATION OF RUNS 93 - 146

| Run | $T_E$ °K | $T_R$ °K | J A/cm$^2$ | d mils | $\Delta V_m$ volts |
|---|---|---|---|---|---|
| 15- 93 | 1755 | 593 | 5 | 4 | .49 |
| 94 | 1755 | 593 | 3 | 4 | .42 |
| 95 | 1755 | 593 | 2 | 4 | .46 |
| 96 | 1750 | 593 | 10 | 4 | .52 |
| 97 | 1725 | 613 | 10 | 4 | .76 |
| 98 | 1750 | 613 | 5 | 4 | .76 |
| 99 | 1725 | 613 | 15 | 4 | .70 |
| 100 | 1825 | 613 | 10 | 4 | .63 |
| 101 | 1855 | 613 | 2.5 | 4 | .75 |
| 102 | 1850 | 613 | 5 | 4 | .77 |
| 103 | 1840 | 593 | 2.5 | 4 | .50 |
| 104 | 1830 | 593 | 5 | 4 | .52 |
| 105 | 1820 | 593 | 10 | 4 | .54 |
| 106 | 1855 | 593 | 2.5 | 2 | .51 |
| 107 | 1830 | 593 | 5 | 2 | .51 |
| 108 | 1825 | 593 | 10 | 2 | .51 |
| 109 | 1815 | 593 | 10 | 4 | .53 |
| 110 | 1845 | 593 | 5 | 4 | .51 |
| 111 | 1840 | 593 | 2.5 | 4 | .51 |
| 112 | 1830 | 593 | 2.5 | 10 | .52 |
| 113 | 1830 | 593 | 5 | 10 | .55 |
| 115 | 1825 | 593 | 10 | 20 | .48 |
| 117 | 1825 | 593 | 2.5 | 20 | .60 |

213

TABLE VII-2 (CONT'D)

TABULATION OF RUNS 93 - 146

| Run | $T_E$ °K | $T_R$ °K | J A/cm$^2$ | d mils | $\Delta V_m$ volts |
|---|---|---|---|---|---|
| 15-119 | 1835 | 573 | 5 | 2 | .35 |
| 120 | 1835 | 573 | 2.5 | 2 | .40 |
| 121 | 1835 | 573 | 2.5 | 4 | .38 |
| 122 | 1845 | 573 | 5 | 4 | .43 |
| 123 | 1835 | 573 | 5 | 2 | .38 |
| 125 | 1835 | 573 | 2.5 | 10 | .36 |
| 126 | 1840 | 573 | 2.5 | 20 | .40 |
| 134 | 1760 | 553 | 2.5 | 2 | .36 |
| 135 | 1750 | 553 | 5 | 2 | .36 |
| 136 | 1750 | 553 | 5 | 2 | .37 |
| 137 | 1750 | 553 | 5 | 2 | .30 |
| 138 | 1750 | 553 | 7.5 | 2 | .40 |
| 139 | 1750 | 553 | 2.5 | 4 | .34 |
| 140 | 1750 | 553 | 5 | 4 | .37 |
| 141 | 1745 | 553 | 7.5 | 4 | .43 |
| 143 | 1745 | 553 | 5 | 10 | .43 |
| 144 | 1755 | 553 | 2.5 | 10 | .37 |
| 145 | 1765 | 553 | 2.5 | 20 | .40 |
| 146 | 1760 | 553 | 5 | 20 | .43 |

214

constructed, corresponding to the four Cs reservoir temperatures used, and are shown in Figures VII-17 through -20. The dependence on current density and perhaps other dependencies are responsible for the scatter in these figures, which is of the order of 0.1 volt. To proceed with the investigation of the pressure dependence, an average line was passed through each set of curves, and these average lines were replotted in Figure VII-21. In addition, the collector work function correlation with $T_C/T_R$ is shown as a da'shed line in Figure VII-21. All curves, of course, have been made coincident at $T_C/T_R = 1$. The $\Delta V$ curves are ordered according to reservoir temperature, the 553 and 573 curves being almost identical while the 593 and 613 lines depart considerably from the first two. The work function correlation line coincides with the 553 and 573 lines up to a $T_C/T_R$ ratio of 1.3. The total change in $\phi_C$ from $T_C/T_R = 1$ to its minimum value is about 0.59 volt. This would be the maximum change in output voltage one could expect by changing the collector work function, since the effect of back emission should be to reduce output voltage. It is obvious from Figure VII-21 that this maximum value of 0.59 volt has been exceeded by the $T_R = 613$ data, and consequently the above argument is in conflict with experimental evidence. This argument assumed that the work function correlation obtained from retarding plots and back emission measurements holds under the conditions of the present experiment.

Three possibilities exist:

1.  The work function correlation does not apply at the conditions of these runs, i. e., at high pressure.
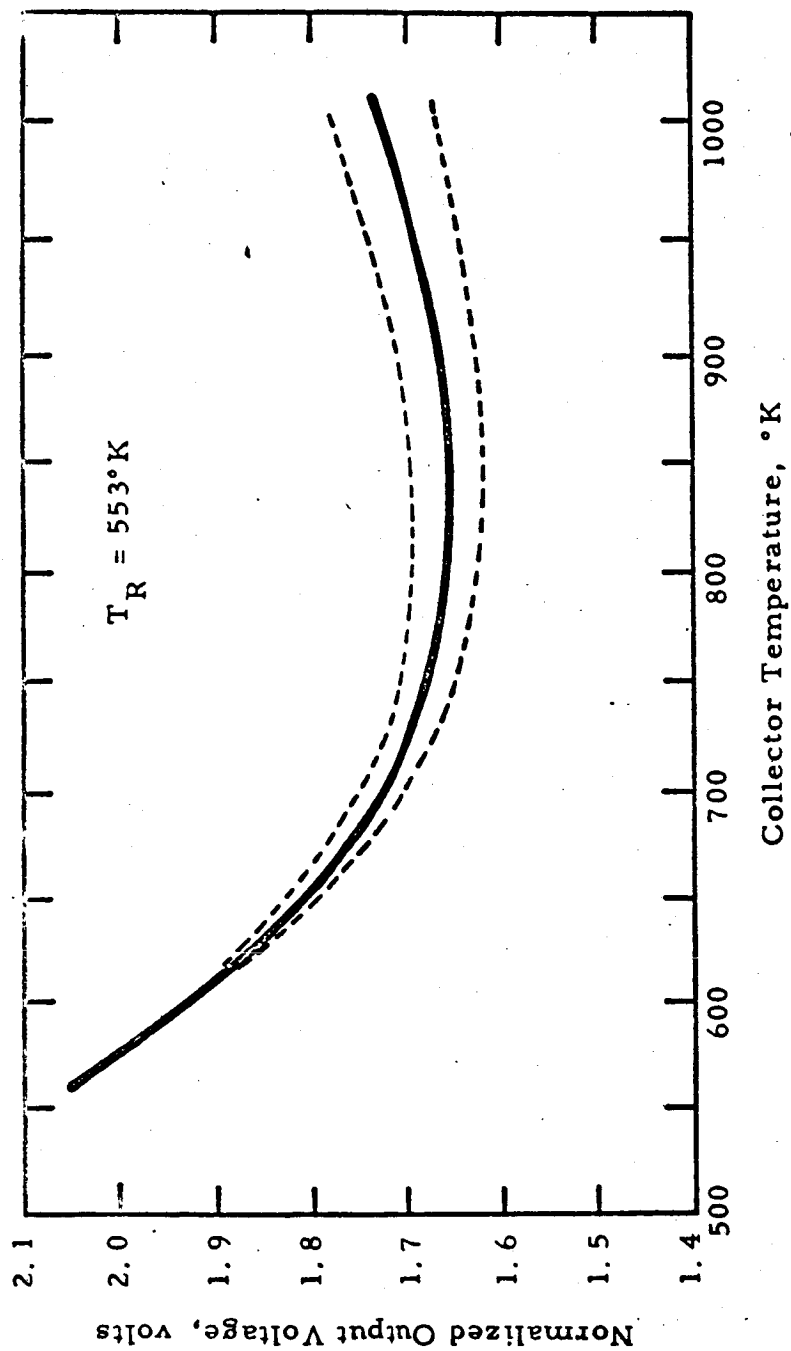
Figure VII-17.   Composite of Variable-Collector-Temperature Runs at $T_R = 553°K$.

216

THERMO ELECTRON
ENGINEERING CORPORATION
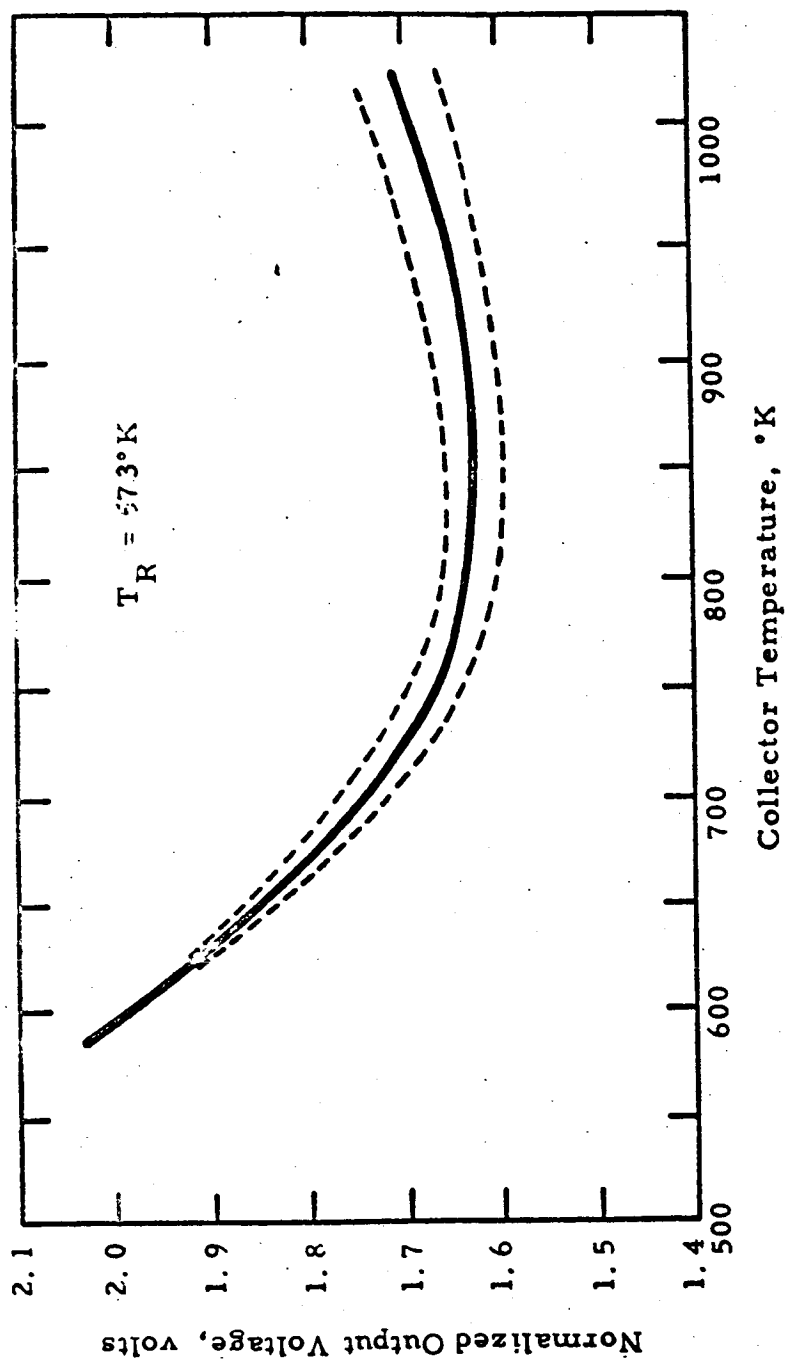


Figure VII-18. Composite of Variable-Collector-Temperature Runs at $T_R = 573°K$.

217
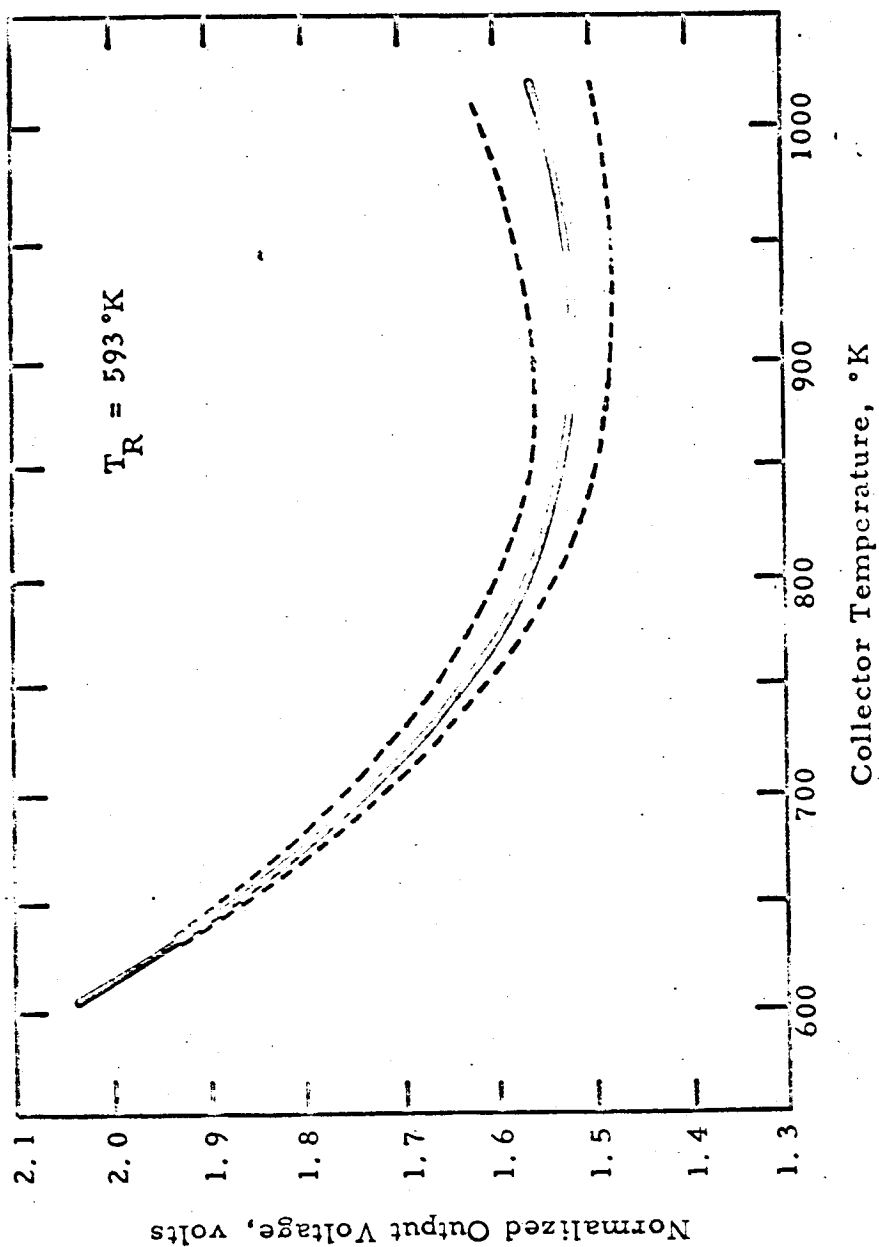
Figure VII-19. Composite of Variable-Collector-Temperature Runs at $T_R = 593°K$.

218
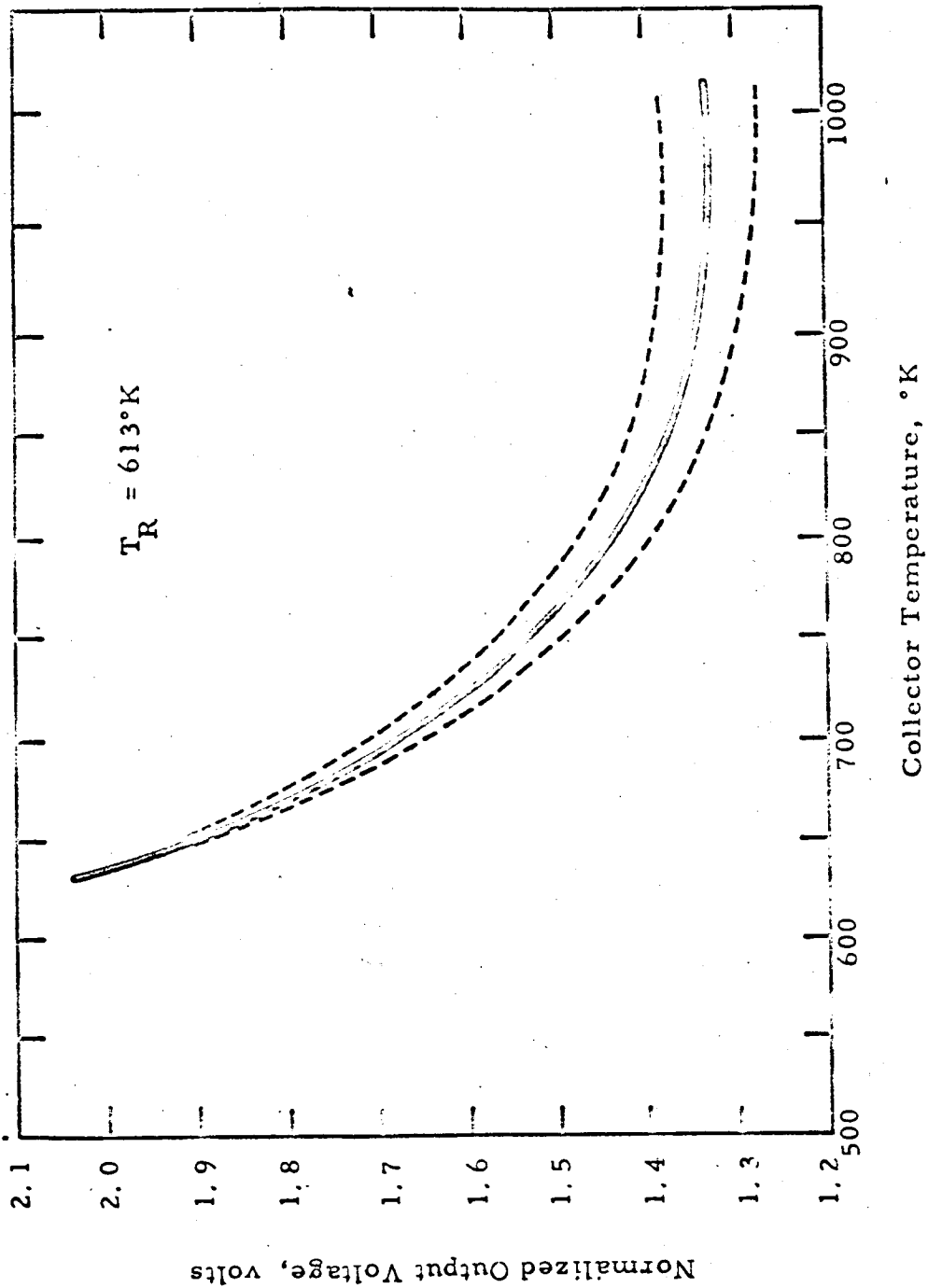
Figure VII-20. Composite of Variable-Collector-Temperature Runs at $T_R = 613°K$.
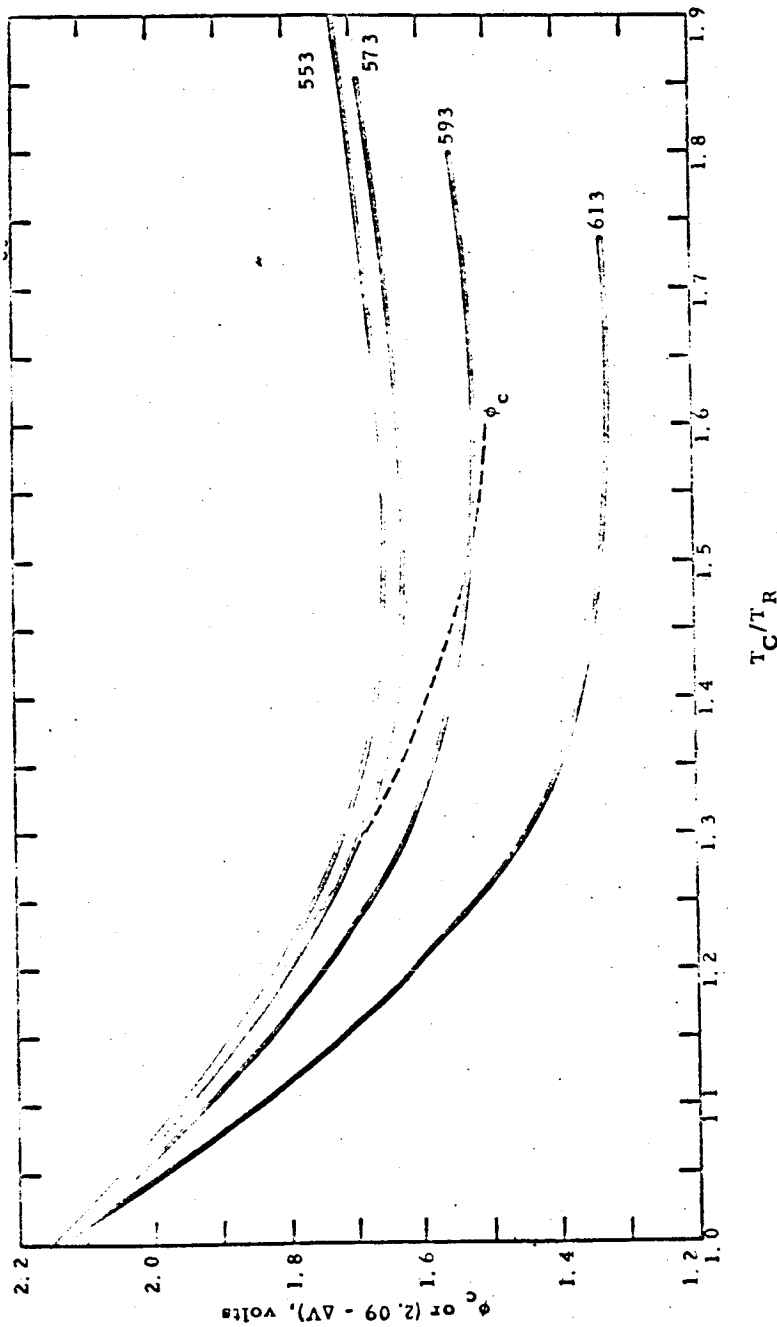
Figure VII-21. Compilation of all Variable-Collector-Temperature Runs.

220

2.  At high pressures the value of work function at $T_C/T_R = 1$ is a function of pressure.

3.  The change in collector temperature causes an additional undetected change in the present runs. Such a possibility might be a change in Cs pressure.

The first hypothesis implies that the variation in collector work function is in fact 0.76 volt in the case of the $T_R = 613°K$ runs. If we require that $\phi_C$ be equal to 2.09 at $T_C/T_R = 1$, then we are faced with absurdly low work function values at $T_C/T_R$ values above 1.3. These values cannot be reconciled with output data. If we require that the minimum be some reasonable value, then we are forced to accept the second possibility, i.e., the $\phi_C$ correlation is not valid at low $T_C/T_R$ values and high pressures. This possibility cannot be rejected on the basis of available evidence, and additional experimentation will be necessary before it can be accepted or rejected.

The third possibility is also probable and would have been investigated, had time allowed.

Unfortunately, at this time the effect of collector temperature on performance is not clearly defined. The present work resulted in obtaining a correlation of the optimum collector-to-reservoir temperature ratio as a function of current, shown in Figure VII-14. It also succeeded in defining the problem much better.

F.    STATIC DATA AND ELECTRON HEATING

All the experimental results discussed up to this point were in the form of J-V curve families generated by imposing a 60-cycle ac

221

signal on the converter and sampling the resulting waveform at a much slower rate. The specific instrumentation used to sweep and monitor the J-V curves is described in Chapter IV. Data generated in this manner is termed "dynamic" and is expected to be identical to data generated by applying a passive resistive load, provided allowances are made for the change in the temperature distribution of the device. It was the objective of the experiments described here to show that this is indeed the case. In addition, static measurements allow the determination of electron heating of the collector, and this was the second objective of this work.

Individual J-V curves were selected whose "knee" was near the maximum-power point of the corresponding variable-cesium-reservoir-temperature family. These curves were reproduced singly by dynamic sweeping. Once the curve was traced, the dynamic sweep supply was disconnected and a static load connected across the converter terminals. Four points on the J-V curve were then selected for static testing. The emitter temperature, spacing, cesium reservoir temperature, collector temperature and output current were set at the predetermined values and the converter was allowed to reach equilibrium. Setting the emitter temperature required an iterative procedure, since the temperature drop across it depends on the heat flux through it. The heat flux, in turn, depends on emitter temperature. When equilibrium was reached with the emitter as close to the desired value as possible, the voltage value was recorded. The heat flux through the collector could be determined from the readings of the two "heat-flux" thermocouples (see Chapter III).

222

The results of these runs are summarized in Table VII-3. The values of the various parameters are listed, along with emitter temperatures and output voltages under static and dynamic conditions. The emitter temperatures under the two kinds of testing differ at times by as much as 20°K. Most values, however, are within 5°K. The differences in output voltage rarely exceed 20 mV. This is considered to be exceptionally good agreement in view of the difficulty of reproducing exactly all conditions under the two kinds of test.

Inspection of the electron heating values obtained revealed a strong dependence on current density but not on any other parameter. The experimental results are plotted in Figure VII-22 in the form of electron heating versus output current density. The points fall on a straight line, the slope of which is $2.5 \text{ W}/\text{A}/\text{cm}^2$. It should be noted that the term "electron heating" is misleading, since it includes not only the energy carried by electrons but also that originating in the plasma in the form of ions, excited atoms, and radiation. From a converter design standpoint, however, the energy associated with electrons leaving the emitter is equal to $(2.5 + V)J$, where $V$ and $J$ are the values of output voltage and output current density.

G.    COMPARISON OF PARAMETRIC DATA

The groups of families of J-V curves described in this chapter can be used to check the reproducibility of the data. Inspection of the original data in Appendix C will show that, in general, J-V curves from different groups taken under the same conditions check to within 50 mV. This type of comparison, however, is quite difficult to make, since the exact temperature values are not usually reproduced from

## TABLE VII-3

## TABULATION OF SELECTED RUNS

| Run # | Dynamic $T_E$ °K | Point # | Static $T_E$ °K | d mils | $T_R$ °K | J A/cm$^2$ | $V_{DYN}$ | $V_{ST}$ |
|---|---|---|---|---|---|---|---|---|
| 15-11 | 1975 | 1 | 1975 | 0.5 | 631 | 50 | .445 | .483 |
| | | 2 | 1985 | | 631 | 32.5 | .63 | .66 |
| | | 3 | 1995 | | 630 | 24 | .74 | .74 |
| | | 4 | 1990 | | 632 | 56 | .38 | .32 |
| 15-15 | 1910 | 1 | 1915 | 0.5 | 622 | 56 | .350 | .385 |
| | | 2 | 1910 | | 623 | 74.5 | .180 | .18 |
| | | 3 | 1910 | | 622 | 37 | .485 | .505 |
| | | 4 | 1915 | | 622 | 15 | .680 | .70 |
| 15-19 | 1825 | 1 | 1825 | 0.5 | 613 | 41 | .350 | .35 |
| | | 2 | 1830 | | 613 | 55 | .225 | .22 |
| | | 3 | 1815 | | 613 | 26 | .470 | .465 |
| | | 4 | 1830 | | 613 | 11.5 | .590 | .59 |
| 15-23 | 1775 | 1 | 1770 | 0.5 | 598 | 32 | .300 | .300 |
| | | 1a | 1770 | | 598 | 31.8 | .300 | .295 |
| | | 2 | 1775 | | 598 | 45 | .175 | .150 |
| | | 3 | 1770 | | 598 | 13.5 | .455 | .435 |
| | | 4 | 1780 | | 598 | 9 | .49 | .500 |
| 15-27 | 1680 | 1 | 1680 | 0.5 | 583 | 23.5 | .23 | .225 |
| | | 2 | 1700 | | 583 | 31 | .16 | .157 |
| | | 3 | 1700 | | 583 | 15.2 | .295 | .308 |
| | | 4 | 1700 | | 583 | 9.3 | .325 | .342 |
| 15-31 | 1960 | 1 | 1960 | 2 | 633 | 46.5 | .46 | .458 |
| | | 2 | 1965 | | 633 | 62.5 | .29 | .271 |
| | | 3 | 1960 | | 633 | 36.5 | .60 | .570 |
| | | 4 | 1955 | | 633 | 21.8 | .69 | .695 |
| 15-35 | 1875 | 1 | 1880 | 2 | 623 | 41 | .41 | .385 |
| 15-36 | 1915 | 1 | 1915 | 2 | 623 | 40.5 | .485 | .48 |
| | | 2 | 1920 | | 623 | 49 | .42 | .425 |
| | | 3 | 1915 | | 623 | 59 | .32 | .312 |
| | | 4 | 1915 | | 623 | 30.5 | .55 | .560 |

225

## TABLE VII-3 (CONT'D)

### TABULATION OF SELECTED RUNS

| Run # | Dynamic $T_E$ °K | Point # | Static $T_E$ °K | d mils | $T_R$ °K | J A/cm$^2$ | $V_{DYN}$ | $V_{ST}$ |
|---|---|---|---|---|---|---|---|---|
| 15-44 | 1845 | 1 | 1840 | 2 | 613 | 27.5 | .38 | .38 |
| | | 2 | 1850 | | 613 | 46 | .175 | .18 |
| | | 3 | 1835 | | 613 | 15 | .495 | .50 |
| | | 4 | 1840 | | 613 | 7 | .580 | .62 |
| 15-51 | 1850 | 1 | 1840 | 3 | 603 | 28.5 | .31 | .32 |
| | | 2 | 1845 | | 603 | 34 | .205 | .21 |
| | | 3 | 1835 | | 603 | 14 | .47 | .48 |
| | | 4 | 1835 | | 603 | 7.5 | .55 | .58 |
| 15-56 | 1910 | 1 | 1905 | 4 | 593 | 15 | .53 | .55 |
| | | 2 | 1905 | | 593 | 24.5 | .36 | .34 |
| | | 3 | 1910 | | 593 | 31.5 | .21 | .21 |
| | | 4 | 1890 | | 593 | 5 | .70 | .7 |
| 15-61 | 1855 | 1 | 1860 | 10 | 593 | 17.5 | .34 | .32 |
| | | 2 | 1850 | | 593 | 23 | .10 | .09 |
| | | 3 | 1845 | | 593 | 14 | .45 | .45 |
| | | 4 | 1845 | | 593 | 10 | .60 | .58 |
| 15-70 | 1860 | 1 | 1870 | 20 | 593 | 13 | .27 | .25 |
| | | 2 | 1875 | | 593 | 19 | .07 | .06 |
| | | 3 | 1860 | | 593 | 10 | .39 | .38 |
| | | 4 | 1850 | | 593 | 7 | .50 | .5 |

225
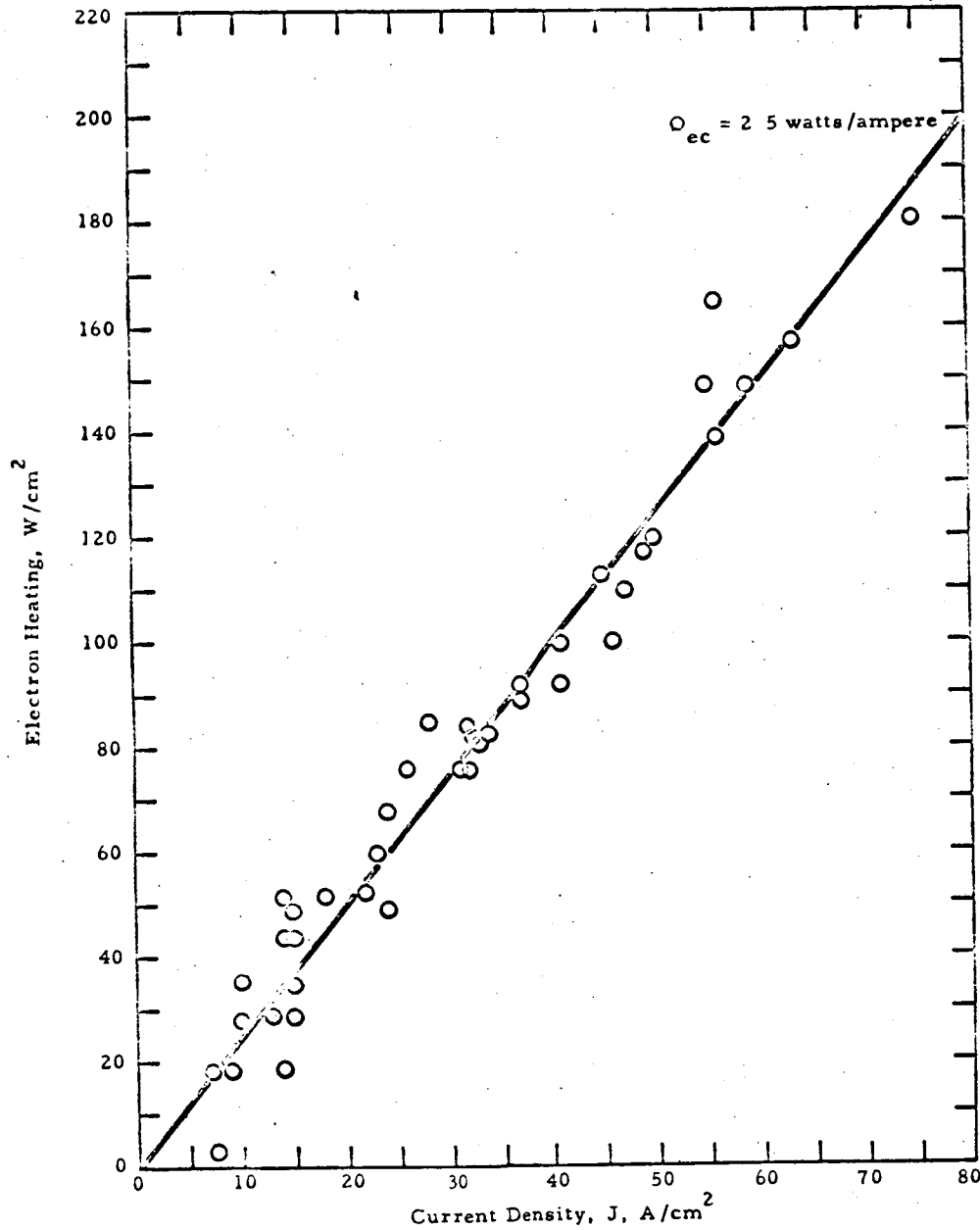
Figure VII-22.  Electron Heating of the Collector as a Function of Current Density.

family to family. A better method of comparison is that of envelopes.
For example, an envelope made up from J-V curves taken at the same
reservoir temperature and spacing but different emitter temperatures
in the variable-Cs-reservoir temperature experiments reproduces quite
well the corresponding envelope of the family of variable emitter temper-
ature. It should be noted that small variations in Cs reservoir temper-
atures can cause significant changes in individual J-V curves, and this
should be taken into account when such comparisons are made.

## H. CONCLUSIONS

The parametric data presented here constitutes the most complete
and extensive such set in existence. The various sub-sets of families
of curves generated by the variation of different parameters are con-
sistent with each other. The two electropolished, heat-treated rhenium
emitters used produced indistinguishable characteristics. The perform-
ance level of this type of emitter is in general among the highest reported.
These data resulted in empirical correlations of the optimum collector
temperature and collector heating in the ignited mode. The analytical
value of the data is discussed in Chapter IX.

227

# CHAPTER VIII
## ADDITIVE CONVERTER STUDY

A. GENERAL

The characteristics of cesium thermionic converters have been extensively studied and documented. In many applications the ideal performance expected from this documentation must be compromised because of limitations imposed by mechanical restrictions such as spacing, electrode temperatures, or material requirements. To obtain further improvements in power output or operating range it appears that a new variable must be introduced into converter behavior. One promising approach is through the use of electro-negative additive elements which would modify the surface work functions.

In this investigation cesium fluoride was added to the guarded collector test converter described elsewhere in this report. To facilitate comparisons with well documented results,[5] a tungsten emitter was incorporated opposite the molybdenum collector. Experiments were made initially to compare the bare surface work function with that in the presence of the additive only. Parametric performance was then measured with cesium and cesium fluoride in the test vehicle.

Of the three vehicles used, the first was utilized primarily for work function measurements with a bare surface and with the CsF additive. In this device with tungsten emitter W4 the CsF charge of 3 pellets or 300 mg was inserted directly into its reservoir while the Cs was contained in a metal capsule which could be cracked when Cs-plus-CsF data was desired.

The second and third test vehicles, using tungsten emitter W6, were similar to the first except that the Cs was distilled into their reservoirs in

228

the normal manner, since only Cs-plus-CsF data was desired. The
additive charge in the second tube (1000) was 3 pellets or 300 mg,
and in the third tube (3000) it was 12 pellets or 1200 mg.. The charge
in the third was increased to provide for any loss during outgassing.

B.　WORK FUNCTION

This series of experiments examined the behavior of the work
function of a tungsten emitter surface with varying cesium fluoride
additive coverage. Using this information, the additive and surface
temperature dependence of the work function can be summarized in a
map similar to those available for cesium-covered surface. The per-
formance of the surface with both cesium and cesium fluoride coverage
should then be predictable in terms of the cesium-fluoride-only and the
cesium-only data. Further experiments must be carried out to verify
these predictions. In addition to these essentially equilibrium experi-
ments, a study of time-dependent phenomena has shown that appreciable
delays in work function change occur with certain variations in surface
and additive temperatures.

1.　Testing

To serve as a control for the additive experiments, the "bare"
work function of the tungsten emitter surface was determined at several
temperatures, and the additive was then introduced into the test vehicle
by raising its reservoir temperature and maintaining the collector and
guard at an equal or greater temperature. Because of the low vapor
pressure of cesium fluoride, considerable delay was expected in estab-
lishing the desired pressure throughout the device. To speed up this
process, the entire collector-guard structure was treated as the

reservoir and maintained at nearly the fluoride temperature. Any time effects in current value were monitored on a strip chart recorder. A second group of several runs was also taken, allowing at least two hours equilibrating time. However, after about ten minutes no further change was observed in the current characteristics. From these curves, using the Richardson equation, the work function for the various conditions was calculated.

At the end of these runs, the ceramics in the bombardment gun had become metallized and caused a high-voltage breakdown. The bell jar was therefore opened after filling with He, and the gun was replaced. At the same time the cesium capsule was cracked to allow cesium to enter the converter. When the converter was re-heated, tests showed that it had failed. This cast some element of doubt upon the most recent data, since it is not known precisely when the leak developed.

## 2. Emitter Steady-State Work Functions

The equilibrium data obtained from these experiments are plotted in Figure VIII-1. The supposedly bare data is shown by the +; but, as indicated both by the changing values with temperature and the slightly high value of 5 eV, some additive is probably present. During the outgassing it is probable that an additive coating formed on the tube surfaces and was able to reach the emitter during these runs.

In the CsF runs a definite trend toward higher work function with lower emitter temperature or higher additive temperature is seen, indicating a strong correlation between additive coverage and work function. If we compare the data represented by the X's corresponding to the later results with that represented by the open circles and the closed

230

THERMO ELECTRON
ENGINEERING CORPORATION
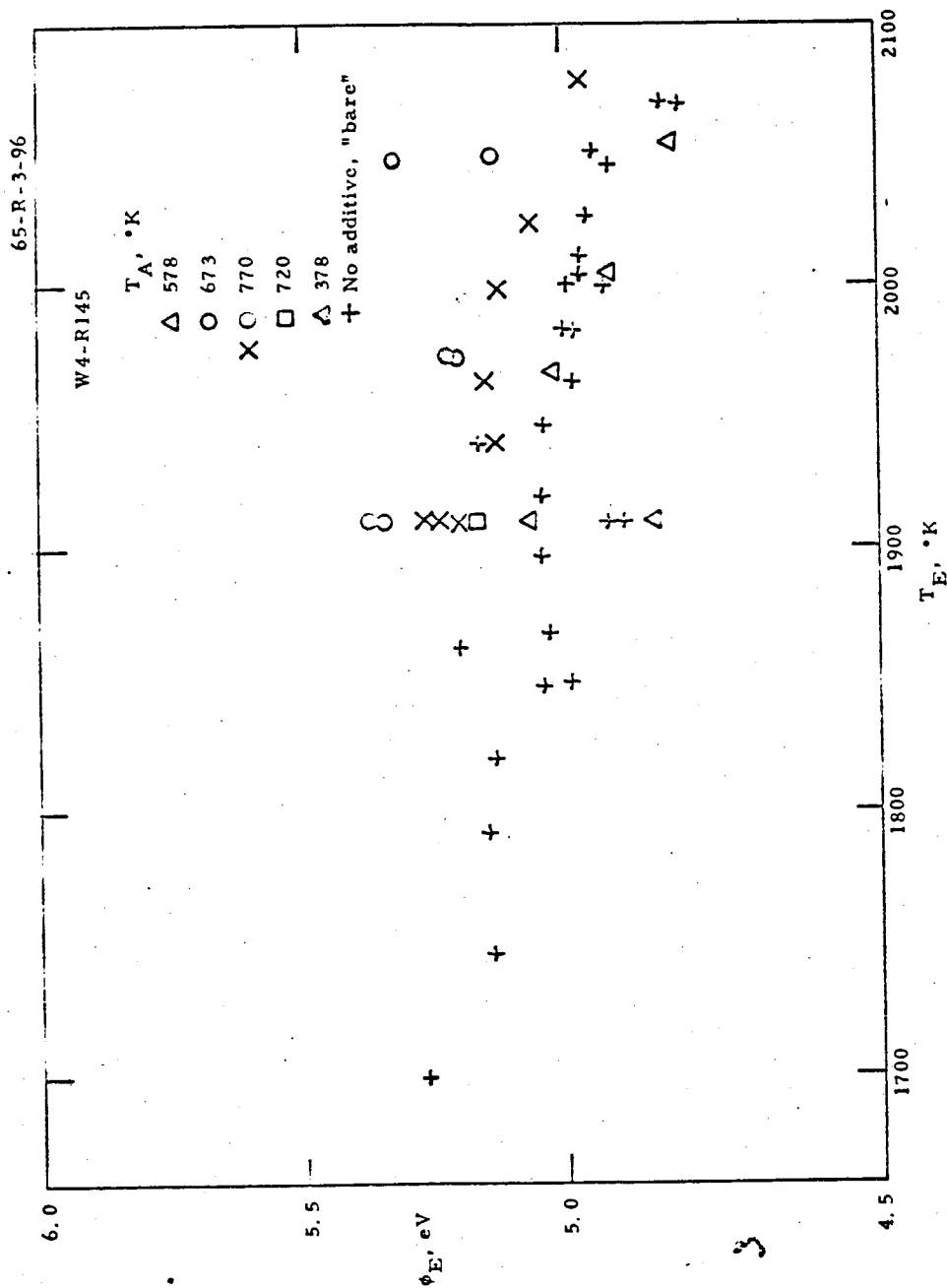


Figure VIII-1. Equilibrium Work Function vs $T_E$.

231

circles on Figure VIII-1, it is found that the additive has become less effective. This observation, together with the failure of the converter as noted above, indicates that either a leak developed during these tests or the additive was disappearing and its full pressure was not maintained. Figure VIII-2 shows the CsF points from Figure VIII-1 plotted with $T_E/T_A$ as the abscissa. These points do not form a single curve, indicating that the dependence on fluoride temperature is not simply related to $T_A$; however, with the limited data and non-reproducibility existing at this point, no definite conclusion can be reached.

Work function values for the Cs-plus-CsF conditions were also calculated from the saturation currents on the parametric curves using the Richardson equation. The data obtained from these calculations is plotted as a function of $T_E/T_R$ in Figure VIII-3 together with a tungsten-Cs-only line. In converter No. 1000, all points show increased covered work functions, contrary to expectations. Converter No. 3000, on the other hand, shows significantly lowered values, 0.6 eV, and enhanced emission at low Cs pressures would be expected in the parametric results. Thus, the higher bare work functions obtained with CsF only produce lower Cs-covered values, as predicted by the Rasor theory. However, the data obtained up to this time is not stable enough to allow quantitative analysis of the results. Because there are two trends acting in this plot, a definite conclusion cannot be drawn as to the relative importance of the loss of additive and the change in coverage. The higher-temperature points have lower coverage due to the higher $T_E/T_A$ ratio and, therefore, approach the Cs-only line, and the later runs have crossed the Cs-only curve by 0.1 eV and give values on the same line as tube 1000. This is further evidence that the additive originally present has somehow become inactive.

232
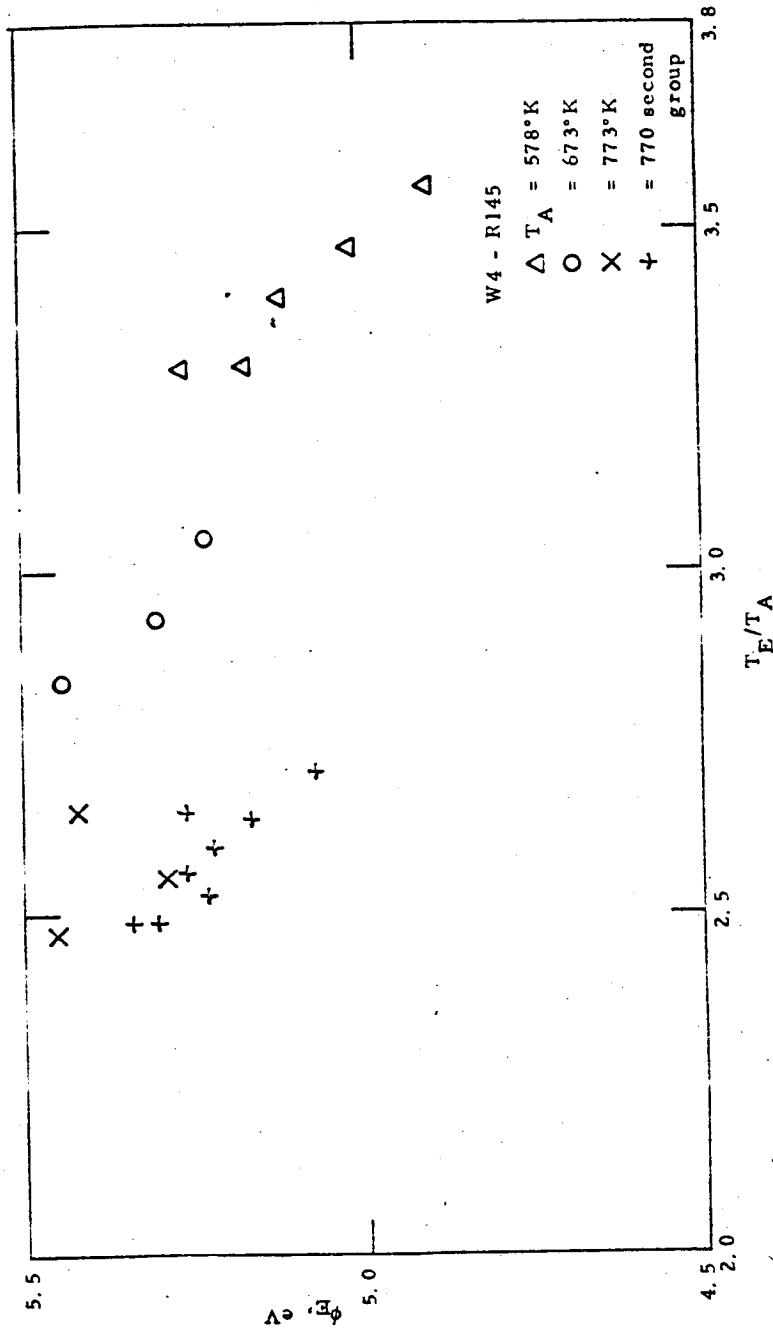
Figure VIII-2. Equilibrium Work Function vs $T_E/T_A$.

233
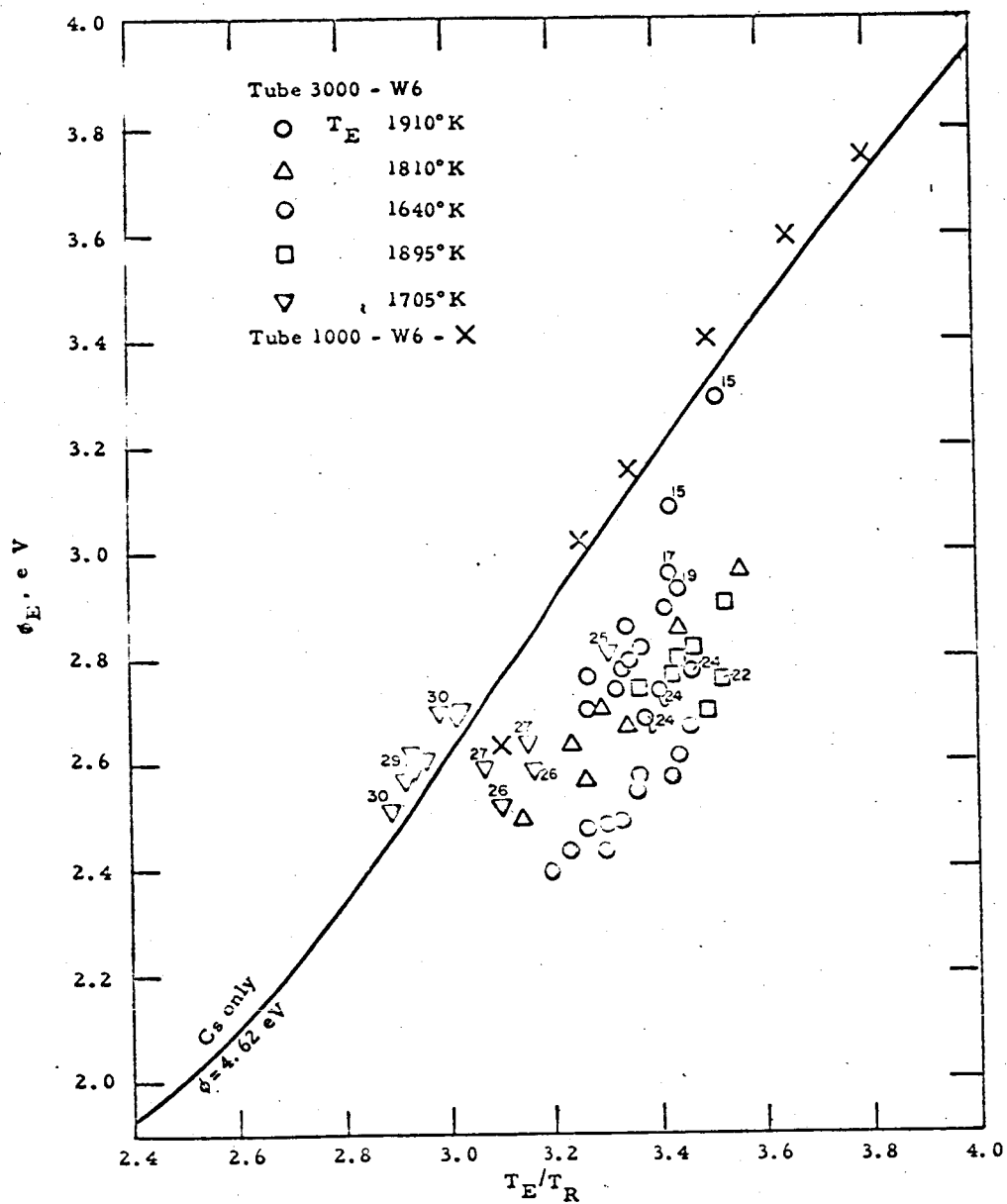
Figure VIII-3. Emitter Work Function vs $T_E/T_R$ for Cs plus CsF.

234

3.    Time Effects

During testing, whenever emitter or reservoir temperatures were changed, a significant delay time appeared before the J-V curves became stabilized. To give added confidence in the data on time effects, the following check was made: The additive reservoir temperature was held at a low value and the emitter temperature was raised. J-V curves for surface work function were then taken at intervals until equilibrium was reached. Calculation of the work function for these runs shows that the values of $\phi$ were initially high, but, as time passed and the surface approached the bare condition, the value of $\phi$ tended to fall between 4.6 and 4.9, which is the range expected for bare tungsten. In Figure VIII-4 the trend towards this value can be seen.

Figure VIII-5 is a semi-log plot illustrating the relative time constants of some of the work function changes. In most cases a straight line has been obtained, indicating an exponential behavior.

C.    PARAMETRIC EXPERIMENTS

These experiments cover the range of converter operation where there are significant electrode currents. Data was obtained primarily in the form of cesium families at various emitter temperatures and spacings in the presence of the cesium fluoride additive. The results in the two converters, numbered 1000 and 3000, were quite different; the first device showed no change or actually deleterious effects with the CsF, while the second produced improved performance in the initial tests.

THERMO ELECTRON
ENGINEERING CORPORATION
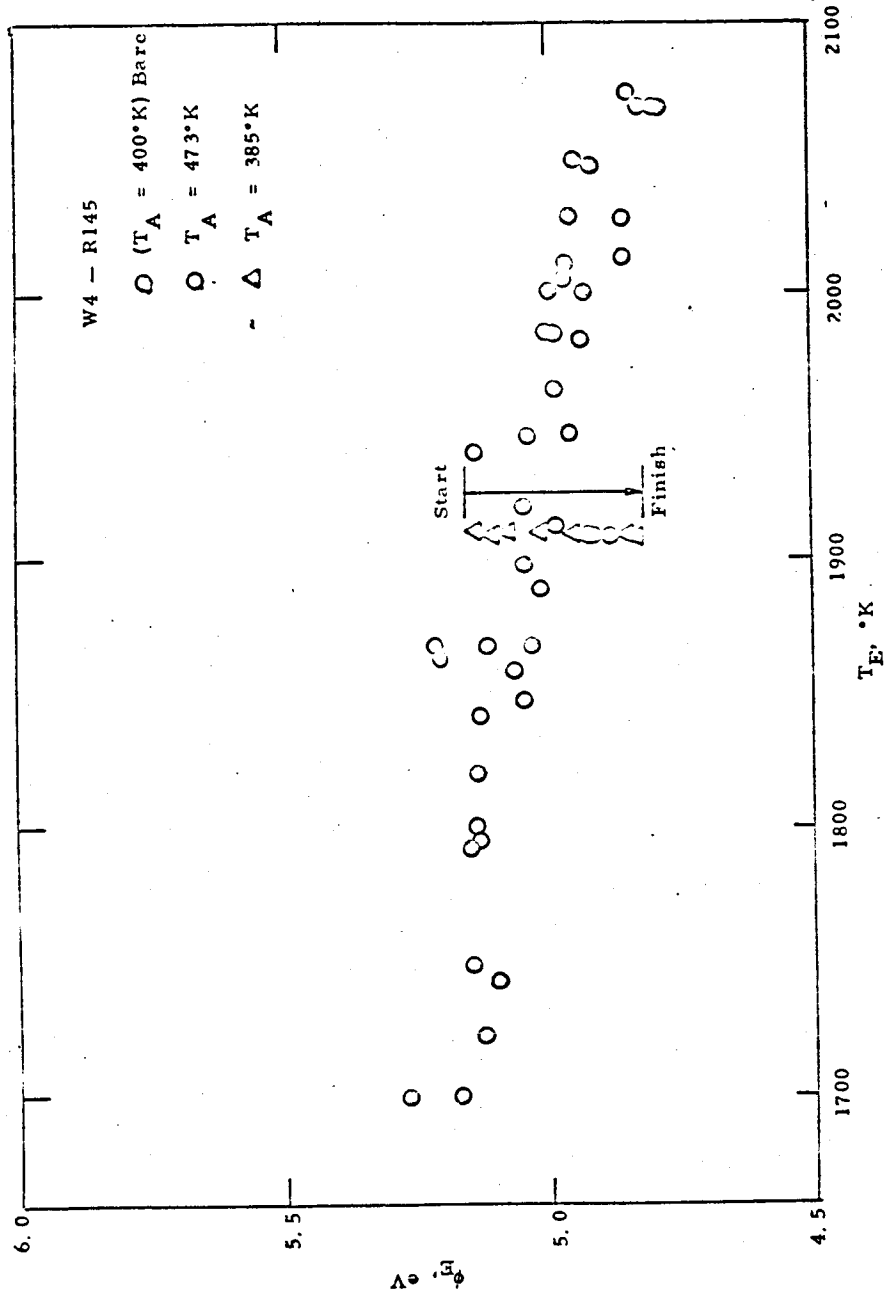


Figure VIII-4.  Emitter Work Function vs $T_E$ at low $T_A$, CsF Only.

236

THERMO ELECTRON
ENGINEERING CORPORATION
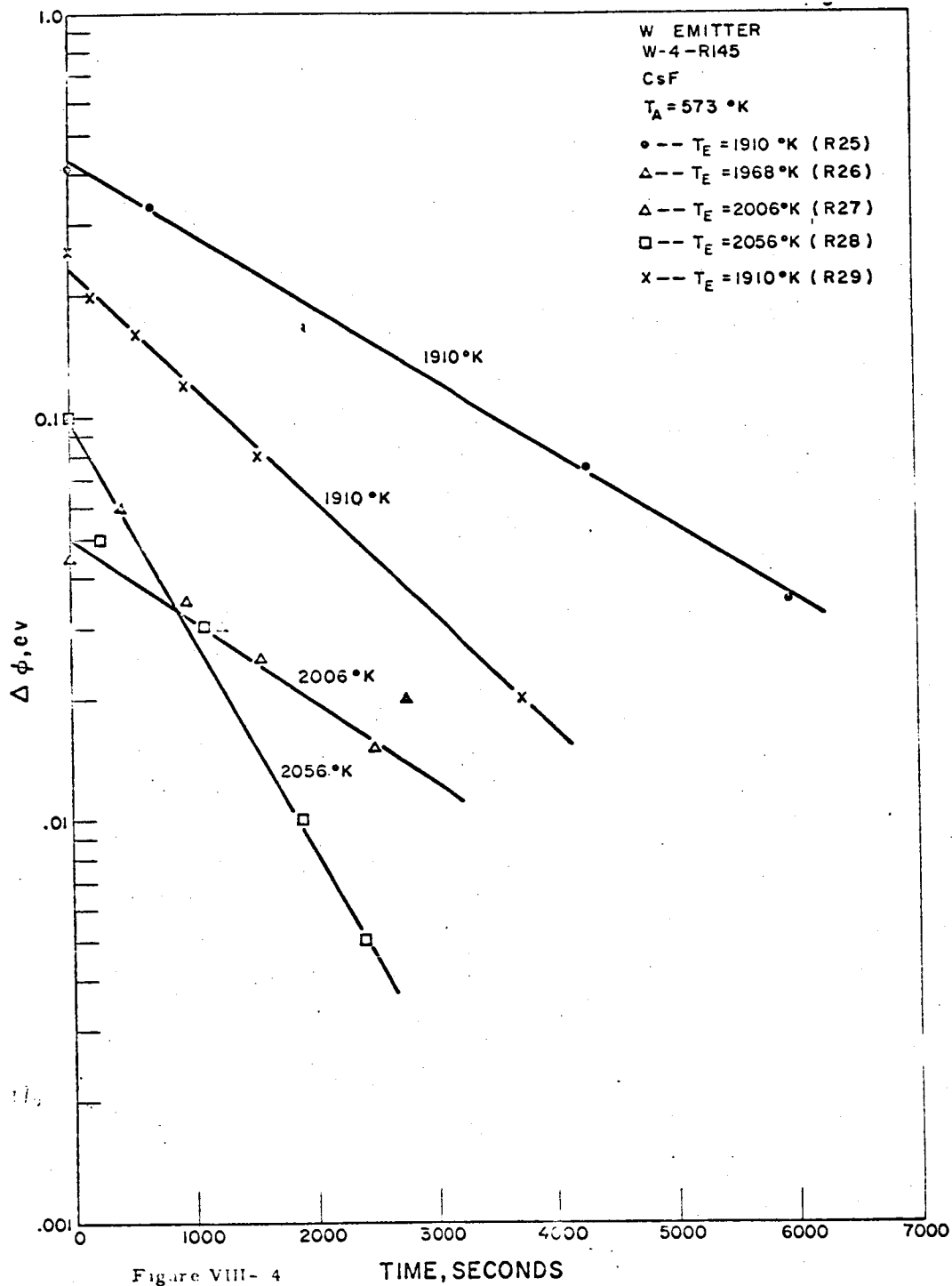


Figure VIII-5.   Relative Time Constants of Work Function Changes.

237

1. Testing

Each test vehicle was evaluated using the dynamic test setup over a range of emitter temperatures from about 1600°K to 1950°K. Families with varying Cs reservoir temperature were obtained at each of several spacings in the range from 0.5 to 30 mils. During these runs additive and collector temperatures were maintained approximately constant.

2. Results

Converter No. 1000

In this device the principal change from Cs-only characteristics appears in the Cs temperature required for a given emitter temperature. Figure VIII-6 is a typical Cs-plus-CsF family and may be compared with the Cs-only curve shown in Figure VIII-7. Noticeable also is a decrease in power output from that observed in the Cs-only converter. Figure VIII-8 summarizes several runs and compares the fully optimized performance with Cs only with the performance at 1/2-mil spacing obtained with Cs plus CsF. In this figure the performance is seen to be significantly poorer than that of the Cs-only devices.

The data obtained from this device was quite reproducible and showed no noticeable time delays. In Figure VIII-9 envelopes obtained from two runs separated by an interval of several days are compared and are practically coincident. A series of experiments, described in a later section, were carried out to try to vary the performance. None of these produced any changes from the results described above.

Converter No. 3000

The performance of this converter was very different from that of the Cs devices; namely, very low Cs pressures and relatively

238
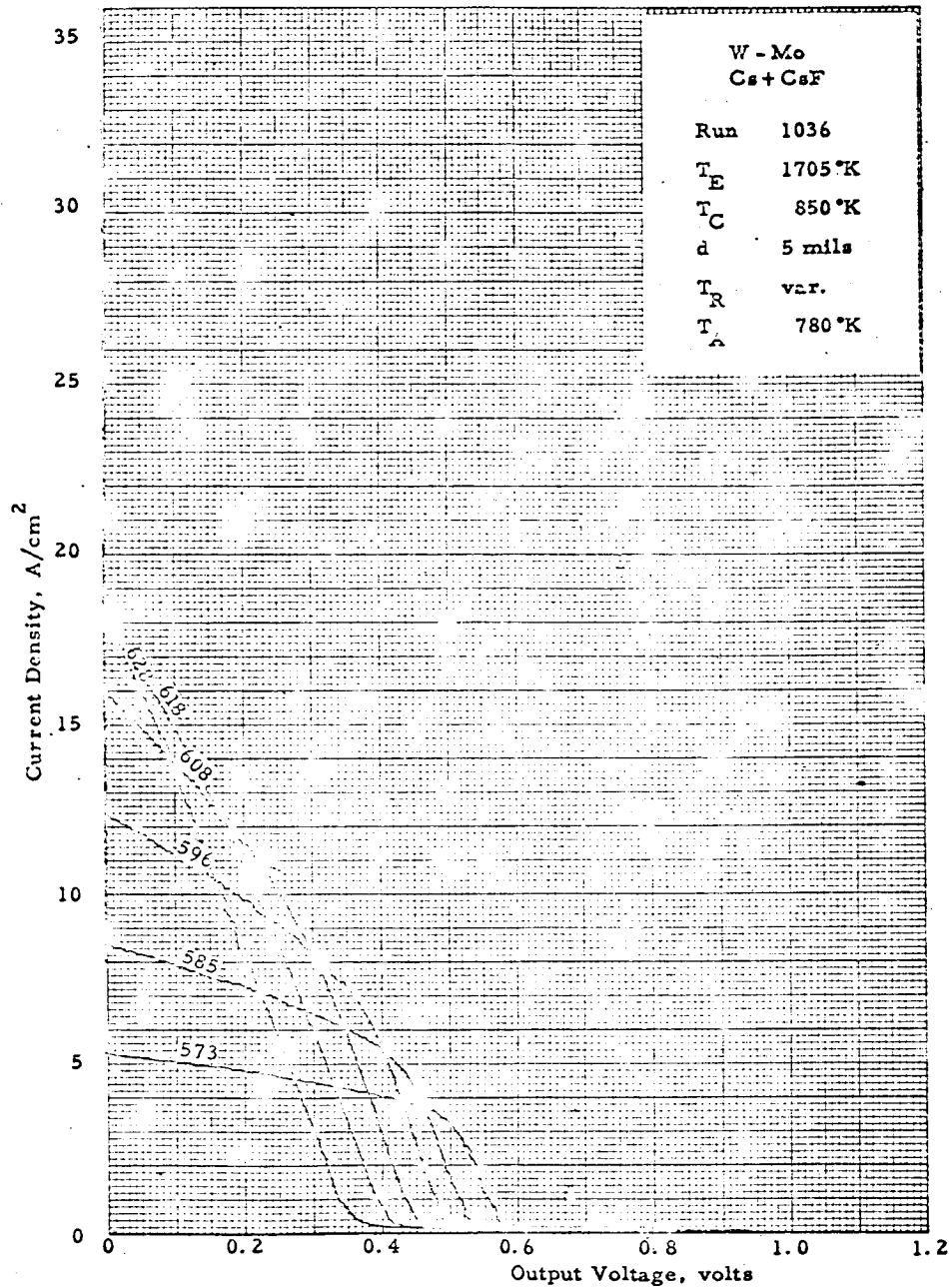
Figure VIII-6. Typical Cs-plus-CsF Family.

239
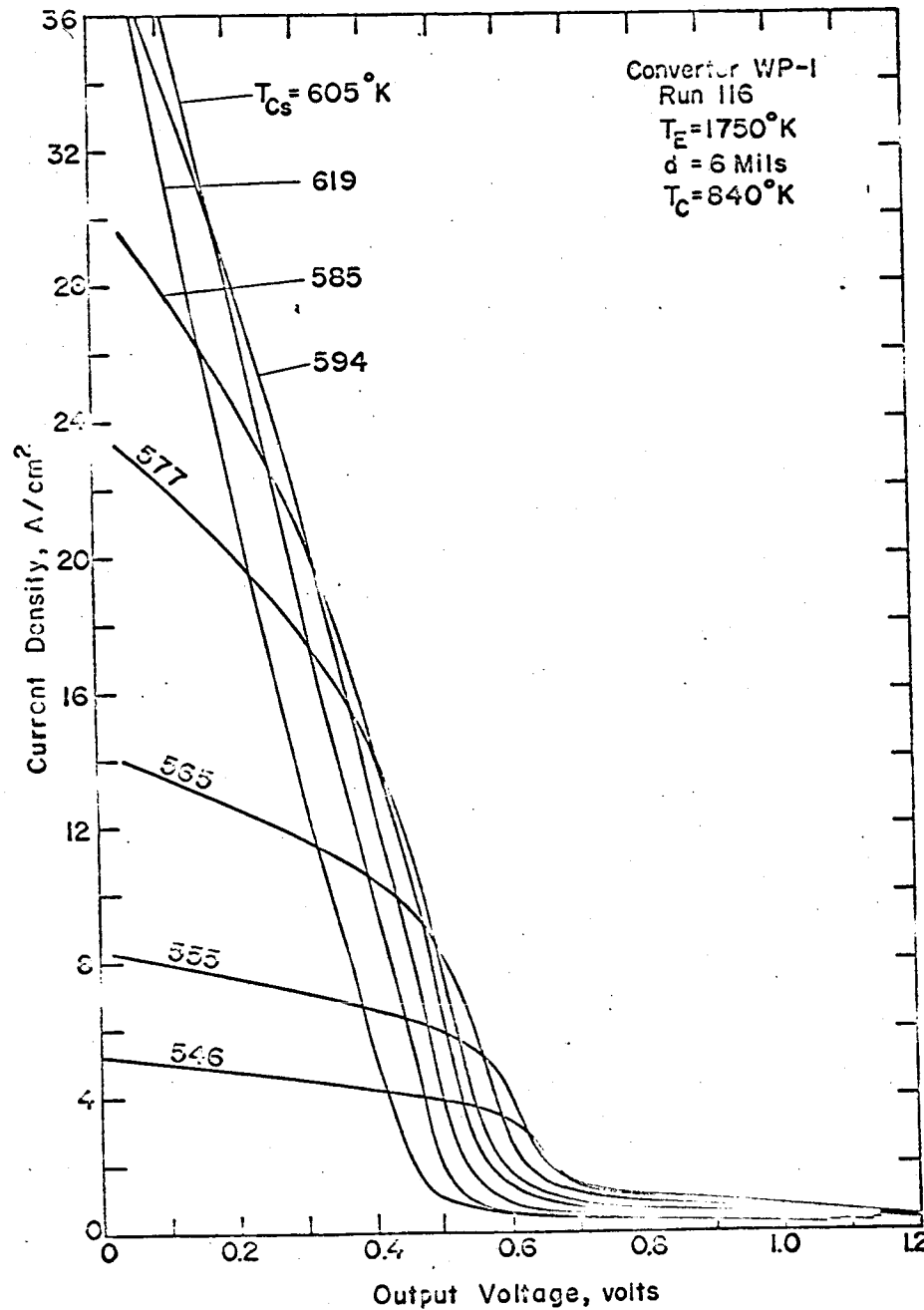
Figure VIII-7.  Typical Cs-Only Family.

240
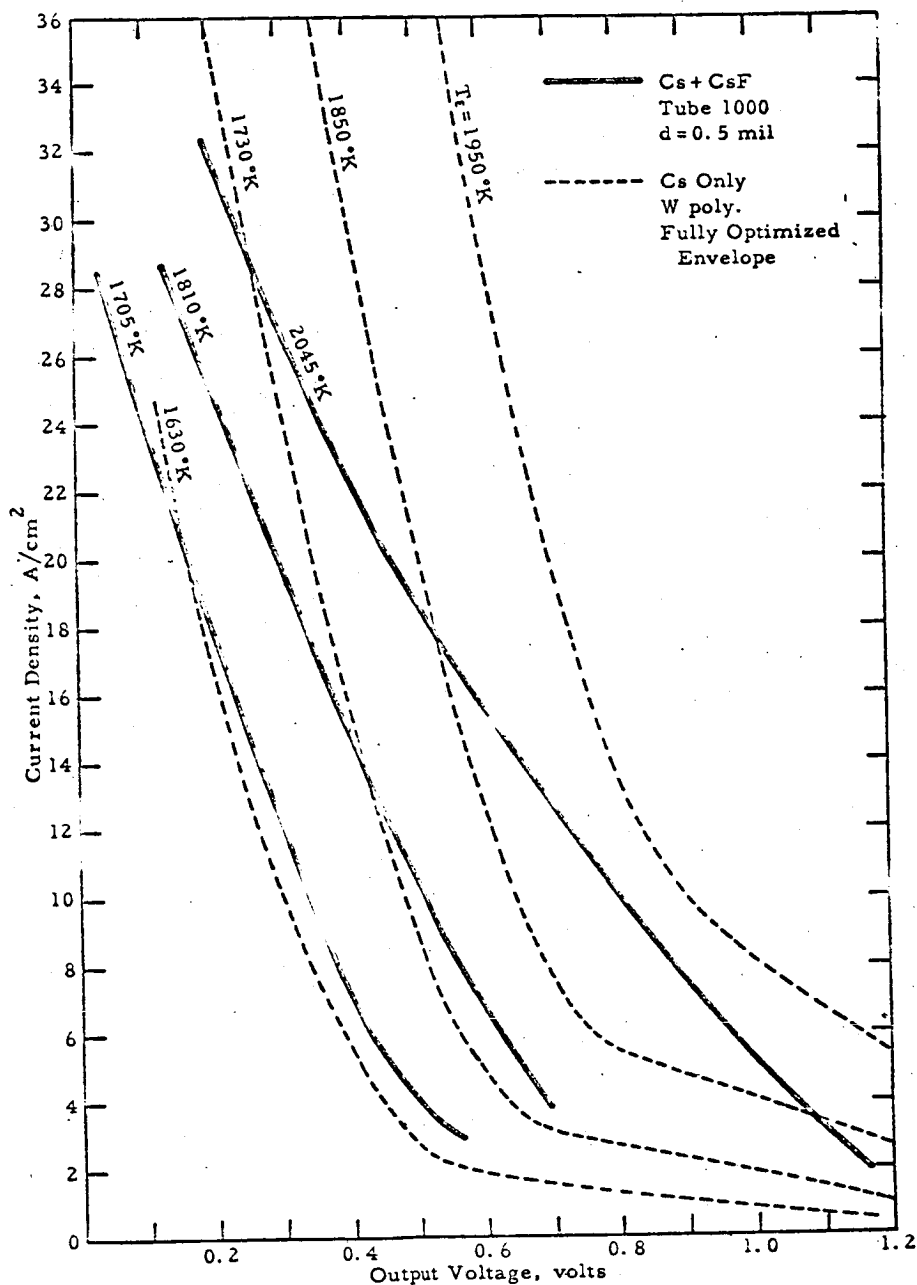
Figure VIII-8.  Tungsten Optimum Performance Summary.
Comparison of Cs-Only with Cs-plus-CsF,
Showing Decreased Output.
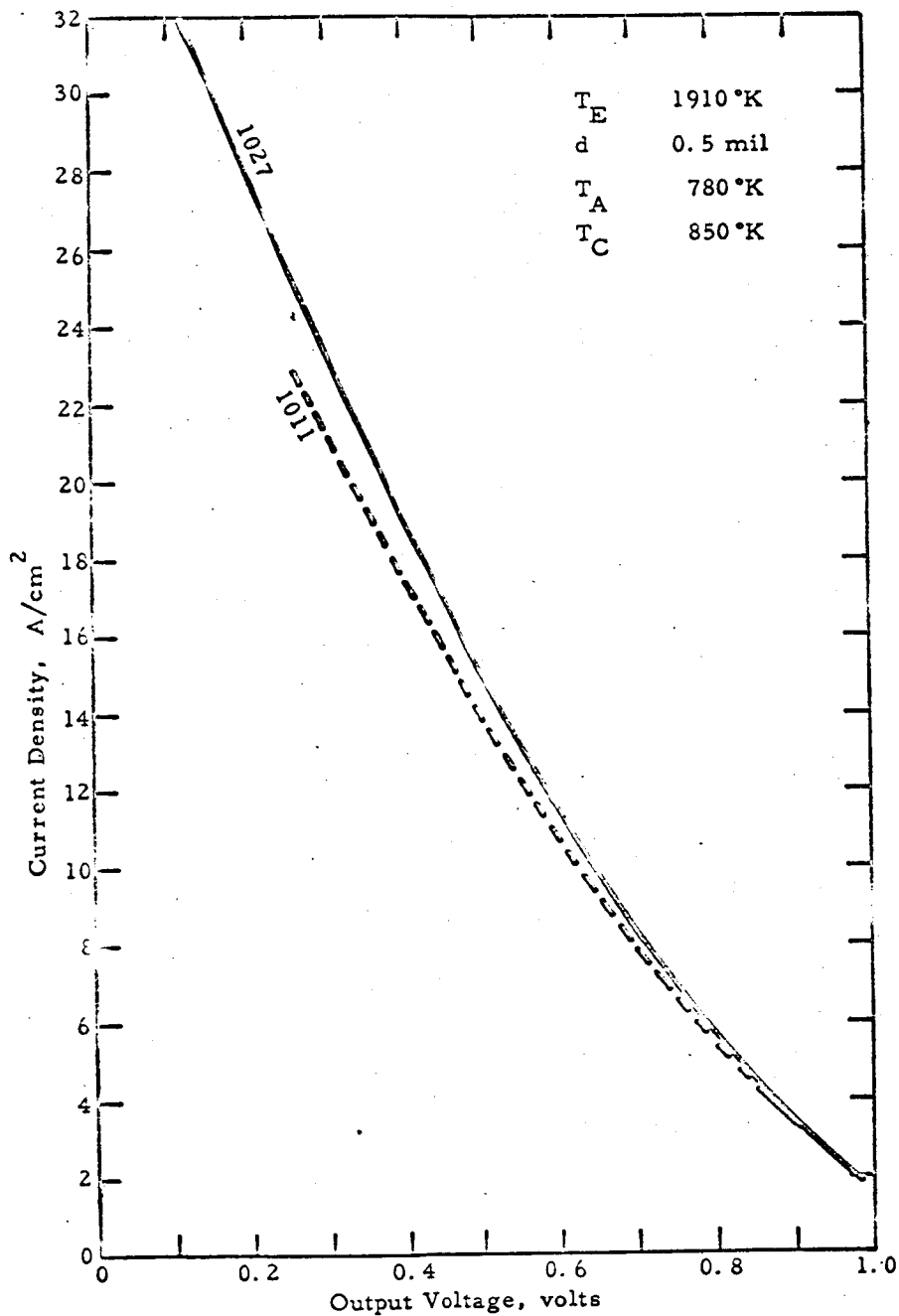
Figure VIII-9.   Cs-plus-CsF  Envelopes  (Runs 1011 and 1027).

242

wide spacing were required to produce J-V characteristics in the power quadrant. Higher than usual lower-mode currents were also observed. Figures VIII-10 through -13 show some typical Cs families obtained. The indicated envelope on the figures represents electrode power and has been corrected for lead loss. Figure VIII-14 is a summary plot of the Cs families at several emitter temperatures and spacings compared with data from a Cs-only converter. After a day or two of testing, the performance began to degrade and approached that of converter 1000. Figure VIII-15 shows a curve obtained later in the testing period, which is seen to be similar to the curve of Figure VIII-16 from tube 1000. For the remainder of the testing period the performance appeared stable at this level.

## D. FLUORIDE TRANSPORT

### 1. Experiments

#### Converter 1000

The work function and performance data obtained from this device indicated that there may have been an incorrect amount of additive on the surface. In previous work insufficient additive did cause such a result. The following series of experiments was then carried out to try to vary the coverage:

1. Increased additive reservoir temperature.
2. Overnight soak with lowered emitter and collector temperatures.
3. Reduced Cs pressure with high additive pressure.
4. Varying additive pressure.

A chart of the temperature history of the outgassing and test is shown in Figure VIII-17. Throughout these experiments almost no change in the characteristics was observed.

243
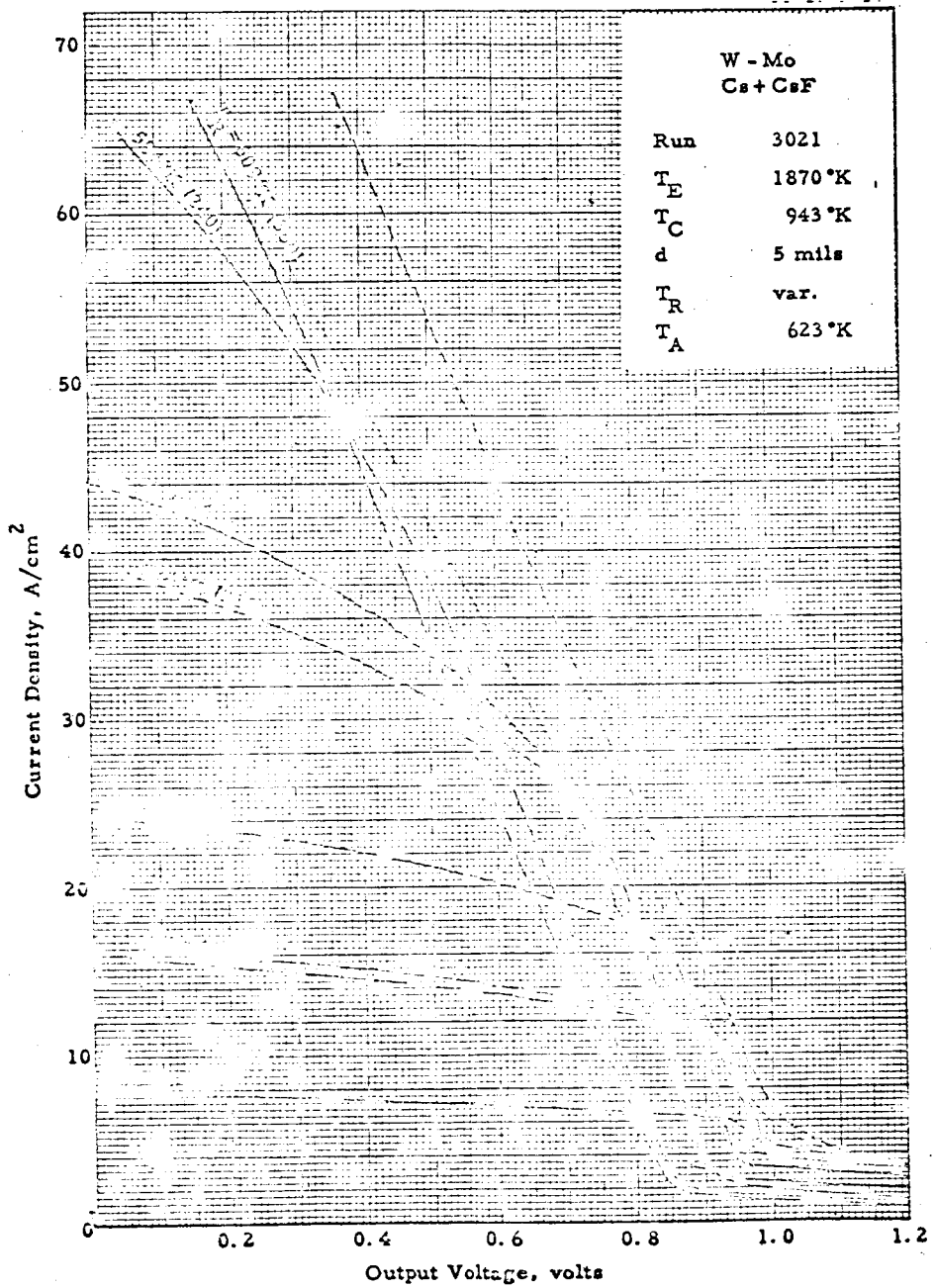
Figure VIII-10.   Typical Cs-plus-CsF Family.

244
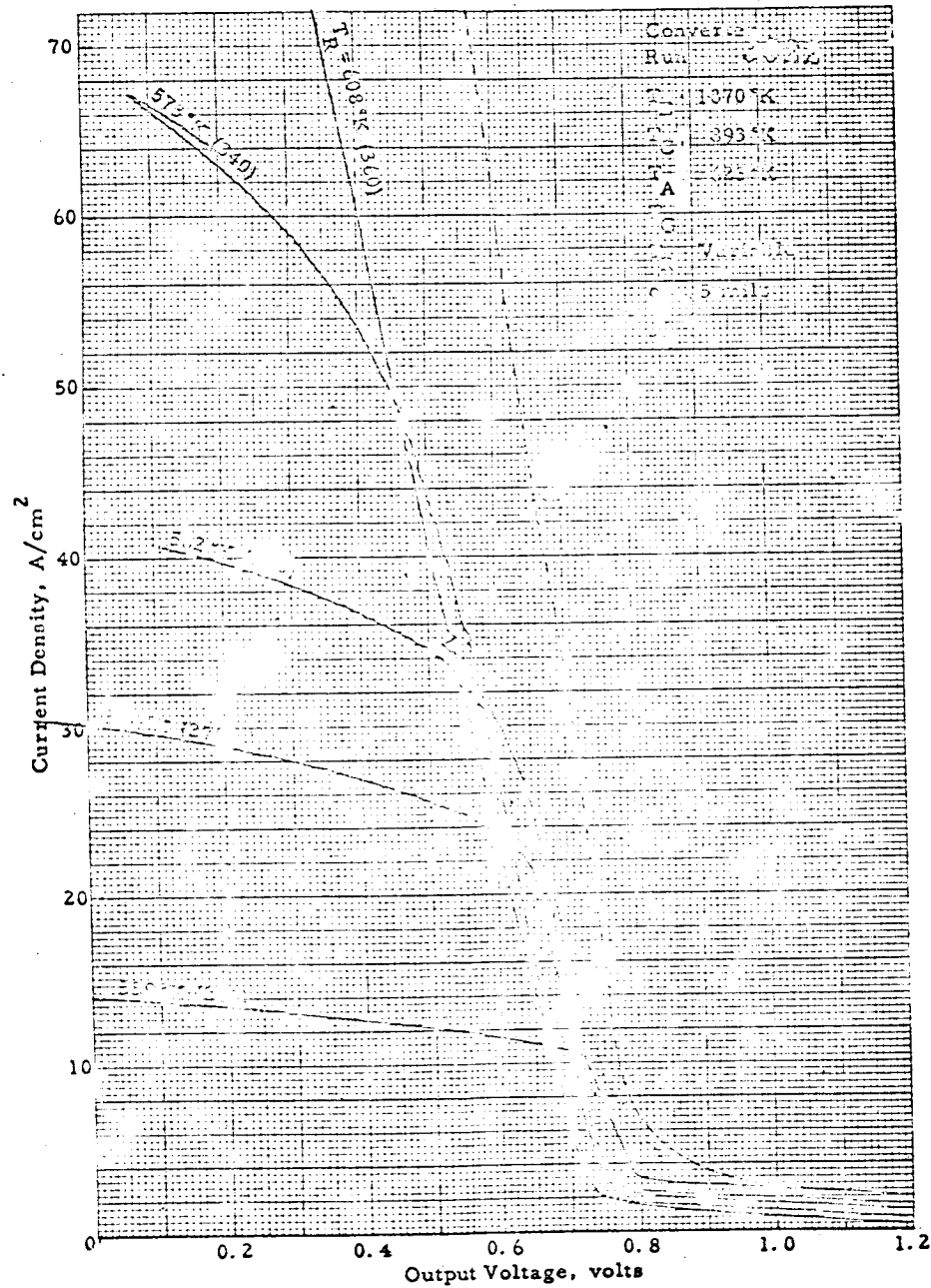
Figure VIII-11. Typical Cs-plus-CsF Family.

| | W – Mo |
| | Cs + CsF |
| Run | 3007 |
| $T_E$ | 1630°K |
| $T_C$ | 843°K |
| d | 20 mils |
| $T_R$ | var. |
| $T_A$ | 568°K |
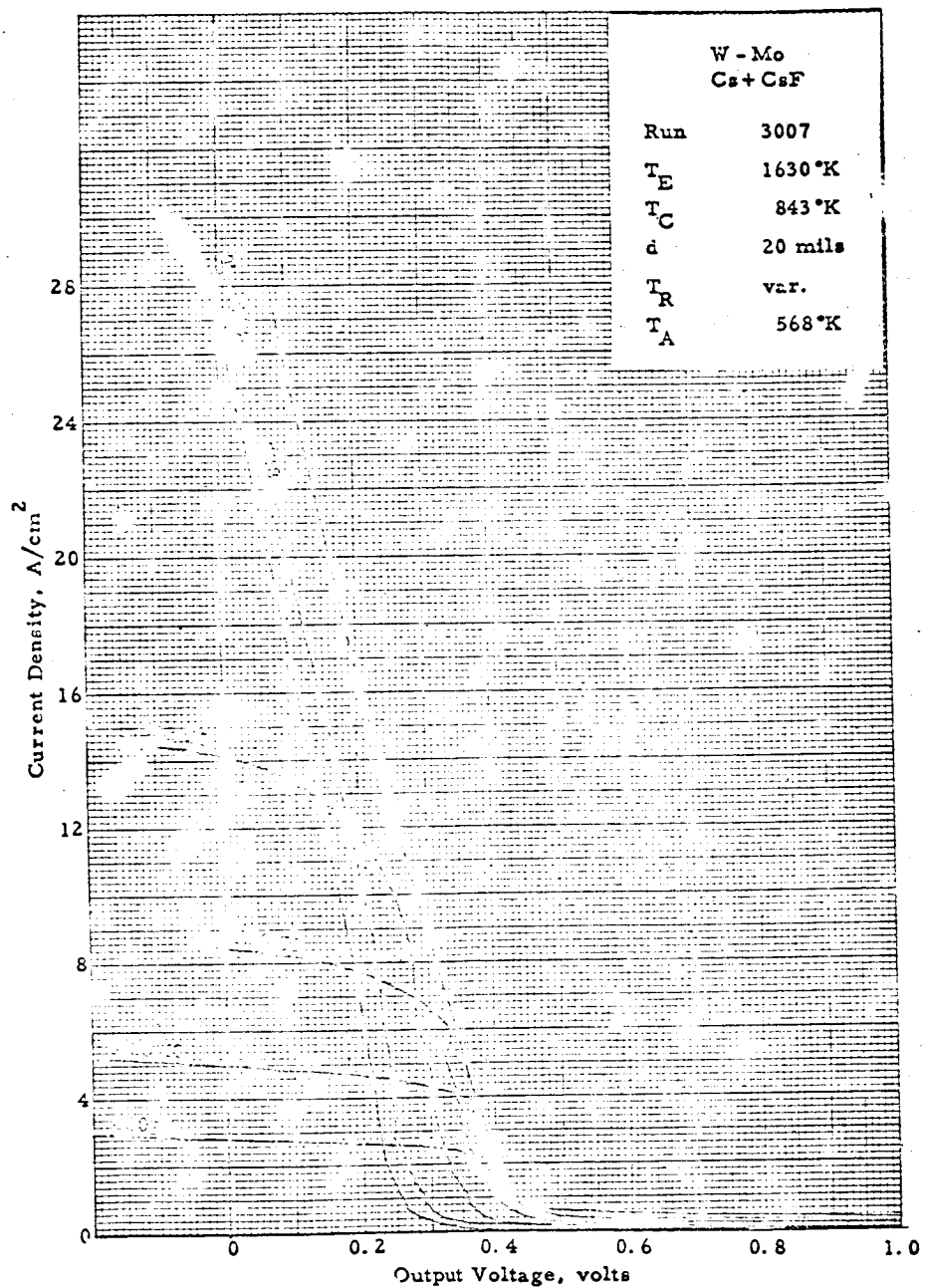
Figure VIII-12.  Typical Cs-plus-CsF Family.

246

| | W – Mo |
| | Cs + CsF |
| Run | 3016 |
| $T_E$ | 1910 °K |
| $T_C$ | 823 °K |
| d | 5 mils |
| $T_R$ | var. |
| $T_A$ | 623 °K |
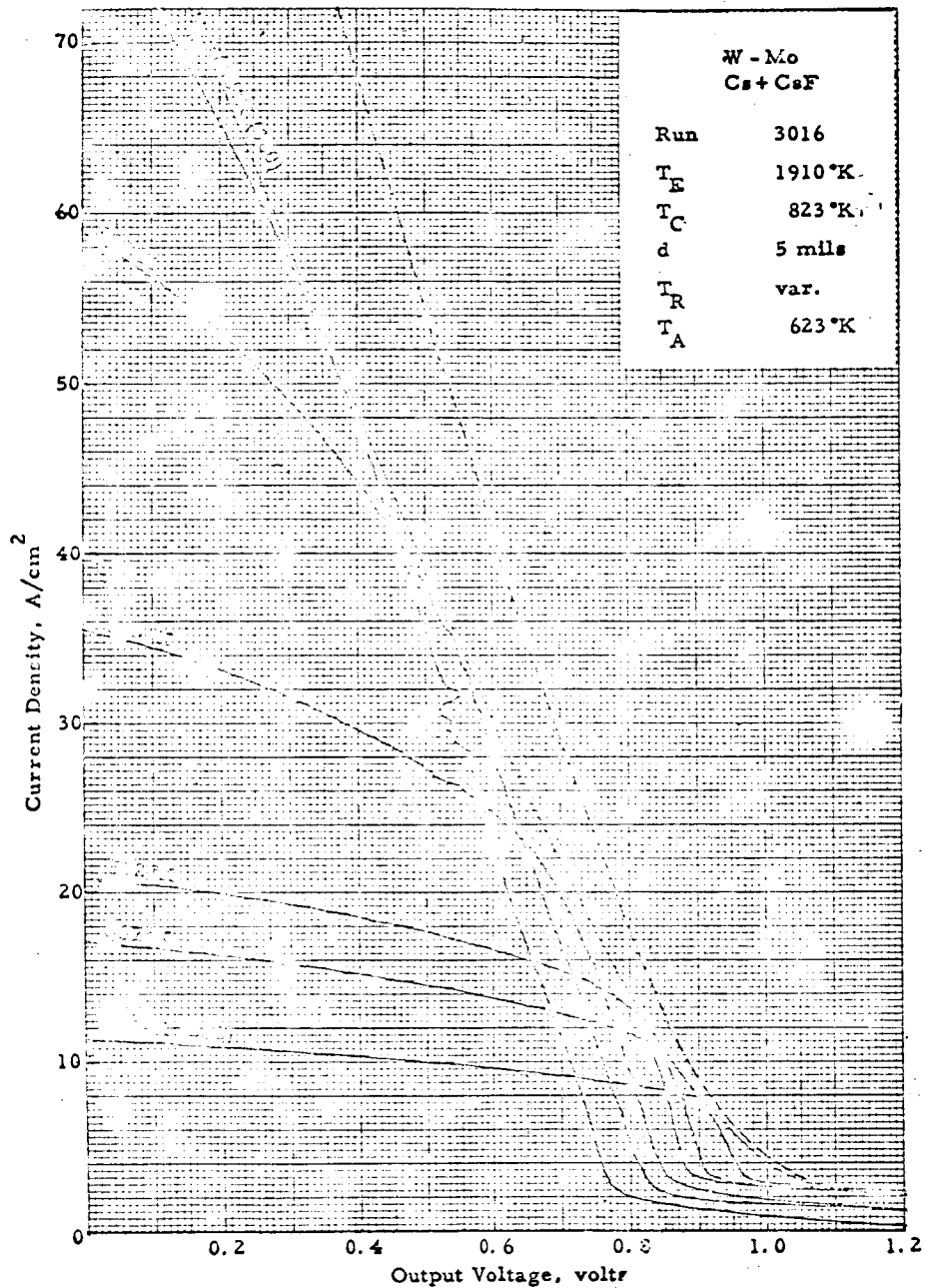
Figure VIII-13.  Typical Cs-plus-CsF Family.
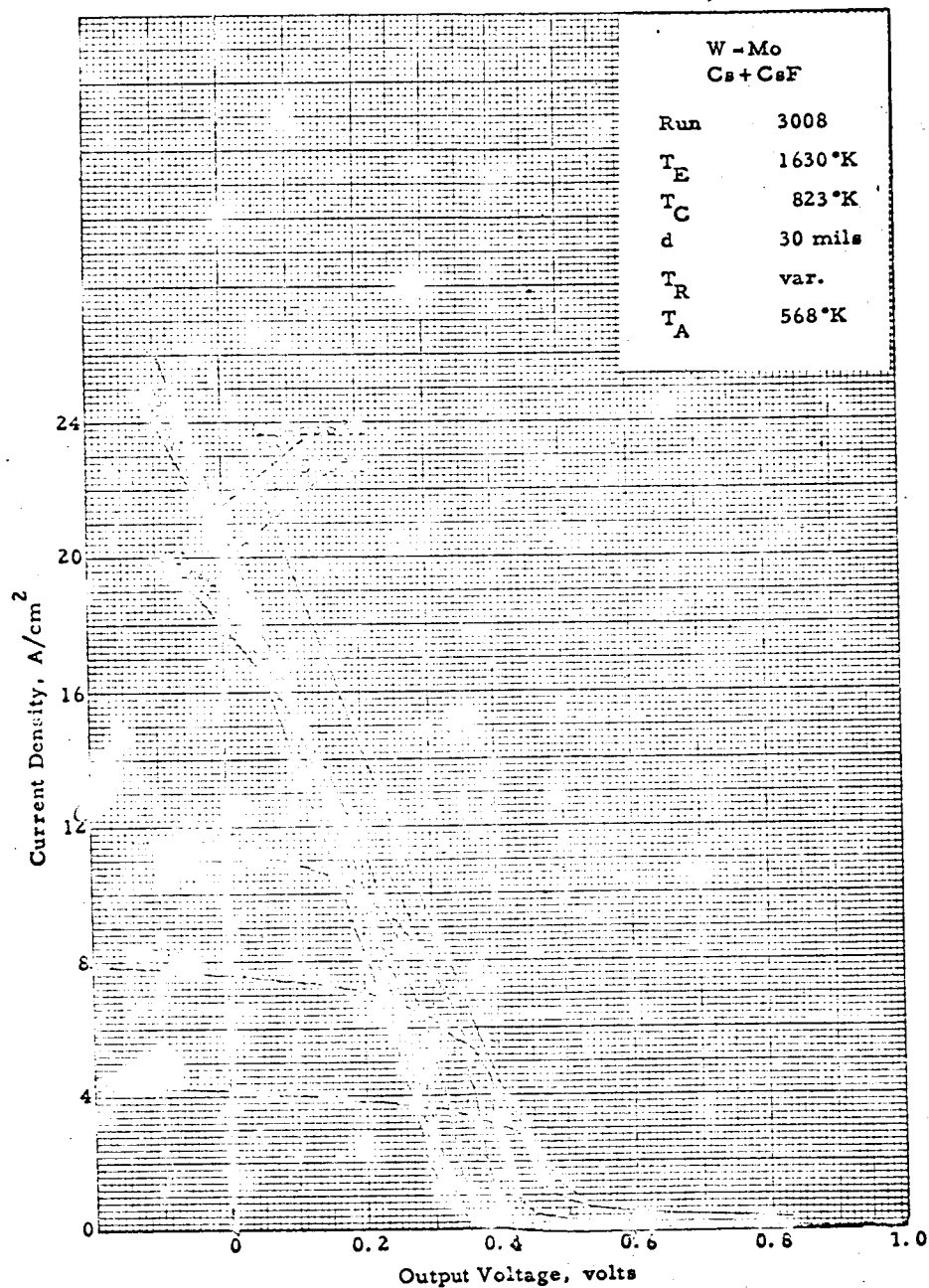
Figure VIII-14.   Typical Cs-plus-CsF Family.

248
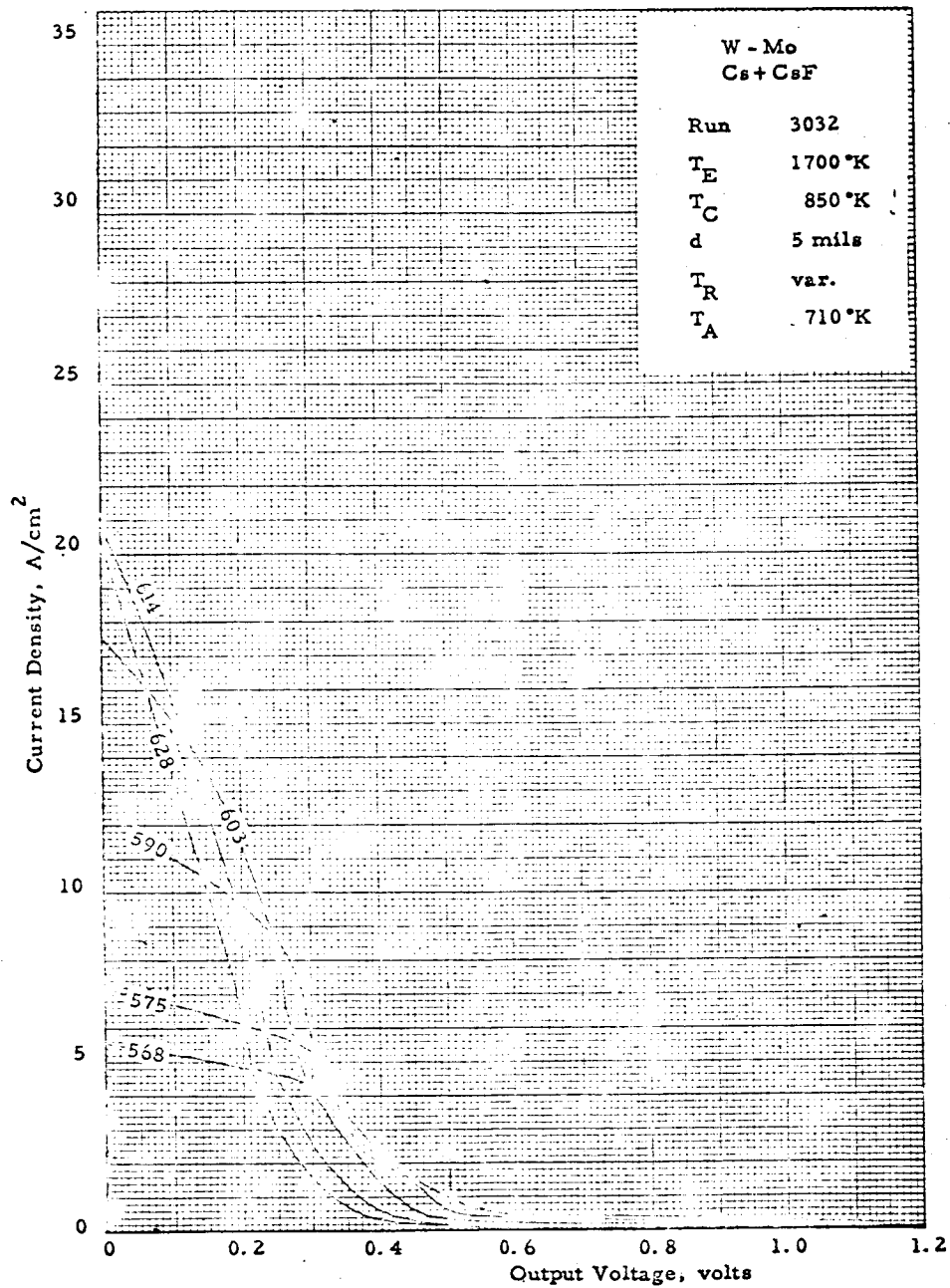
Figure VIII-15.   Typical Cs-plus-CsF Family.

249

Figure VIII-16. Typical Cs-plus-CsF Family.
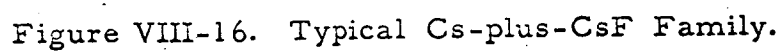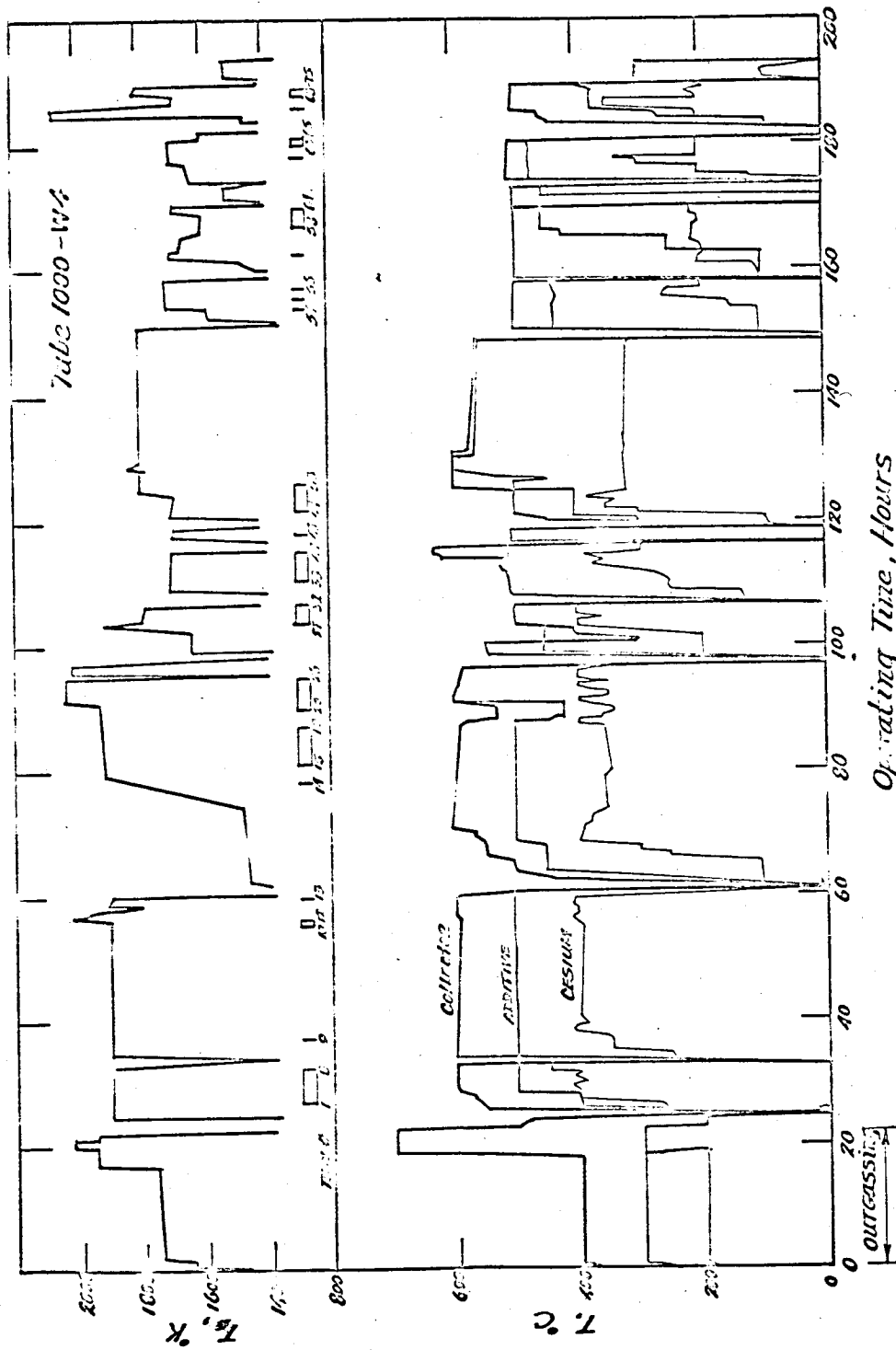
Figure VIII-17.  Temperature History of Outgassing and Test of Converter 1000.

At the conclusion of tests the converter was cut apart under an argon atmosphere and the various surfaces examined for fluoride deposits. A fine whitish film was observed on the collector and guard face, but the emitter surface was clean and shiny. Only about 10 percent of the original charge was recovered, and about 90 percent of this was in the reservoir rather than in the active portion of the test vehicle. A large portion of the original charge may have been lost during outgassing, when the reservoir was maintained at an elevated temperature for a relatively long period. For this reason a larger charge, outgassed at a lower temperature, was used in the second converter.

### Converter 3000

As described above, the performance of this converter was at first enhanced by the additive, and then, after about 28 hours of operation, the additive effect disappeared and the behavior of the device approached that of the previous converter, with its unusually high Cs pressure requirements and low power output. The temperature history chart is shown in Figure VIII-18.

At the conclusion of these tests, this converter was also cut apart under an argon atmosphere and examined for fluoride deposits. The appearance of this device was similar to No. 1000. The additive reservoir was also cut open, and the original 12 pellets were found to be almost intact. Apparently only a small amount of the additive ever reached the active portion of this test vehicle, but very little was lost from the reservoir prior to testing. Analysis of the collector assembly showed there was < 0.5 mg of fluoride which was not soluble, i. e. tightly bound to the metal surfaces.

### 2. Discussion

In order for the additive to modify the performance of the converter,
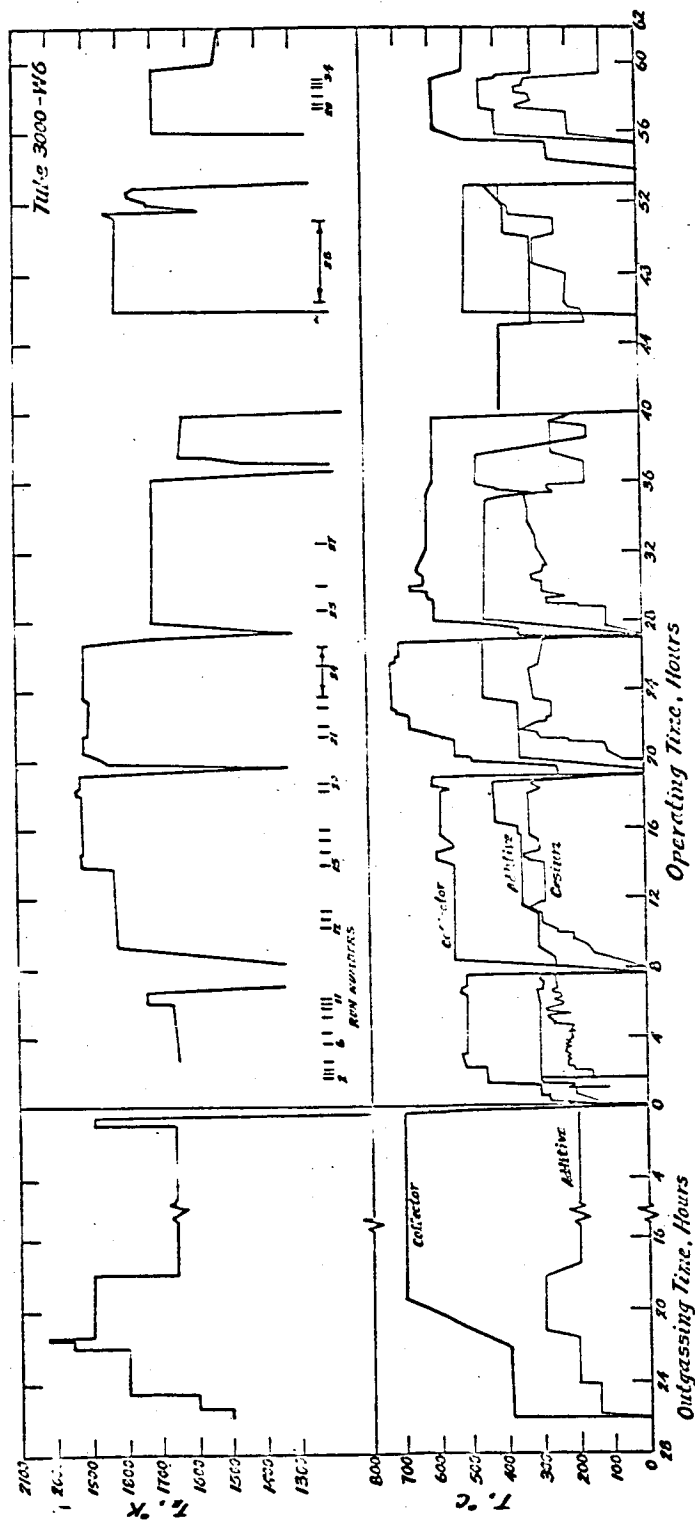
Figure VIII-18. Temperature History of Outgassing and Test of Converter 3000.

it must reach the active portions of the device, the emitter, collector and guard surfaces. There are three main processes limiting and controlling the transport of the CsF vapor from the pellets in the reservoir to the active surfaces. First the fluoride must evaporate from the pellets; it must then diffuse through the tubulation and diode spaces which are permeated with the Cs vapor, and finally the active surfaces must compete with the much larger inactive area for the fluoride that does get through.

At present the diffusion process is most susceptible to calculation, and, assuming no limitation imposed by the evaporation, and that the concentration of additive molecules in the active converter space is ten percent of the original concentration, an order-of-magnitude estimate can be made for the amount of fluoride per second diffusing from the reservoir. Since the CsF and Cs molecules are of about the same mass and size, collisions between the two will be important, and the diffusion constant of the fluoride will be greatly influenced by the Cs pressure.

For the purposes of this calculation the molecules are assumed to be identical and the diffusion constant the same as that for self diffusion. Figure VIII-19 shows the diffusion constant as a function of Cs reservoir temperature. For this plot, the equation:

$$D = \frac{\nu\lambda}{3}$$

was used, where $\nu$ is average molecular velocity and $\lambda$ the mean free path. Also shown is another more approximate formula:

$$D = \frac{1}{2p}$$

where p is the Cs pressure in atmospheres. Using this value for D, the diffusion rate down the additive reservoir tube tubulation was calculated for the boundary conditions shown in the sketch on the following page.

254
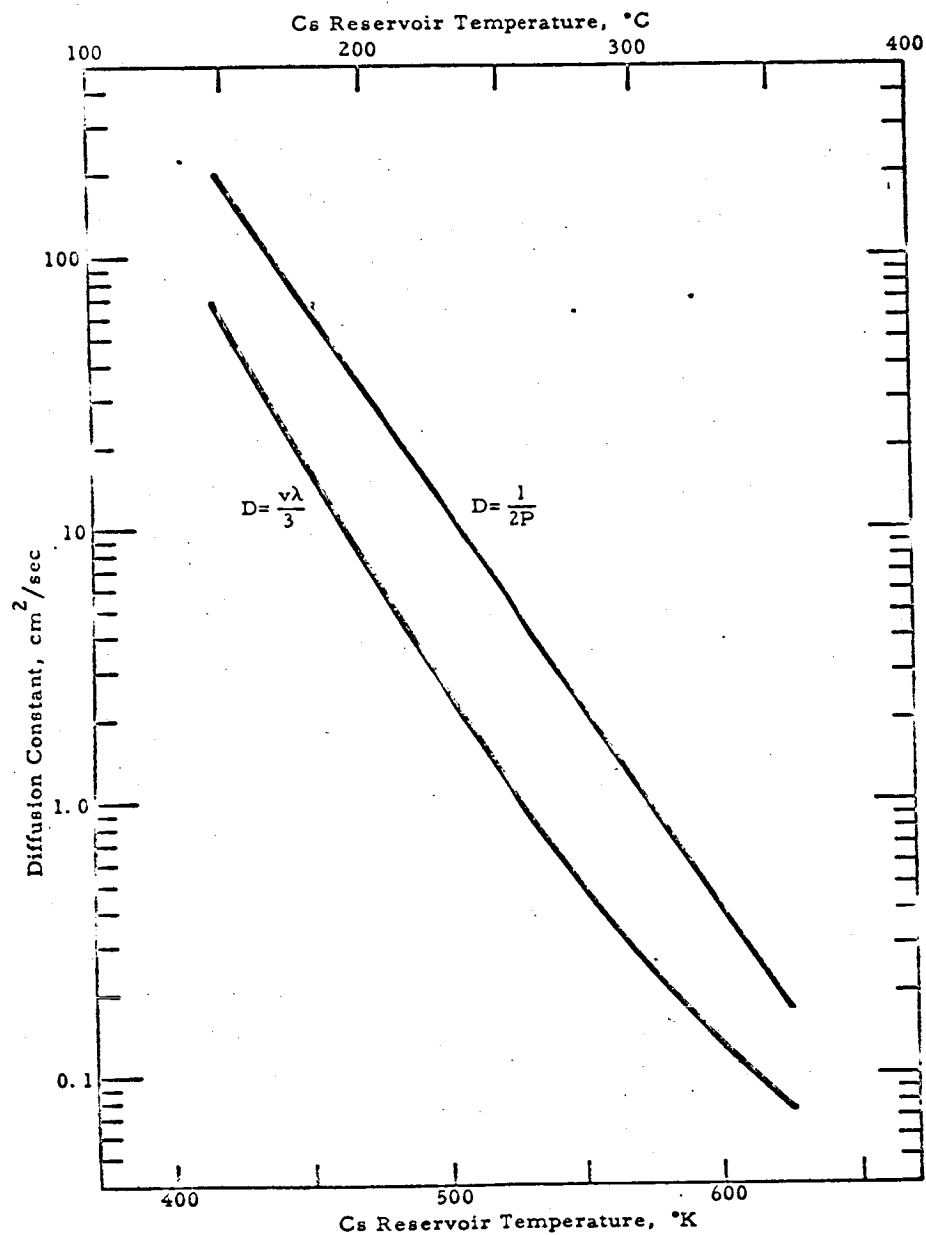
Figure VIII-19.  Diffusion Constant as a Function of
Cs Reservoir Temperature.

$$J = \frac{.9n_o}{l} D$$
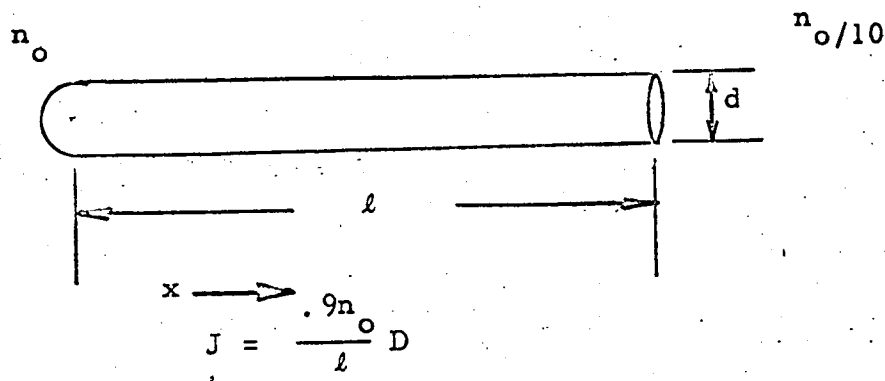
In steady state, the solution to the diffusion equation will be a straight line with uniform concentration gradient. The rate of flow J is then:

$$J = -D\nabla n = -Da$$

where $\nabla n$ is the concentration gradient or "a".

The initial concentration $n_o$ will be dependent on the additive pressure and hence on the reservoir temperature. Figure VIII-20 is plot of the rate of additive flow through the tubulation 7.5 cm in length and 0.5 cm in diameter for various cesium and fluoride temperatures. The dashed lines indicate possible error limits in the approximations. From this chart an outgassing time at 300°C fluoride reservoir temperature will result in the loss of about 170 mg of additive. This is an appreciable fraction of the original charge in converter 1000 and is consistent with the results of the tests. At a CsF reservoir temperature of about 300°C and a Cs temperature of about 300°C, the additive flux is only about 0.5 mg per hour. Most of the conditions of operation in converter 3000 correspond to this situation, and it seems likely that if any additive was absorbed in the diode space it would not be replenished. During outgassing and set-up sufficient additive may have been transferred in the absence of Cs, but during

256
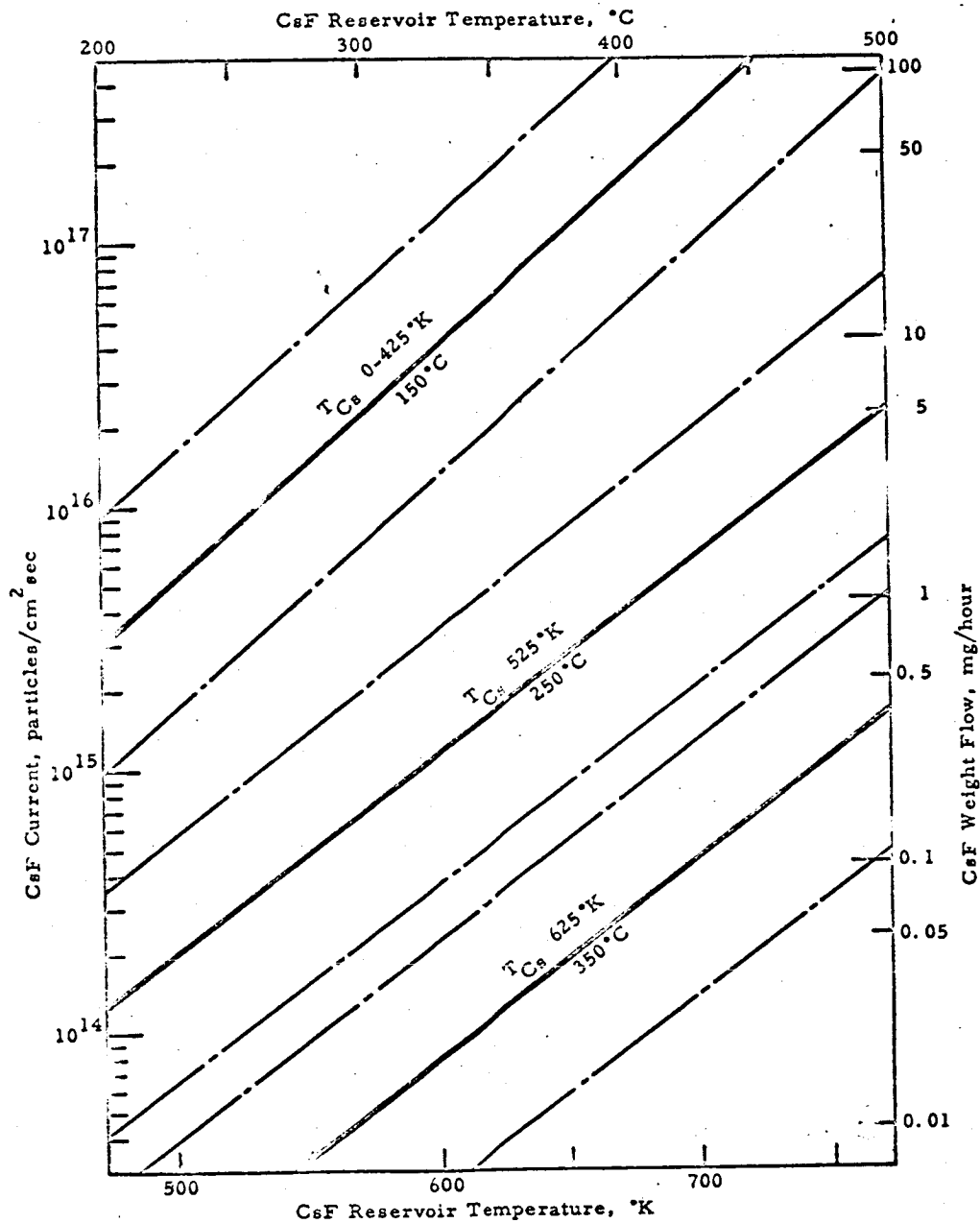
Figure VIII-20. Rate of Additive Flow for Various Cesium and Fluoride Temperatures.

operation this fluoride was gradually depleted and the behavior degraded to that of converter 1000.

## E.  CONCLUSIONS

The additive investigation described in this chapter had indicated the extent of the influence of the additives on device performance and the nature of its action.  It has also pointed out several problems in maintaining this performance.  The most significant change produced was the lowering of the cesium pressure corresponding to a given emitter temperature.  Because of the optimum Pd relationship, the lower-pressure device must operate at wider spacings, thereby relaxing mechanical construction of many practical devices.  One source of the action has been identified as the increased uncesiated emitter work function.  In the devices tested, however, it was found quite difficult to obtain this effect in the presence of cesium.  In the device having satis-factory behavior, the effect lasted only for a period of 28 operating hours out of a total of about 300 hours on the three devices.

The improved performance obtained at wider spacings is immedi-ately evident from the comparison shown in Figures VIII-21, -22 and -23 for J-V envelopes and VIII-24, -25 and -26 for power output. These figures compare Cs-only data with additive data at roughly the same spacing.  Significantly greater power was achieved at wider spac-ings.  However, if the characteristics are compared regardless of spacing, they are similar except that the additive optimizes at about 10 times the cesium-only spacing.  Figures VIII-27 and -28 illustrate this comparison.  These eight figures summarize the changes produced by the introduction of CsF into the tungsten emitter - molybdenum collector converter.

258
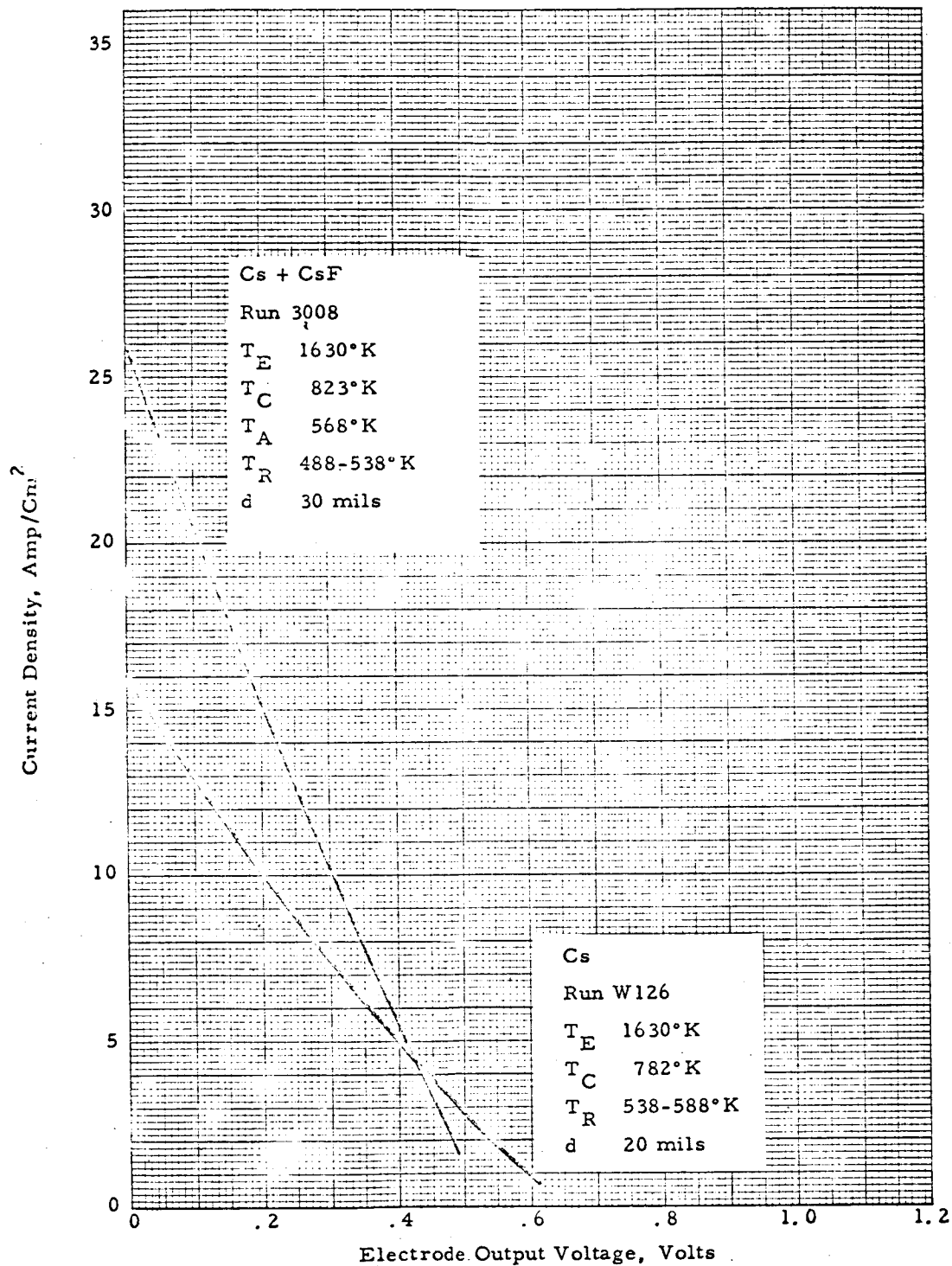
Figure VIII-21. Comparison of J-V Envelopes with and without Additive.
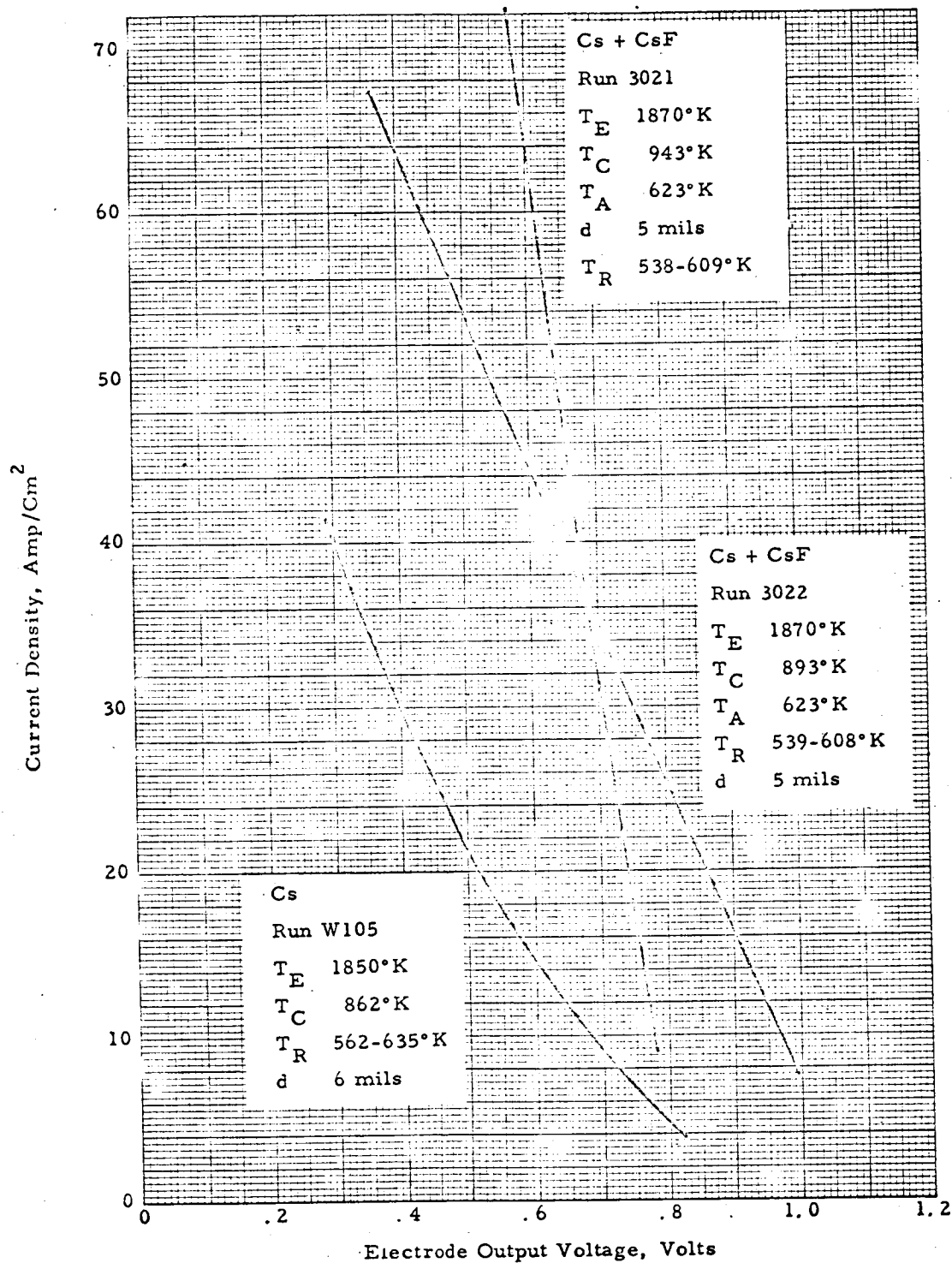
Figure VIII-22. Comparison of J-V Envelopes with and without Additive.

260

Figure VIII-23. Comparison of J-V Envelopes with and without Additive.

Within the figure:

Cs + CsF

Run 3016

$T_E$    1910°K

$T_C$    823°K

$T_A$    623°K

$T_R$    558-608°K

d     5 mils

Cs

Run W112

$T_E$    1950°K

$T_C$    890°K

$T_R$    573-645°K

d     6 mils

Current Density, Amp/Cm$^2$

Electrode Output Voltage, Volts

Figure VIII-24. Comparison of Power Output with and without Additive.

262
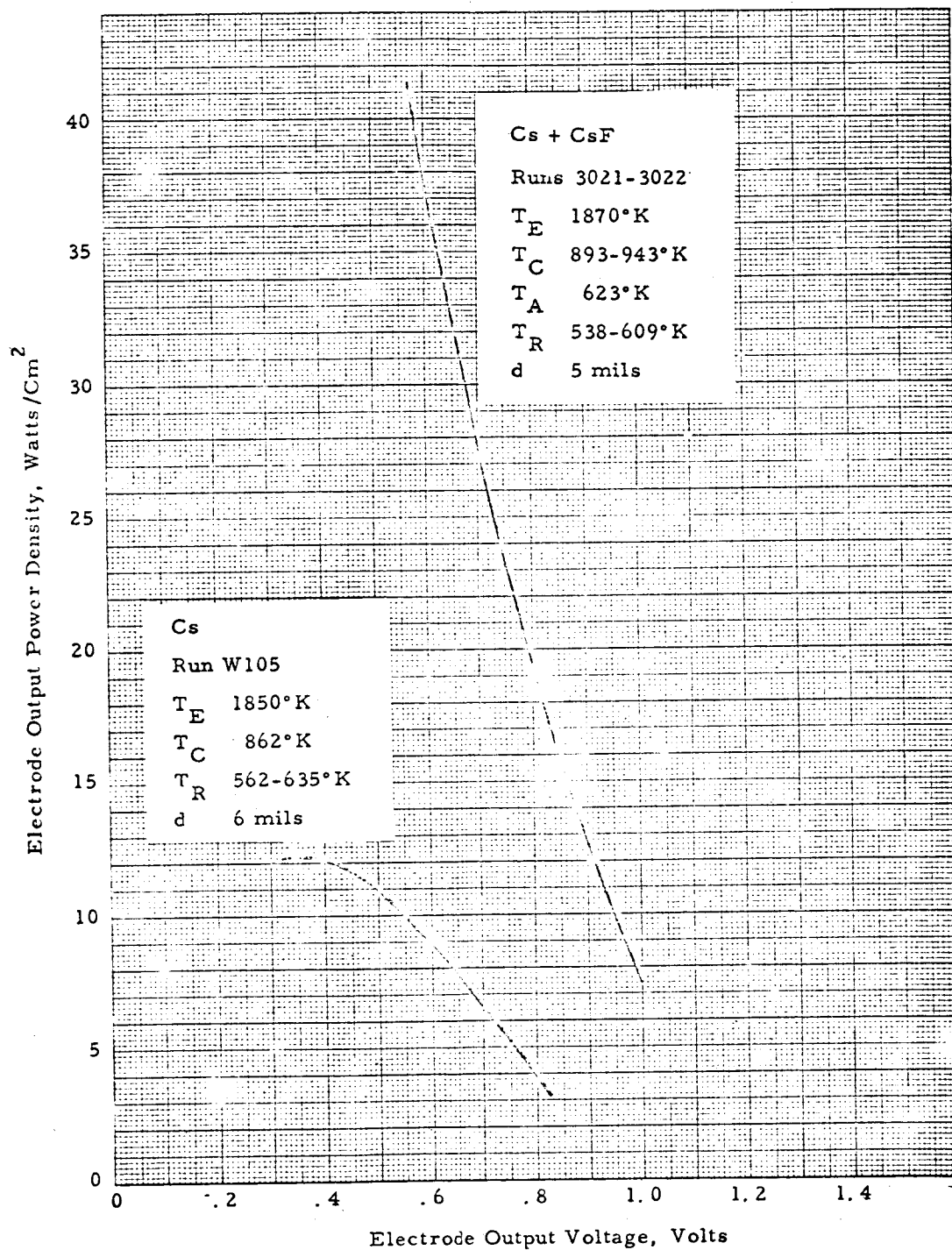
Figure VIII-25. Comparison of Power Output with and without Additive.
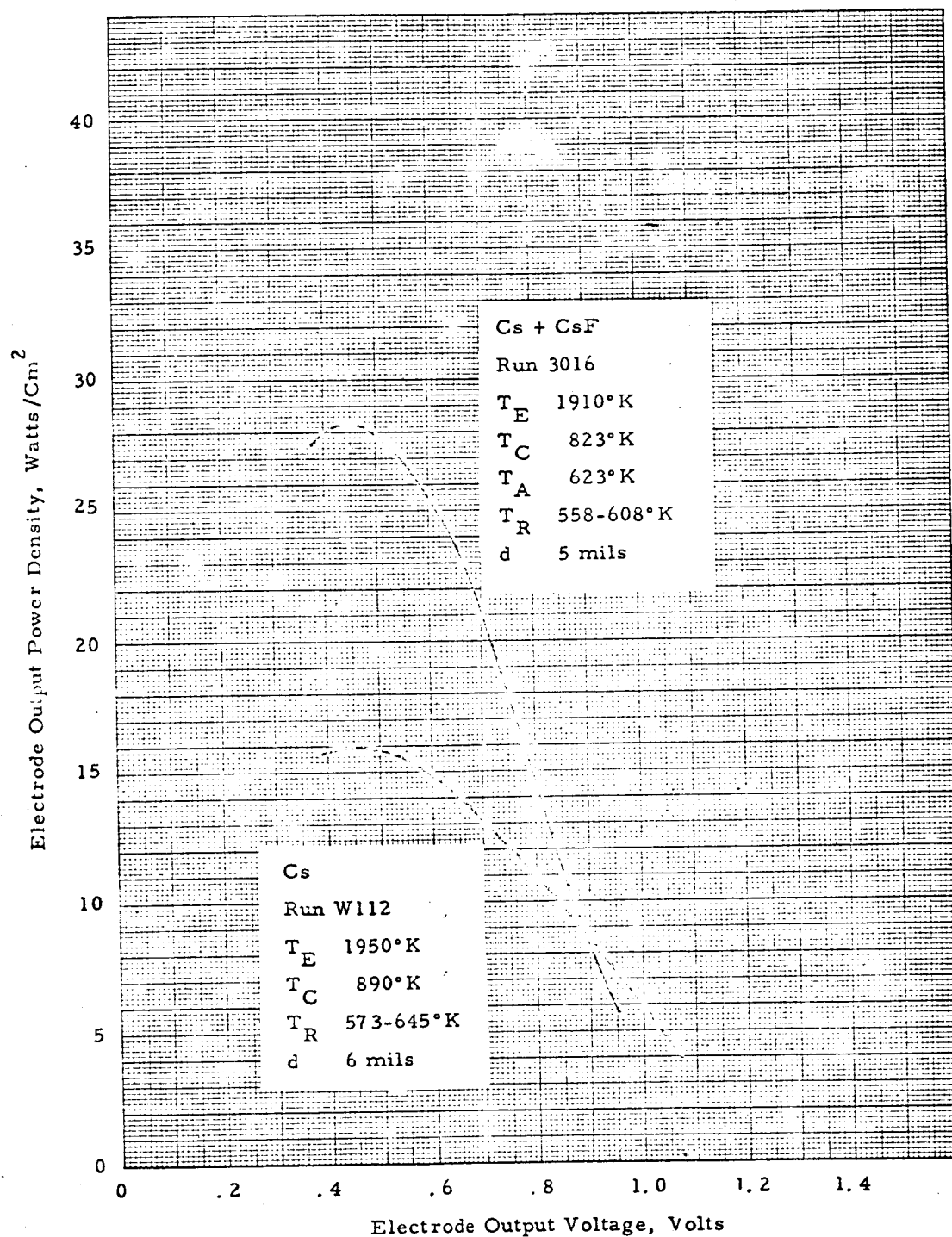
Figure VIII-26. Comparison of Power Output with and without Additive.

264
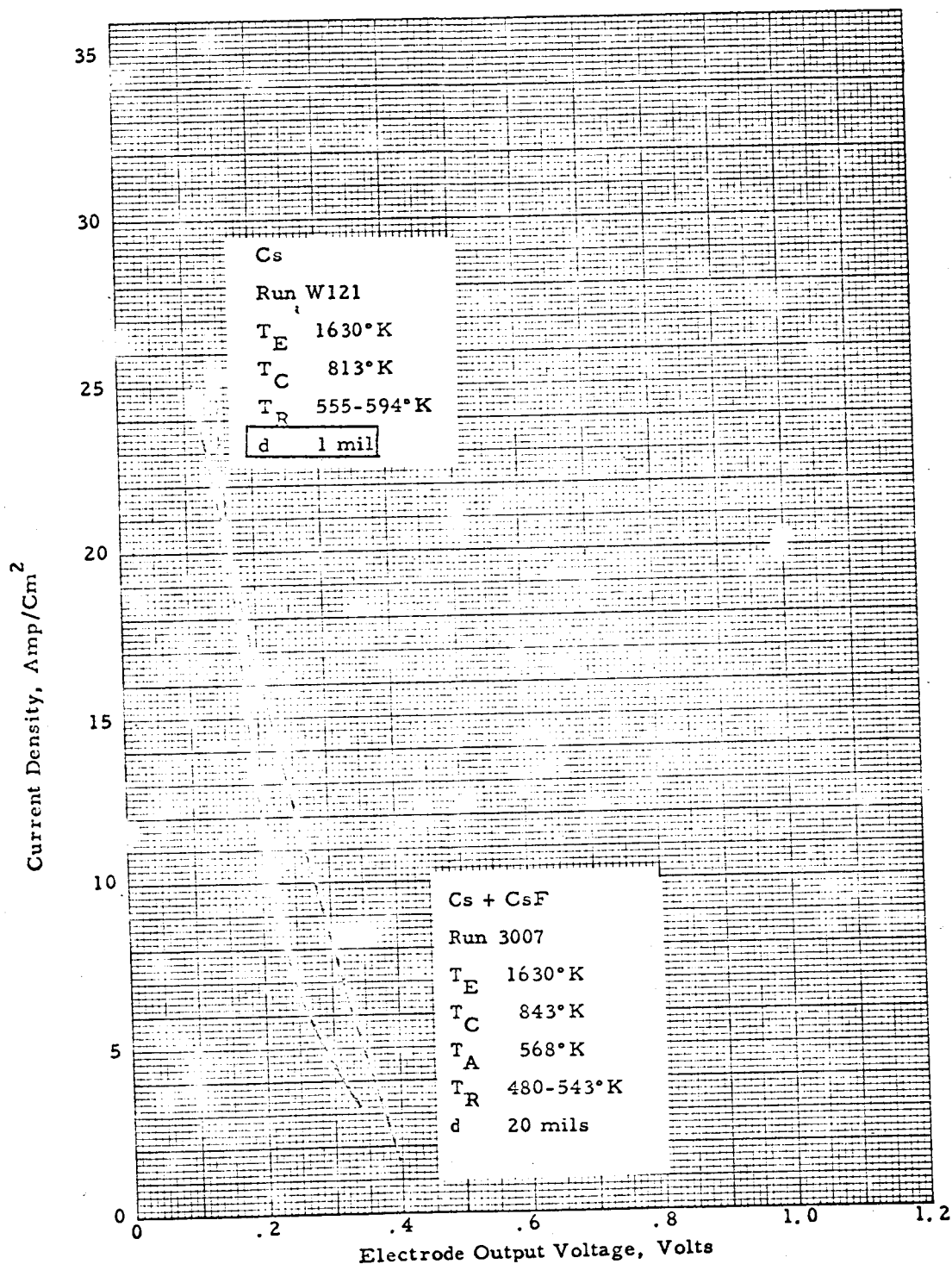
Figure VIII-27.   Comparison of Optimum J-V Envelopes with and without Additive.
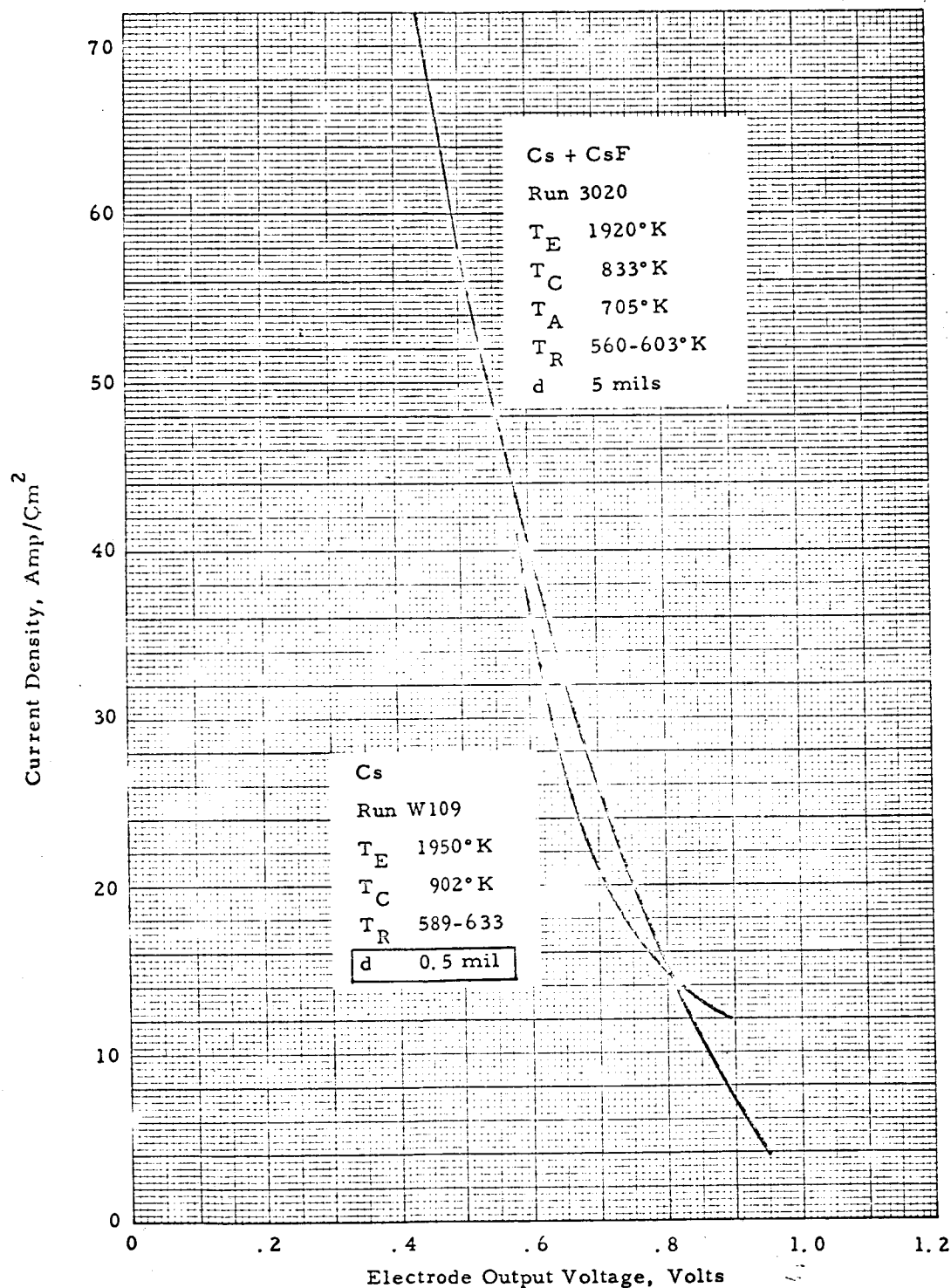
Figure VIII-28.  Comparison of Optimum J-V Envelopes
with and without Additive.

266

At present, there is not enough data to evaluate any changes in fully optimized performance or to investigate changes in collector work function occurring in the presence of CsF. It is believed that the loss of additive effect was due to the inability of the fluoride to diffuse through the high-pressure cesium vapor. It should be possible to counteract this by including in the testing procedure a diffusion period during which the cesium reservoir would be maintained at low temperature while that of the additive is high. Further experiments must be carried out in this direction.

These experiments have indicated that the use of surface additives through the modification of electrode work functions has introduced a new parameter into device design. It is thus possible to relax some of the restrictions previously imposed on spacing. Additional experiments will be necessary to determine whether these advantages can be maintained, or additional benefits can be obtained at higher pressures.

The original data for these figures are shown in Figures VIII-10 through VIII-14, and VIII-29.

267

| W – Mo | |
|---|---|
| Cs + CsF | |
| Run | 3020 |
| $T_E$ | 1920°K |
| $T_C$ | 833°K |
| d | 5 mils |
| $T_R$ | var. |
| $T_A$ | 705°K |
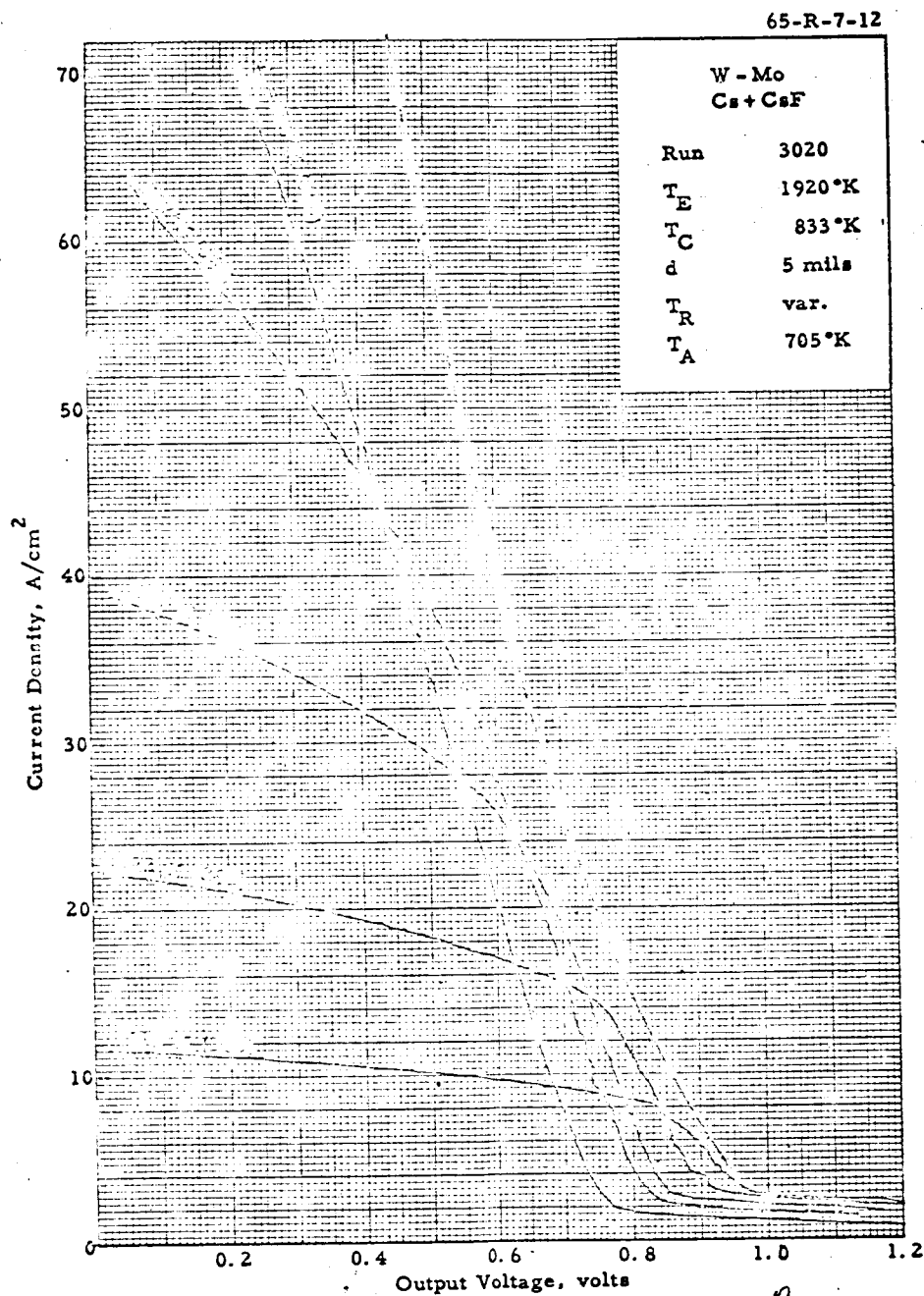
Figure VIII-29.  Typical Cs-plus-CsF Family.

268

# CHAPTER IX

## ANALYSIS

In this chapter a number of analytical models are developed to explain the behavior of a cesium diode under various operating conditions. In section A a simple theory is developed to describe the diode operation in the retarding region. In section B an attempt is made to explain the volt-ampere characteristics of the ignited mode by postulating a dark and a bright plasma. A different model is suggested in section C that describes the ignited mode of discharge quite successfully. This model has been correlated with experimental data in section D.

## A. DEPENDENCE OF APPARENT COLLECTOR WORK FUNCTION ON SPACING

Determination of collector work function by the retarding method was described in Chapter VI. It was also shown that the work function measured by this technique depends on the interelectrode spacing. A quantitative investigation of this behavior is of appreciable importance for the understanding of various transport mechanisms of electrons in the retarding region. This information will also result in a more accurate measurement of work function in fixed-spacing thermionic diodes, since it provides the means of extrapolating the measured values to zero spacing.

The predicted motive diagram in the retarding region appropriate for collector work function measurement is shown in Figure IX-1. Deviation of the measured work function from the true value can be attributed to electron scattering. To obtain a first-order analytical relation for this effect, two cases are considered: long and short electron mean free path, $\lambda_e$, as compared with spacing, d.

### 1. Short Mean-Free-Path Solution

If all other effects were absent, the electron current according to Figure IX-1 would be given by:

269
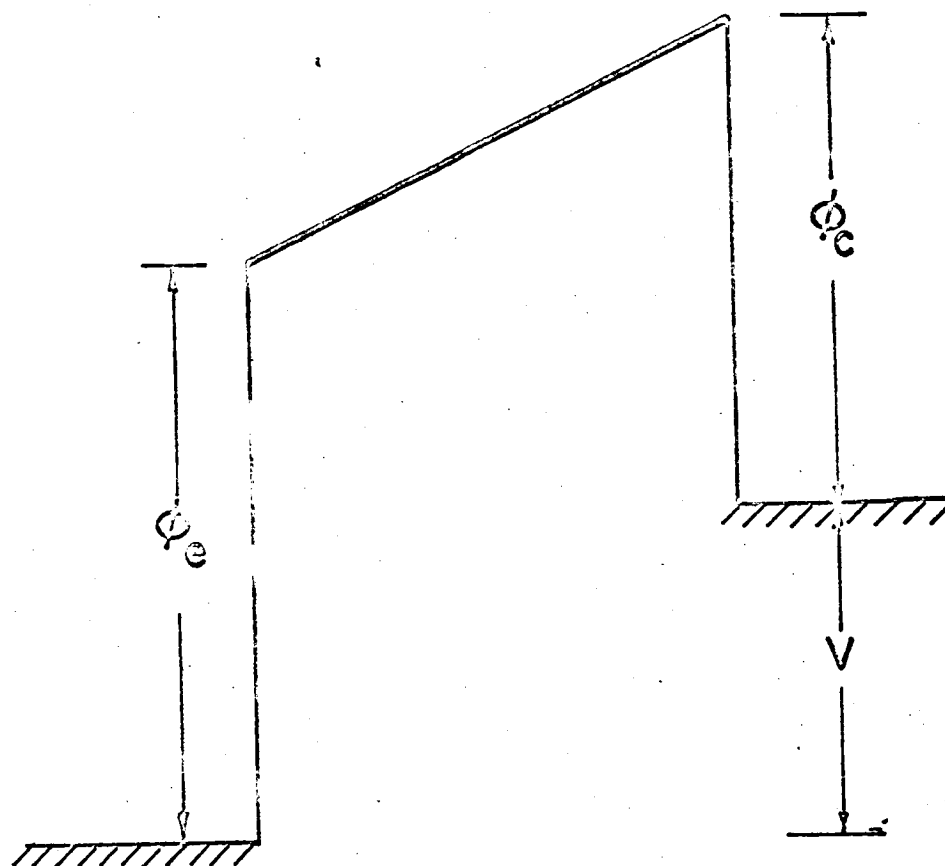
Figure IX-1.   Motive Diagram — Retarding Region.

270

$$J_b = AT_e^2 \exp\left[-\frac{\phi_c + V}{kT_e}\right] \tag{1}$$

where
$J_b \equiv$ electron current

$A \equiv$ Richardson constant

$T_e \equiv$ emitter temperature

$\phi_c \equiv$ collector work function

$V \equiv$ output voltage

$k \equiv$ Boltzmann constant

The condition $d/\lambda \gg 1$ implies a large number of collisions, and therefore the diffusion equation applies. Assuming that the recombination rate of electrons is negligible, the diffusion equation,

$$\nabla^2 n = 0, \tag{2}$$

where n is the electron density, is solved with the following boundary conditions:

At the emitter

$$\frac{v_e n}{4} - \frac{1}{2} D_e \nabla n = J_b \qquad \text{at } x = 0 \tag{3}$$

At the collector

$$\frac{v_e n}{4} + \frac{1}{2} D_e \nabla n = 0 \qquad \text{at } x = d \tag{4}$$

where:
$x \equiv$ distance from emitter to collector

$d \equiv$ interelectrode spacing

$v_e \equiv$ average electron velocity

$D_e \equiv$ electron diffusion coefficient $= \dfrac{v_e \lambda_e}{3}$

271

Solution of equation (2) with boundary conditions (3) and (4) yields:

$$\frac{J}{J_b} = \frac{1}{1 + \frac{3}{4}\frac{d}{\lambda_e}}$$ (5)

J is the current that is attenuated due to scattering and corresponds to the apparent collector work function $\phi_{ca}$. Hence

$$\Delta\phi_c \equiv \phi_{ca} - \phi_c = kT_e \, \ln\left(1 + \frac{3}{4}\frac{d}{\lambda_e}\right)$$

where d is the spacing.

The above equation shows the dependence of apparent collector work function on emitter temperature and spacing. This relationship remains to be checked against experimental data at high $d/\lambda$.

2.    Long Mean-Free-Path Solution

In this case the diffusion equation does not apply, and a collision probability must be computed. The electron current that can reach the collector, in the absence of all collisions, is again denoted by $J_B$. Hence, when collisions are present, the actual current will be given by:

$$J = J_b p$$ (6)

where P is the probability that an electron leaving the emitter surface, toward the collector, will reach the collector. For this long mean-free-path case, the simplest expression for p is

$$p = e^{-\Omega d/\lambda_e} \tag{7}$$

where $\Omega$ is the fraction of scattered electrons that are reflected towards the emitter. Using expressions of the type (1), we get

$$\Delta \phi_c \equiv \phi_{ca} - \phi_c = kT_\epsilon \, \Omega d/\lambda_e. \tag{8}$$

This equation shows a linear dependence of apparent collector work function on spacing and emitter temperature, for $d/\lambda \ll 1$. The limited data taken at variable spacing (Figure VI-24) demonstrates this effect. At this time more variable-spacing data is needed at different emitter temperatures.

## B.   ANALYSIS OF J-V CHARACTERISTICS IN THE IGNITED MODE

Since all power-producing converters are normally operated in the ignited mode, the need for improved analytical understanding of this mode is obvious. Therefore, this program has closely coupled the experimental work with a strong analytical effort. In the following pages the initial formulation of the problem is presented.

Warner[10] has analyzed the extinguished mode of the volt-ampere curve with the assumptions that the only ion source is at the emitter surface, and the electrons arriving into the plasma from the emitter are thermalized and attain Maxwellian distribution.

A first-order analysis of the ignited mode is attempted by modifying Warner's solution to include an ion source at the collector side of

the plasma. In section C of this chapter, the ignited mode is treated
with the assumption that the interelectrode spacing consists of a neutral
field-free plasma, bounded by emitter and collector sheaths. The two
treatments are independent and consistent with the models chosen. The
validity of the physical models, however, depends on the operating con-
ditions of the diode and must be determined from experimental data.

The basic assumptions in this treatment are as follows:

1)    The interelectrode volume is divided into sheath and plasma
regions.

2)    In the plasma region $n_e \approx n_p = n$, where $n_e$ and $n_p$ are the
electron and ion densities, respectively.

3)    The electrons in the plasma region have Maxwellian distri-
bution.

The electron and ion currents in the plasma are due to density
gradient and electric field. The basic equations governing these quan-
tities are the following:

$$J_e = -D_e \nabla n - \mu_e E n \tag{9}$$

$$J_p = -D_p \nabla n + \mu_p E n \tag{10}$$

where      $J \equiv$ current

$D \equiv$ diffusion coefficient

$\mu \equiv$ mobility $= \dfrac{e}{kT} D$

$E \equiv$ electric field

The subscripts $e$ and $p$ refer to electron and ion, respectively.

Eliminating the electric field in (9) and (10), we get

$$\nabla n = -\frac{1}{2}\left(\frac{J_e}{D_e} + \frac{J_p}{D_p}\right). \tag{11}$$

In the case of planar emitter and collector surfaces, equation (11) gives:

$$n(x) = n(0) - \frac{1}{2}\left(\frac{J_e}{D_e} + \frac{J_p}{D_p}\right)x \tag{12}$$

where $n(0)$ is the particle density at $x = 0$. To obtain the electron and ion currents, a motive diagram with the appropriate boundary conditions must be chosen.

1.  **Ion Source at Collector Edge of the Plasma Only, Positive Emitter Sheath**

    Consider the motive diagram shown in Figure IX-2. $V_e$ and $V_p$ are the sheath heights at the emitter and collector ends, respectively, of the plasma. We define two dimensionless quantities:

$$\eta_o \equiv \frac{V_e}{kT_e} \qquad \text{and} \qquad \eta_d \equiv \frac{V_p}{kT_e}. \tag{13}$$

If we consider the plasma level as the reference point, $\eta_o > 0$ and $\eta_d < 0$.

   The boundary conditions are as follows:

   1) The ion source is in the bright plasma only.

   2) There are no electrons flowing from the bright plasma to the dark plasma.
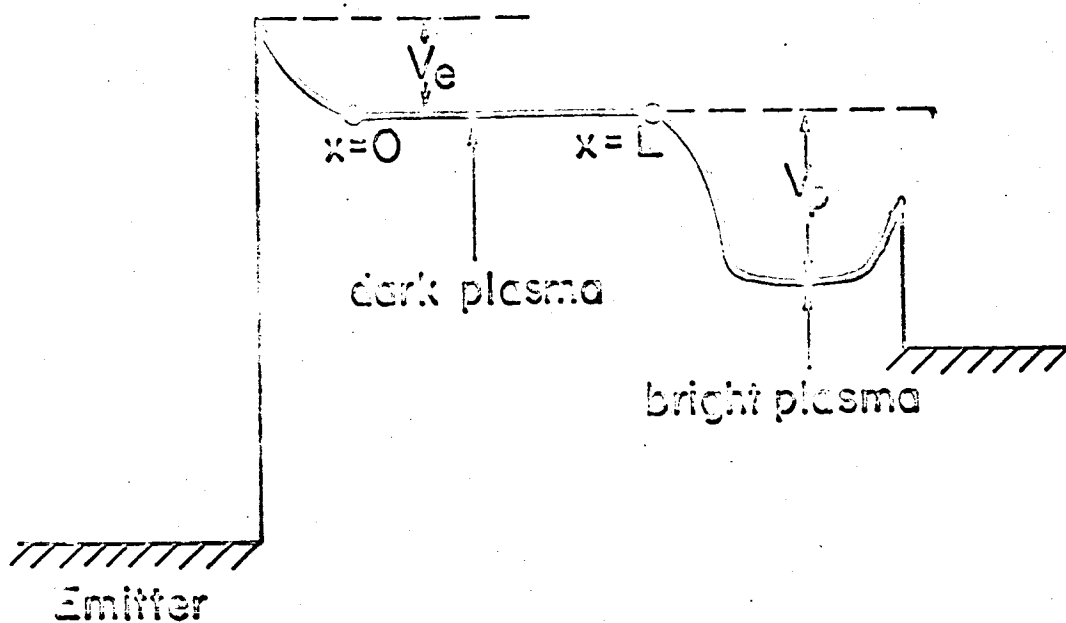
Figure IX-2. Motive Diagram for Positive Emitter Sheath.

276

Expressed mathematically,

$$v_e \, n(d) - 2J_e = 0 \tag{14}$$

$$J_p = \left( \frac{n(d)v_p}{4} + \frac{J_p}{2} \right) e^{\eta_d} - q_p \tag{15}$$

$$J_e = J_{es} - \left( \frac{n(0)v_e}{4} - \frac{J_e}{2} \right) e^{-\eta_o} \tag{16}$$

$$\frac{n(0)v_p}{4} + \frac{J_p}{2} = 0 \tag{17}$$

where    $v$   $\equiv$ average velocity

$J_{es}$ $\equiv$ electron source strength at the emitter,
i.e. saturation current

$q_p$ = ion source strength in the bright plasma

There are four unknowns, $J_p$, $e^{-\eta_o}$, $e^{\eta_d}$ and $n(0)$, to be found for every $J_e$ from equations (14), (15), (16) and (17). For algebraic convenience, we will use the quantity defined by Warner,

$$R \equiv \frac{D_e}{D_p} \frac{J_p}{J_e} . \tag{18}$$

Hence the unknowns are now R, $e^{-\eta_o}$, $e^{\eta_d}$ and $n(0)$. Algebraic manipulation of equations (14) and (15) gives:

277

$$e^{\eta_d} = \frac{2R\left[1 + \frac{q_p}{J_p}\right]}{R + \frac{\lambda_e}{\lambda_p}} = \frac{2\left[R\,\frac{D_e}{D_p} + \frac{q_p}{J_e}\right]}{R\,\frac{D_e}{D_p} + \frac{v_p}{v_e}} \tag{19}$$

where we have used the relation $D = \frac{1}{3}\,v\lambda$, and $\lambda$ is the mean free path. Equations (12) and (14) give:

$$J_r \equiv \frac{n_o v_e}{4} = \frac{J_e}{2}\left[1 + \frac{3d}{4\lambda_e}(1 + R)\right]. \tag{20}$$

Equations (16) and (20) give:

$$e^{-\eta_o} = \frac{1 - \frac{J_e}{J_{es}}}{\frac{3d}{8\lambda_e}\,\frac{J_e}{J_{es}}(1 + R)} \tag{21}$$

Equations (17) and (20) give:

$$R = -\,\frac{1 + \frac{3d}{4\lambda_e}}{\frac{3d}{4\lambda_e} + \frac{\lambda_p}{\lambda_e}}. \tag{22}$$

Note that, if $d \gg \lambda_e$, $R \approx -1$.

Hence the unknowns are determined. However, this solution, as well as the solutions of the following cases, should now be checked by Poisson's Equation to make sure that the assumption $n_e \approx n_p = n$ was justified.

These results can be expressed in other terms to check with experimental data. Equations (21) and (22) can be reduced to:

$$\frac{J_{es}}{J_e} = 1 - \frac{1}{2} \frac{1 - \frac{\lambda_p}{\lambda_\epsilon}}{1 + \frac{4\lambda_p}{3d}} e^{-\eta_o} \tag{23}$$

Equation (23) shows how the ratio of saturation current to the actual current passing through the dark plasma is dependent on spacing and mean free path.

2. **Ion Source at Emitter and Collector Edges of the Plasma, Positive Emitter Sheath**

Consider the motive diagram of the previous section (Figure IX-2). Under the conditions where surface ionization is also an important source of ions, this effect must be included in the boundary conditions. In this case the boundary conditions (14), (15) and (16) are valid, but (17) must be replaced by:

$$J_{ps} e^{-\eta_o} = \frac{n(C)v_p}{4} + \frac{J_p}{2} \tag{24}$$

where $J_{ps}$ is the surface ion source strength.

279

The results are given by equations (19), (20) and (21), along with

$$1 - \frac{J_e}{J_{ps}} = \frac{1}{\beta}\left(\frac{3d}{4\lambda_e}\right)^2 \left(\frac{1+R}{2}\right)^2 \left(\frac{J_e}{J_{ps}}\right)^2 \left[1 + \frac{1 + \frac{\lambda_e}{\lambda_p}R}{(1+R)\frac{3d}{4\lambda_e}}\right] \qquad (25)$$

where $\quad \beta = \dfrac{v_e}{v_p}\dfrac{J_e}{J_{ps}}$ .

The parameter $R$ can be eliminated in equation (25) by equation (15) to give:

$$\frac{J_{es}}{J_e} = \frac{\left(1 - \frac{\lambda_p}{\lambda_e}\right)\frac{e^{\eta_o}}{2} - \left(1 + \frac{4\lambda_p}{3d}\right)e^{2\eta_o}}{\beta - \left(1 + \frac{4\lambda_p}{3d}\right)e^{2\eta_o}} \qquad (26)$$

This relation gives the ratio of saturation current to the actual current through the dark plasma for the more general case where ions are produced both in the bright plasma and on the emitter surface. For the case where surface ionization is negligible, $\beta = 0$, and equation (26) will become identical to equation (23).

3.    Ion Source at Emitter Side of Plasma Only, Negative Emitter Sheath

The motive diagram may also have the characteristics shown in Figure IX-3, i.e., $\eta_o < 0$, $\eta_d < 0$. There are two kinds of boundary conditions that may be used, which correspond to different states of

281
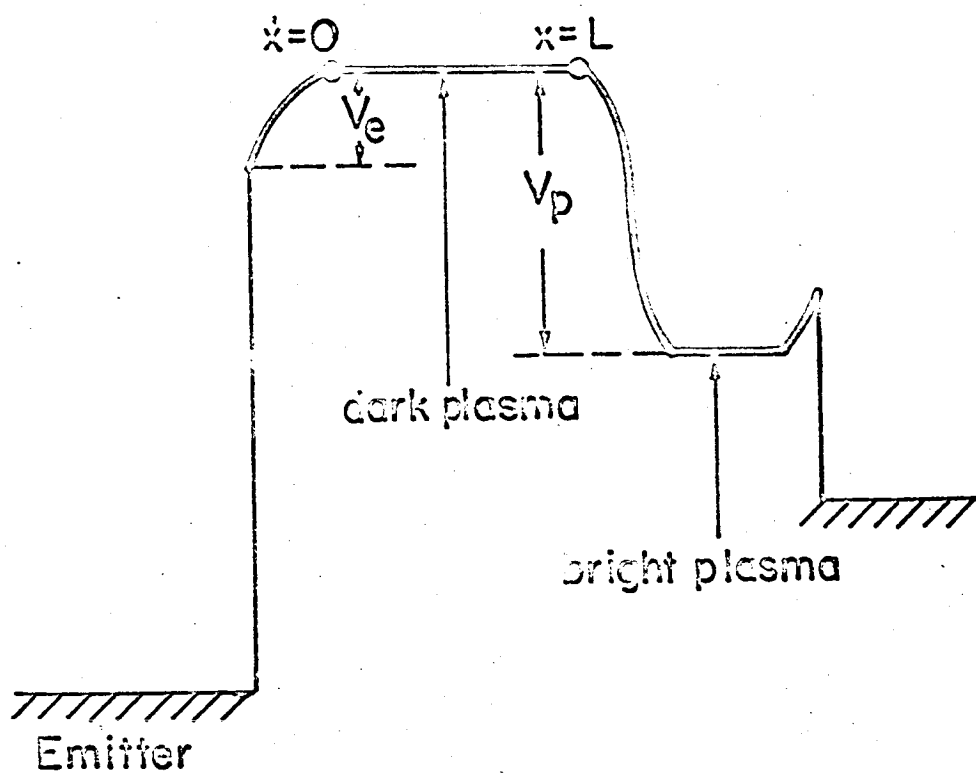
Figure IX-3.   Motive Diagram for Negative Emitter Sheath.

operation. The first kind, which will be treated in this section, is when the only source of ions is in the bright plasma. The second kind is when there is a source of ions at the emitter face as well as that in the bright plasma, and this will be treated in the next section. The boundary conditions of the first kind are expressed by the following equations:

$$v_e n(d) - 2J_e = 0 \tag{27}$$

$$J_p = \frac{n(d)v_p}{4} + \frac{1}{2} J_p e^{\eta_d} q_p \tag{28}$$

$$J_{es} e^{\eta_o} - \frac{n(0)v_e}{4} + \frac{J_e}{2} = J_e \tag{29}$$

$$J_p = -\left(\frac{n(0)v_p}{4} - \frac{J_p}{2}\right)e^{\eta_o} \tag{30}$$

Equations (27) and (28) give

$$e^{\eta_d} = \frac{2R\left[1 + \dfrac{q_p}{J_p}\right]}{R + \dfrac{\lambda_e}{\lambda_p}} = \frac{2R\left[\dfrac{D_e}{D_p} + \dfrac{q_p}{J_p}\right]}{R\,\dfrac{D_e}{D_p} + \dfrac{v_p}{v_e}} \tag{31}$$

Equations (12) and (27) give:

$$J_r \equiv \frac{n_o v_e}{4} = \frac{J_e}{2}\left[1 + \frac{3d}{4\lambda_e}\,(1 + R)\right] \tag{32}$$

282

Equations (29) and (32) give:

$$e^{\eta_o} = \frac{J_e}{J_{es}} \left( 1 + \frac{1+R}{2} \frac{3d}{4\lambda_e} \right) \tag{33}$$

and finally R can be found from equations (30) and (31):

$$\frac{J_e}{J_{es}} = \frac{-\frac{2\lambda_p}{\lambda_e} R}{\left[ 1 + \frac{3d}{4\lambda_e}(1+R) - R \frac{\lambda_p}{\lambda_e} \right] \left( 1 + \frac{1+R}{2} \frac{3d}{4\lambda_e} \right)} \tag{34}$$

Eliminating R between equations (33) and (34), the ratio of saturation current to the current flowing through the dark plasma is found to be:

$$\frac{J_{es}}{J_e} = \frac{\left( 2 \frac{4\lambda_p}{3d} + \frac{\lambda_p}{\lambda_e} \right) \left( 1 - 2e^{-\eta_o} \right) - 1}{2 \frac{4\lambda_p}{3d} \left( 1 - 2e^{-\eta_o} \right) - 2} \tag{35}$$

4.   Ion Source at the Emitter and Collector Edges of the Plasma, Negative Emitter Sheath

As mentioned above, this section will treat the case where surface ionization cannot be neglected as a source of ions. The boundary conditions expressed by equations (27), (28) and (29) will still hold, but equation (30) must be replaced by the following equation:

283

$$J_p = J_{ps} - \left(\frac{n(0)v_p}{4} - \frac{J_p}{2}\right) e^{\eta_o}. \tag{36}$$

The solutions for the unknowns $e^{\eta_d}$, $J_r$ and $e^{\eta_o}$ were given previously by equations (31), (32) and (33). The solution for R, however, is obtained by eliminating $e^{\eta_o}$ in equation (36), using equation (33).

$$\frac{J_e}{J_{es}} = \frac{\lambda_e}{\lambda_p} \; \frac{2}{R} \; \frac{1 - \left[\beta\left(\frac{3d}{4\lambda_p}\right)^2 \left(1 + \frac{1}{R}\right)^2 F + 1\right]^{1/2}}{\left(\frac{3d}{4\lambda_p}\right)^2 \left(1 + \frac{1}{R}\right)^2 F} \tag{37}$$

where

$$F \equiv \left[1 + \frac{1 - R\frac{\lambda_p}{\lambda_e}}{\frac{3\lambda}{4\lambda_e}(1 + R)}\right]\left[1 + \frac{2}{\frac{3d}{4\lambda_e}(1 + R)}\right] \tag{38}$$

Again these results can be put in better form by eliminating R from equations (36) and (37). The final relation for $J_{es}/J_e$ is:

$$\frac{J_{es}}{J_e} = \frac{\left(1 + \frac{4\lambda_e}{3d}\right)\left[\frac{\lambda_p}{\lambda_e} - \frac{1}{2}\left(\frac{\lambda_p}{\lambda_e} - \frac{3d}{4\lambda_e}\right)e^{\eta_o}\right] - \frac{1}{2}\left(1 + \frac{3d}{4\lambda_e}\right)e^{\eta_o}}{2\left[\frac{\lambda_p}{\lambda_e} - \frac{1}{2}\left(\frac{\lambda_p}{\lambda_e} - \frac{3d}{4\lambda_e}\right)e^{\eta_o}\right] - \beta} \tag{39}$$

This equation applies to the motive diagram in Figure IX-3 for the general case where ion source is both at the emitter surface and the bright plasma. For $\beta = 0$ (no surface ions) it is identical to equation (35).

Equations (23), (26), (35) and (39) give the ratio of saturation current to the actual current passing through the plasma.

The bright plasma has been observed near the collector in high-spacing devices such as scanners. Equations (23), (26), (35) and (39) give the ratio of saturation current to the actual current passing through the plasma for various conditions and the motive diagrams shown in Figures IX-2 and IX-3. It would be useful at this point to take variable-spacing data under the conditions where usual observation of inter-electrode spacing suggests these motive diagrams. It will also be attempted to see if other regions of the ignited mode can be approximated according to the present model.

## C.  ANALYTICAL DESCRIPTION OF CESIUM DIODE PHENOMENOLOGY

### 1.  Introduction

The work described here has a practical phenomenological basis; i.e., it springs from a body of data obtained by systematically varying all primary converter variables over the range of values giving practically useful output power densities. Theoretical inquiry into the basic origin of correlations observed among the variables has given critical insight into the nature of the fundamental processes which dominate converter operation for conditions of practical importance. The choice among various possible analytical models is greatly narrowed by the

285

restriction that the model must be consistent with observed converter

phenomenology over a great variety of conditions as well as being

self-consistent.

Figure IX-4 summarizes the features of the electrical character-
istics associated with distinct visible forms of the discharge (described
later), and includes the dark "plasmatron" or space charge mode AHK
which appears at high emitter temperatures where ion emission from the
emitter is significant.' The plasmatron, anode glow, and ball-of-fire
modes have been discussed and analyzed extensively elsewhere[9,13,14,17,18]
and thus will not be treated analytically here. However, an analytical
model which successfully describes many features of the obstructed and
saturation modes will be outlined here and compared quantitatively with
experimental data. The distinction between these particular modes,
and their quantitative understanding, are of considerable importance
since they constitute virtually the entire practical operating regime of
the cesium diode thermionic converter. In fact, the transition point
between them (point F) is generally where maximum power output occurs.

During the past few months, due to the availability of data from
improved experimental apparatus, rapid progress has been made in
synthesizing a coherent physical model which is consistent both with
the qualitative visual phenomenology of the discharge and with the
quantitative electrical output characteristic over a wide variety of
conditions. Furthermore, the constants relating the observed data
to the analytical model are in much better agreement with probable
values of the atomic properties of cesium than for the earlier models.[11,12]

286
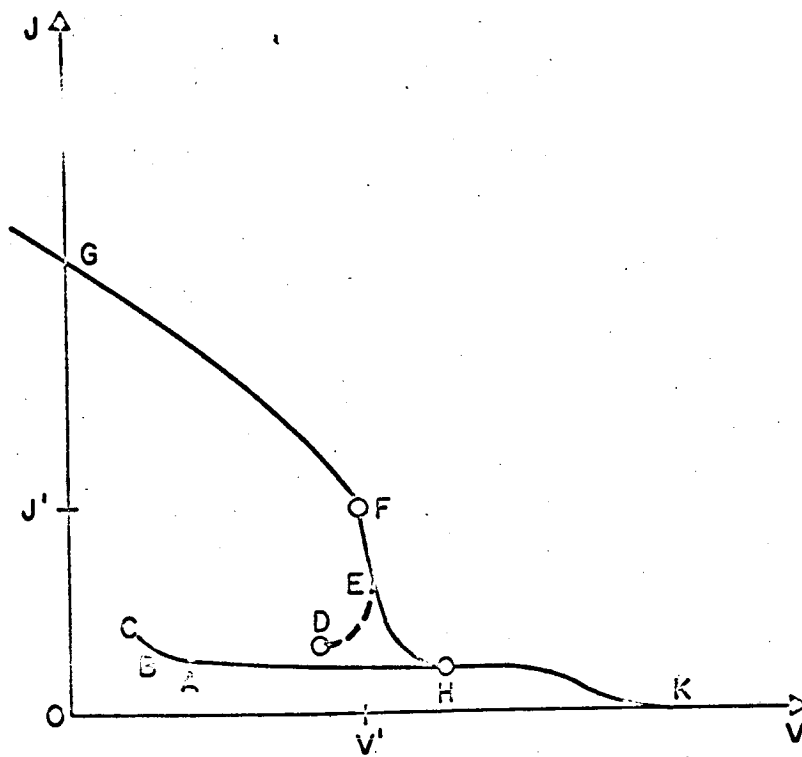
Figure IX-4. Identification of Discharge Modes in Electrical Output Characteristics.

287

2. Saturation Mode of the Cesium Diode Discharge

    a. Analytical Model

    The region FG of the representative electrical output char-
acteristic in Figure IX-4 is designated here as the "saturation mode,"
and the corresponding motive diagram postulated is shown in Figure
IX-5a. The stream of electrons from the emitter, equal to the satura-
tion current density $J_s$, gains an energy $V_e$ as it is accelerated across
the emitter sheath, and this energy is dissipated in the plasma a short
but finite distance from the emitter. The resulting average electron
temperature in this region $T_e$ is sufficiently high to produce the ions
required to sustain the plasma. Assuming a neutral plasma of width
d much greater than the electron mean free path $\lambda$, it is shown in
Appendix E that the current density of electrons reaching the collector
is given by

$$J = \frac{J_s}{1 + \exp\ (-V_e/kT_{\epsilon e})\left[\frac{3}{4}\frac{d}{\lambda} + R\right]} \quad \text{for } V < V' \quad (40)$$

where

$$R = \exp\ (V_c/kT_{\epsilon e}) - 1 \quad (41)$$

$T_{\epsilon e}$ and $T_{\epsilon c}$ are the respective electron temperatures at the emitter
and collector edges of the plasma, and $V_c$ is the potential energy drop
across the collector sheath.

    The physical significance of equation (40) is that the current
$J_s - J$ returning to the emitter from the plasma is made up of two com-
ponents: R is the fraction of J which is reflected by the collector
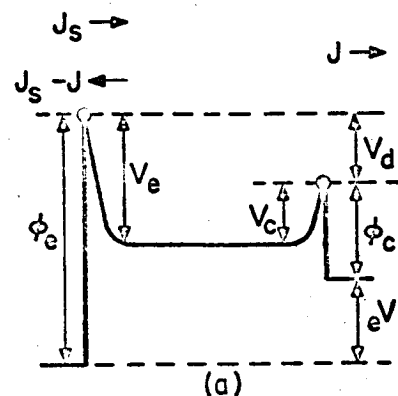
(a)
SATURATION MODE (FG)
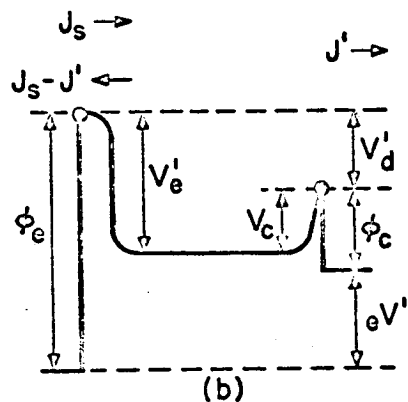
(b)
TRANSITION POINT (F)
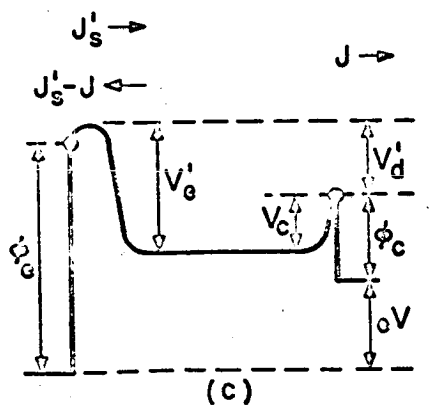
(c)
OBSTRUCTED MODE (FH)

Fig. IX-5.

289

sheath barrier $V_c$, and $3d/4\lambda$ is the fraction which is reflected by the plasma. The fraction of these reflected currents which then surmounts the emitter sheath barrier is $\exp(-V_e/kT_{\epsilon e})$. A more general interpretation of R would include the electron reflection coefficient of the collector surface as a factor.

It is shown in Appendix F that for $d \gg \lambda$ the transport of energy across the plasma requires

$$kT_{\epsilon c} = kT_{\epsilon e} - V_c/2 \tag{42}$$

Also, as may be seen in Figure IX-5a,

$$V_e = \phi_e - \phi_c + V_c - eV \tag{43}$$

Thus, equations (40)-(43) prescribe the electrical output characteristics J(V) in the saturation mode.

b.     Analysis of Data

To facilitate comparison with experimental data, equations (40)-(43) combine to give

$$\frac{J_s}{J} = 1 + A(Pd + D) \exp\left[\frac{eV}{kT_{\epsilon e}}\right] \tag{44}$$

where   P is the gas pressure, and the quantities

$$A = \frac{3}{4(P)\lambda} \exp\left[-\frac{\phi_e - \phi_c + V_c}{kT_{\epsilon e}}\right] \tag{45}$$

and

$$D = \frac{4}{3} (P\lambda) \left[\exp(V_c/kT_{\epsilon c}) - 1\right] \tag{46}$$

290

should be essentially constant under conditions were $T_{\varepsilon e}$ does not change appreciably.

Figure IX-6 is a family of output characteristics in which only the electrode spacing is changed; all other experimental variables are held constant. The device used to obtain these data is a research diode[12] employing a guard ring which suppresses edge effects. In Figure IX-7 it may be seen that these data give a linear relationship between $1/J$ and Pd for constant values of $V > V'$, as do data taken at other cesium pressures and emitter temperatures.

These lines converge at a single point which, according to equation (44), defines the values of $J_s$ and D. Furthermore, according to equation (44),

$$\ln m = \ln \frac{d\left(\frac{J_s}{J}\right)}{d(Pd)} = A + \frac{e}{kT_{\varepsilon e}} V \qquad (47)$$

where m is the slope of the curves in Figure IX-7. Thus A and $kT_{\varepsilon e}$ are easily found from the slope and intercept of the straight line obtained when ln m is plotted versus V.

The value of $\phi_e$ can be computed from the value of $J_s$ obtained in Figure IX-7 using the Richardson equation

$$\phi_e = kT_e \ln \left(\frac{AT_e^2}{J_s}\right) \qquad (48)$$

and $\phi_c$ is known from independent data.[9] Thus, these known values of $\phi_e$ and $\phi_c$, D, A and $kT_{\varepsilon e}$ can be used to compute $V_c$ and $(P\lambda)$ from

IX-23

291
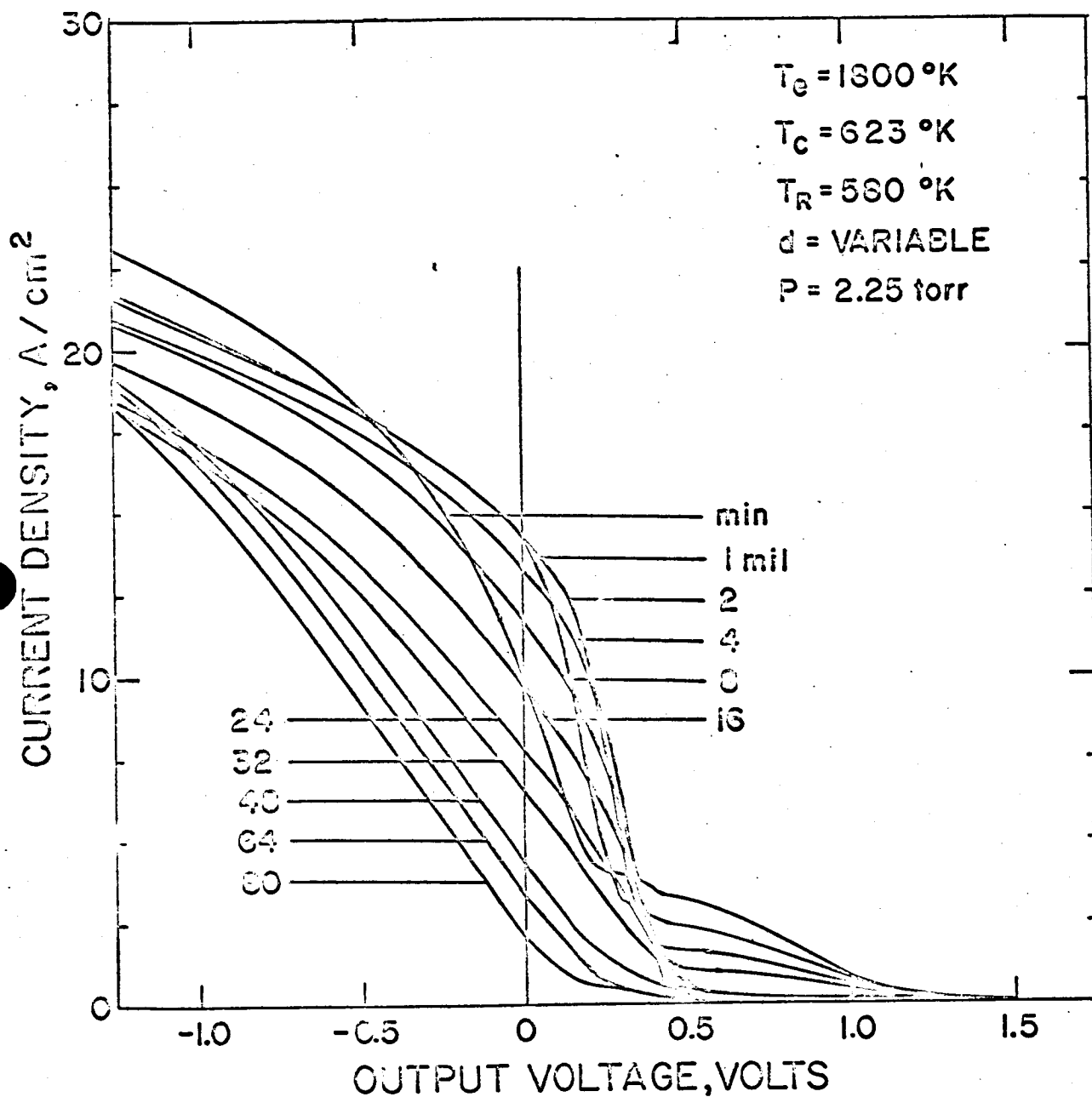
Figure IX-6. Typical Variable-Spacing J-V Characteristics.
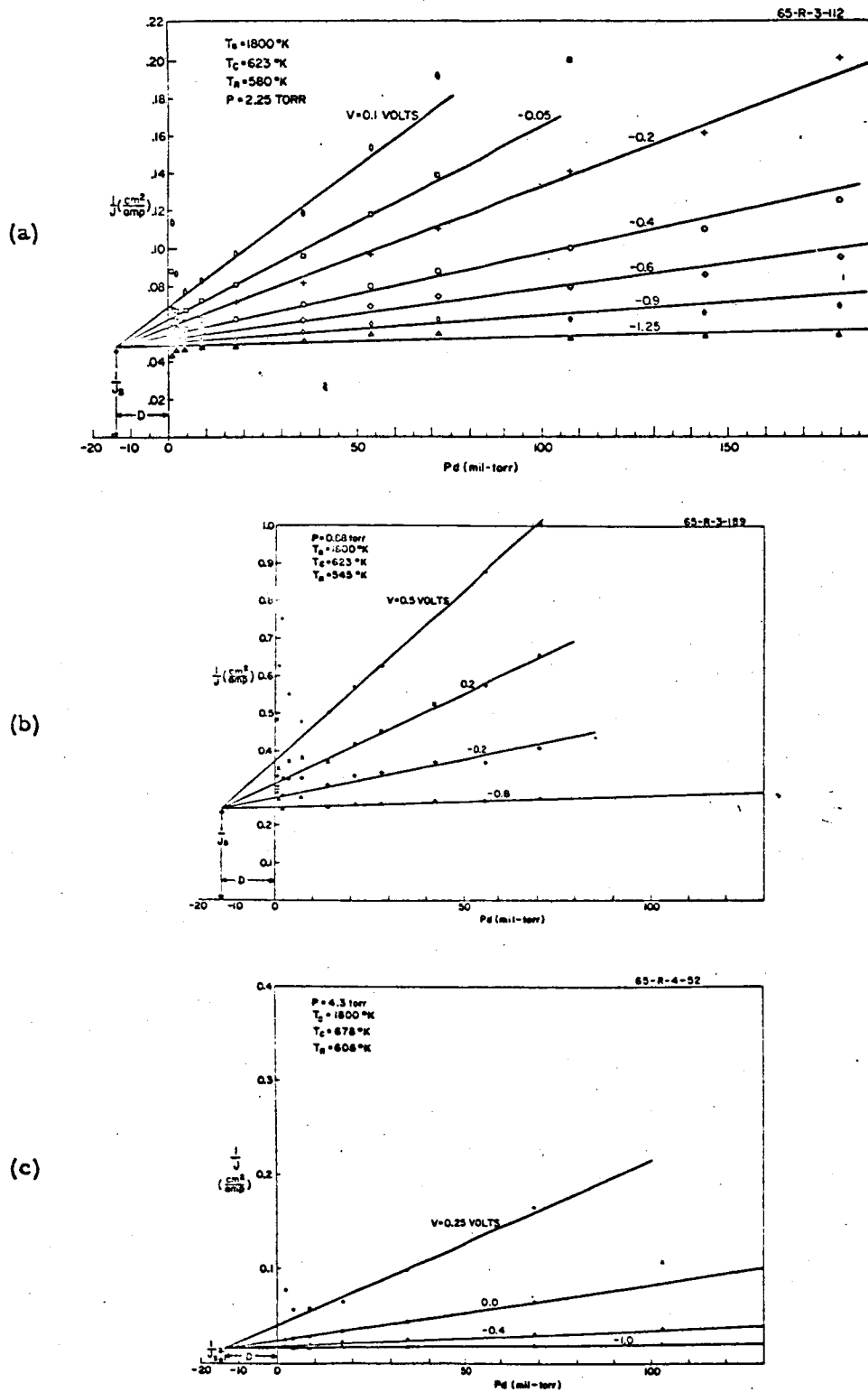
Figure IX-7. Plots for Obtaining Constants A, D and $J_s$ in Eq. 44.

293

equations (45) and (46).

Inspection of Figure IX-7 shows that equation (44) describes the data in Figure IX-6 for the following sets of values:

For Figure IX-7a

$T_e$ = 1800°K  $T_c$ = 623°K  $T_R$ = 580°K(P = 2.25 torr)

$J_s$ = 21.1 A/cm$^2$  A = 0.025 (mil-torr)$^{-1}$  D = 14 mil-torr

which are consistent with equations (45), (46) and (48) for

$\phi_e$ = 2.60 eV  $\phi_c$ = 1.90 eV  $V_c$ = 0.4 eV

$(P\lambda)$ = 2 mil-torr  $(\sigma$ = 500 Å$^2$)  $kT_{\epsilon e}$ = 0.4 eV

For Figure IX-7b

$T_e$ = 1800°K  $T_c$ = 623°K  $T_R$ = 545° (P = 0.88 torr)

$J_s$ = 4.08 A/cm$^2$  A = 0.013 (mil-torr)$^{-1}$  D = 14 mil-torr

which are consistent with equations (45), (46) and (48) for

$\phi_e$ = 2.85 eV  $\phi_c$ = 1.85 eV  $V_c$ = 0.4 eV

$(P\lambda)$ = 3 mil-torr  $(\sigma$ = 300Å$^2$)  $kT_{\epsilon e}$ = 0.5 eV

For Figure IX-7c

$T_e$ = 1800°K  $T_c$ = 678°K  $T_R$ = 606°K (P = 4.3 torr)

$J_s$ = 63 A/cm$^2$  A = 0.036 (mil-torr)$^{-1}$  D = 14 mil-torr

which are consistent with equations (45), (46) and (48) for

$\phi_e$ = 2.43 eV  $\phi_c$ = 1.88 eV  $V_c$ = 0.3 eV

$(P\lambda)$ = 1 mil-torr  $(\sigma$ = 1000 Å$^2$)  $kT_{\epsilon e}$ = 0.3 eV

If electron temperature is assumed to be a weak function
of V, its dependence on Pd can be estimated by plotting the output char-
acteristics in Figure IX-6 as in Figure IX-8, using the value of $J_s$ in
Figure IX-7a. Now equation (44) becomes

$$\ln\left[\frac{J_s}{J} - 1\right] = \ln\left[A(Pd + D)\right] + \frac{eV}{kT_{\epsilon e}} \tag{49}$$

Hence electron temperature is obtained from the slope of each curve in
Figure IX-8 and is shown in Figure IX-9. The vertical lines correspond
to the variation of electron temperature with voltage.

c.    Comparison with Basic Physical Constants

The foregoing has shown that the analytical model satis-
factorily correlates the experimental variables. A more critical test
of the model is the extent of quantitative agreement of the correlation
constants with those computed from the physical properties of the cesium
atom.

(1)    Electron Mean Free Path $\lambda$. The value of $(P\lambda)$ from the
three sets of data and the associated electron-atom cross section $\sigma$, agree
reasonably well with the values $(P\lambda) = 1.2$ to $2.6$ mil-torr reported or
estimated by others[13] for the same region of electron temperature.

(2)    Collector Sheath Height $V_c$. It is shown in Appendix G
that $V_c$ should be approximately proportional to electron temperature
$T_{\epsilon e}$. The values of $V_c$ and $T_{\epsilon e}$ observed here imply, through equations
(42) and (G-3), that the effective thickness of the collector sheath remains
constant at about $N = 2$ Debye lengths, a quite satisfactory result.
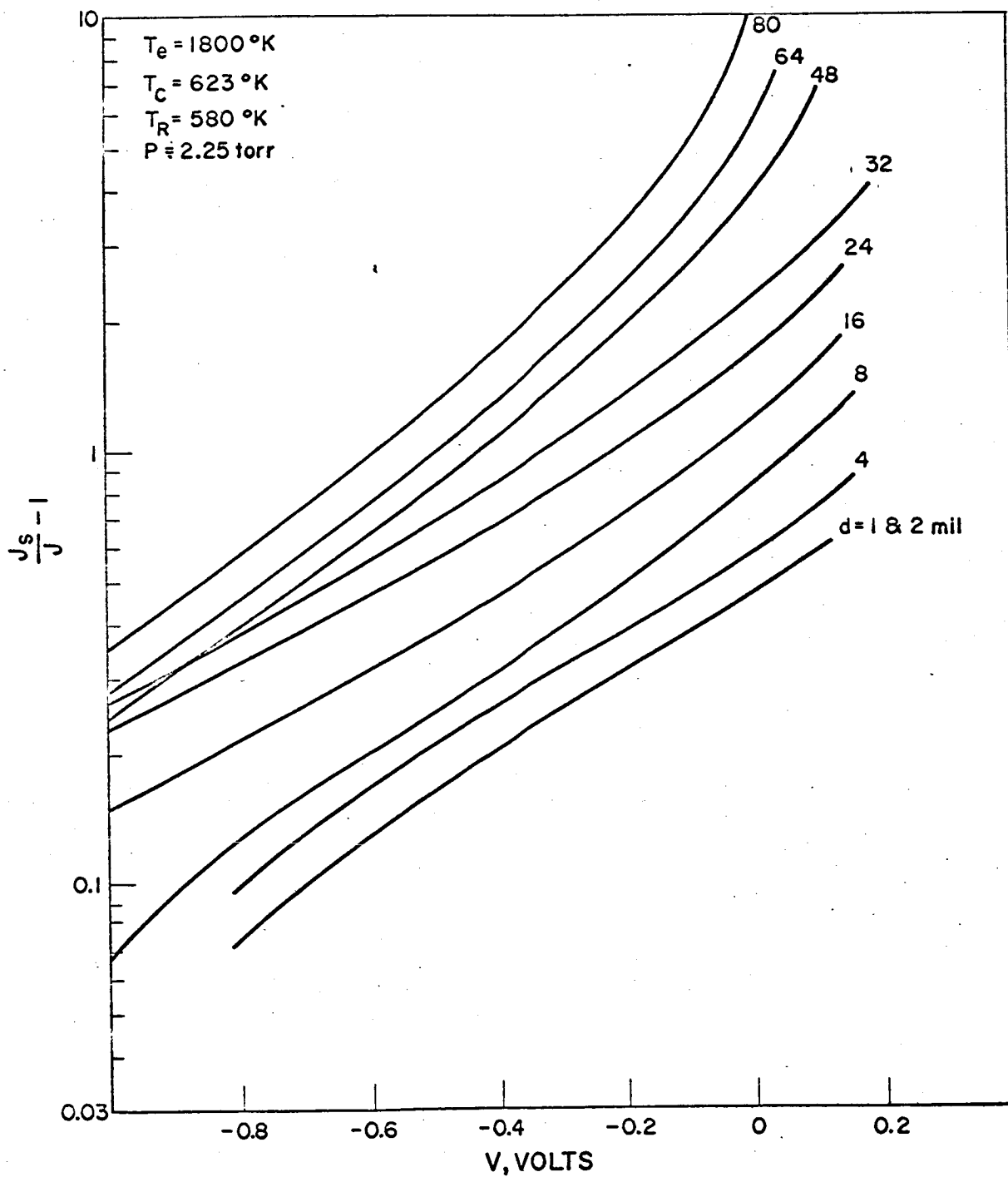
Figure IX-8. Output Characteristics Plotted according to Eq. 49.
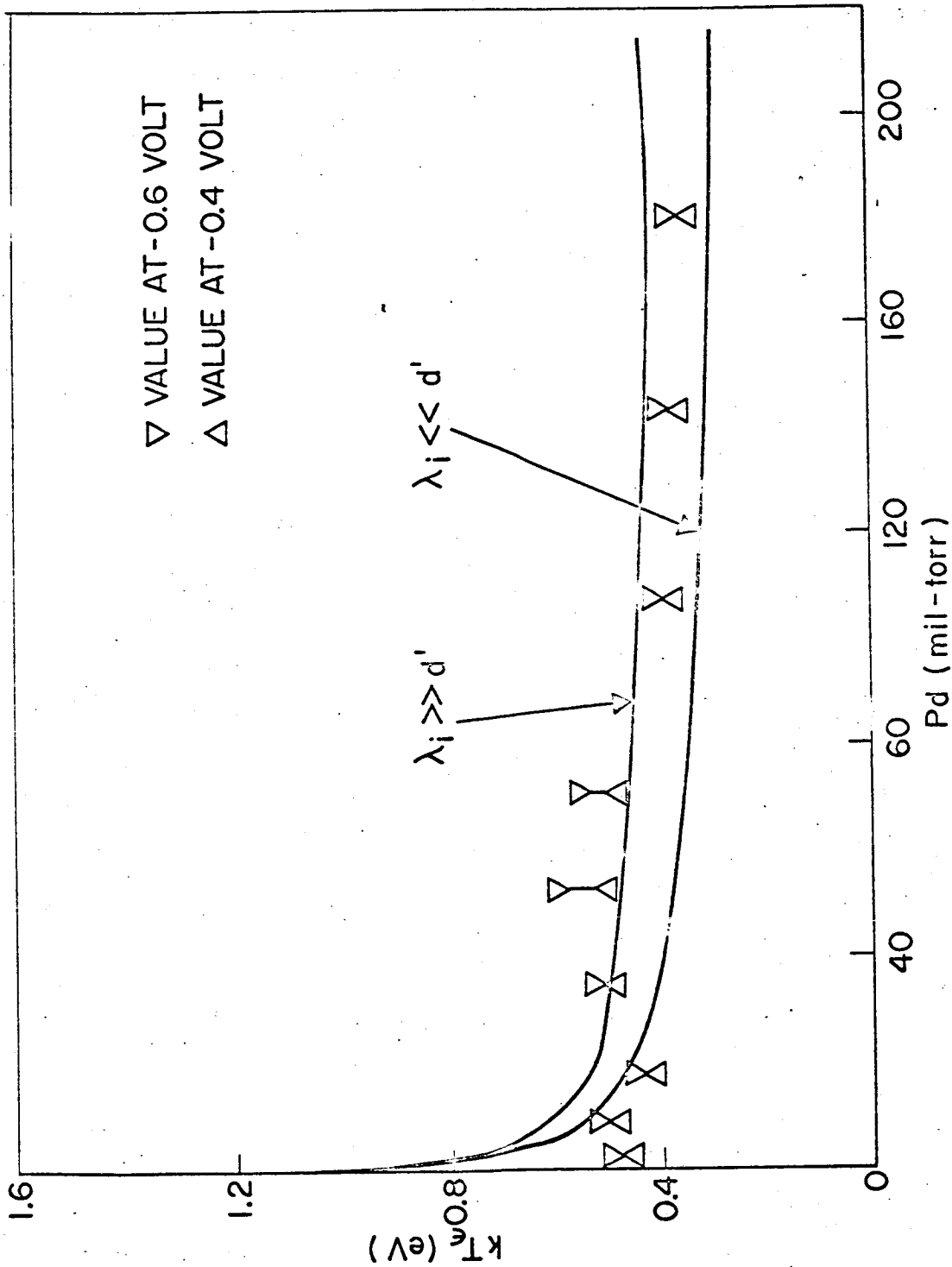
Figure IX-9. Comparison of Observed and Computed Electron Temperatures.

297

(3)    Electron Temperature $T_{\varepsilon e}$.  The electron temperature required to produce the ions diffusing out of the plasma is derived in Appendix H.  As may be seen in Figure IX-9, the required electron temperature, computed using the probable[16] values of the ionization and diffusion cross section, agree reasonably well with those observed here and approximate the dependence on Pd.  Furthermore, these temperatures and the associated temperature drop across the plasma, are in reasonably good agreement with values obtained spectroscopically.[19]

3.    Obstructed Mode of the Discharge

a.    Analytical Model

The power input to the plasma is $J(V_e + 2kT_e)$.  As V is increased, $V_e$ is decreased, and this power must eventually fall below that required to maintain the high electron temperature sustaining the plasma under the conditions in Figure IX-5a.  It is evident, from observed data such as Figure IX-6 and from the energy balance considered in Appendix J, that the plasma can continue to exist through impact ionizatio.. at still higher V only if a certain minimum emitter sheath height $V_e'$ is maintained.[11]  This results in the situation in Figure IX-5c, where a space charge barrier exists at the emitter of sufficient height to maintain this minimum value of $V_e'$ for $V > V' = \phi_e - \phi_c + V_c - V_e'$.  The region EF of Figure IX-4 where this barrier exists and thus limits the electron emission current from the emitter, is designated as the "obstructed mode. "

In the obstructed mode, the saturation electron emission current $J_s$ in equation (40) is replaced by the current $J_s'$ emitted over the new barrier of height $V - V'$, and $V_e$ is replaced by $V_e'$; so equation (40) becomes

$$J = J' \exp\left(\frac{V' - V}{kT_e}\right) \qquad \text{for } V > V' \qquad (50)$$

where $J'$ is the value given by equation (40) with $V_e = V_e'$. The transition point $V'$, designated $F$ in Figure IX-4 and illustrated in Figure IX-5c, is of considerable practical significance since maximum power output typically occurs there. It usually is readily identified in experimental output characteristics as a point of inflection.

b.   Analysis of Data

Values of $V_e'$ are most easily obtained from such directly observed values of the point of inflection $V'$. A more precise method is to plot the J-V characteristics on a log plot and identify $V'$ as the point of intersection between a linear extrapolation of the obstructed mode and of the saturation mode. Values of $V_e'$ obtained from the data in Figure IX-6, using the values of $\phi_e$, $\phi_c$ and $V_c$ determined previously are shown in Figure IX-10, showing that $V_e'(Pd)$ is essentially independent of pressure and $\phi_e - \phi_c$.

c.   Comparison with Physical Model

The electron energy balance for the plasma is shown in Appendix J to enforce a unique relationship between $V_e$ and Pd. In the saturation mode, where $V_e$ is dependent on V, a large part of the energy input to the plasma is returned to the emitter by the electrons back-scattered from the plasma, due to the direct communication between emitter and plasma. As a result, both electron temperature $T_\epsilon$ and plasma size d can remain relatively constant over a wide range of V. In the obstructed mode, however, the dark barrier region between

IX-31

299
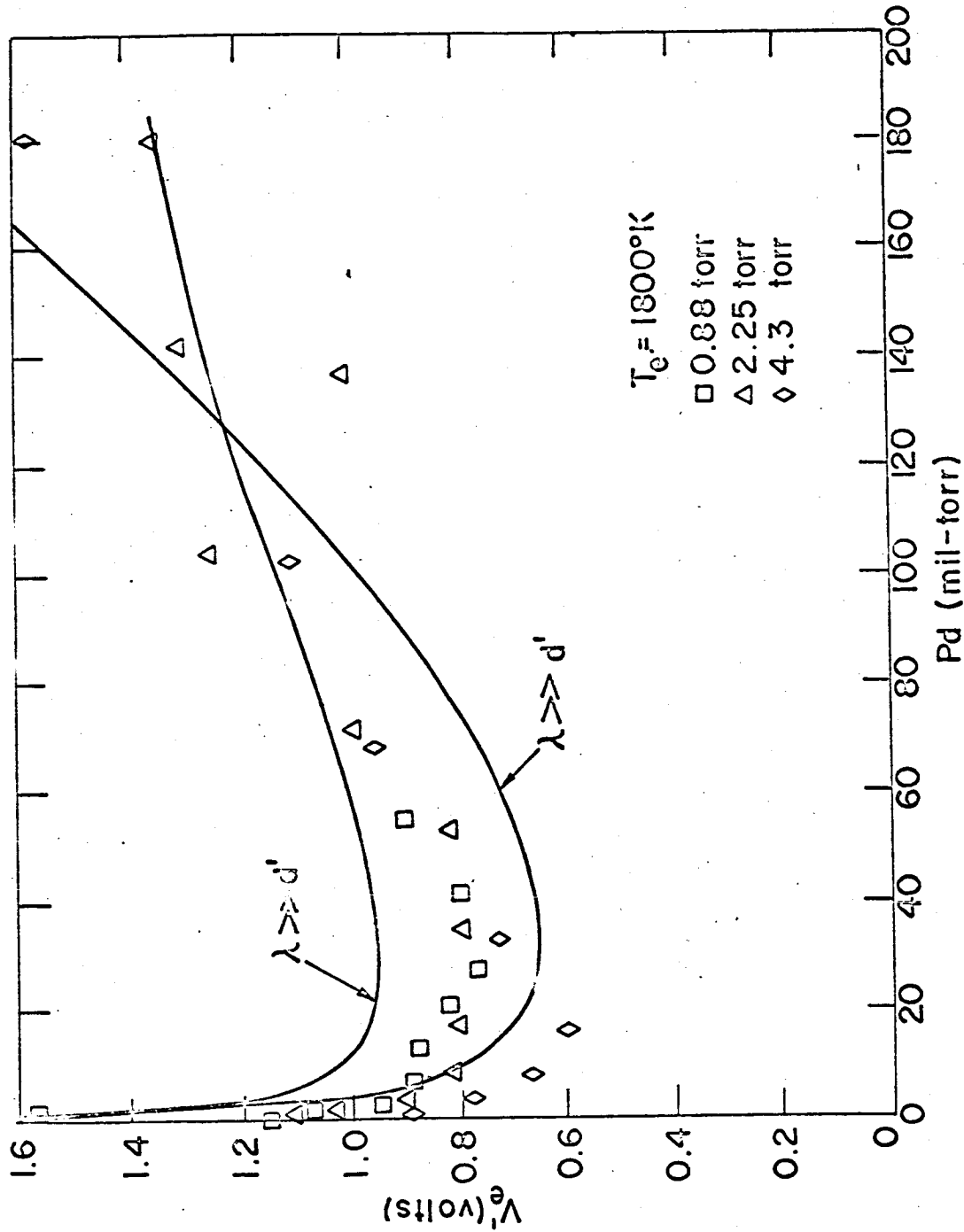
Figure IX-10.  Comparison of Observed and Computed Emitter Sheath Height.

the emitter and bright plasma (Figures IX-5c, -11d and -13) greatly reduces both the emission into the plasma and the amount of high-energy electrons back-reflected to the emitter from the plasma. The value of $V'_e$ which characterizes the obstructed mode, therefore, is independent of current, as given in equation ( J-5), and has the computed dependence on Pd shown in Figure IX-10, using equations ( H-3) and ( H-4).

The value of C which best fits the data in Figure IX-10 corresponds to a value for the ratio of excitation and ionization cross section of $K_x/K_i \approx 0.3$ for the short MFP case, and $K_x/K_i \approx 2$ for the long MFP case, which are far different from the estimated[16] most probable value of 18. While there is considerable uncertainty in this estimated value, the disagreement is well outside the probable range of error. Preliminary computations[20] suggest that this discrepancy is of the approximate magnitude expected due to the transfer of excitation energy from excited atoms back into the electron gas, i. e. , the inverse of the electron impact excitation process.

4.    Ball-of-Fire Mode

In the obstructed mode, the energy requirements of the plasma imposed by equation ( J-5) (Figure IX-10) are met for $V_e < V'_e$ through the existence of an energy barrier at the emitter of sufficient height to accommodate the required emitter sheath $V'_e$ associated with electrode spacing d. An alternate mode by which the discharge can satisfy (J-5) is to exist with an emitter sheath of height $V_e = V'_e$ associated with a smaller d; i. e. , the plasma occupies only a small part of the interelectrode space with an effective plasma width of $d' < d$, as observed visually in the region DE of the output characteristics in Figure IX-4 (see Figure IX-11c. )
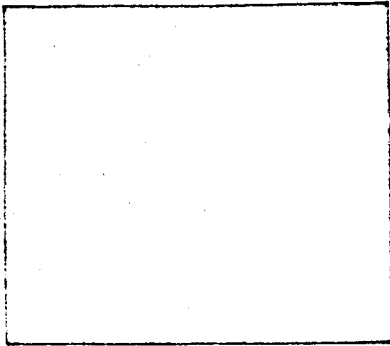
(a) Anode Glow Mode, A
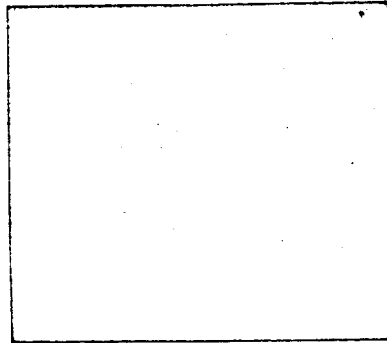
(b) Anode Glow with Detached Ball-of-Fire, C.
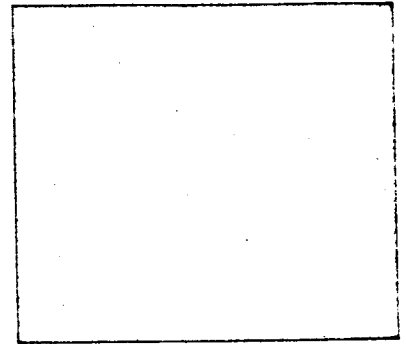
(c) Ball-of-Fire Mode.
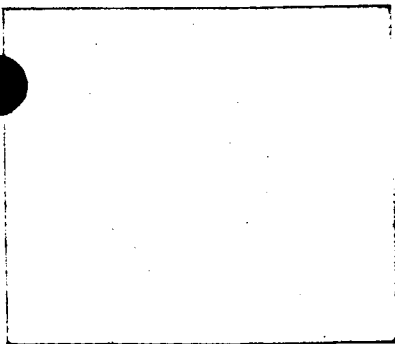
(d) Obstructed Mode, E.
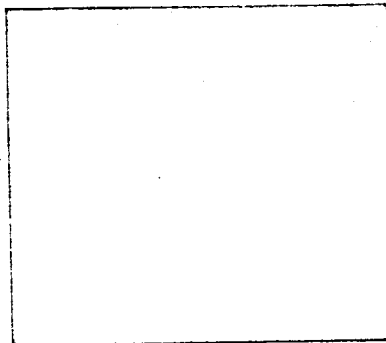
(e) Critical Point, F.
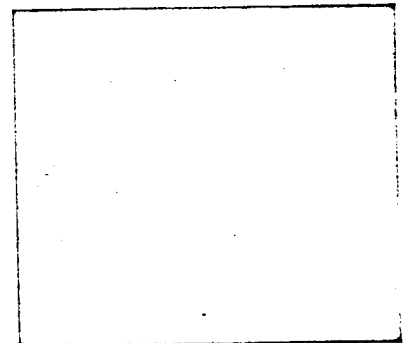
(f) Saturation Mode, G.

Figure IX-11.  Visible Modes of the Cesium Discharge.  Circle is boundary of window;  emitter is at top, collector at bottom ($T_e = 1100\,°K$,  $P = 0.04\,torr$).

## 5. Extinguished Mode

Equation (40) has been shown previously[17,18] also to describe the extinguished mode for ion-rich emission identified as region AHK in Figure IX-4. In this case the emitter sheath height is essentially independent of V and Pd, now having the form

$$V_e = kT_e \ln\beta \tag{51}$$

where $\beta = \left(\dfrac{M}{m}\right)^{1/2} \dfrac{\mu e}{J_s}$ is the ion richness ratio and $\mu$ is the cesium atom arrival rate. The collector sheath height now depends on V to satisfy equation (43), and $kT_{\varepsilon e} \approx kT_{\varepsilon c} \approx kT_e$.

## 6. Photographic Identification of Cesium Diode Discharge Modes

Figures IX-11a through -11f are color photographs of the cesium discharge in a ceramic-metal thermionic converter fitted with a sapphire window. To allow such ready observation, it is necessary to operate the emitter at relatively low temperatures (e. g. 1100°K in Figure IX-11) so that light from the emitter does not dominate that from the discharge. Also, it is necessary to employ a sufficiently wide spacing (e. g. 0. 35 inch in Figure IX-11) so that the longitude structure of the discharge is discernible with the lens aperture required by the low light intensities. To ensure that the electron flow is essentially one-dimensional, a magnetic field of about 500 gauss is applied along the axis of the discharge. Figure IX-12 is taken at the same Pd as Figure IX-11, but at lower emitter temperatures where the patch structure of the emitter is more pronounced. The parallel streamers, and the non-divergent nature of the streamer emanating from each patch, are more direct evidence of the one-dimensional nature of the electron current flow. Furthermore,

303
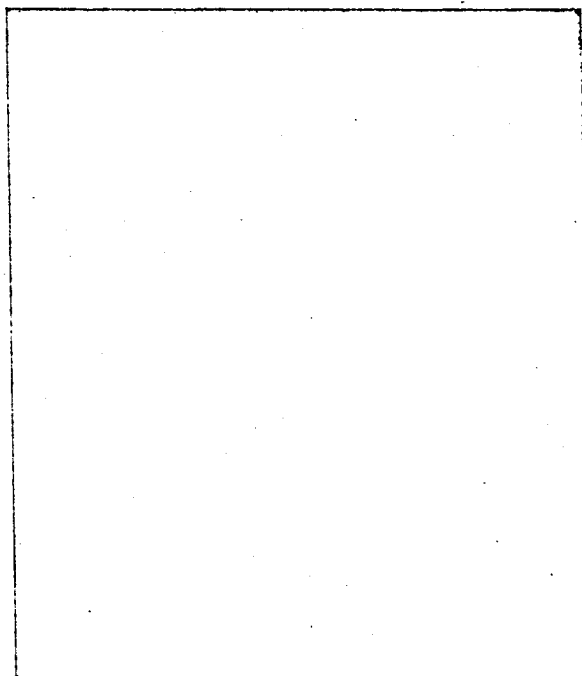
Figure IX-12.    Streamers in Discharge due to Emitter Patches
($T_e$ = 800 °K, P = 0.04 torr).

the electrical characteristics obtained for the conditions of Figure IX-11, as shown in Figure IX-14, are essentially the same in the ignited mode as those obtained for a closer-spaced practical converter at the same Pd (e. g. Pd = 15 mil-torr in Figure IX-11).

Each photograph in Figure IX-11 is identified with the corresponding point of the J-V characteristic in Figure IX-14 where it was taken. The discharge is completely dark until the electrode potential difference reaches point A in Figure IX-14a, where the current begins to increase perceptibly, and a yellow glow appears on the collector as in Figure IX-11a. This well-known "anode glow" increases in intensity as the current is increased, but has no perceptible thickness until point B is reached, whereupon a "tuft" or ball of yellow glow abruptly detaches from the collector and rests a short distance from it. With higher current, this tuft begins to oscillate among several stable positions, eventually appearing as a diffuse region of yellow glow accompanied by an alternating-current component. In the region of point C a faint violet-pink luminous ball appears adjacent to, but detached from, the emitter. It exists simultaneously with the anode glow, and also oscillates among several stable positions, one of which is shown in Figure IX-11b.

At point D, the anode glow disappears and the potential drop across the discharge abruptly decreases. As shown in Figure IX-11c, a relatively intense and stable violet-pink ball appears next to the emitter, separated from it by a relatively narrow but distinct dark space. This presumably is the well-known "ball-of-fire" mode of the discharge. The diode has a negative dynamic resistance in this region. As the current is increased, the ball expands transversely

305
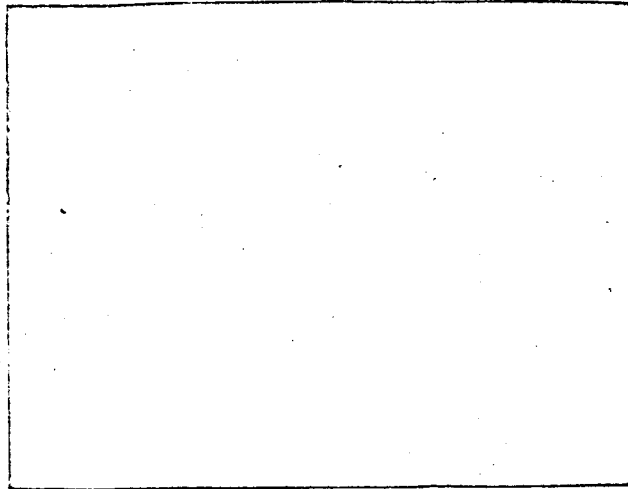
(a) Visible
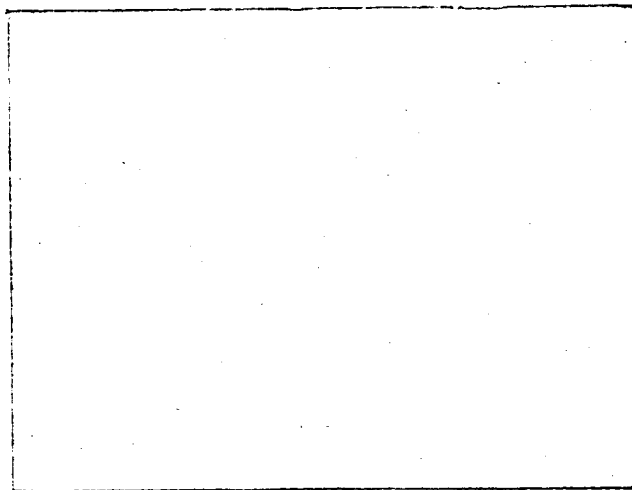
(b) Infrared

Figure IX-13.   Obstructed Mode, EF, Conditions same as in
                Figure IX-11.

306

(a)

0.2 A/cm$^2$

J

V ⟶

(b)

3 A/cm$^2$

J

V ⟶
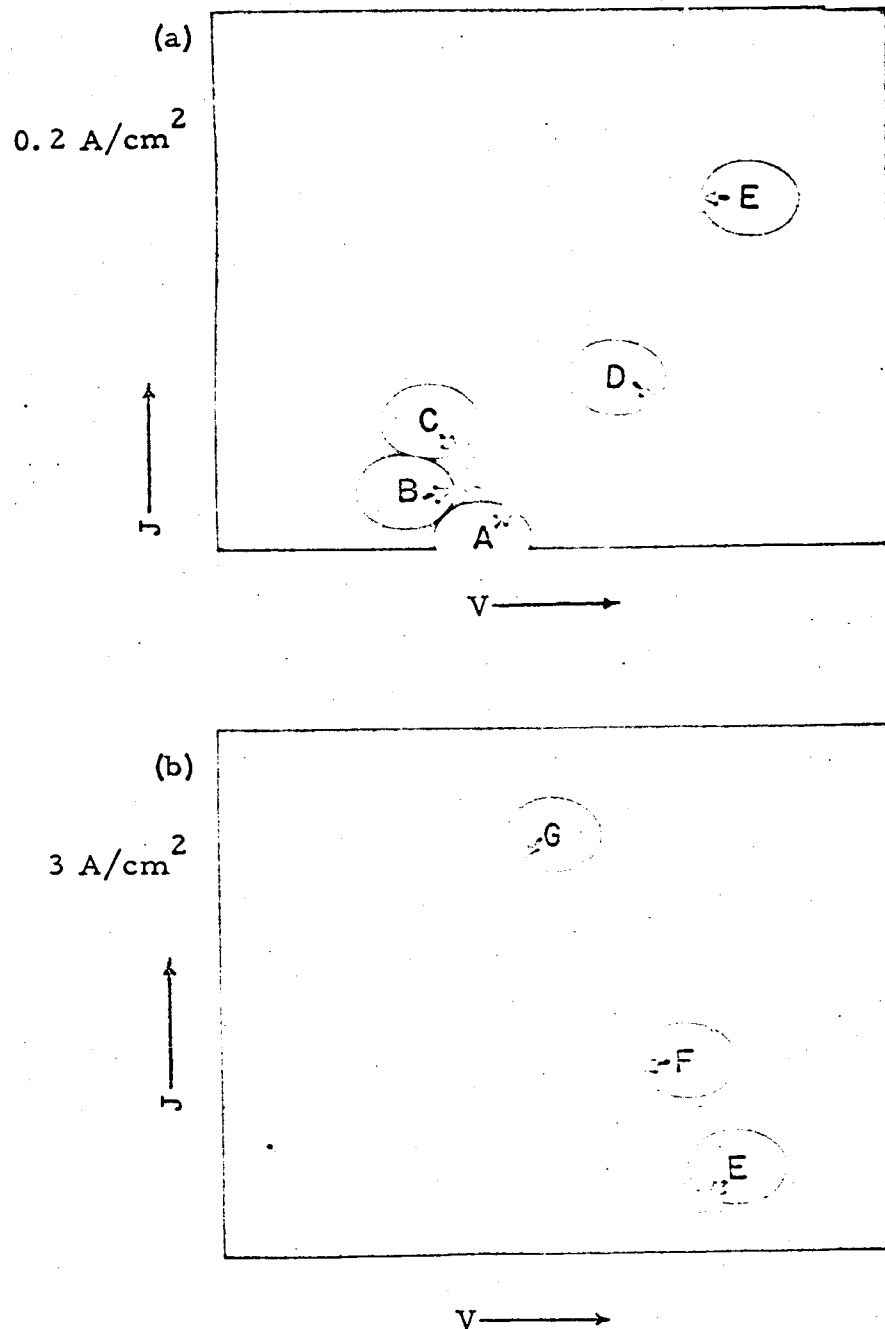
Figure IX-14.  Electrical Characteristics identifying Conditions
for Photographs in Figure IX-11.

307

to the current flow until, at point E, it has the same transverse area as the electrode, as in Figure IX-11d. A distinct narrow dark space still separates it from the emitter, and the glow gradually diminishes toward the collector, leaving the half space next to the collector essentially dark.

When the current increases further, as in the greatly expanded J-V oscillogram in Figure IX-14b, the dynamic resistance becomes positive and the emitter dark space becomes narrower, disappearing completely just as the point of inflection F is reached. Thus, both the visible and electrical characteristics of this important region are substantially different from those in the ball-of-fire mode. For reasons discussed previously, the region EF is designated herein as the "obstructed mode" of the discharge. The principal effect of current increase above F is to increase greatly the visible light intensity of the discharge, with an emerging dominance of violet over pink. The luminosity of the collector dark space, relative to that of the bright emitter region, does not change appreciably until the point G is exceeded, whereupon the bright portion of the discharge becomes an intense blue-white, and progressively expands to fill the entire interelectrode space uniformly as in Figure IX-11b. The region FG is that designated as the "saturation mode" in the previous analytical discussion. While the characteristic size of the tufts and balls in the ignition modes BCDE appear to depend directly on cesium pressure, the spatial distribution of light intensity in the obstructed and saturation modes EFG is relatively insensitive to pressure.

308

It should be noticed that the intensely emitting patches at the left side of the emitter tend to cause a more intense discharge in this region for all modes. This situation exists even in the absence of the magnetic field.

A set of photographs were taken under conditions similar to those in Figure IX-11 using Polaroid Type 413 infrafed film, in conjunction with an 87C Wratten filter. This combination very effectively isolates the 8528 Å and 8944 Å "resonance" radiation from the lowest excited state of the cesium atom. The most significant results can be summarized as follows:

No resonance radiation was detected in the anode glow.

The spatial distribution of resonance radiation in the ignited modes is essentially identical with that of visible radiation, as shown in Figure IX-13 (which also more clearly shows the emitter dark space than does Figure IX-11d).

The intensity of resonance radiation is several orders of magnitude greater than that of the visible radiation.

The intensity of resonance radiation is virtually independent of diode current, whereas the visible intensity increases by more than an order of magnitude progressing from point D to point G.

7.   Summary

A coherent formalism has been obtained which describes most of the phenomenology of the cesium diode discharge, and which correlates the variables satisfactorily for the several cases analyzed to date. Furthermore, the correlating constants agree well with those computed from basic physical constants, with a single notable exception. Future

309

work will extend the generality of this formalism over a greater range

and variety of experimental variables (e. g. , the effect of collector

temperature[12]).

## D. EXPERIMENTAL CORRELATION OF CONVERTER VARIABLES IN THE IGNITED MODE

### 1. Introduction

The ignited mode of the current-voltage characteristics of therm-

ionic diodes can be divided into two regions. The division occurs at the

inflection point F, identified in Figure IX-4. The region FG is

saturation-like in that the current is a weak function of voltage. The

region FH is characterized by an exponential dependence of current on

voltage.

The analytical treatment of both regions is given in Section C of

this chapter. The results of that analysis are given below and will be

used to correlate a large number of current-voltage curves. For the

saturation region the current-voltage curve is defined by:

$$\frac{J_s}{J} = 1 + A(Pd + D) \exp\left[\frac{eV}{kT_{\epsilon e}}\right].\tag{52}$$

where A and D are given by:

$$A = \frac{3}{4(P\lambda)} \exp\left[-\frac{\phi_e - \phi_c + V_c}{kT_{\epsilon e}}\right]\tag{53}$$

$$D = \frac{3}{4}(P\lambda) \exp\left[(V_c/kT_{\epsilon c}) - 1\right]\tag{54}$$

where $J_s$ is the emitter saturation current, J is the output current, P

is the cesium pressure, d is the interelectrode spacing, e is the

3/0

electronic charge, V is the output voltage, k is Boltzmann's constant, $T_{ee}$ is the electron temperature in the plasma near the emitter sheath, $T_{ec}$ is the electron temperature in the plasma near the collector sheath, $\lambda$ is the electron mean free path in cesium vapor, $\phi_e$ is the emitter work function, $\phi_c$ is the collector work function, and $V_c$ is the collector sheath height.

## 2.  Correlation with Experimental Results

The method of determining the values of a number of quantities occurring in equations (52), (53) and (54) has been described in Section C of this chapter, along with experimental results obtained specifically for this purpose.  The results are summarized below:

$$P\lambda = 2 \text{ mil-torr} \qquad\qquad D = 14 \text{ mil-torr}$$

$$kT_{ee} = 0.4 \text{ eV} \qquad\qquad kT_{ec} = 0.2 \text{ eV}$$

$$V_c = 0.4 \text{ eV}$$

Substituting these values in (52), (53) and (54) and combining these equations gives:

$$\frac{J_s}{J} = 1 + \frac{3}{8}(Pd + 14)\exp\left[\frac{V - \phi_e + \phi_c - 0.4}{0.4}\right] \qquad (55)$$

This equation is valid for the branch of the current-voltage curve at voltages lower than the inflection point.  The inflection point coordinates are defined as V' and J' where:

$$V' = \phi_e - \phi_c - V'_d \qquad (56)$$

and J' is the value of J from equation (55) with V = V'.  $V'_d$ has been determined experimentally in previous work[3] and is a function of Pd only.

$$V_d' = 0.535 - 6 \times 10^{-3} Pd + 1.6 \times 10^{-4} (Pd)^2 - 0.75 \times 10^{-6} (Pd)^3 \quad (57)$$

for PD > 10 mil-torr

Equation (55), then, is valid for $V < V'$.

For values of $V > V'$:

$$J = J' \exp \left[ -\frac{V - V'}{kT_e} \right] \quad (58)$$

where $T_e$ is the emitter temperature.

Equations (55), (57) and (58), combined, describe the ignited mode of any current-voltage curve for Pd > 10 for given $T_e$, $T_R$, $\phi_e$, $\phi_c$ and d. This relationship has been plotted in a useful form in Figure IX-15. The abscissa is the ratio of output current to saturation current. The ordinate is output voltage with the effect of the difference in electrode work functions subtracted. The true output voltage can be obtained by selecting the correct $\Delta\phi$ value on the left-hand scale, where $\Delta\phi = \phi_e - \phi_c$, and reading the output voltage at the intersection of this line with the vertical. $J/J_s$-versus-V lines are shown in this plot corresponding to constant Pd values. At voltages less than $V'$ the $J/J_s$-vs-V line is independent of emitter temperature. At voltages greater than $V'$ there is an emitter temperature dependence, as indicated by the fanning out into several lines of each "Pd curve."

The correlation in Figure IX-15 was tested by comparing the $J/J_s$ values calculated from it with experimental J-V curves. Data from devices using Re and W emitters opposite Mo collectors was used. The ranges of variation of parameters were as follows:
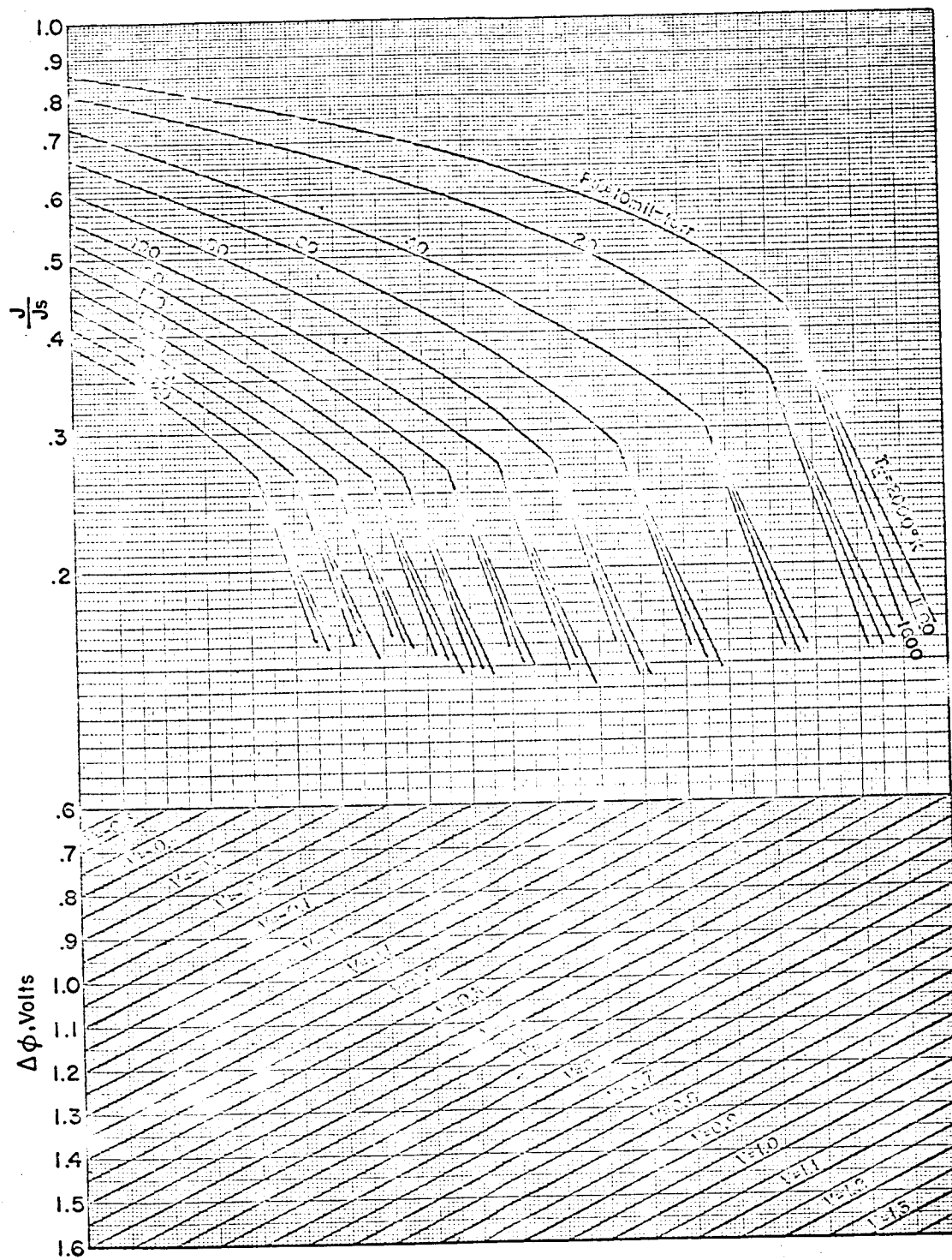
Figure IX-15.   Correlation of the Ignited Mode for $Pd > 10$ mil-torr.

$$T_e = 1640 - 1950\,°K \qquad\qquad T_c = 772 - 910\,°K$$

$$P = 1.048 - 4.15\ \text{torr} \qquad\qquad d = 6 - 20\ \text{mils}$$

$$J = 2 - 25\ A/cm^2$$

The results of this comparison are shown in Figure IX-16. To evaluate the scatter in the data, the probable error in $J/J_s$ was calculated based on the following probable error values in the measurement of the independent variables:

$$\Delta T_e = \pm 10\,°K \qquad\qquad \Delta T_R = \pm 2.5\,°K$$

$$\Delta T_c = \pm 10\,°K \qquad\qquad \Delta d = \pm 2\ \text{mils}$$

The probable error $\Delta\dfrac{J}{J_s}$ in the quantity $\dfrac{J}{J_s}$ is given by:

$$\Delta\frac{J}{J_s} = \pm\left(\left[\frac{\partial(J/J_s)}{\partial T_e}\right]^2 \Delta T_e^2 + \left[\frac{\partial(J/J_s)}{\partial T_c}\right]^2 \Delta T_c^2 + \left[\frac{\partial(J/J_s)}{\partial T_R}\right]^2 \Delta T_R^2 + \left[\frac{\partial(J/J_s)}{\partial d}\right]^2 \Delta d^2\right)^{1/2}$$

where:

$$\frac{\partial(J/J_s)}{\partial T_e} = C\,(Pd + D)\,\frac{1}{kT_{\epsilon e}}\,\frac{\partial \phi_e}{\partial T_e}$$

$$\frac{\partial(J/J_s)}{\partial T_R} = C\left[\frac{1}{kT_e}\,(Pd+D)\left(\frac{\partial \phi_e}{\partial T_R} - \frac{\partial \phi_c}{\partial T_R}\right) + \left(\frac{\partial P}{\partial T_R}\right)d\right]$$

$$\frac{\partial(J/J_s)}{\partial d} = -CP$$
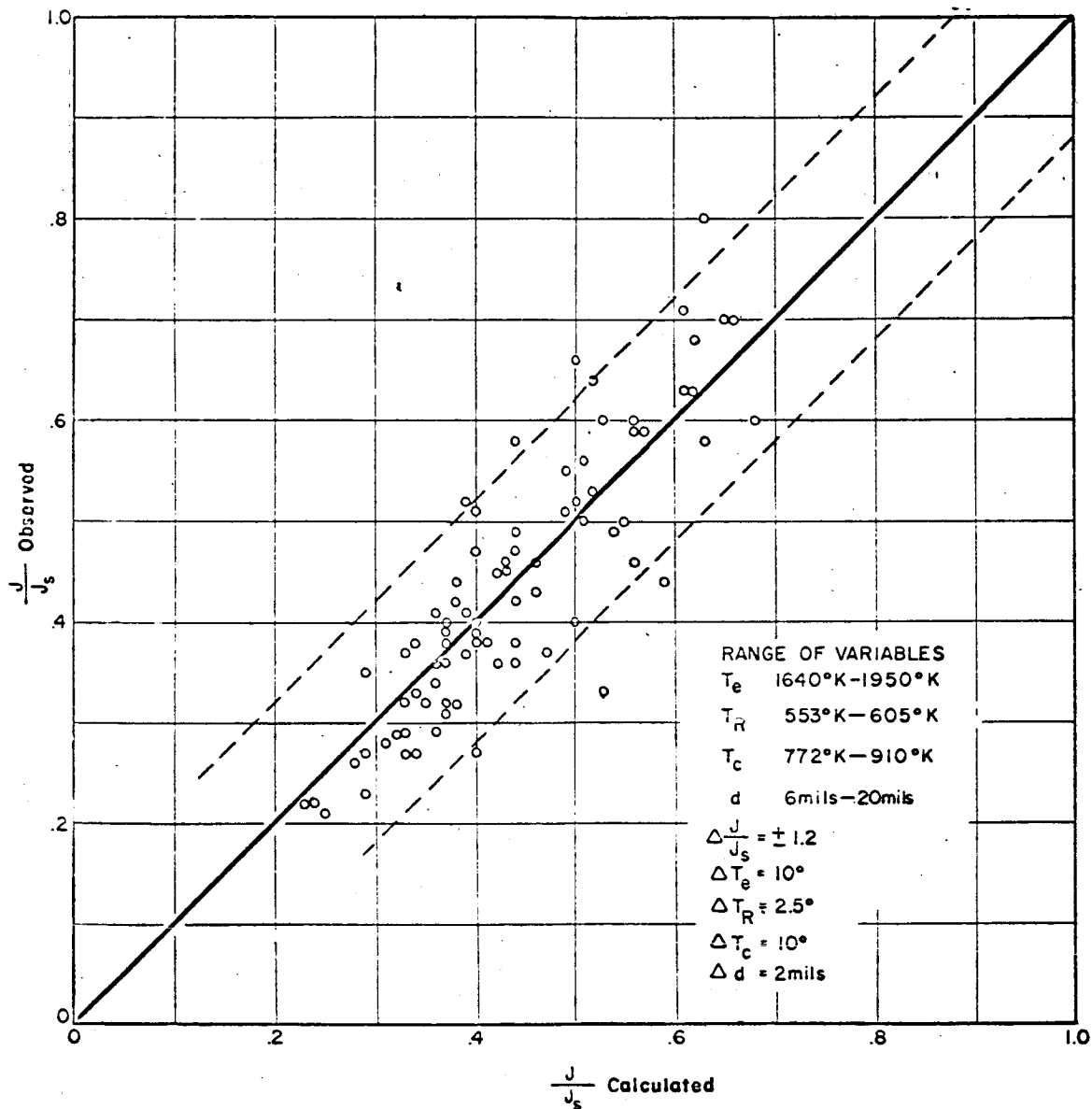
Figure IX-16. Comparison of Observed $J/J_s$ Values with $J/J_s$ Values Predicted Using Figure IX-15.

$$\frac{\partial (J/J_s)}{\partial T_c} = -C (Pd + D) \frac{1}{kT_{\epsilon c}} \frac{\partial \phi_c}{\partial T_c}$$

$$C = \frac{\frac{3}{4P\lambda} \exp\left[\frac{eV}{kT_{\epsilon e}} - \frac{\phi_e - \phi_c + V_c}{kT_{\epsilon c}}\right]}{1 + \frac{3}{4P\lambda} \exp\left[\frac{eV}{kT_{\epsilon e}} - \frac{\phi_e - \phi_c + V_c}{kT_{\epsilon c}}\right]}$$

The resulting probable error $\Delta J/J_s$ is $\pm 0.12$. This probable error band is identified by dashed lines in Figure IX-15. About 95% of the experimental points fall within this band.

The relationships developed here and summarized in Figure IX-15 can be used to predict any current-voltage characteristic of a diode with electrodes whose work function dependence on surface temperature and cesium pressure is known, as long as the quantity Pd is larger than 10 mil-torr. The changes in the output characteristics as a function of deviations in the various parameters from given design values can be readily determined; this knowledge is of particular value in thermionic system design.

3. Envelopes of Volt-Ampere Families

Families of J-V characteristics are generated by varying one parameter while all the others are held constant. The envelope of such a family is of special practical importance, since it represents the maximum current that is obtained for a given voltage by varying the chosen parameter. The envelope of a family of curves, $F(x, y, m)$, is defined as the curve M such that every member of the family is tangent to M,

and M is tangent, at each of its points, to some member of the family. The equation of the envelope is given by:

$$\frac{\partial F(x, y, m)}{\partial m} = 0 \qquad \text{and} \qquad F(x, y, m) = 0$$

The relations developed in Section D of this chapter can be used to obtain the equations of the envelopes.

a.   Emitter Temperature Envelope

The equation for a variable-emitter-temperature family is given by equation (55) with $T_e$ as the parameter. The envelope is given by

$$\frac{J_s}{J} = 1 + \frac{3}{8} \ (Pd + 1) \ \exp \left[ \frac{V - \phi_e + \phi_c - 0.4}{0.4} \right] \qquad (59)$$

and

$$\left[ \frac{\partial J}{\partial T_e} \right]_{T_R, \ T_c, \ d} = 0 \qquad (60)$$

where $J_s$ and $\phi_e$ are given by:

$$J_s = AT_e^2 \ \exp \left[ - \phi_c / k \ T_e \right]$$

$$\phi_e = 1.29 \left( \frac{T_e}{T_R} \right) - 1.33 \qquad \text{for } 3.2 > \frac{T_e}{T_R} > 2.8$$

Hence equation (60) becomes:

$$\frac{J}{J_s} = 1 + 0.62 \ \frac{T_R}{T_e} - 4.78 \times 10^3 \ \frac{T_R}{T_e^2} \qquad (61)$$

3/7

Equations (59) and (61) represent a single relation for the envelope of the family with parameter $T_e$, since $T_e$ can be eliminated between the two equations. To test these relationships, several variable $T_e$ families were obtained experimentally. Figure IX-17 shows a sample of such data at $T_R = 577°K$, $T_C = 980°K$, d = 22 mils. The theoretical J-V characteristic of the saturation mode is plotted in Figure IX-18 for the same conditions, and the envelope is shown by the dashed curve. The agreement between the experimental data and theoretical relations is reasonably good for $V > 0.5$ volt, but the correlation breaks down at lower voltages. The discrepancy is probably due to the following reasons:

(1) In Section C of this chapter, the saturation and obstructed modes of discharge were treated separately, and appropriate relations were developed for each mode. These relations, however, are not valid in the transition region of the two modes, since they assume a sharp transition point. It is evident from the experimental data that there is a gradual transition from the saturation mode to the obstructed mode, and the transition region becomes broader with decreasing $T_e$. This effect can explain the departure of theoretical and experimental envelopes at lower emitter temperatures ($V < 0.5$). The analytical treatment of the transition region is a difficult task at this stage, and an empirical approach is necessary.

(2) The relations developed for the modes of discharge are strongest in predicting the dependence of volt-ampere characteristics on spacing. It will be shown in the following section that the cesium reservoir temperature dependence

318

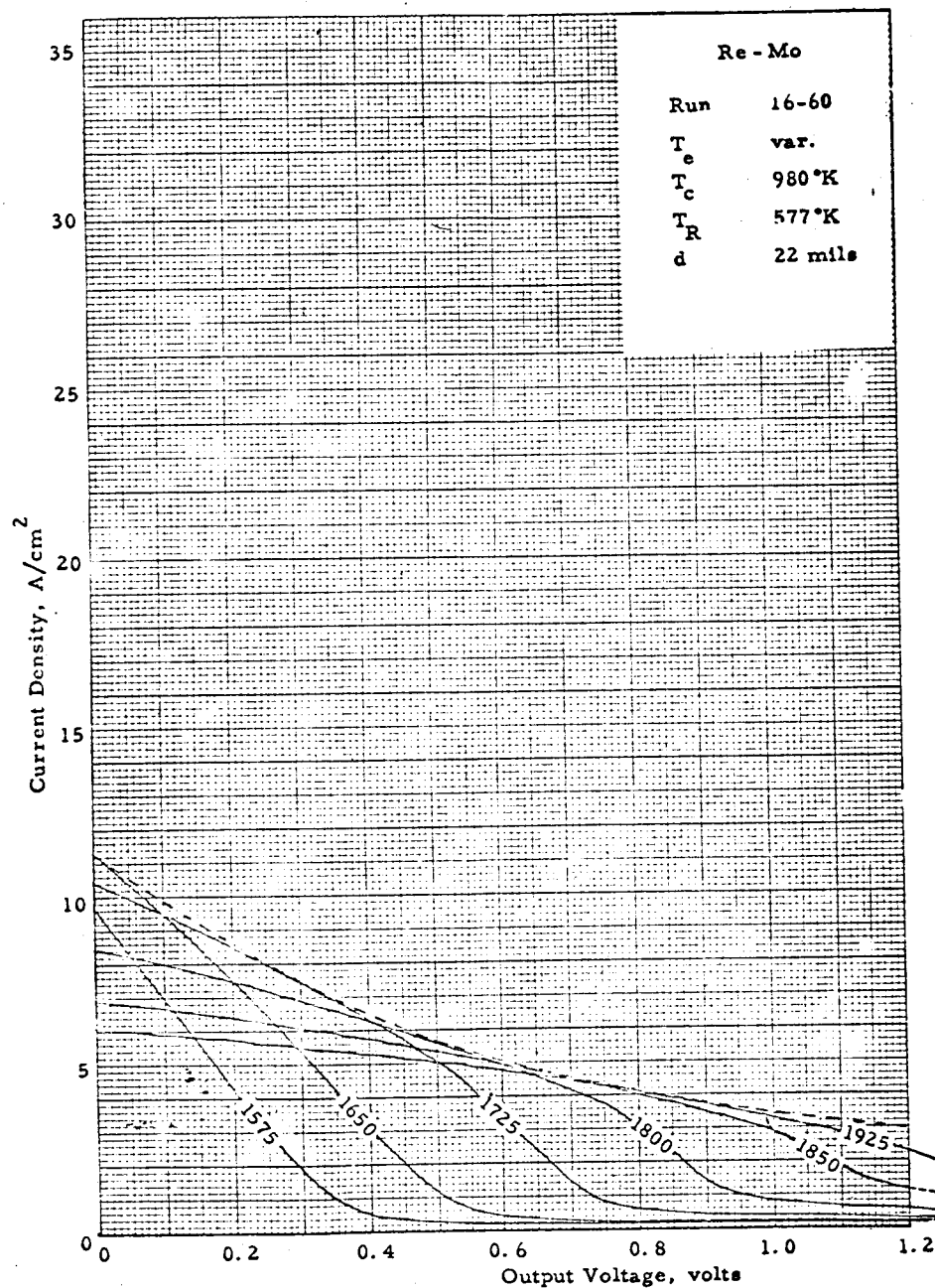| Re - Mo | |
|---|---|
| Run | 16-60 |
| $T_e$ | var. |
| $T_c$ | 980 °K |
| $T_R$ | 577 °K |
| d | 22 mils |

Figure IX-17.   Typical Experimental Variable-Emitter-Temperature
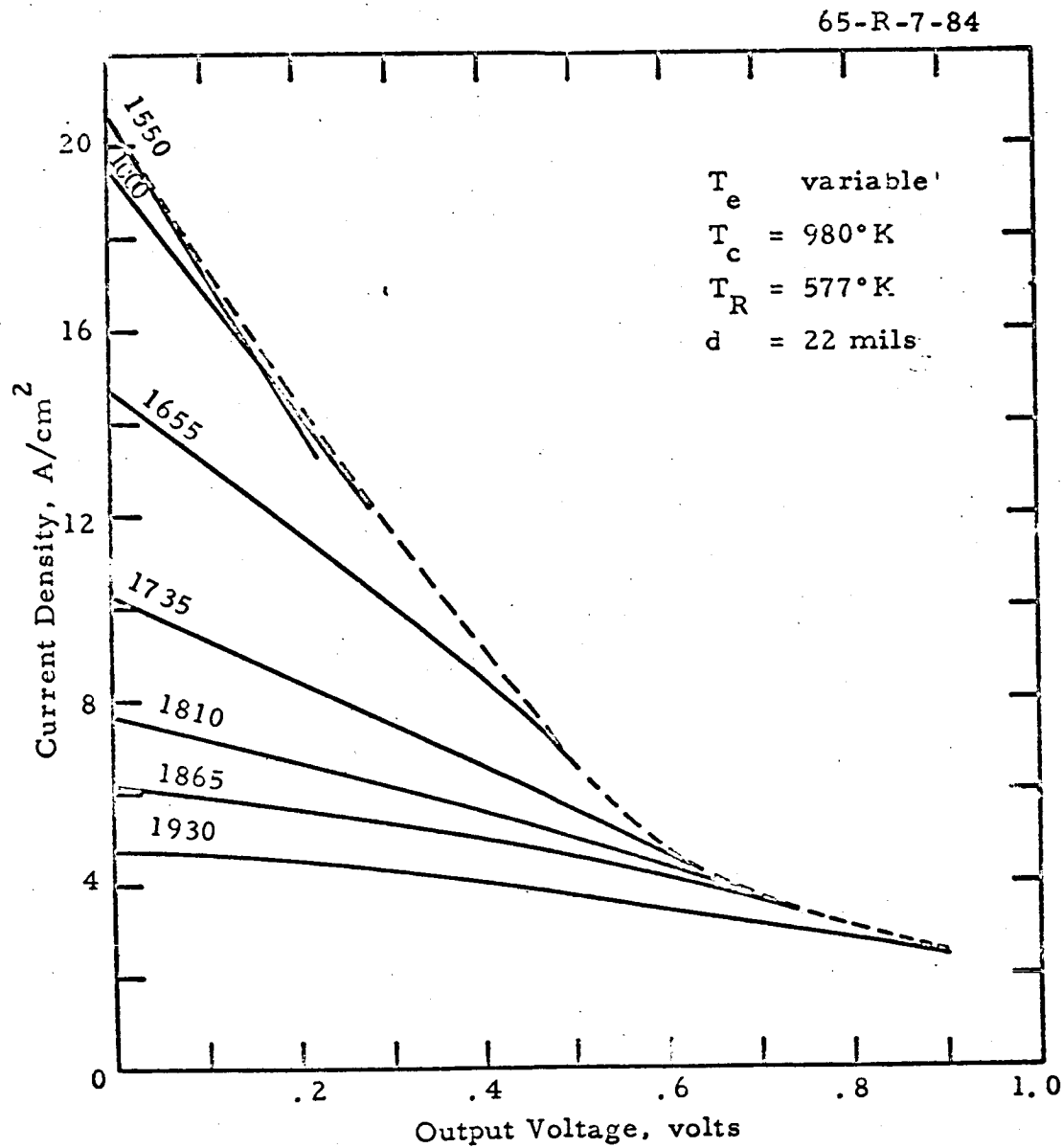J-V Characteristics.

319

Figure IX-18.  Calculated J-V Characteristics corresponding
to Figure IX-17.

is also predicted reasonably well by these relations. The
disagreement of the theory with the experimental results
at lower emitter temperatures suggests that there might
be a $T_e$ dependence which is not included in equations (52),
(53), and (54). The parameters $T_e$ and $V_c$ are examples
of those likely to be emitter-temperature dependent.
Another possibility is that these parameters are a function
of output voltage. Since lower emitter temperatures corres-
pond to lower voltages, V or $T_e$ dependence cannot be dis-
tinguished from this data.

b.    Cesium Reservoir Temperature Envelope

This envelope has been identified previously[3,12,21] as the
locus of the inflection of each member of the family. The inflection
point was discussed in Section 2 and is defined by equation (56). Hence,
equations (55) and (56) represent a single relation for the envelope since
the parameters P, $V_d$, $\varphi_e$ and $\varphi_c$ are functions of $T_R$, which can be
eliminated between the two equations.

Several variable-reservoir-temperature families have been
obtained experimentally and are shown in Appendix C. The envelopes
calculated from equations (55) and (56) have been compared with the
experimental data, and the agreement was within 0.1 volt. Figures
IX-19 to IX-22 are examples of such a comparison. The dashed curves
represent the experimental data taken from runs in Appendix C, corrected
for lead losses. The solid curves calculated from equations (55) and (56)
agree quite well with the experimental curve for $T_e$ = 1800°K (Figures
IX-20 and IX-21). The correspondence at the two ends of the temperature
range covered is not so good and is shown in Figures IX-19 and IX-22.

321
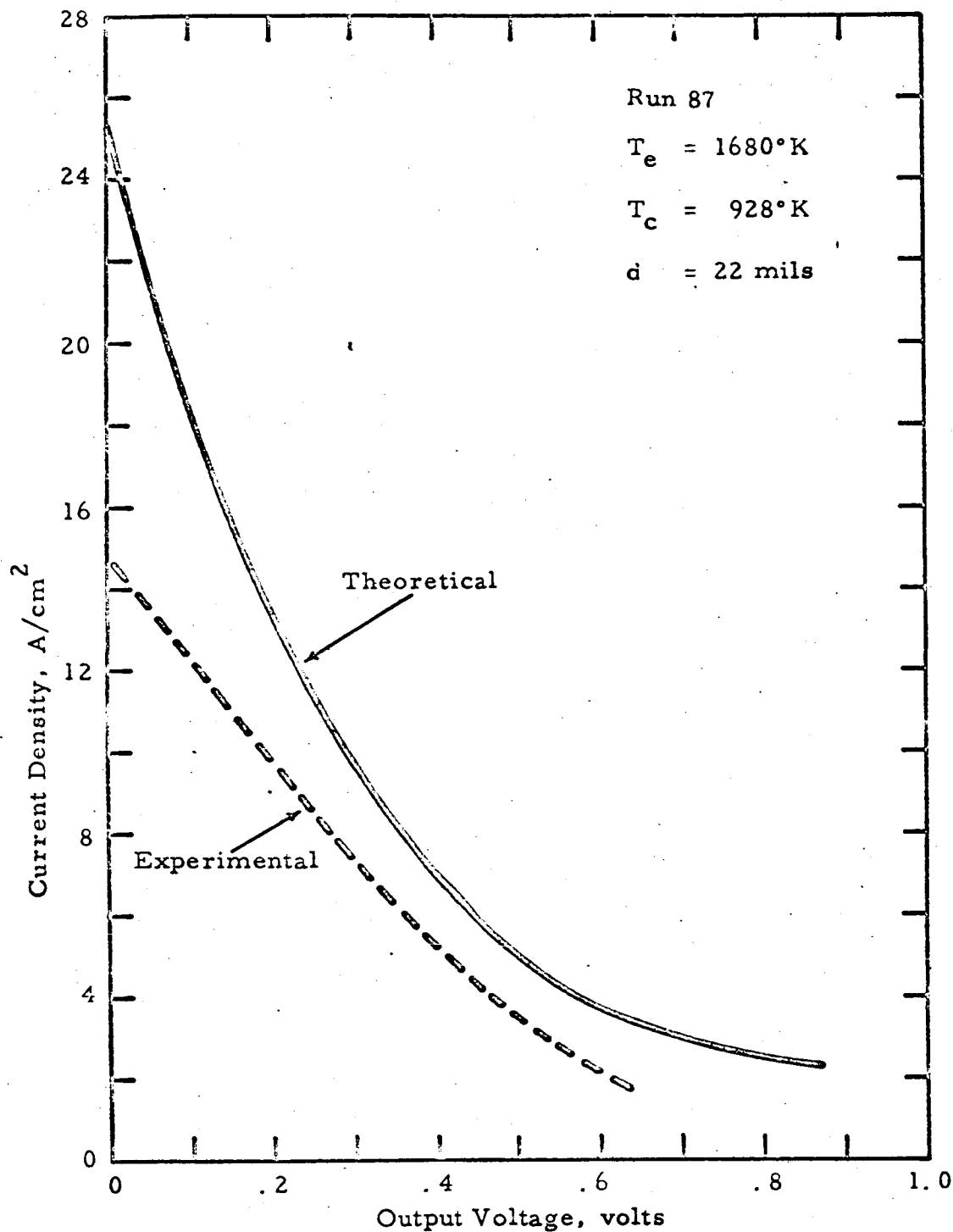
Figure IX-19. Comparison of Theoretical $T_R$ Envelope with Experimental Data.
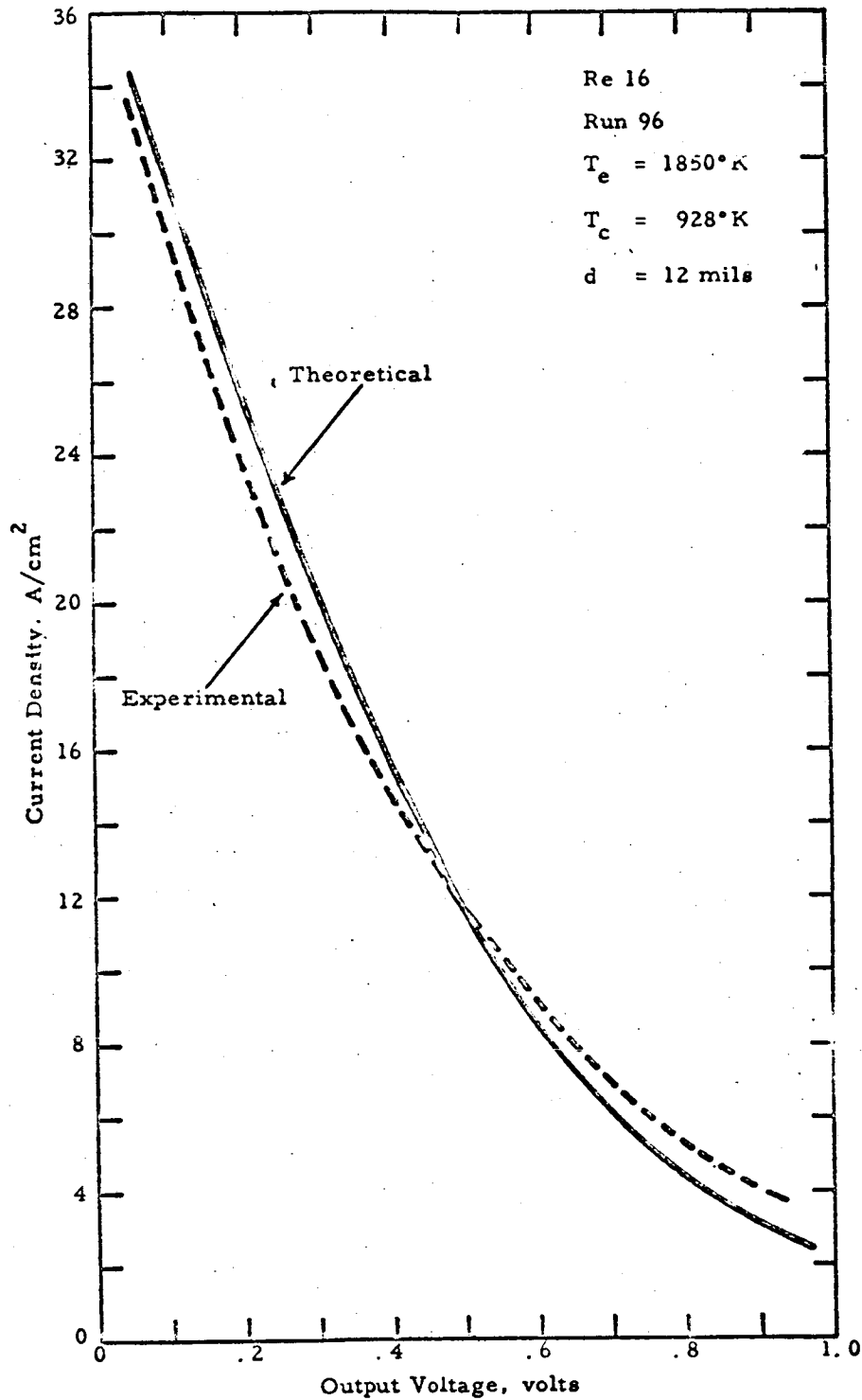
Figure IX-20.  Comparison of Theoretical $T_R$ Envelope
with Experimental Data.

323
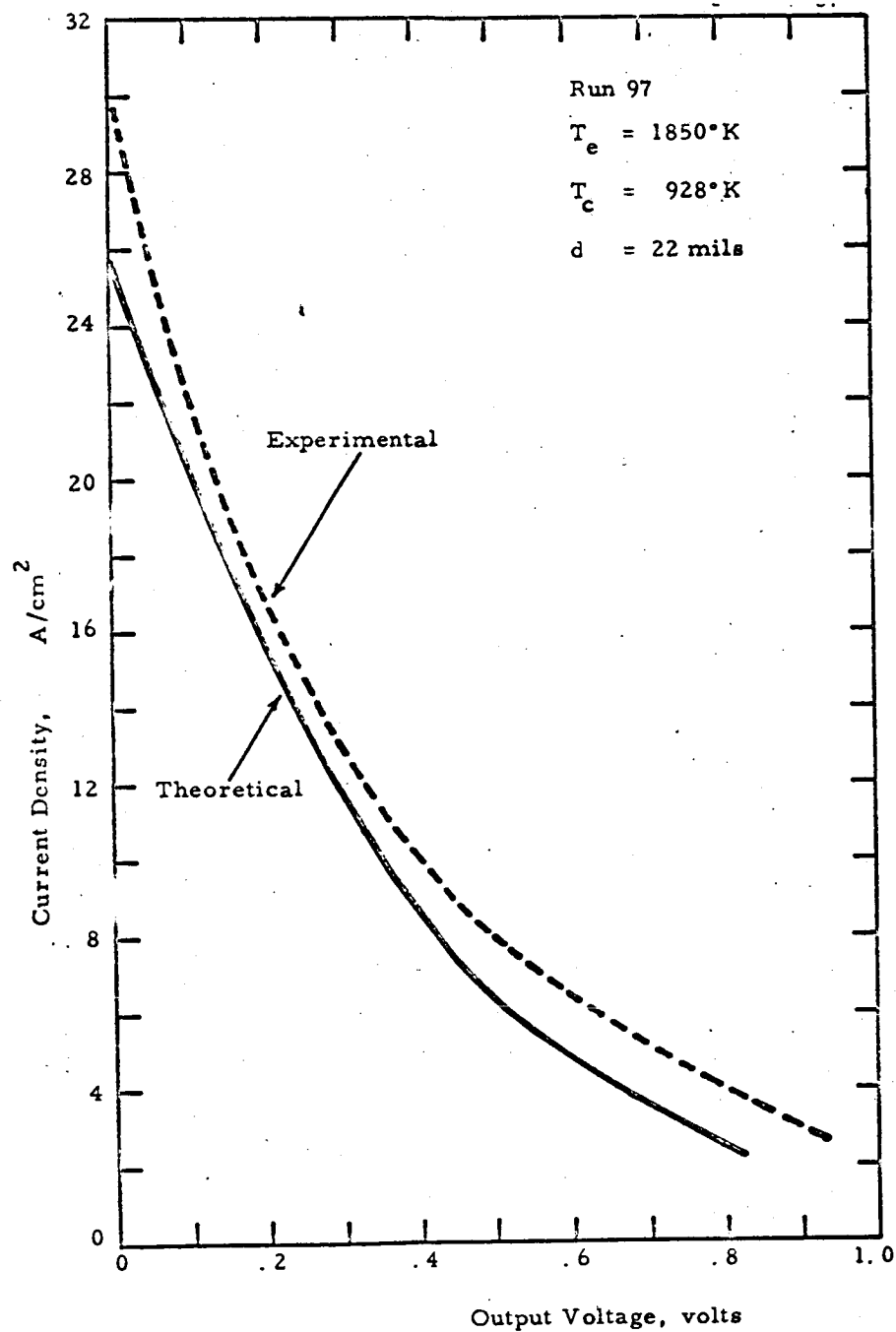
Figure IX-21. Comparison of Theoretical $T_R$ Envelope
with Experimental Data.
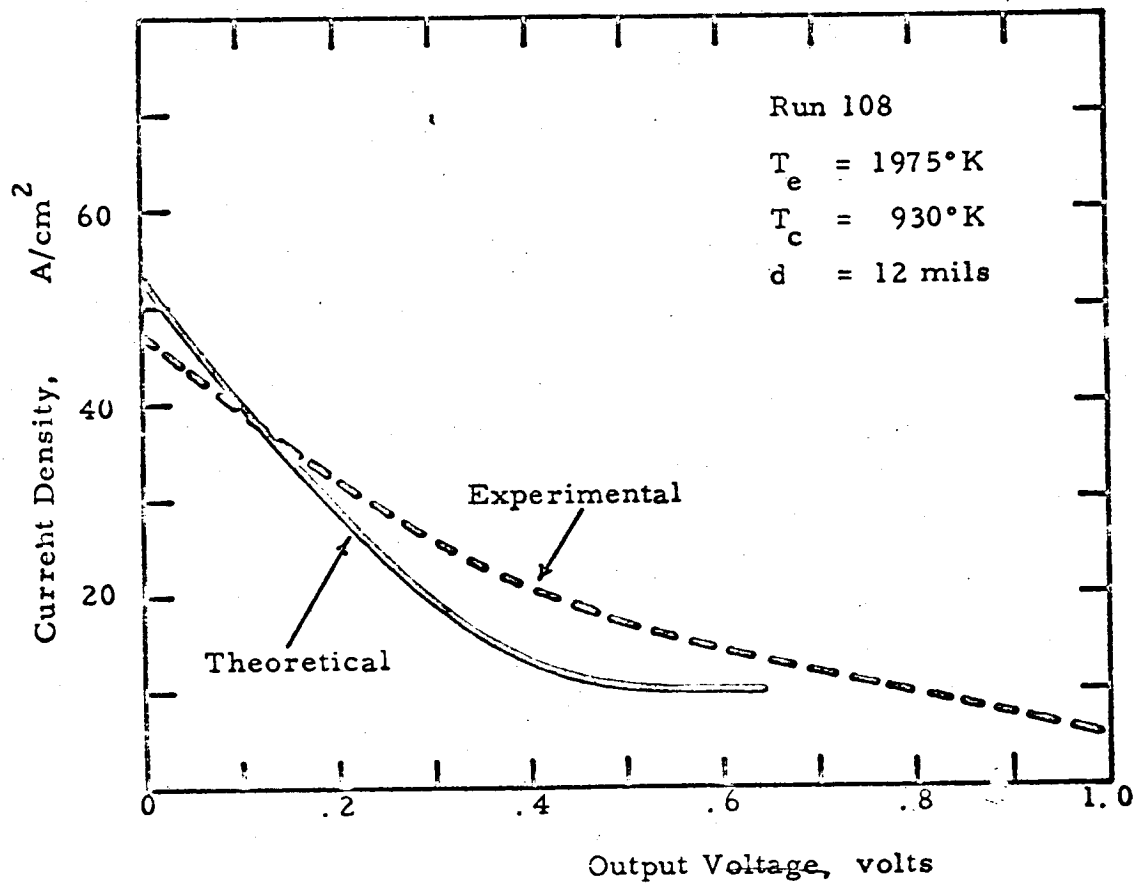
Figure IX-22.   Comparison of Theoretical $T_R$ Envelope
with Experimental Data.

325

The $T_e$ dependence of the parameters $V_c$ and $T_\epsilon$ discussed previously seems to be appearing again. From examination of Figures IX-19 to IX-22 it is evident that the theory overestimates the current at lower voltages. This departure suggests that the parameters $V_c$ and $T_\epsilon$ are functions of voltage also.

The inadequacies of the theory uncovered by this type of extensive testing with experimental results will be the subject of refinements planned in future work. The usefulness of discovering such discrepancies lies in the fact that experimental work can be designed to provide the exact data necessary for revising the theory.

326

# REFERENCES

1. Thermophysical Properties Research Center Data Book, Vol. 1, "Metallic Elements and their Alloys," published by Purdue Univ., Lafayette, Indiana.

2. S. S. Kitrilakis, M. E. Meeker, N. S. Rasor, Annual Technical Summary Report for the Thermionic Emitter Materials Research Program (1 July 1961 through 30 June 1962), Contract NONR-3563(00); prepared for Office of Naval Research, Power Branch, Dept. of the Navy, Washington 25, D. C., Report No. TE 2-63.

3. S. S. Kitrilakis and J. H. Weinstein, Second Annual Technical Summary Report for the Thermionic Emitter Materials Research Program (1 July 1962 through 30 September 1963), Contract NONR-3563(00); prepared for Office of Naval Research, Power Branch, Dept. of the Navy, Washington 25, D. C.; Report No. TE 27-64.

4. S. S. Kitrilakis and J. H. Weinstein, Additive Converter Studies, Technical Documentary Report No. APL-TDR-64-2, Contract No. AF33(657)-10130; prepared for Air Force Aero Propulsion Laboratory, Research and Technology Division, Air Force Systems Command, Wright-Patterson Air Force Base, Ohio; Report No. TE 35-64.

5. G. Miskolczy et al, Final Technical Report, Emitter Crystal Structure Study, Contract No. 950228, February 1964, prepared for the Jet Propulsion Laboratory, Pasadena, California, Report No. TE 36-64.

6. L. van Someren, Preparation of Thermionic Emitters, Trans. Thermionic Converter Specialists Conference, Cleveland, Ohio, Oct. 1964, p. 11.

7. Drayton, Trans. AIME, 116, 405, and 117, 119 (1935).

8. Mullins, W. W., J. Appl. Phys., 28, 333 (1957).

9. A. Shavit and S. S. Kitrilakis, Third Annual Technical Summary Report, AFCRL-64-721, March 1964, "Effect of Electrode Configuration on Thermionic Converter Output Characteristics," Report No. TE 7-65.

327

## REFERENCES (cont. )

9.     Warner, et al, Second Annual Technical Summary Report for
       Basic Research in Thermionic Energy Conversion, Al-7979.

10.    S. Kitrilakis, A. Shavit and N. Rasor, Rept. of MIT Physical
       Electronics Conf. (Mar. 1964), p. 171.

11.    N.S. Rasor and S.S. Kitrilakis, "Basic and Engineering Implica-
       tions of Correlated Converter Phenomenology, " presented at the
       Thermionic Conversion Specialist Conference, Cleveland, Ohio,
       Oct. 1964. Published in the Proceedings.

12.    E.O. Johnson, RCA Rev. XVI, 498 (1955).

13.    L. Hansen and C. Warner, Rept. of Thermionic Conv. Specialist
       Conf., Gatlinburg (Oct. 1963), pp. 44, 51.

14.    L. Tonks and I. Langmuir, Phys. Rev. 33 195 (1929).

15.    J. Houston, Rept. of Thermionic Conv. Specialist Conf.,
       Cleveland (Oct. 1964).

16.    L. Hansen and C. Warner, ibid, p. 310.

17.    A. Shavit and G. Hatsopoulos, ibid, p. 206.

18.    W.H. Reichelt, ibid, p. 266.

19.    C. Warner, private communication

20.    S.S. Kitrilakis, "Correlation of Internal Voltage Loss in
       Optimized Thermionic Converters, " presented at the Third
       Annual Symposium on High Temperature Conversion Heat to
       Electricity, University of Arizona, February 1964. Published
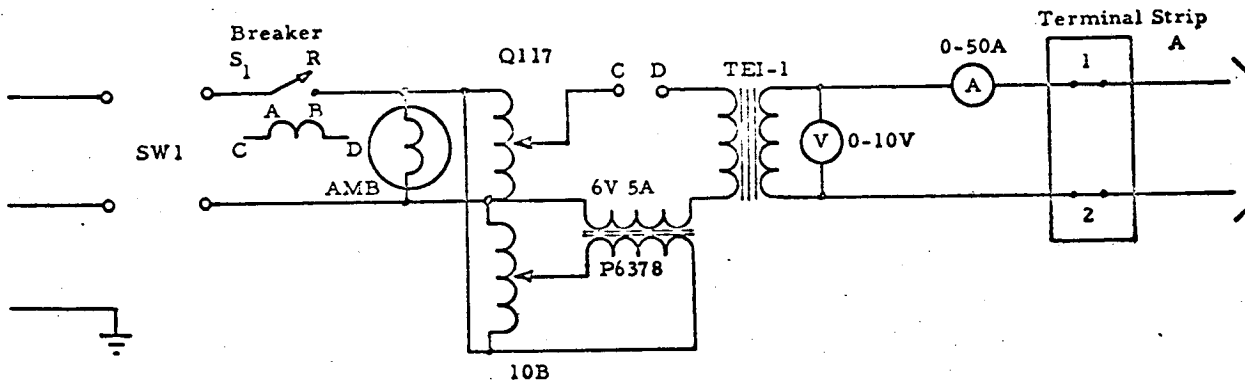       in the Proceedings.

APPENDIX A

INSTRUMENTATION SCHEMATICS

329

Figure A-1. Circuit Diagram of E.B. Supply.

330
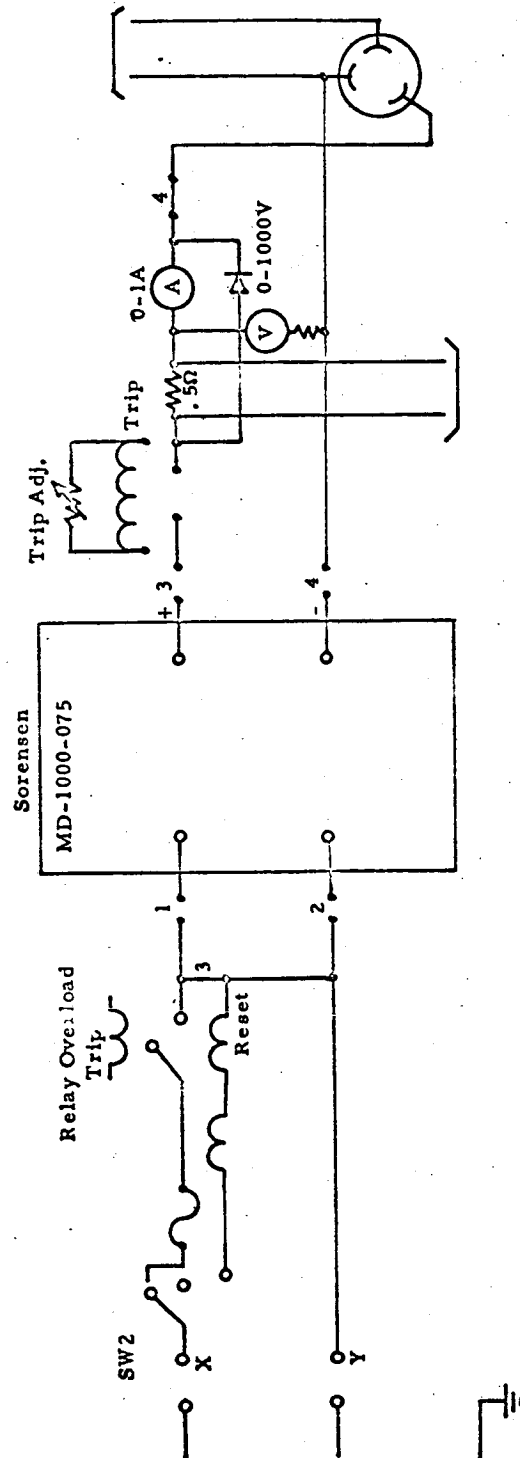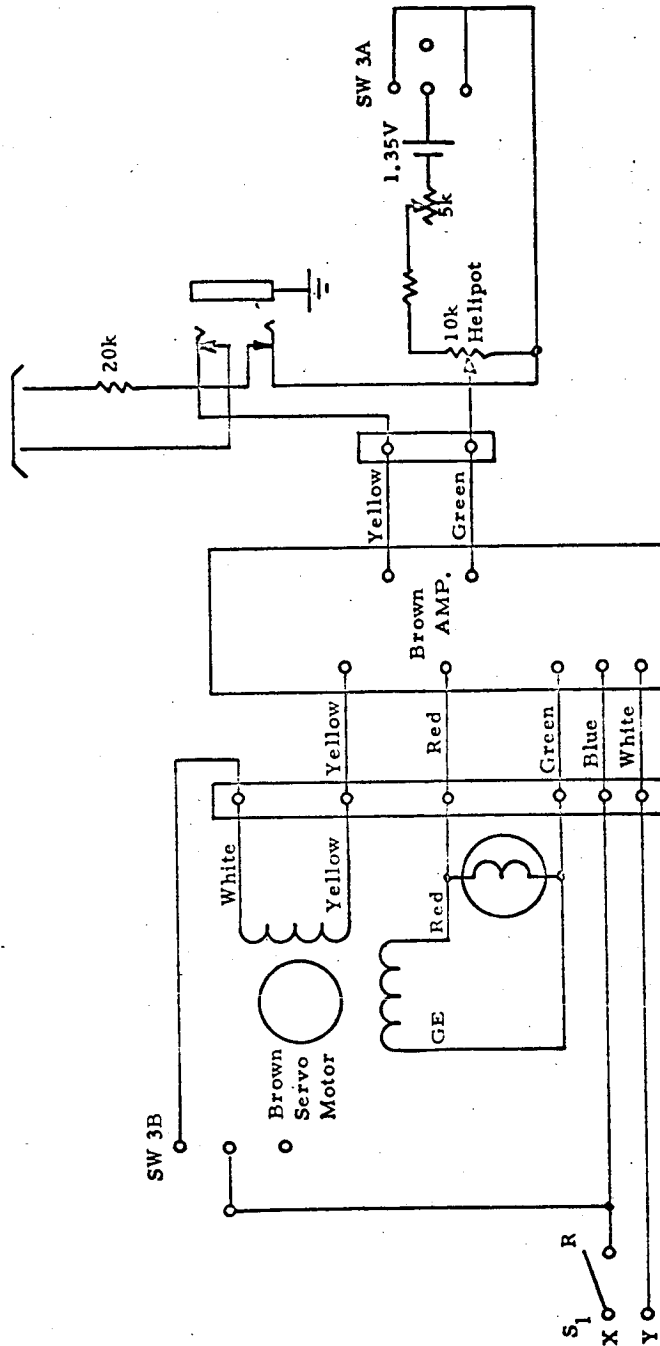
Figure A-2. Circuit Diagram of E.B. Supply.

331

Figure A-3.  Circuit Diagram of E. B. Supply.

332
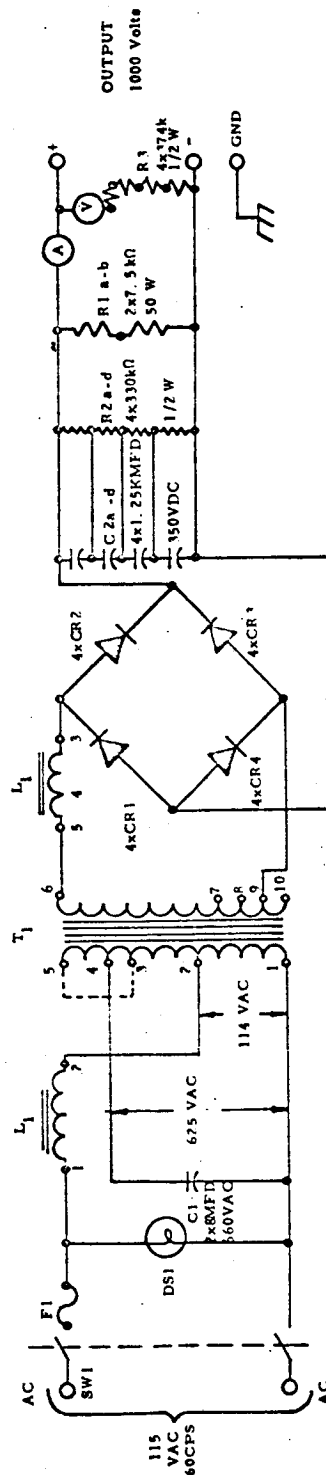
Figure A-4.   Circuit Diagram of Sorensen B200-2681C Power Supply.
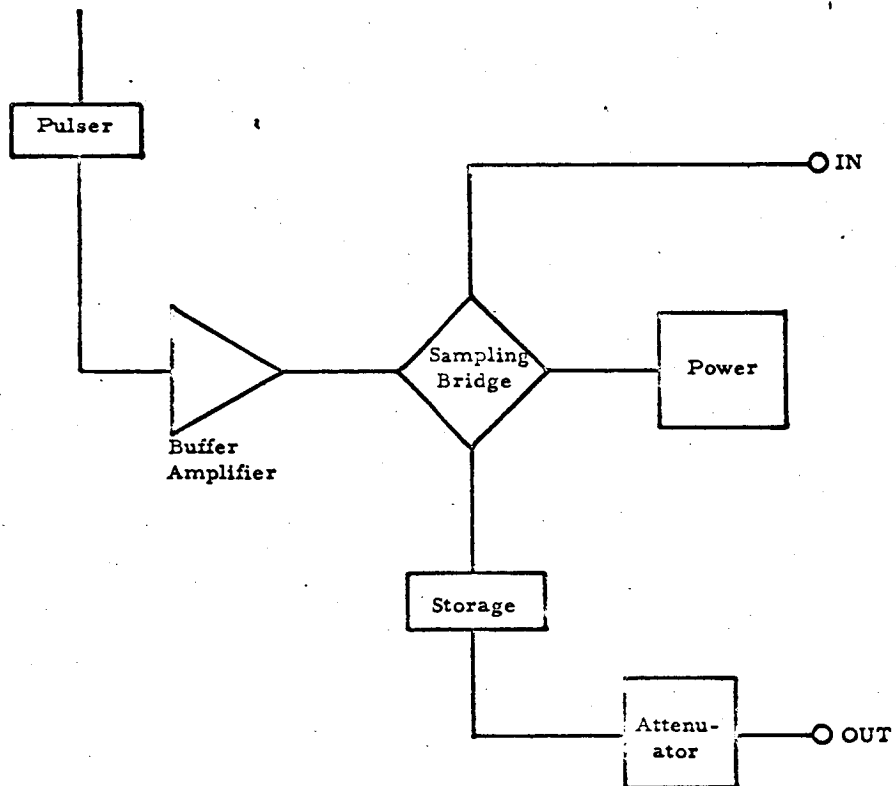
Figure A-5.   Block Diagram for Sampler.

33.4

Figure A-6. Sampler Circuit Diagram.
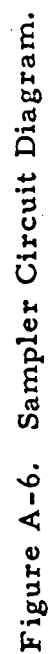
## APPENDIX E

## DIFFUSION OF ELECTRONS THROUGH PLASMA

This treatment is similar to that by C. Warner[9] for the extinguished mode.

A neutral, field-free plasma, bounded by emitter and collector sheaths of height $V_e$ and $V_c$, as in Figure IX-5a, is assumed. Since no significant source or sink of electrons exists in the plasma,

$$\frac{d^2 n}{dx^2} = 0 \qquad (E-1)$$

where n is the density of electrons at a distance x from the emitter side of the plasma. The solution of equation (E-1) is

$$n = Mx + N \qquad (E-2)$$

where M and N are constants determined by the boundary conditions.

At the emitter side of the plasma (x = 0) the electron current entering the plasma is

$$\frac{n_e \bar{v}}{4} + \frac{J}{2} = J_s + \left( \frac{n_e \bar{v}}{4} - \frac{J}{2} \right) \left\{ 1 - \exp \left[ -V_e / kT_{ee} \right] \right\} \qquad (E-3)$$

Similarly, at the collector side (x = d),

$$\frac{n_c \bar{v}}{4} - \frac{J}{2} = J_{cs} + \left( \frac{n_c \bar{v}}{4} + \frac{J}{2} \right) \left\{ 1 - \exp \left[ -V_c / kT_{ec} \right] \right\} \qquad (E-4)$$

where $n_e$ and $n_c$ are the respective electron densities at the emitter and collector edges of the plasma, $\bar{v}$ is the average electron velocity,

E-1

336

$J_s$ and $J_{cs}$ are the respective saturation emission currents from the emitter and collector, J is the net electron current received by the collector, $T_{\epsilon e}$ and $T_{\epsilon c}$ are the respective electron temperatures at the emitter and collector edges of the plasma, and k is Boltzmann's constant. The variation of $\bar{v}$ with the electron temperature is neglected for simplicity here.

The diffusion of the net electron current J through the plasma is required by Fick's law to be

$$J = \frac{\bar{v}\lambda}{3} \frac{dn}{dx} \tag{E-5}$$

where $\lambda$ is the electron mean free path.

Combining equations (E-2) through (E-5) gives

$$\frac{J_s}{J} = a + b\left(\frac{d}{\lambda}\right) \tag{E-6}$$

where
$$a = \frac{\exp(V_e/kT_{\epsilon e}) + \exp(V_c/kT_{\epsilon c}) - 1}{\exp(V_e/kT_{\epsilon e}) - \dfrac{J_{cs}}{J_s}\exp(V_c/kT_{\epsilon c})}$$

$$b = \frac{3/4}{\exp(V_e/kT_{\epsilon e}) - \dfrac{J_{cs}}{J_s}\exp(V_c/kT_{\epsilon c})}$$

If the collector emission is negligible, equation (E-6) simplifies to the form given as equation (40) in Chapter IX.

337

# APPENDIX F

## ELECTRON TEMPERATURE DROP ACROSS PLASMA

A general consequence of electron flow through a plasma is an electron temperature gradient. In analogy with the well-known electron heating and cooling effects at electrode surfaces, a large heat flux is similarly introduced into the emitter side of the plasma by the incoming electrons, and a large fraction of this heat is removed from the collector side by the outgoing electrons. For any distance x from the emitter side, where the electron temperature is $T_\epsilon$, continuity of heat flow requires that

$$J(V_c + 2kT_{\epsilon c}) = 2kT_\epsilon J + K_\epsilon (dT_\epsilon/dx) \qquad (F-1)$$

This equation states that the electron cooling of the plasma at the collector side equals the heat of transport $2kT_\epsilon J$ due to the net electron flow plus the thermal conduction down a temperature gradient in the electron gas of thermal conductivity $K_\epsilon$. Elementary kinetic theory gives $K_\epsilon = 2k\lambda J_r$ for $d \gg \lambda$, where $J_r$ is the random electron current density. Integration of equation (F-1) and substitution for $K_\epsilon$ gives

$$T_{\epsilon e} - T_{\epsilon c} = \frac{V_c}{2k} \left( 1 - \exp\left[ -\frac{J}{J_r} \frac{d}{\lambda} \right] \right) \qquad (F-2)$$

Therefore, for small $d/\lambda$ the electron temperature approaches uniformity. However, as $d/\lambda$ exceeds $J_r/J$, the electron temperature drop across the plasma approaches $V_c/2k$.

The heat removed by excitation, and the x-dependence of $J_r$ are neglected in this simplified treatment.

## APPENDIX G

## HEIGHT OF COLLECTOR SHEATH

If $\exp(-V_c/kT_{\epsilon c}) \ll 1$, positive ion space charge predominates over most of the collector sheath. Assuming that ion scattering is insignificant in the sheath itself, the Langmuir-Child space charge equation gives

$$J_{ic} = en_{ic}\left(\frac{2kT_c}{\pi M}\right)^{1/2} = \frac{1}{9\pi e}\left(\frac{2}{M}\right)^{1/2}\left(\frac{V_c}{w^2}\right)^{3/2} \tag{G-1}$$

where $T_c$ is the temperature of the collector, $w$ is the thickness of the collector sheath, and $n_{ic}$ is the ion density at the collector edge of the plasma. Since the collector sheath thickness cannot greatly exceed the Debye length $h$, it is convenient to express $w$ in terms of $h$,

$$w = Nh = N\left(\frac{kT_{\epsilon c}}{4\pi n_{ic}e^2}\right)^{1/2} \tag{G-2}$$

where $N$ is the number of Debye lengths in the sheath. Equations (G-1) and (G-2) combine to give

$$\frac{V_c}{kT_{\epsilon c}} = \frac{1}{\pi^{1/3}}\left(\frac{3}{2}\right)^{4/3}\left(\frac{T_c}{T_{\epsilon c}}\right)^{1/3}N^{4/3} = 1.17\left(\frac{T_c}{T_{\epsilon c}}\right)^{1/3}N^{4/3} \tag{G-3}$$

For present plasma conditions ($T_c \approx 700°K$ and $T_{\epsilon c} \approx 2500°K$),

$$\frac{V_c}{kT_{\epsilon c}} \approx 0.8 N^{4/3},$$ and $N$ should be near unity.

339

## APPENDIX H

## ELECTRON TEMPERATURE REQUIRED TO SUSTAIN THE IGNITED MODE

The rate at which ions are produced in a gas from impact ionization by an electron gas at temperature $T_\epsilon$ is

$$\frac{dn_i}{dt} = n_e p K_i \left(2 + \frac{V_i}{kT_\epsilon}\right)\left(\frac{T_\epsilon}{T_o}\right)^{1/2} \left(\frac{M}{m}\right)^{1/2} \left(\frac{kT_o}{2\pi M}\right)^{1/2} \exp\left(-\frac{V_i}{kT_\epsilon}\right) \quad \text{(H-1)}$$

where $n_i$ and $n_e$ are, respectively, the ion and electron densities; $p$, $T_o$, $M$ and $V_i$ are, respectively, the pressure, temperature, atomic mass and ionization energy of the gas, $m$ is the electron mass; and $K_i$ is the initial rate of increase of ionization cross section $\sigma_i$ with electron energy. $U$ above the threshold, i.e., $K_i = (d\sigma_i/dU)_{U=V}$. This equation assumes that the density of excited atoms is much less than the gas density. The rate at which ions leave unit area of such a plasma, for a symmetrical one-dimensional system, has been shown to be[14]

$$\left.\begin{aligned} \mu_{iL} &= 0.345\, n_\epsilon \left(\frac{2kT_\epsilon}{M}\right)^{1/2} && \text{for } \lambda_i \gg d' \\[2em] \mu_{is} &= 0.895\, \pi \frac{n_\epsilon}{Pq} \left(\frac{kT_o}{M}\right)^{1/2} \frac{kT_\epsilon}{d} && \text{for } \lambda_i \ll d' \end{aligned}\right\} \quad \text{(H-2)}$$

where $\lambda_i$ is the ion mean free path, $q$ is the cross section for ion diffusion through the plasma, and $d'$ is the effective width of the ion generation region.

Because of the large electron temperature drop across the plasma (Appendix F), most of the ions are produced on the emitter side of the plasma, so it is assumed that most ions leave the plasma at the emitter side. Accordingly, at steady state, the rate at which ions leave the plasma at the emitter, $\mu_{iL}$ or $\mu_{is}$, must equal the total rate of ion production per unit area of plasma, $(dn_i/dt)d'$. Therefore, equations (H-1) and (H-2) combine to give

$$
\left.
\begin{aligned}
kT_\epsilon &= \frac{V_i}{\ln(B_L Pd')} \qquad && \text{for } \lambda_i \gg d' \\[1em]
\text{or} && \\[1em]
kT_\epsilon &= \frac{V_i}{2\ln(B_s Pd')} \qquad && \text{for } \lambda_i \ll d'
\end{aligned}
\right\} \qquad \text{(H-3)}
$$

where

$$
\left.
\begin{aligned}
B_L &= 3.2 \left(\frac{M}{m}\right)^{1/2} \left(2 + \frac{V_i}{kT_\epsilon}\right) \frac{T_\epsilon}{T_o} K_i \approx 60 \,(\text{mil-torr})^{-1} \\[1.5em]
B_s &= 0.75 \left(\frac{M}{m}\right)^{1/4} \left(2 + \frac{V_i}{kT_\epsilon}\right)^{1/2} \left(\frac{T_\epsilon}{T_o}\right)^{3/4} \left(\frac{K_i q}{kT_\epsilon}\right)^{1/2} \approx 3.6 \,(\text{mil-torr})^{-1}
\end{aligned}
\right\} \text{(H-4)}
$$

The values $K_i = 4 \,\overset{\circ}{A}{}^2/eV$ and $q = 1200 \,\overset{\circ}{A}{}^2$, used to compute the values of $B_L$ and $B_s$ shown, have been estimated by Houston[15] to be the most probable. The uncertainties introduced by the unsymmetrical plasma, the non-uniform electron temperature, and the relation of d to d', are probably no greater than the combined uncertainties in these values. In any event, the computed electron temperature is quite insensitive to the value of B or d' for Pd' >> 10 mil-torr.

## APPENDIX J
## ENERGY BALANCE FOR PLASMA

Equating energy input and energy loss for the plasma gives

$$J'_s (V_e + 2kT_e) = J (V_c + 2kT_{\epsilon c}) + (J'_s - J)(V_e + 2kT_{\epsilon e}) + e\mu_x V_x \qquad (J-1)$$

The first three terms are the energies carried into and out of the plasma by the electron currents identified in Figure IX-5c. The last term is the energy removed from the plasma by the current of excited atoms $\mu_x$ or their decay photons, where $V_x$ is the excitation energy. The rate of production of excited atoms is given by equation (G-1) with $V_x$ substituted in place of $V_i$, and the analogous quantity $K_x$ for $K_i$. Accordingly,

$$\frac{\mu_x}{\mu_i} = \frac{K_x}{K_i} \frac{2 + V_x/kT_\epsilon}{2 + V_i/kT_\epsilon} \exp\left(\frac{V_i - V_x}{kT_\epsilon}\right) \qquad (J-2)$$

If the Langmuir double sheath relation holds at the emitter

$$J = \left(\frac{M}{m}\right)^{1/2} \mu_i e \qquad (J-3)$$

Equations (J-1) to (J-3) combine to give

$$V_e = (2kT_{\epsilon e} - 2kT_e) \frac{J'_s}{J} + C\,[\,B\,Pd'\,]^{b(1-V_x/V_i)} \qquad (J-4)$$

where $\qquad C = V_x \left(\frac{m}{M}\right)^{1/2} \frac{K_x}{K_i} \frac{2 + V_x/kT_\epsilon}{2 + V_i/kT_\epsilon}$

$B = B_s$ and $b = 2$ for $\lambda_i \ll d'$; $B = B_L$ and $b = 1$ for $\lambda_i \gg d'$. In view of the relations in equations (40), (42), and (50), equation (J-4) enforces a unique relationship between $V_e$ and $Pd'$.

For the obstructed mode, as discussed in the text, the fraction of back-reflected current from the bright plasma which reaches the emitter becomes negligibly small, eliminating the term in $J'_s - J$ in equation (J-1). Equation (J-4) then becomes

$$V'_e = 2kT_e - 2kT_e + C(BPd')^{b(1 - V_x/V_i)} \qquad (J-5)$$